THÈSE DE DOCTORAT

$$\rho\left(\frac{\partial v}{\partial t} + v \cdot \nabla v\right) = -\nabla p + \nabla \cdot T + f$$

$$e^{i\pi} + 1 = 0$$

Dynamique et statistiques de particules allongées et flexibles dans des écoulements turbulents

Sofía Allende Contador

Centre de mise en forme de matériaux - MINES ParisTech

Présentée en vue de l'obtention du grade de Docteur en Physique de l'Université Côte d'Azur

Dirigée par Jérémie BEC

Soutenue le 4 mars 2021

Devant le jury, composé de :

Mme.	Mireille Bossy	DR INRIA, Université Côte d'Azur	Examinatrice
Mme.	Lydia Bourouiba	Professor, MIT (Etats-Unis)	Examinatrice
Mme.	Olivia du Roure	DR CNRS, Université PSL	Examinatrice
Mme.	Francisca Guzmán-Lastra	Associate professor, Universidad Mayor (Chili)	Examinatrice
M.	Stefano Musacchio	Chercheur, Università di Torino (Italie)	Rapporteur
M.	Gautier Verhille	CR CNRS, Aix-Marseille Université	Rapporteur
M.	Dario Vincenzi	CR CNRS, Université Côte d'Azur	Examinateur
M.	Jérémie Bec	DR CNRS, Mines ParisTech	Directeur de thèse

ABSTRACT

This thesis analyses the dynamics of small complex objects immersed in a turbulent environment. Turbulent flows are akin to apparent random fields, that usually display very non-Gaussian and fluctuating statistics, and which are known to enhance the mixing and the transport of the objects that they carry. Here, we focus on the transport of small complex particles, which are characterized by a non-trivial interplay between their mass, their shape and their rheology. Our aim is to gain a physical understanding on how turbulent fluctuations prescribe the dynamics of such complex particles, and lead to various physical phenomena, including preferential concentration, their deformation or catastrophic events such as their fragmentation. Studying such phenomena is relevant for both industrial and sustainability issues. For instance, while volcanic ash has direct impacts for the commercial flight industry, the blooming of diverse types of species such as jellyfishes or phytoplankton has consequences both for the maintenance of power plants and for the thermodynamics of our planet.

Our approach relies on a systematic use of massive numerical simulations of the Navier-Stokes equations to generate homogeneous isotropic turbulence at high Reynolds number, and analyze in details the statistics of various types of particles such as inertial spheroids and flexible fibers. For small inertial spheroids, our numerical work shows that the translational and the rotational motion are essentially decoupled. While the translational motion can be described by the motion of a sphere with a suitably defined effective mass, the rotational dynamics displays more intricate features. This reflects in the statistics of the rotation rate and in the concentration properties. Conversely to translational motion, the rotational dynamics is therefore non-universal and depends on the specific shape of the spheroids.

For small inertialess fibers, which constitute a paradigmatic example of flexible elongated particles, we find that the dynamics is most of the time closely resembling that of a stiff rod. Yet, in very rare and intermittent episodes, the fibers experience violent buckling events, which correlate to strong local compressions exerted by the local turbulent flow. Besides, detailed statistical investigations reveal that flexibility also produces misalignments of the fibers, *e.g.* deviations in the statistics of the orientation compared to the dynamics of a completely stiff rod. Our most salient observation is that the coupling between such flexible fibers and the turbulence can be phenomenologically modeled in terms of various activation processes, both for the buckling rate and for the misalignments statistics.

We finally investigate scenarios for turbulent fragmentation of brittle fibers. To that end, we implement in our numerics two mechanisms leading to the fibers breaking in smaller pieces, either because of tensile failure or because of flexural failure. We sketch a stochastic description of such violent events that paves the way to better parametrization of turbulent-induced fragmentation of brittle material in industrial codes.

Keywords: Turbulent flow, complex particles, Lagrangian description, fibers, spheroids, fragmentation.

RÉSUMÉ

Cette thèse analyse la dynamique de petits objets complexes immergés dans des environnements turbulents. Les champs turbulents peuvent être vus comme des champs aléatoires très fluctuants, dont les statistiques sont en général fortement non-Gaussiennes et se caractérisent par la présence de fluctuations très violentes, tant du point de vue Eulérien que Lagrangien. En pratique, la turbulence est le mécanisme dominant régissant le transport et le mélange de matière aux échelles humaines, industrielles et planétaires. Dans leurs détails, les propriétés statistiques du transport turbulent dépendent de la nature des particules considérées. Ici, nous nous concentrons sur le transport de petites particules complexes, qui sont caractérisées par une interaction non triviale entre leur masse, leur forme et leur rhéologie. Notre objectif est d'acquérir une compréhension physique de la façon dont les fluctuations turbulentes prescrivent la dynamique de ces particules complexes, et se manifestent au travers à la fois des phénomènes collectifs comme la concentration préférentielle, ou des phénomènes individuels allant de la déformation de particules jusqu'à leur fragmentation. Ces manifestations physiques de la turbulence ont des conséquences tant au niveau industriel que du développement durable. Un exemple bien connu du secteur aéronautique commercial est celui de la gestion des risques liés au transport atmosphérique de cendres volcaniques sur des échelles continentales. Un exemple moins connu est celui de la floraison de méduses ou de phytoplancton dans des environnements maritimes, un phénomène spectaculaire susceptible d'avoir des conséquences à la fois sur la maintenance des circuits de refroidissement des centrales thermiques, et sur la thermodynamique de la Terre.

Nos recherches s'appuient sur des simulations numériques massives et systématiques basées sur l'intégration directe des équations de Navier-Stokes incompressibles, ce pour générer une turbulence isotrope homogène à très haut nombre de Reynolds. A partir de ces simulations, nous analysons en détail les statistiques de différents types de particules tels que des sphéroïdes inertiels ou des fibres flexibles, susceptibles ou non de se casser. Pour les sphéroïdes, nos travaux montrent que les dynamiques translationnelles et rotationnelles sont essentiellement découplées. Alors que le mouvement de translation se rattache à celui d'une sphère avec une masse effective convenablement définie, la dynamique de l'orientation présente des caractéristiques plus complexes. Cette complexité se reflète dans les statistiques du taux de rotation et dans les propriétés de concentration. Ainsi, et à l'inverse du mouvement de translation, la dynamique de rotation n'est pas universelle et dépend de la forme spécifique des particules, ici caractérisée par différents rapports d'aspect.

Pour les fibres, qui sont un exemple type de particules allongées flexibles, nous constatons que leur dynamique est qualitativement très semblable à celle d'une tige rigide, en tout cas pour la plupart du temps. En des occasions très rares et intermittentes, nous observons en effet que les fibres flambent violemment, et ces événements se corrèlent aux fortes compressions locales exercées par le fluide turbulent. En outre, les statistiques détaillées de l'orientation des fibres diffèrent sensiblement des statistiques de tiges parfaitement rigides, même en dehors de ces événements de flambages. Ces déviations peuvent être comprises comme des "anomalies d'alignement" causées par la flexibilité. Notre observation principale est le fait que le couplage entre les fibres et la turbulence peut se modéliser en termes de différents processus d'activation, qui rendent compte à la fois des statistiques du flambage et des anomalies de l'alignement.

Nous étudions enfin des scénarios de fragmentation dus à la turbulence. À cette fin, nous implémentons dans nos codes numériques deux mécanismes de rupture distincts, à savoir un mécanisme de rupture par flexion et un mécanisme de rupture par tension. Nous esquissons un cadre stochastique de tels événements catastrophiques, qui justifie l'usage d'équations cinétiques du type Smoluchowski pour la description statistique de la fragmentation en temps long, et ce malgré la présence des corrélations temporelles non triviales dans les fluctuations turbulentes Lagrangiennes. Cette description ouvre des perspectives pour mieux quantifier la fragmentation des matériaux fragiles dans les codes utilisés pour la prévention des risques dans des cadres industriels, et en particulier dans le Code Saturne développé par EDF.

Mot-clefs: Écoulements turbulents, particules complexes, description Lagrangienne, fibres élastiques, sphéroïdes, fragmentation.

Contents

1 | Introduction

Contents

1.1 Particles in fluids

Turbulence in nature. The word **turbulence** comes from the Latin "turba" meaning disorder, tumult or crowd. In its scientific meaning, it describes "certain complex and unpredictable motions of a fluid" which materialize for example in " the volutes of smoke from a cigarette, the elegant arabesques of cream poured into coffee and the vigorous eddies of a mountain stream" (Benzi R. and Frisch U., 2010). It has been evidenced long ago that turbulent fluctuations enhance the transport and mixing of particles (Taylor, 1922; Richardson, 1922): Above centimetric scales, small particles suspended in the air diffuse several orders of magnitude faster than prescibed by their molecular diffusivity. As a rough estimate, Lewis Fry Richardson estimates the turbulent diffusion in the atmosphere as $0.2\ell^{4/3}$ with ℓ expressed in *cm* (Davidson et al., 2011; Richardson, 1922). Richardson's formula implies that the turbulent diffusion is already a thousand times more efficient than Brownian diffusion on metric scales, and ten million times more efficient on kilometric scales. As such, turbulence is a fundamental ingredient of nature, that plays a crucial role in shaping our planet and mitigating the human activities.
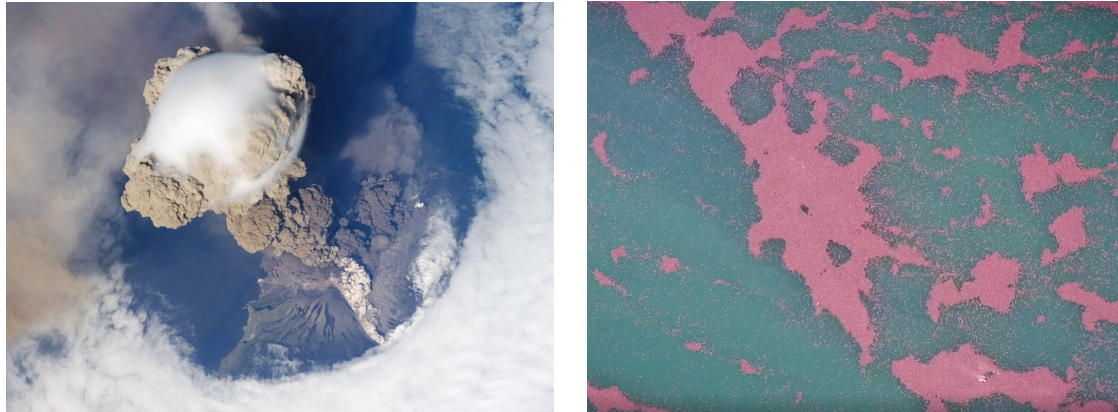
At the time of completion of this thesis, where the deadly COVID-19 pandemic has triggered new standards in social distancing in most of the countries around the globe, it has probably become clear for a large fraction of the population, that the propagation of diverse types of infectious objets within the air, from micron-size aerosol to droplets particles, is a key issue in driving the dynamics of airborne pathogens between human beings. While standard epidemiological studies rely on population models and ad-hoc statistical fitting to estimate the propagation of a disease among a given crowd (Li et al., 2020; Gross et al., 2020; Masrur et al., 2020), realistic quantitative estimates of transmission risks in various social configurations require clarifying the physics beneath airborne transmissions. Not surprisingly, this physics involves turbulent transport, and this has been demonstrated explicitly in a series of numerical and experimental studies (Bourouiba et al., 2014; Verma et al., 2020; Prather et al., 2020). As an illustrative example, Fig. 1.1 shows a schematic representation of aerosol particles and experimental results of droplets with sizes of the order of micrometers propagating in a turbulent environment.

Figure 1.1: Left panel: Illustration of the propagation of aerosol particles in a turbulent environment. Right panel: Cough droplets from violent expirations in a turbulent environment (©Bourouiba Group MIT 2020). Images taken from Verma et al. (2020) and Bourouiba et al. (2014).
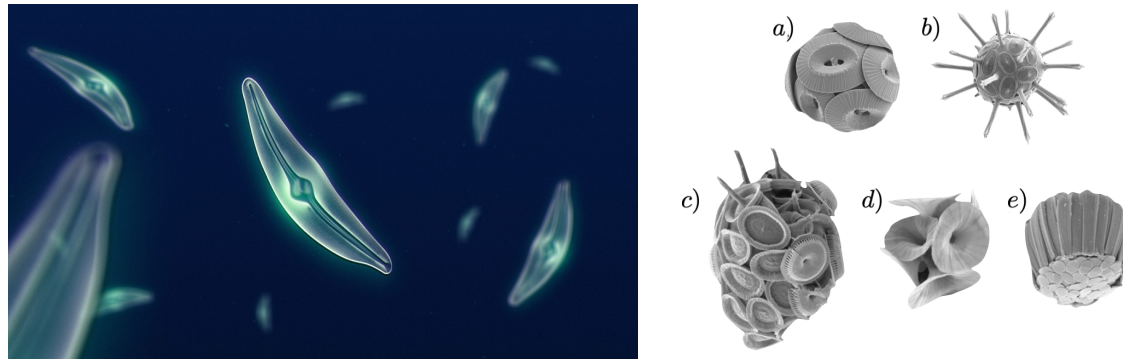
Naturally, apart from dictating reliable social-distancing rule at the scale of an individual (Lohse, 2020), turbulence also shapes the transport of matter and energy on larger scales with clear industrial and economic consequences. For example, atmospheric turbulence may propagate hazardous material such as volcanic ash on continental scales within days, with direct impact on the commercial flight industry. Volcanic ash consists of small millimetric-fragments of rock and glass as shown in the left panel of Fig 1.2, which may lead to the engine failures of commercial flights (Mecikalski et al., 2007; Del Bello et al., 2015). One may recall that in 2009, this risk had the European sky shut down for close to a month after the violent eruption of the small Icelandic Volcano Eyjafjatallökull (Winker et al., 2012; NCAS, 2010). In the oceans, turbulent transport of micro-particles of plastic origin (Thompson, 2015; Kukulka et al., 2016) generate large-scale pollution. The microplastics are very small piece of plastic debris that tend to accumulate in marine environments. Ocean and lakes present high levels of plastics of the order of millimetres, almost imperceptible to the human eye. They are coming from a variety of sources, including cosmetics, clothing, and industrial processes. These small pieces of plastic are the result of the material fragmentation due to several factors (GESAMP, 2015). The most common factor, it is their degradation by solar UV radiation. However, these small debris of plastic can be produced also by the forces involved in a turbulent flow (Ballent et al., 2012; NOAA, 2020). They constitute a huge source of water pollution, with consequences on availability of drinking water for humans (Koelmans et al., 2019), and on the aquatic food chain.

Beyond transport, turbulent fluctuations conspire in generating extremely heterogeneous patterns of concentration and temperature in the ocean, hereby triggering or at the very least conspiring to the blooming of diverse types of particles on scales from kilometric to planetary. An example is the blooming of jellyfishes observed in early 2020 away from the coast of the Philippines islands (see the right panel of Fig. 1.2), where Jellyfishes seem to be organized in a random spatial configuration. Such blooming can have dramatic industrial consequences. For instance, in 2007 in Scotland, two reactors of a nuclear plant had to be stopped from functionning: Jellyfishes had there been found to obstruct the cooling water filters, compromising the safety standards of the plants (Reuters, 2020). Of course, an assembly of jellyfishes swimming in the ocean is an example of a complex system, whose collective behavior is shaped not only by the random fluctuations of their living environment but also by their active nature, the presence or absence of certain nutrients, the presence of predators, the temperature, etc.
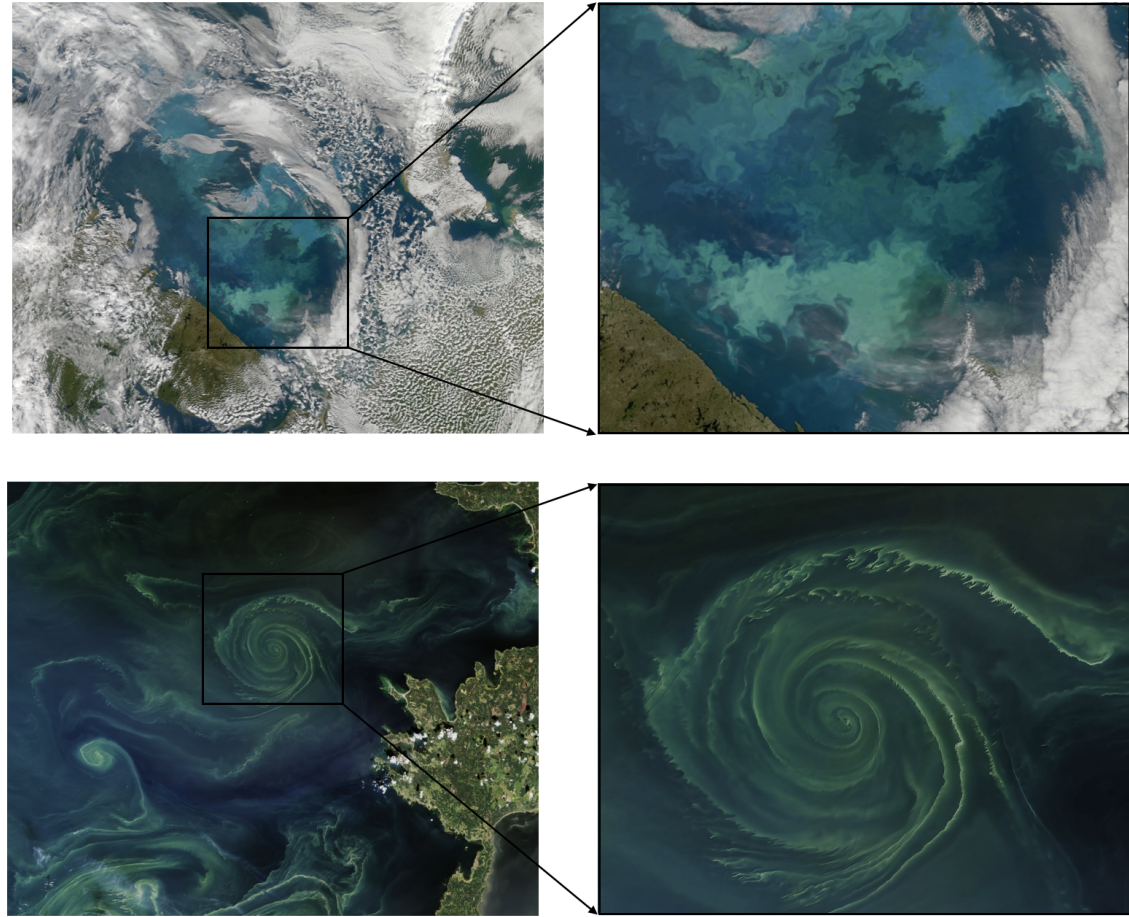
Figure 1.2: Left panel: Sarychev Volcano (Kuril Islands, northeast of Japan) in an early stage of eruption. Image taken from NASA (2009). Right panel: Screenshot of a bloom of jellyfishes observed in early 2020 in the coast of the Philippines islands. Image taken from Thiaville (2020).

This kind of large-scale blooming favored by turbulence impacts not only the industry, but also the sustainability of Planet Earth. As an example, one can mention the role of turbulence on the life-cycle of certain aquatic species such as phytoplankton. The phytoplankton are microscopic organisms, which, like plants, use chlorophyll to capture sunlight and undergo photosynthesis. In the oceans, the most typical species are the diatoms and the coccolithophores (see Fig. 1.3). Those small microorganisms grow beneath the surface in Nordic waters and have important collective effects in regulating the concentration of CO_2 within the ocean and in the thermodynamical balance of the planet (Abraham, 1998; Estrada and Berdalet, 1997; Durham et al., 2013; Barton et al., 2014; Sengupta et al., 2017). Turbulence appears in full sight beneath the spectacular patterns exhibited by "phytoplankton blooms" in oceans (Obata et al., 1996; Boyd et al., 2000; Arrigo et al., 2012). This phenomenon consists in a fast, explosive, growth of the phytoplankton in aquatic environments and is visible because the phytoplankton reflects the light.

Figure 1.3: Left panel: Diatoms phytoplankton algae in the ocean. Right panel: Diversity of coccolithophores: a) Coccolithus pelagicus, b) Rhabdosphaera clavigera, c) Syracosphaera pulchra d) Umbellosphaera irregularis and e) Gladiolithus flabellatus. Imagen taken from NASA (2015) and Wikipedia (2020a).

Fig. 1.4 shows an example of large-scale bloomings of those microorganisms, as photographed by a satellite from NASA in the Barents and in Baltic sea. There, the assembly of phytoplankton traces the edges of a kilometer size vortex, as well as more complex structures. The variations in brightness and color is related to the concentration of phytoplankton and to the depth in the oceans. It has been argued that collective blooms of such simple algae may be key in scenarios of evolution of life (Glibert et al., 2018; IISD, 2017). The patterns exhibited by the phytoplankton look very much alike the patterns observed either on controlled experiments of passive transport by chaotic flows (left panel of Fig. 1.5), or to the direct numerical simulations of passive temperature fields advected by turbulent flows (right panel of Fig. 1.5).
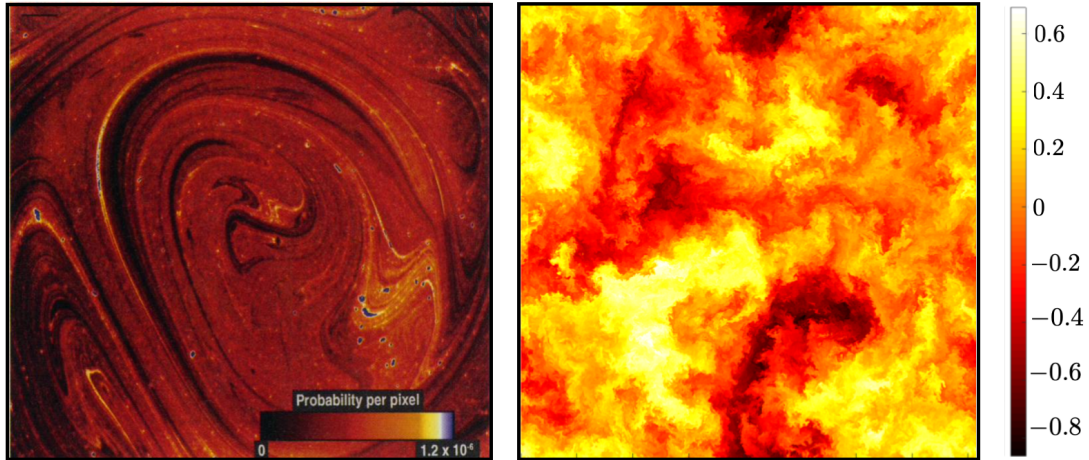
Figure 1.4: Top panel: phytoplankton bloom in the Barents sea. NASA image courtesy Norman Kuring, NASA Ocean Color Group (NASA, 2010). Bottom panel: summer blooms in the Baltic sea. Image taken from NASA (2018).

The blooms of phytoplankton have an impact on the underlying ecosystems. In a balanced ecosystem, those microorganisms provide nutrient and food for a large range of systems, but in a huge quantity they induce damaging effects. Studies show that such blooms lead to the formation "dead zones", because the phytoplankton consumes huge quantities of nutrients in the oceans, hindering the proliferation of other kinds of life in the seas (NASA, 2010). In addition, blooms of phytoplankton can prevent light from reaching organisms that are lower in the water column.

Turbulence in computers.   A common feature to the examples of turbulent mixing and transport mentioned above is their apparent random nature and often hazardous consequences, as well as the extreme regimes of flow parameters that they involve. To understand and model transport of matter in turbulent environments, it seems extremely natural to rely on computer simulations, as the fluid equations at the origin of turbulent motion are known and can be simulated using numerics. Anticipating on Chapter 2, it turns out that while fluid equations such as the Navier-Stokes equations are indeed a powerful tool towards that end, their practical use is often limited to the range of parameters relevant for daily life turbulence only, rather than industrial, atmospheric, or oceanic turbulence. For that reason, industrial codes trying to reach relevant regimes of parameters have to rely on small-scale parametrizations, in order to simulate turbulent fluids at scales larger than particle sizes. If one wants to incorporate turbulent fluctuations for the transport, those codes need to rely on stochastic models coupling fluid structures and the dynamics of the particles (Wilson and Sawford, 1996; Jones et al., 2007; Thomson, 1990; Minier and Peirano, 2001; Bossy et al., 2016). Computational fluid dynamics (CFD) softwares such as **Code Saturne** of EDF (EDF, 2020), use approximations from

Reynolds-Averaged models (RANS models) to Large-Eddy Simulation (LES models). In order to simulate the Navier-Stokes equations for 2D, 2D-axisymmetric and 3D flows, steady or unsteady, laminar or turbulent, incompressible or weakly dilatable, isothermal or not, with transport of scalars if required.

In order to derive faithful models, one needs to gain a fundamental knowledge on the statistics of turbulent transport. This has motivated numerous studies in that field both from experimental and numerical viewpoint (Bec et al., 2005; Mordant et al., 2002; Monchaux et al., 2012; Salazar et al., 2008). Obviously, the detailed description of transport of particles and of concentration patterns is largely dependent not only on the type of turbulence, but also on the type of particles (Voth and Soldati, 2017; Marchioli and Soldati, 2013), which may exhibit various degrees of complexity.
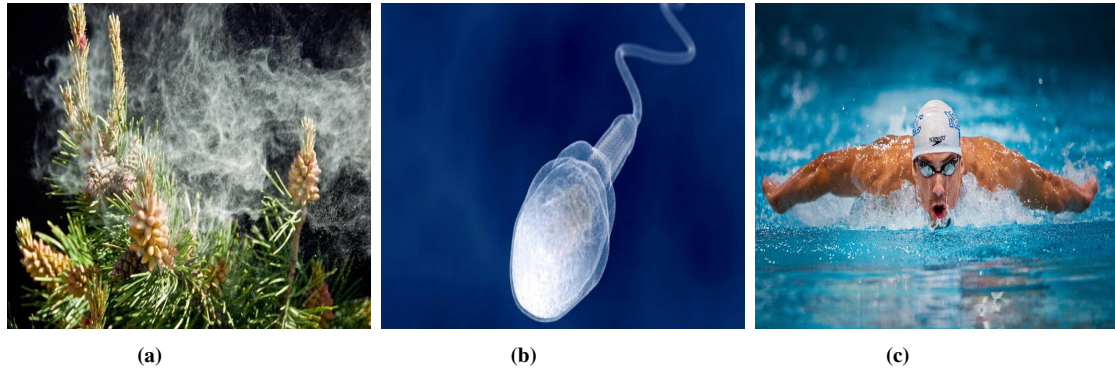
Figure 1.5: Left panel: Radiometrically inferred distribution of tracer particles after experiment has settled into steady-state behavior for a given iteration. Image taken from Sommerer and Ott (1993). Right panel: Passive scalar at $T_L/8$ in the $x - y$ plane, using the 3D simulation with 4096^3 collocation points. Courtesy of C. Siewert.

1.2   Complex particles

The notion of complex particles is very large and as such slightly ill-defined. In our view, any particle that is not a tracer could be qualified as "complex", but obviously, not being a tracer is not an unambiguous defining property! One can distinguish several features that contribute to the degree of complexity of a particle, among which their active or passive nature, their coupling with the external environments and their coupling among one another.

Active *vs* passive particles.   In full generality, there is a two-way coupling between the fluid and the particles within it: The fluid prescribes the particle dynamics, which in turn alters the flow. When such a two-way coupling is taken into account in models, we refere to the particle as an **active particle**. Among mechanisms that make the particle alter their environment, one can think of boundary effects due to their finite-size, or presence of internal source of energy. Please note, that our definition of active particles is larger than the usual definition used in statistical physics, for which active particles are particles with an internal source of energy (Guzman L. and Soto, 2011). Conversely, when the particle does not alter the flow, it is called a **passive particle**. In reality, there is no such object as a passive particle. Yet, modeling particles as being passive is a major simplifying assumption and is physically justified when dealing with very small or very thin objects that are sufficiently dilute within the flow. As an illustration, two kinds of active particles are represented in Panels (b) and (c) of Fig. 1.6, together with an example of a passive particle such as pollen particles in Panel (a). In Panel (b) a human spermatozoo acts as an active particle with its own energy source. The fluid around it is forced with a typical velocity of $U \approx 200\,\mu m s^{-1}$ and a typical length of $L \approx 50\,\mu m$, achieving a Reynolds number of $R_e \approx 10^{-2}$ (Lauga and Powers, 2009). Panel (c) features the

former professional swimmer Michael Phelps spanning a scale $L = 1.93\,m$, who needs to propel the fluid at approximately $U \approx 2\,ms^{-1}$, to be competitive when swimming the $200\,m$ freestyle competition, hereby generating a Reynolds number of $R_e \approx 10^6$.

**(a)**   **(b)**   **(c)**
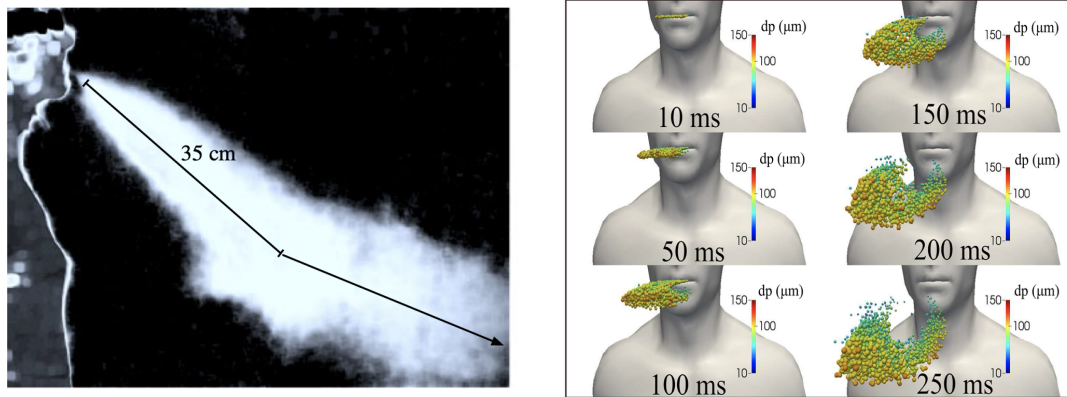
Figure 1.6: Panel (a): pollen in the air. Panel (b): spermatozoo in semen ($\nu \approx 0.0094\,Pas$) with $R_e \approx 10^{-2}$. Panel (c): Michael Phelps in water ($\nu \approx 10^{-3}\,Pas$) with a $R_e \approx 10^6$.

Coupling with the external environment. The interplay between the fluid and the particles depend on the physical properties of both the particles and the fluids. Among distinctive properties, one can think of:

- **Inertia**: When inertia is taken into account, massive (or heavy) particles do not in general follow the streamlines of the carrier flow. For massive particles gravity may be non-negligeable (Saw et al., 2008; Bewley et al., 2013) and lead to their gravitational settling.

- **Buoyancy**: Low-density particles are generally buoyant, and Archimede's force opposing the gravity to make the particle float. An example in turbulence is Mathai et al. (2015).

- **Shape**: The shape of the particle determines their coupling with the flow. Anisotropic particles have different drag coefficients depending on the axis of symmetry (Voth and Soldati, 2017). This means that depending on their orientation, the particles may experience more or less drag for the same flow realization.

- **Size**: The size of a particle determines whether or not it affects the carrier flow through boundary effects (Cisse et al., 2015). In turbulence, which is a multi-scale environment, a criterion is to define as small particle any particle smaller than the Kolmogorov scale, which we will later precisely define. In the ocean or in the atmosphere, the Kolmogorov scale is typically millimetric or centimetric. Hence, small particles like microplastics are indeed small compared to the smallest scale of the flow, and it becomes physically reasonable to model them as passive particles. Such is not the case for a plane or for a whale.

- **Charge**: Charged particles are additionally subject to the Lorentz forces, and this may affect their clustering patterns, with lesser charges leading to larger concentrations (Homann et al., 2009).

- **Rheology**: The rheology describes the material properties and the internal degrees of freedom of the particle. A particle with several internal degrees of freedom may be qualified as flexible. The material properties define if the object is plastic or elastic, and their potential breaking thresholds.

Fig. 1.7 shows the influence of various of these ingredients in the description of the human "sneeze cloud". The droplet particles present in a sneeze cloud have various of the features described above: They are massive, buoyant, anisotropic and fragile. The correct physics describing the sneeze clouds needs to balance those properties.

Figure 1.7: Left panel: The effect of buoyancy on the sneeze cloud is apparent in its upward curvature. Right panel: Saliva droplet cloud kinematics show the diameter of the droplets resulting from a human cough. The diameter sizes are tabulated in the lateral color bar. Images taken from Bourouiba et al. (2014) and Dbouk and Drikakis (2020).

Coupling between one another. Modeling the interaction between particles may be required to describe certain complex problems, such as the formation of rain in warm clouds (Lanotte et al., 2010; Saw et al., 2015) through successive coalescences, or the collisions of dust particles with planetesimals in protoplanetary disks (Homann et al., 2016). Active living particles may also interact, leading to potential flocking and this may also be an ingredient beneath the jellyfishes blooms. The list is obviously long and way beyond the scope of the present thesis. A final remark, we note that turbulent transport is determined not only by the type of particles but also by the type of turbulence at play. Depending on the problem and the scales considered, one may wish to consider geophysical flows, wall bounded flow (channel flow), fully developed homogeneous isotropic 3D flows, etc.

Intent of the thesis In this thesis, we restrict our attention to studying the statistical behavior of small particles, but with different degrees of complexity, as determined by the modeling of their shapes, their mass and their rheology. We expose here a few of the most salient results relating to previous studies of this kind of interplay, although not necessarily in a turbulent context. Each section describes the behavior of particles, depending on the interplay between two or three parameters, chosen among their shape, their mass, and their rheology.

1.3 Heavy anisotropic particles

Considering the interplay between mass and shape leads to the study of heavy anisotropic particles.
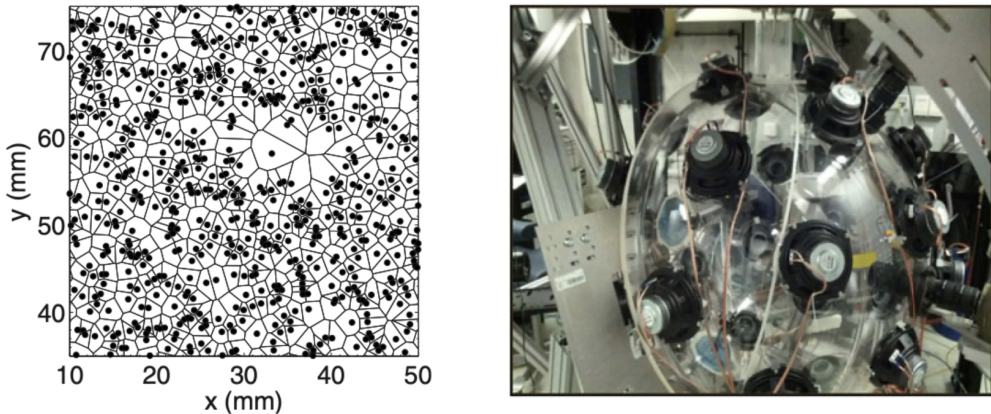
1.3.1 Heavy spherical particles

The effects of inertia in the Lagrangian statistics have been extensively studied for spherical particles (Toschi and Bodenschatz, 2009; Bec et al., 2011; Calzavarini et al., 2008; Boffetta et al., 2004). In particular, the presence of inertia leads to the preferential concentration of the particles, being distributed in a strongly inhomogeneous manner (Sumbekova et al., 2017; Monchaux et al., 2012; Yoshimoto and Goto, 2007; Aliseda et al., 2002; Balkovsky et al., 2001; Squires and Eaton, 1991). We present here studies related to those behaviors, from an experimental and numerical point of view.

Experimental results. Different experimental settings have been used in order to reproduce homogeneous isotropic turbulence (Monchaux et al., 2012); The most popular set-ups are wind-tunnels (Sumbekova et al., 2017; Qureshi et al., 2007; Aliseda et al., 2002), as well as the Von Kármán settings (Volk et al., 2010; Salazar et al., 2008; Xu and Bodenschatz, 2008). In addition, new facilities have been introduced such as synthetic jets (Petersen et al., 2018; Goepfert et al., 2010) or the soccer ball (Good et al., 2014).

The left panel of Fig. 1.8 highlights the result obtained by Monchaux et al. (2010) using a wind-tunnel. The clustering of heavy particles is analyzed in terms of Voronoï tessellations. This method of tessellation divides the domain in polygons with areas proportional to the local particle concentration field. The authors recover the behavior of expulsion of inertial particles from strong vortex regions to calm zones of the flow, where an optimal preferential concentration is around a Stokes number of the order of unity.

Fig. 1.8 also shows a more recent set-up used by Good et al. (2014) to reproduce homogeneous isotropic turbulence. Their experimental setting consists in a ball with water droplets, carried by air turbulence generated by 32 loudspeakers jets. Homogenous isotropic statistics are found in the bulk of the ball within a volume $\sim 10cm^3$. They show that combined effects of inertia and gravity tend to reduce the velocity of the particles.
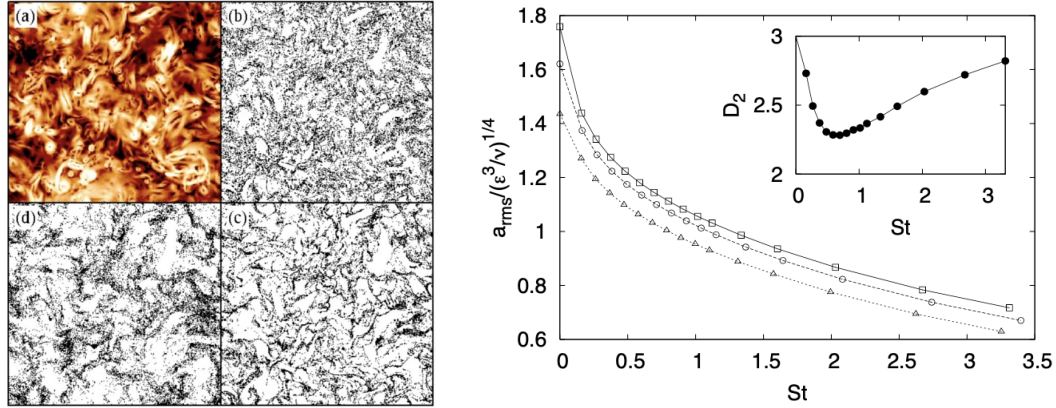

Figure 1.8: Left panel: Voronoï diagram from a picture of the set-up of particles. Right panel: Experimental setting of the soccer ball apparatus with 32 loudspeakers jets. Panels are taken from Monchaux et al. (2010) and Good et al. (2014).

DNS results.   From a numerical point of view, a full description of the clustering of small massive particles has been done by Bec et al. (2007). The study reports on numerical simulations at different resolutions of the flow involving millions of particles, with several Stokes numbers $St = \tau_p/\tau_\eta$. This quantity measures the relation between the particle response time τ_p and the Kolmogorov timescale τ_η, which is the smallest timescale of the flow. The observation is that within regions of the size of the order of the dissipation scale η, the preferential sampling of particles does not depend on the Reynolds number and achieves its maximum of concentration for particle response times of the order of the Kolmogorov timescale ($St \approx 0.7$).

The inset of the right panel of Fig. 1.9 shows this behavior, measuring the correlation dimension D_2. This quantity estimates, at small scales, the probability to find two particles within a distance smaller than r as $p(r) = r^{D_2}$. When particles are uniformly distributed, D_2 is equal to the space dimension, *e.g.* $D_2 = 3$. The maximum of concentration corresponds to minimal values for D_2 and is found at $St \approx 0.7$. As observed in Subpanel (d) of Fig. 1.9, the particle distribution is not longer scale-invariant in the inertial range.

The preferential sampling of heavy particles reflects on the acceleration statistics. In Bec et al. (2005), the authors show that mass effects lead to a sharp decrease in the root-mean-square acceleration (see the right panel of Fig. 1.9), essentially explained by two mechanisms. For small but not vanishing Stokes number, particles concentrate in regions of low vorticity, characterized by strong shear. This results in a drastic decrease of the acceleration. For large Stokes numbers, this effect becomes subdominant and statistics reflect the long-time correlation of the acceleration (memory effects).
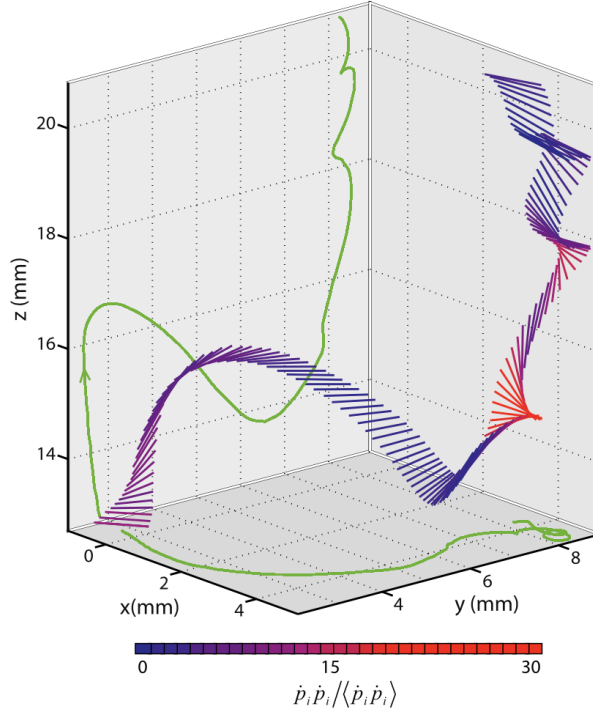
Figure 1.9: Left panel: Slices of the modulus of the fluid pressure, where black colors represent low values and white represents high values (panel (a)); together with the particle positions for Stokes number 0.16, 0.8 and 3.3 (respectively in (b), (c) and (d)). Right panel: Normalized root-mean square acceleration $a_{\mathrm{rms}}/(\varepsilon^3 \nu)^{1/4}$ as a function of Stokes number for various values of Reynold number: squares represent a $Re_\lambda = 185$, circles represents $Re_\lambda = 105$ and triangles represents $Re_\lambda = 65$. Inset: Correlation dimension D_2 as a function of the Stokes number for the highest Reynolds number. The correlation dimension is fitted with a exponential law $p(r) = r^{D_2}$ where $p(r)$ is the probability to find two particles at distance smaller than r ($r \ll \eta$). Images taken from Bec et al. (2007) and Bec et al. (2005).
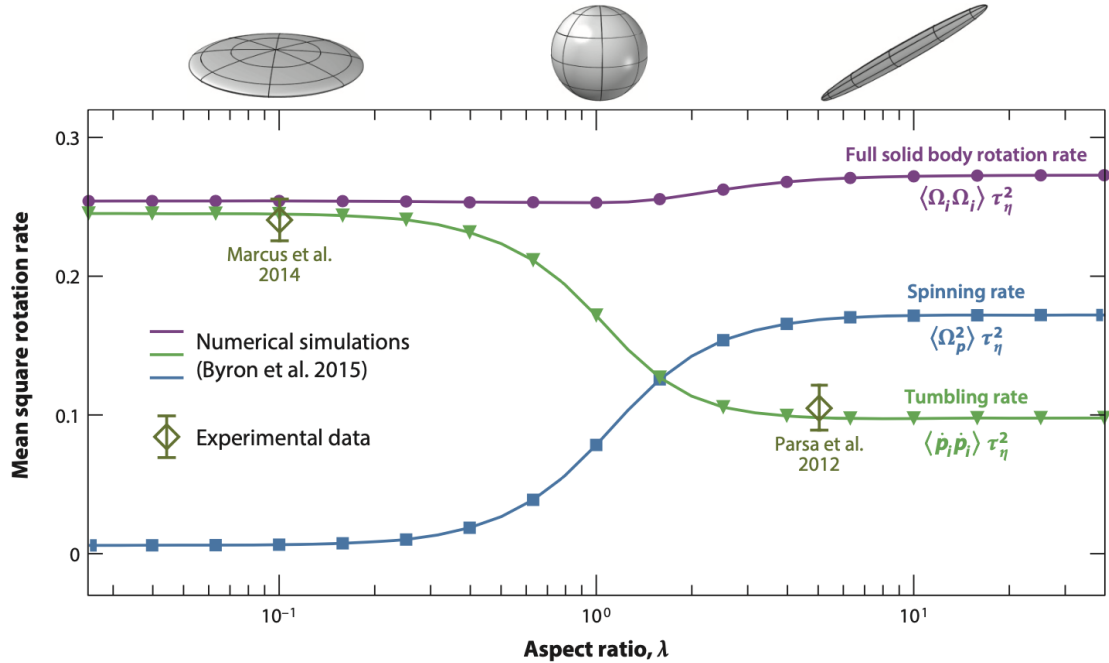
1.3.2 Anisotropic particles

Anisotropic particles are particles which lack or possess non-trivial symmetry properties. The dynamics of anisotropic particles is prescribed by specifying their translational and their rotational parts. Compared with tracers, these particles are expected to display more complex patterns of concentration. Historically, anisotropic particles have been studied using ellipsoids (Jeffery, 1922; Bretherton, 1962; Brenner, 1964); the simplest case is the case of axisymmetric ellipsoids also known as spheroids particles, for which two out of the three axis lengths are equal. Two relevant cases have been well studied in the last years: spheroids in homogeneous isotropic flows and spheroids in channel flows (Voth and Soldati, 2017; Ardekani et al., 2017). A non-trivial feature of their dynamics is the fact that those particles occasionally tumble, *e.g.* rotate half-turn about their greater axis. Fig. 1.10 shows the evolution of the tumbling rate of a rod particle, obtained from experimental measurements in a nearly homogeneous turbulent field (Parsa et al., 2012). We can appreciate that tumbling events are seldom; they are separated by calm periods where the particle keeps their orientation. This can probably be interpreted as one of the signatures of turbulent intermittency.

The rotation rate of spheroids illustrates the preferential direction of these objects with the flow. This quantity has been well studied in channel flows by Marchioli and Soldati (2013). They describe how the presence of a wall affects the rotation statistics for inertial spheroids, and a similar study was done by Challabotla et al. (2015) for disks. In Zhao et al. (2015), the authors decompose the rotation rate into the spinning and the tumbling rate, in the zone of the channel flows where turbulent fluctuations are similar to the homogeneous isotropic case. Fig. 1.11 shows these rates for different types of inertialess spheroids, with either oblate, spherical and prolate shapes. In this region of the channel, the effect of intertia is to decrease both rates. Conversely, the behavior of such particles closer to the wall displays stronger effects. More recently, statistical models of the orientation for inertial particles have been developed by Gustavsson et al. (2017).
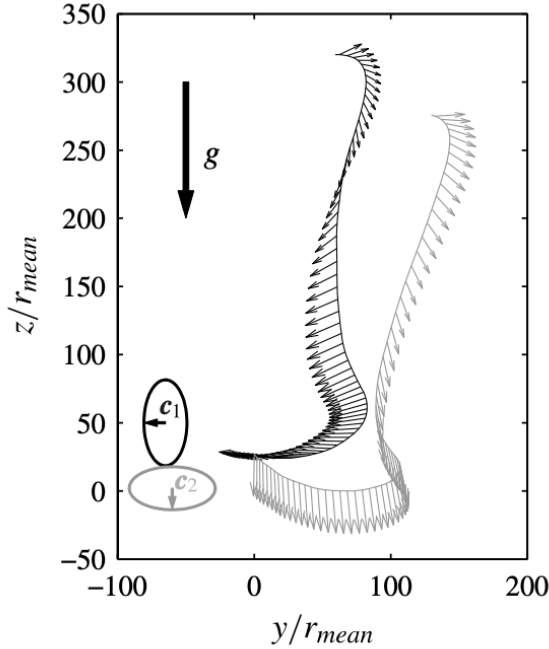
Figure 1.10: Evolution of a spheroid (with aspect ratio $\lambda = 5$ and a length of $L = 1$) evolving a turbulent flow ($R_\lambda = 214$). The 3D image hase been obtained from multiple-camera high-speed video measurements. The color of the rod represents the tumbling rate, with blue representing a low tumbling rate and red a high tumbling rate. The green lines show the projection of the center of the rod onto the y-z and x-y planes. Image taken from Parsa et al. (2012).

Figure 1.11: Mean square rotation rate as a function of aspect ratio for tracer particles in homogeneous isotropic turbulence. Image taken from Voth and Soldati (2017).

Following a different viewpoint, the study of Siewert et al. (2014b) reports on the collisions between ellipsoids particles. Fig. 1.12 illustrates two ellipsoidal particles with their positions and orientations before a collision. The study shows that compared to spheres with the same volume, ellipsoid have a higher collision rate, because the settling velocity depends on the particle orientation.
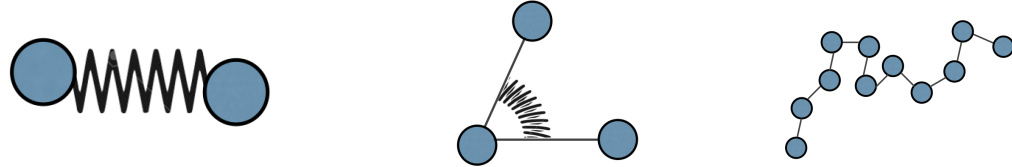

Figure 1.12: Position and orientation of two ellipsoidal disks before a collision projected onto the y-z plane. Image taken from Siewert et al. (2014b).

1.4   Flexible elongated particles

Considering the interplay between shape and rheology leads to the study of flexible elongated particles. Small particles suspended within a continuous medium generate a two-phase flow known as a "colloidal suspension". They appear in a wide variety of applications such as fog, clouds, hand cream, gelatine, smoke, among others. Colloidal particles are solid particles whose sizes are between the Angstrom ($1\text{Å} = 10^{-10}$m) and the micron ($1\mu = 10^{-6}$m), whose shapes may vary (Happel and Brenner, 2012). In this context, such particles are essentially subject to three forces: drag forces, Brownian forces and elasticity forces. The balance between those three forces define two classes of complex particles, polymers and fibers.

On the one hand, when elastic forces are negligible compared to Brownian forces, the colloidal particles are referred to as polymers. They are present in natural and biological environments under the form of proteins (Szleifer, 1997), cellulose (Simon et al., 1998; Ng et al., 2015), DNA (Tang and Szoka, 1997; Mavila et al., 2018) as well as the basic component of mineral such as coal or diamond (Hayatsu et al., 1981; Lee et al., 1993). Moreover, we can find them in synthetic materials such as concrete, glass and plastics (Mignon et al., 2017; McKenna and Simon, 2017; Gewert et al., 2015). For infinitely flexible polymers only the Brownian forces and the viscous drag compete, while the elastic forces are negligible. In this asymptotics, we observe the transition between a colloidal state promoted by thermal noise, and the polymer stretch induced by fluid shear (De Gennes, 1979). There exist many idealized models of polymers, the most simple of which is probably the elastic dumbbell model introduced by De Gennes (1979); Watanabe and Gotoh (2010); Musacchio and Vincenzi (2010). This model formed by two beads joined by a spring (see the left side of Fig. 1.13) is often used to investigate the rheology of polymer suspensions (Li et al., 2006; Pereira et al., 2017). More sophisticated models include for example three beads attached by two

springs (Plan and Vincenzi, 2016; Ali et al., 2016) and is called the trumbbell model (see middle panel of Fig. 1.13). More generally, chain models (see the right side of Fig. 1.13) have N beads joined by $N-1$ rigid inextensible bonds (see Henry et al. (2018)) that add an elastic effect in the polymers.
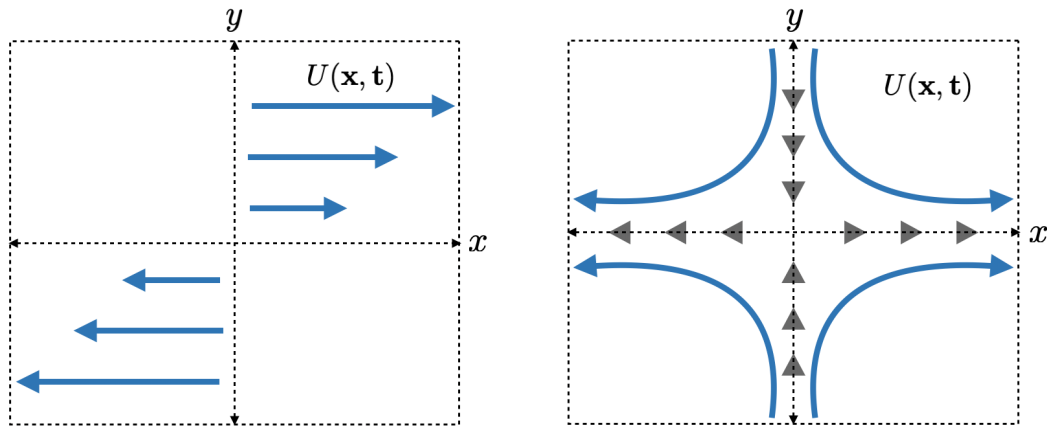

Figure 1.13: Illustration of various models of polymers. From left to right: dumbbell, trumbbell and chains models.

On the other hand, when Brownian forces are negligible and elasticity forces become important, the colloidal particles are referred to as fibers. The fiber asymptotics is relevant to describe macroscopic particles, such as cellulose fibers in papermaking industry (see Lundell et al. (2011)), or diatom phytoplankton colonies (see Ardekani et al. (2017)) that significantly participate to the CO_2 oceanic pump (see Smetacek (1999)).

1.4.1 Fibers in viscous fluids

Fibers have been mostly studied in viscous fluids in the limit of very low Reynolds numbers. In this limit, the fluid is characterized by the Stokes equations, a simplified form of the Navier-Stokes equations (later described in Chapter 2). To analyze the fiber behavior in such regimes, it proves instructive to consider some specific steady flows solving the Stokes equations. 2D shear flows, *e.g.* $U(\mathbf{x}, t) = (y, 0)$ and 2D linear extensional flows, *e.g.* $U(\mathbf{x}, t) = (x, -y)$ are two paradigmatic examples (see Fig. 1.14). Such flows are easy to simulate with numerics and can also be generated using various experimental setups from Taylor-Couette apparatus and Channel flows (shear flows) to cross-sectional geometries (extensional flows) (see Du Roure et al. (2019); Lindner and Shelley (2015) and references therein). In the latter case, careful experiments manage to keep the object at the stagnation point.

Even in these apparently simple configurations, the deformation induced by the fluid to these flexible elongated objects yields a nontrivial and rich phenomenology.
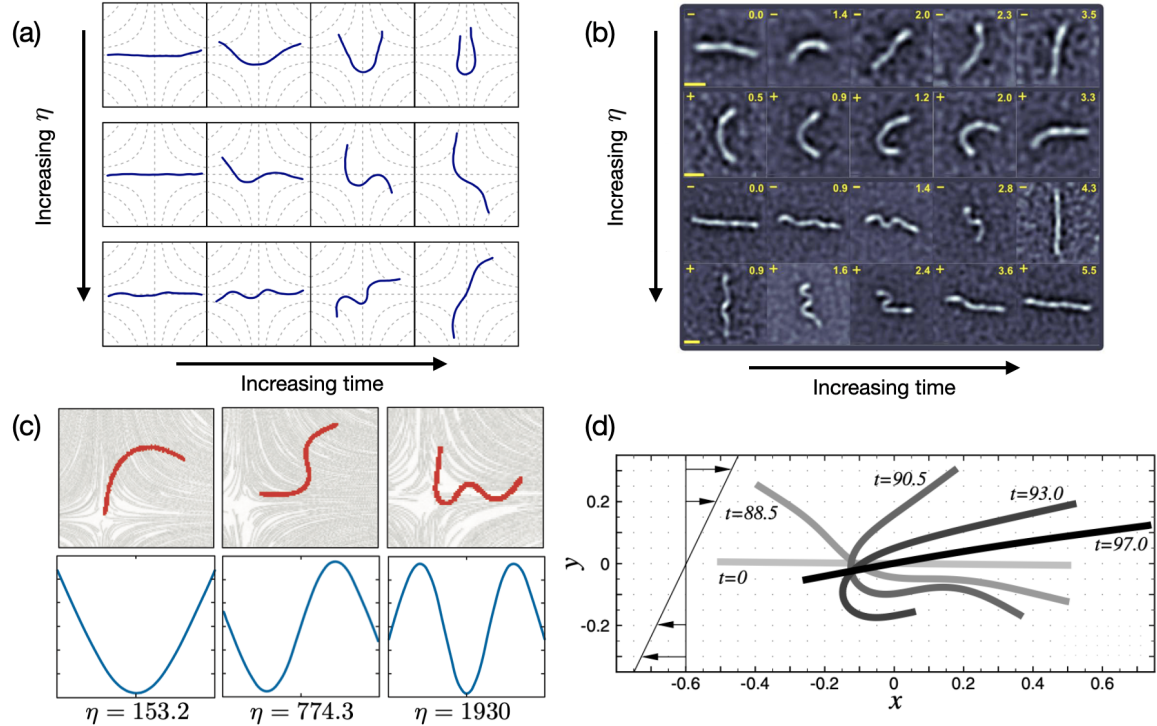

Figure 1.14: Illustration of the spatial configuration of a shear flow, (left side) and extensional flow (right side) in the x-y coordinates. Streamlines of the periodic background flow are shown in blue.

One of the crucial ingredients is the notion of fiber instability, in particular the buckling instability.

This phenomenon has been studied in many papers, both experimentally (Schroeder et al., 2003; Kantsler and Goldstein, 2012) and numerically (Young and Shelley, 2007).

It is typically observed that fibers buckle when they are compressed along their main axis. This phenomenon is illustrated in Panels (a) and (b) of Fig. 1.15, which display the dynamics of a fiber during a buckling event for three different values of the parameter η. This control parameter measures the ratio between the fluid compression and the elastic force: the larger, the stronger the compression by the flow. It is readily seen from those experiments that increasing the parameter η produces wavy buckling patterns involving shorter and shorter wavelengths. This hints that in the limit $\eta \to 0$ the fiber behaves like a straight rod; inversely, when $\eta \to \infty$ the fiber is like a flexible thread.

Figure 1.15: (a) Fiber simulation in an extensional flow during a buckling event. Three simulations are shown using different values of the critical control parameter η. Image taken from Manikantan and Saintillan (2015). (b) Experimental images of actin filaments in a microfluidic device. Fibers are in the stagnation point of the extensional flow. Image taken from Kantsler and Goldstein (2012). (c) Fiber configurations for the first three excited modes, corresponding to the critical values of the control parameter η. Top panel: experimental results. Bottom panel: results from the linear stability analysis. Image taken from Quennouz et al. (2015). (d) Dynamics of a fiber during a buckling event at $\eta = 7000$ from simulations using the local slender body theory (SBT). Image taken from Becker and Shelley (2001).

To get more quantitative insights, one needs to rely on specific mathematical models; in that context a popular tool is the so called "slender body theory" which we will later describe at length in Chapter 4. In this theory, the limit $\eta \to 0$ when the fiber behaves as a rod is described in terms of a solution obeying the so-called Jeffery's equations. To address buckling, one can then analyze the linear stability of this solution with respect to small perpendicular perturbations. Schematically, two cases can occur, depending on the local configuration of the background flow.
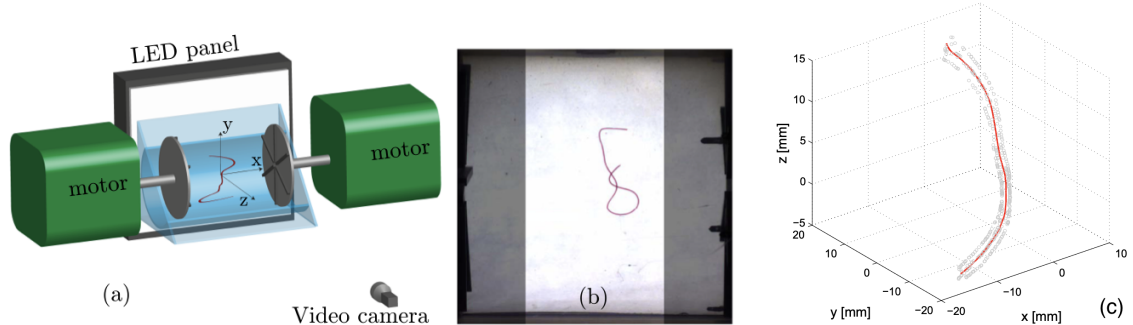
- When the background flow is extensional, the fiber is found to be aligned with the direction of compression. This configuration is always unstable for the fiber orientation, as we can appreciate in Panel (a) of Fig. 1.15 where the fiber is rotating. In that case, a linear stability analysis as the one performed by Quennouz et al. (2015) provides critical values for the control parameter η, describing when the fiber buckles. Specifically, when $\eta < \eta_1 \approx 153.2$, the fiber is stable along the compressing

direction. When $\eta_1 < \eta < \eta_2 \approx 774.3$ the fiber is unstable and the first mode is the most unstable. When $\eta_2 < \eta < \eta_3 \approx 1930$ the second mode becomes the most unstable, etc. This dependence of the buckling pattern with the parameter η is compatible with the behavior displayed in the panel (c) of Fig. 1.15.

- When the background flow is a pure shear, the fiber is not steady but rather rotates at a constant rate. This configuration can also be destabilized. Physically, throughout the rotation the fiber alternatively experiences stretching and compression along its main axis, and this provides the buckling mechanism. Mathematically, a linear stability analysis determines which mode becomes unstable depending on the control parameter η (Becker and Shelley, 2001). As in the extensional case, buckling first happens at $\eta > \eta_1 \approx 153.2$, with mode one becoming unstable. Higher critical values differ from the extensional case. This kind of instability is indeed the one seen in panel (d) of Fig. 1.15.

1.4.2   Fibers in turbulence

3D turbulence.   Studying fibers in very viscous flows is not merely an educational subject, it also has practical relevance in the field of bio-physics. Most natural and industrial flows are however prone to exhibit turbulent behaviors. We expect that the dynamics of fibers will then display highly non-trivial features, but there are only very few studies that address non-spherical flexible particles in turbulent environments. The recent years however witnessed the improvement of numerical and experimental techniques, enabling the development of new perspectives in this field.
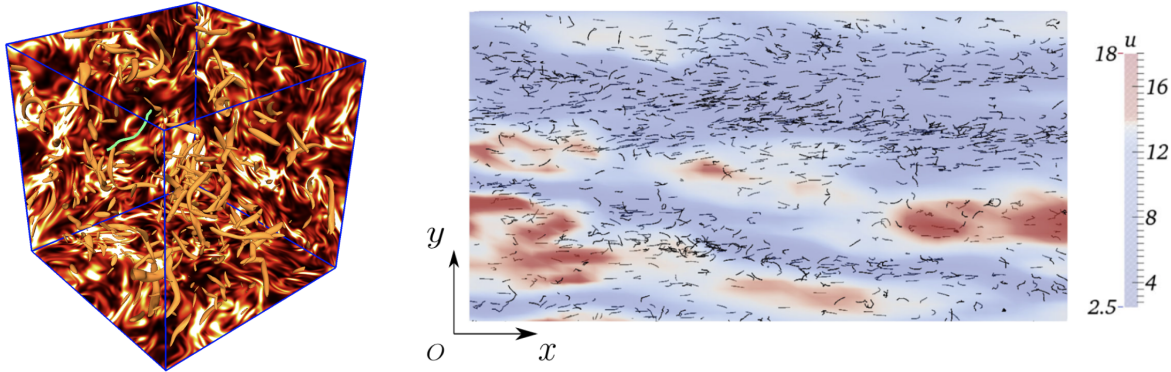

Figure 1.16: (a) Illustration of the experimental setup of the von Kármán flow. (b) Image of the working visual area, limited by the withe square zone. (c) Illustration of the fiber reconstruction: data from the 3D reconstruction is represented by the gray points, while the red curve is the cubic spline fit. Panels (a) and (b) taken from Brouzet et al. (2014). Panel (c) stolen from Verhille and Bartoli (2016)

From an experimental side, we have in mind the recent results obtained by Brouzet et al. (2014), who employed techniques of image reconstruction to analyze the fate of fibers carried by a turbulent von Kármán flow. The experimental setup of the von Kármán flow is shown in the panel (a) of Fig. 1.16. Turbulence is created by the centrifugal forces generated by the two opposite disks. This configuration allows to reach a Reynolds number of the order of $10^5 - 10^6$ with a dissipation scale between $12 - 19\,\mu m$. The measures have been performed in the center of the flow, as delimited by the white zone in the panel (b) of Fig. 1.16, where the turbulence is approximately close to being homogeneous isotropic. Macroscopic fibers, with length in the inertial range, have been individually immersed in this turbulent flow. The study establishes a close relation between the configuration of fibers in a turbulent environment and polymers suspended in a fluid flow. The authors focus on a very natural observable, namely the end-to-end vector, defined as the distance between the two extremes of the fiber; measured by its projection in the plane $x - y$. The authors show that depending on their size, the fibers may follow two different regimes. For fibers smaller than a critical elastic length ℓ_e, the fibers remain stretched out throughout the experiment and regardless of the flow fluctuations. Conversely, for fibers larger than ℓ_e, the flexibility of the fibers is not negligible and the fibers may bend. This critical value depends on the stiffness of the fiber and on the turbulent level of the flow. Indeed, in the later work presented by Verhille and Bartoli (2016), using now a three dimensional reconstruction image of the fiber (see panel

(c) of Fig. 1.16), it is shown that the fiber deformation depends also on its own length L: the larger the fiber, the more flexible. This is in constrast with the behavior of polymers, whose deformations are dictated by Brownian noise.

From a numerical point of view, given the huge number of degrees of freedom involved in the integration of the NS equations (see Chapter 2 for discussion), simulating turbulent flows is a cumbersome task. Naturally, coupling turbulent flows with complex deformable objects that also carry a large number of degrees of freedom, makes the problem even more complicated. Some studies (Rosti et al., 2018, 2020; Svenning et al., 2012) use immersed boundary conditions (IBM) to resolve the full coupled dynamics, induced by the fibers-fluid interaction. For instance, the study presented by Rosti et al. (2018) focuses at better understanding the role of turbulent fluctuations. The authors use fibers, with length of the order of the inertial turbulent range, as experimental probes that measure the two-point statistical observables of turbulence. In particular, they recover the scaling exponents of the longitudinal structure functions described in the next chapter. In the left side of Fig. 1.17 we show their three dimensional fully developed turbulent flow, coupled with a single fiber. While accurate, this direct method entails a huge numerical cost. A more accessible line of attack is to rely on simplified modeling of the coupling, using passive models of complex particles, such as elastic dumbbells (Ahmad and Vincenzi, 2016; Davoudi and Schumacher, 2006), trumbbells (Plan, 2017; Ali et al., 2015) and elastic chains (Singh et al., 2020; Picardo et al., 2020).

Boundary effects have been studied by Dotto and Marchioli (2019); Dotto et al. (2020) with inertial flexible fibers carried in a turbulent channel flow (see the right side of Fig. 1.17). Similar to what is observed for spherical or elongated rigid particles within turbulent channel flows; fibers are also found to have a preferential sampling in the very-near-wall region. The authors deal with fibers longer than the Kolmogorov dissipative length scale. This preferential sampling seems to be conducted by turbo-phoresis, in other words fibers have the tendency to move towards less turbulent regions. It is also observed that the fibers bend more systematically near the center, where turbulence is approximately homogeneous and isotropic. Conversely, near the wall, fibers are most of the time stretched by the mean shear.
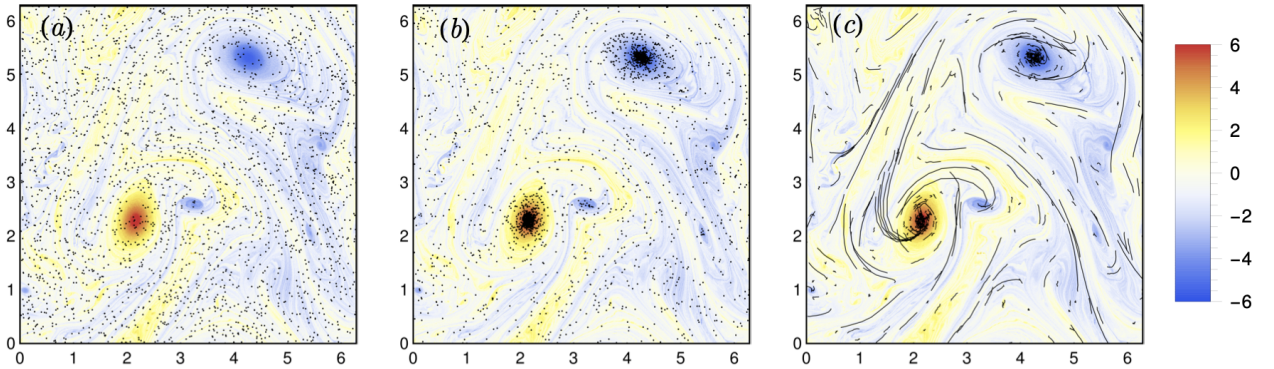

Figure 1.17: Left panel: Illustration of a single fiber immersed in a homogeneous isotropic turbulent flow. The instantaneous vorticity field is represented by the orange surfaces, while the three back planes show the contours of the enstrophy field. Right panel: Snapshots of fibers in the near-wall region of the channel flow. The colormap shows the streamwise fluid velocity fluctuations. Panels taken from Rosti et al. (2018) and Dotto and Marchioli (2019)

2D turbulence. Another line of research relates to fibers within two-dimensional fluids, a line of work which carries applications in geophysics, for example to describe the patchiness of plankton or the dynamics of plastic debris on oceanic scales (Powell and Okubo, 1994; Abraham, 1998; Van Sebille et al., 2015). From a fundamental viewpoint, 2D turbulence is obviously very different from 3D turbulence, but provides a flexible environment to analyze multi-scale dynamics. Picardo et al. (2018) have studied the dynamics in the so-called direct enstrophy cascade regime. The authors show a preferential sampling behavior of elastic particles within the large-scale vortices, which depends on the level of flexibility of the fibers.

Fibers are represented with the elastic-chain model, and have a length of the order of the large-scale

injection scale. The authors use the dimensionless Weissenberg number $W_i = \tau_{chain}/\tau_{fluid}$ to measure the chain elasticity, where τ_{chain} is the relaxation time of the chain, which depends on the number of degrees of freedom of the chain. As observed in Fig. 1.18, increasing the level of elasticity increases the preferential sampling. Panels (a) and (b) display the center of mass of the fiber, for two different values of W_i. Fibers act like fluid tracers, when W_i is small. Conversely, the preferential sampling in the vortex zones is observed when the flexibility increases. In addition, panel (c) displays the full fibers with their stretching-compression dynamics.

      The authors also investigate the influence of the turbulent structures on the fiber dynamics. In regions where the flow stretching is strong, the elastic chains remain stretched, and their lengths increase. Due to the increase in size, fibers then start to follow their own dynamics until they reach a vortex. The stretching becomes then negligible, and the chain folds. Fibers remain in the vortex structure until the latter disappears because of dissipation or friction.
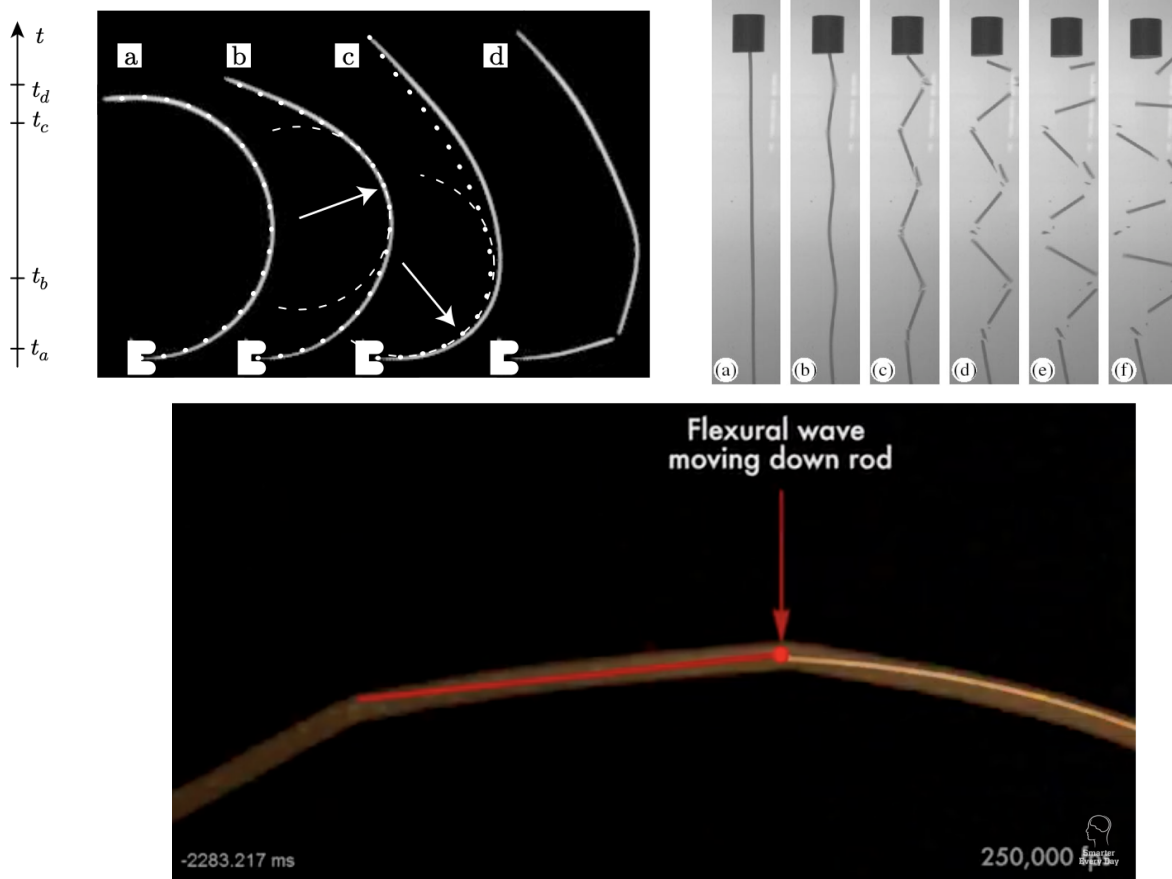

Figure 1.18: Snapshots of elastic chains in a two-dimensional turbulent flow. The background color shows the underlying vorticity ($\ell_f = 2$ and $\tau_f = 2.3$). Panel (a) shows the center of mass for chains with $W_i = 0.004$. Panel (b) shows the center of mass for chains with $W_i = 0.9$. Panel (c) shows the entire chains for $W_i = 0.9$. Parameter values: $\nu = 10^{-6}$, $\mu = 10^{-2}$ and $f_0 = 0.2$. Panels stolen from Picardo et al. (2018)

1.5   Heavy flexible elongated particles

Combining the effects of mass, shape and rheology lead to the study of heavy flexible elongated particles.

Flexural failure: a venture into pasta science.   Flexural failure is an efficient way to break elongated particles. This problem is notorious in rheology as it relates to the fragmentation of dry spaghetti pasta. The rheology of dry spaghettis is not only a practical problem arising in kitchens around the world, but it is also an interesting scientific problem in itself. The reason why spaghetti pasta do not simply and systematically break into two pieces when they are bended is a question that even caught the attention of at least two Nobel-Prized physicists, Richard Feynman and Pierre-Gilles de Gennes (see Sykes (1994)). The resolution of this puzzling problem was found by Audoly and Neukirch (2005) who received an *Ig Nobel Award* price in 2006 (see APS-physics (2006)) for this achievement. The results of Audoly and Neukirch (2005) describe the fragmentation of dry spaghetti pasta in terms of a cascade of fractures. A first break-up of the rod pasta occurs at the position where the curvature is maximal, as is observed in Fig. 1.19. This event triggers a flexural wave which propagates into the two daughter pieces. In one of the pieces, this wave locally increases the curvature and generates a new fragment, possibly leading to successive secondary breakups and to the formation of many small-size fragments. The 2014 youtube channel "Smarter Every Day" (see SmarterEveryDay (2014)) shows this effect clearly using an ultra-fast camera with 250,000 frames per second, and shows how fractures can even cascade throughout the spaghetti. Fig. 1.19 shows how the flexural wave is moving down, here increasing the curvature of the rod pasta on the left piece, which leads to the production of a small fragment

rotating clockwise.

Figure 1.19: Top left panel: Bending of a dry spaghetti pasta leading to an increase of curvature. Image taken from Audoly and Neukirch (2005). Top right panel: buckling and fragmentation of dry pasta ($d = 1.9\,mm$, $L = 24\,cm$) under the action of an aluminium projectile ($U_0 = 3.5\,ms^{-1}$). The images have been taken with time intervals of $236\,\mu s$. Image taken from Gladden et al. (2005). Bottom panel: Screenshot of the breaking of a dry spaghetti pasta filmed in ultra-slow motion. The image was obtained with a fast camera at 250000 fps. Image taken from SmarterEveryDay (2014).

The outcome of this rather complex mechanism is the observation that the number of pieces as well as their sizes is very sensitive to the specifics of the compression. Even in lab controlled experiments, compressing an elongated brittle material is not deterministic. For example, the right panel of Fig. 1.19 shows a rod bending and breaking under an axial compression and realized by Gladden et al. (2005). The initial buckling is subordinated to a selected wavelength, which determines the first breaking point, at the position where a critical curvature is reached. Conversely, it is still unclear what happens next. We observe in Fig. 1.19 that the dry pasta is broken in several pieces. The exact number of dry pasta pieces at the end of the fragmentation is not easily predictable, nor are their sizes. As discussed by Vandenberghe and Villermaux (2013), the propagation of elastic flexural waves after the first breakup may conspire with the presence of material defects acting as "weak points", in order to produce fragmentation in apparently random positions along the body.

1.6 Scope and layout of the thesis

In this thesis, we use massive numerical simulations to perform a systematic statistical analysis of the dynamics of small complex particles in a turbulent environment. As explained previously, we restrict our

attention to small particles with complexities prescribed by non-trivial interplay between the effects of mass, shape and rheology. Following the studies previously presented, we identify several natural and non-trivial questions which guide the course of this thesis:

- *How do turbulent flows prescribe the dynamics of complex particles?*

- *How do turbulent flows prescribe the concentration patterns of complex particles?*

- *How to model fragmentation processes caused by turbulence?*

Naturally, specific answers to those questions will depend on the types of particles that we investigate. As such, the thesis is organized as follows.

In Chapter 2, we introduce the incompressible Navier-Stokes equations, which we use to generate a turbulent velocity field with numerics. We recall a few of the salient statistical features expected for turbulence at infinite Reynolds number, and compare those to the properties observed in our numerics.

Chapter 3 is devoted to the interplay between mass and shape. We consider small massive spheroids within a homogeneous isotropic turbulent flow. We provide a full description of their translational and rotational dynamics. We also characterize their preferential sampling properties.

In Chapter 4, we report on a systematic analysis of small elongated flexible fibers passively transported by the homogeneous isotropic turbulent flow, hereby focusing on the interplay between shape and rheology. We describe in details the hypothesis behind the slender body theory, on which our numerics rely. We then provide statistical analysis of the different types of instabilities experienced by the fibers.

Building on this analysis, Chapter 5 describes an implementation of the material consequences of turbulent extreme events: if brittle, fibers can break. We describe two types of failures, which we implement in our numerics. We also sketch a stochastic model which relates the fragmentation statistics to the waiting times between dangerous turbulent events.

Finally, in Chapter 6, we summarize our results and give some perspectives for future studies related to modeling complex particles in fluids.

2 | From Navier-Stokes equations to turbulence

Contents

This chapter introduces basic concepts and definitions related to fluid mechanics and the Navier-Stokes equations. It highlights the key statistical signatures of turbulent flows which are referred to throughout this manuscript, and discusses their relevance in the context of direct numerical simulations at large but finite Reynolds number.

2.1 Navier-Stokes equations

In concept, a fluid with viscosity ν can be thought of either as an ensemble of fluid particles or as a continuous medium evolving with time throughout a prescribed region $\mathcal{D}$ of the space. This dichotomy provides two different ways to describe the motion of a fluid, *e.g.* either from the **Eulerian** or from the **Lagrangian** perspective. Specifically, the Eulerian viewpoint describes the fluid in terms of the local velocity field $\mathbf{u}(\mathbf{x}, t)$, computed as the average among the fluid particles contained in the vicinity of a prescribed position $\mathbf{x}$ at time t (see the book by Huang (2009)). Conversely, the Lagrangian viewpoint describes the fluid in terms of the dynamics of distinguishable fluid particles. The flow is then prescribed in terms of the dynamical history of each fluid parcel. In other words, rather than sitting on a beach staring at the water as its Eulerian counterpart, the Lagrangian observer sits in a boat and drifts down the river.

In the Eulerian viewpoint, the fluid motion is fully prescribed by the dynamics of the velocity field $\mathbf{u}(\mathbf{x}, t)$ (with $\mathbf{x} \in \mathcal{D}$), and the latter evolves according to the incompressible Navier-Stokes equations:

$$\partial_t \mathbf{u} + (\mathbf{u} \cdot \nabla)\,\mathbf{u} = -\frac{1}{\rho}\nabla p + \nu\,\nabla^2 \mathbf{u} + \mathbf{f} \quad \text{and} \quad \nabla \cdot \mathbf{u} = 0, \tag{2.1}$$

where p is the pressure field solving the Poisson equation $\nabla^2 p = -\mathrm{Tr}(\nabla \mathbf{u}^2)$; $\mathbf{f}$ is the forcing term, representing the external source of energy. We hereafter assume that the forcing is large-scale, which means that it is correlated over a prescribed distance L_f. This defines the injection scale. ρ is the fluid density. Due to the incompressibility condition, ρ is a constant, that we hereafter set to unity. In this manuscript, the Navier-Stokes equations are solved within a triply periodic cube with edge 2π.
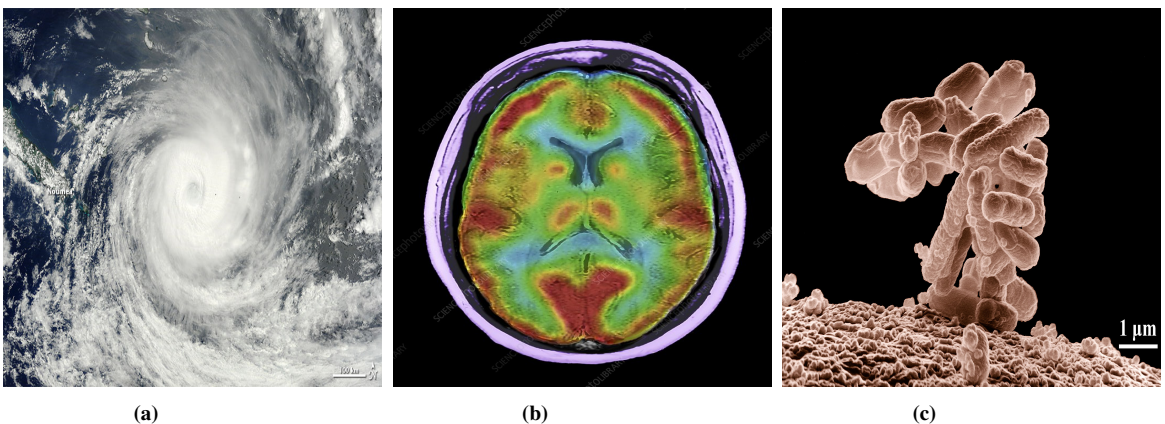
The Navier-Stokes equations involve the interplay between the non-linear advection term $(\mathbf{u} \cdot \nabla) \mathbf{u}$ and the linear diffusion term $\nu \nabla^2 \mathbf{u}$. The prevalence of one term over the other can be quantified by estimating the ratio between them. More precisely, let us introduce the non-dimensional variables $\mathbf{u}' := \mathbf{u}/U_\ell$, $\mathbf{x}' := \mathbf{x}/\ell$ and $t' := t/(U_\ell \ell)$, where U_ℓ represents the typical velocity amplitude at scale ℓ. In terms of those, the Navier-Stokes equations become:

$$\partial_{t'} \mathbf{u}' + (\mathbf{u}' \cdot \nabla') \mathbf{u}' = -\nabla' p' + \nu_\ell \nabla'^2 \mathbf{u}' + \mathbf{f}' \quad \text{and} \quad \nabla \cdot \mathbf{u}' = 0, \tag{2.2}$$

where the ∇' operator here denotes gradient with respect to the primed variables. The new forcing is $\mathbf{f}' = \mathbf{f}\ell/U_\ell^2$. The inverse of the rescaled viscosity $\nu_\ell := \nu/(U_\ell \ell)$ defines a dimensionless number, $Re_\ell = 1/\nu_\ell = U_\ell \ell/\nu$. The primed pressure field is still defined implicitly through the Poisson equation.

Choosing ℓ as the macroscopic **integral scale** L which will be defined precisely in the next paragraph and which for the time being can be identified to the injection scale, and choosing U_L a large-scale velocity, *e.g.* prescribed by the so-called root-mean-squared (rms) velocity $U_L = U := 1/\sqrt{3} (|\mathcal{D}|^{-1} \int_{\mathcal{D}} \|\mathbf{u}\|^2)^{1/2}$, this dimensionless number becomes the celebrated (macroscopic) **Reynolds number** $Re = UL/\nu$. In the present manuscript, the turbulent state of a fluid characterizes the stationary solution generated by the Navier-Stokes equations at "sufficiently high-values" for the Reynolds number. As such, and by a somewhat roundabout definition, the Reynolds number quantifies how turbulent the flow is: the larger, the more turbulent.

For $Re \gg 1$, the dynamics is multi-scale. The scales $\eta \ll \ell \ll L$ define the so-called **inertial range**. The scale $\ell = \eta$ for which $Re_\eta = \nu_\eta^{-1} = 1$ formally defines the onset for the dissipative scales. On scales $\ell < \eta$, the dissipative term dominates over the advection term and the velocity diffuses. The dissipative scale η is also known as the **Kolmogorov dissipation scale**. As for the integral scale, it requires further physical hypothesis to be fully specified. A brief overview of the standard description of turbulent flow is therefore provided in the next section. Let us here just mention that typical values for the Reynolds numbers range from 10^{12} in atmospheric tropical cyclones (Fig. 2.1a) down to 10^2 for blood flowing through the human brain (Fig. 2.1b) and 10^{-4} for E. coli bacteria swimming at $\approx 10 \mu m s^{-1}$ (Fig. 2.1c) (Lauga and Powers, 2009; Vogel, 2020).

(a)   (b)   (c)

Figure 2.1: Natural exemples of turbulent flows with different Reynolds numbers. Panel (a) shows the tropical cyclone Jasmine ($^{©}$ NASA image courtesy Jeff Schmaltz 2012 (NASA, 2012)); Panel (b) illustrates the blood flow within a typical human brain. The image is obtained from composite coloured magnetic resonance imaging (MRI) and single-photon emission computed tomography (SPECT) (Zephyr, 2020); Panel (c) shows a low-temperature electron micrograph of a cluster of E. coli bacteria ($^{©}$ Eric Erbe, digital colorization by Christopher Pooley, both of USDA, ARS, EMU.)

2.2 The statistical description of turbulence

The well-posedness of the Navier-Stokes equations is a formidable challenge for the mathematicians and a rigorous description of the turbulent state from first principles is to this day elusive (Caffarelli, 2000). Since the seminal work of Reynolds in the 19th century, physicists and engineers have however been steadily working to develop a heuristic description of turbulence based on various tools and concepts, such as stochastic processes, data analysis, dimensional analysis, scaling laws, toy models, approximations, and so on. To this day, the prevalent picture accounting for the statistical properties of turbulence originates from the pioneering work of Richardson. In a nutshell, Richardson describes a turbulent flow as a hierarchical field intertwining energetical structures with a multitude of different sizes, the so-called "turbulent eddies". The large eddies leak energy to the smaller ones, in a cascade process only ending when dissipative scales are reached. This cascade picture of turbulence anticipates on Kolmogorov 1941 theory (K41), which provides a conceptual framework describing turbulence in terms of statistically self-similar flow fields. A modern reformulation of K41 theory can be found in (Frisch, 1995, Chap. 6,7). It provides an axiomatic description of turbulence in the limit of infinite Reynolds number, the so-called "fully developed turbulence", under the following hypothesis:

H1 *(Fully-developed) turbulent flows are homogenous, isotropic and stationary within the inertial range of scales*

In other words, all the possible symmetries are statistically restored at inertial scales. This means that a turbulent flow is invariant under time-translation, space-translation and space-rotation. Inertial scales refer to scales far away from the boundaries, smaller than the injection length scale and unaffected by dissipation.

H2 *They have self-similar statistics, fully prescribed by a unique scaling exponent h.*

Roughly said, self-similar structures are structures that look alike at any level of zoom. Mathematically, this concept formalizes Richardson's vision of turbulent eddies being analogous to Russian doll. Defining the velocity increments

$$\delta\mathbf{u}(\mathbf{x}, \ell) = \mathbf{u}(\mathbf{x} + \ell) - \mathbf{u}(\mathbf{x}), \tag{2.3}$$

the second hypothesis implies the existence of a scaling exponent $h \in \mathbb{R}$ such that the velocity increments behave as

$$\delta\mathbf{u}(\mathbf{x}, \lambda\ell) \stackrel{law}{=} \lambda^h \delta\mathbf{u}(\mathbf{x}, \ell) \qquad \forall \lambda \in \mathbb{R}_+ \tag{2.4}$$

for all $\mathbf{x} \in \mathcal{D}$ and all increments ℓ and $\lambda\ell$ lying within the inertial range. The equality in law used in the above equation identifies the probability distribution of the rhs and lhs considered as random objects.

H3 *In the limit of vanishing viscosity, the mean rate of energy dissipation ε_ν converges towards a finite non-negative value.*

Explicitly, $\varepsilon_\nu = \nu\langle\|\nabla\mathbf{u}\|^2\rangle \to \varepsilon < \infty$ in the limit $\nu \to 0$. Physically, this means that lowering the viscosity produces sharper velocity gradients, and that turbulent flow fields are therefore very irregular in the limit of vanishing viscosity.

Under those hypothesis, the statistics of turbulent velocity fields within the inertial range are then fully prescribed by the scale ℓ and the value of ε. Dimensional analysis prescribes the value $h = 1/3$ for the scaling exponent introduced in H2. This entails the scaling $\delta\mathbf{u} \sim (\varepsilon\ell)^{1/3}$ within the intertial range. We can now further specify the **Kolmogorov dissipative scale**, for which effects of viscosity become apparent, as

$$\eta = \left(\frac{\nu^3}{\varepsilon}\right)^{1/4}, \tag{2.5}$$

and we also define the integral scale L from the rms velocity U as

$$L = U^3/\varepsilon, \quad \text{where } U = \frac{1}{\sqrt{3}} \left\langle \|\mathbf{u}\|^2 \right\rangle_{\mathcal{D}}^{1/2},$$ (2.6)

and $\langle \cdot \rangle_{\mathcal{D}}$ denotes spatial averaging over the domain.

In terms of timescales, we define the eddy turnover times $\tau_\ell = \varepsilon^{-1/3}\ell^{2/3}$ relevant for inertial range statistics. This prescribes the Kolmogorov (dissipative) timescale τ_η and the integral timescale τ_L, which can respectively be interpreted as the fastest and the slowest timescales within the inertial range. Note, that by construction of the integral scale, the large-scale eddy turnover time satisfies $\tau_L = \varepsilon^{-1/3}L^{2/3} = L/U$. The ratio between the integral and the dissipative timescales is used to define a new dimensionless number, also called the Taylor-scale Reynolds number [1]

$$Re_\lambda := \sqrt{15}\,\frac{\tau_L}{\tau_\eta} = \sqrt{15}Re^{1/2}.$$ (2.7)

Those definitions allow to further illustrate the connection between Reynolds number and multi-scale statistics. Indeed, assuming that inertial range statistics pertain to the full range of scales $\eta \le \ell \le L$, one can use the estimates $\varepsilon = U^3/L = u_\eta^3/\eta$ to obtain

$$\left(\frac{L}{\eta}\right)^4 = Re^3, \quad e.g. \; \frac{L}{\eta} = Re^{3/4} \sim Re_\lambda^{3/2} :$$ (2.8)

the higher the Reynolds, the larger the ratio between the integral and the dissipative scales, both in terms of length-scales and in terms of time-scales. Naturally those estimates rely on dimensional analysis and do not define sharp delimiters. We will explicitly illustrate this feature using our numerics.

2.3 Turbulence in spectral space

2.3.1 From experiments and numerical simulations

Experimental and observational studies of turbulence remain the most convenient way to reach huge Reynolds numbers relevant for the study of fully developed turbulence. Measurement techniques have been improved for years and allow for some fine characterization of multi-scale statistics in turbulent fluid flows, along with finite-Reynolds effects (Champagne, 1978; Klewicki et al., 1998; Castaing et al., 1990; Arneodo et al., 1996; Baudet et al., 2015; Kharche et al., 2019; Saw et al., 2016). Over the past 40 years, the growth of computer power and numerical ressources have however allowed simulations of turbulent flows to have an increasing impact. To understand fluid dynamics at high Reynold number, the advantages of using numerics are many, among them well-defined initial conditions, better conditioning of statistics, closer contact to the mathematical theory of the Navier-Stokes equations and chief of all detailed access to the full flow field (in terms of velocity, acceleration, pressure, dissipation, both in Eulerian and Lagrangian perspective). This flexibility is particularly appreciable when dealing with transport problems, as is the case in the present manuscript. Systematic analysis of the dynamics of potentially complex Lagrangian particles is then easily accessible, without having to worry about water shortage.

Yet, generating turbulence with numerical solvers is both an easy and a hard task, depending on the chosen parameters. On the one hand, it suffices to integrate the Navier-Stokes equations for sufficiently long time, and this is the spirit behind **direct numerical simulations** (DNS) of the Navier-Stokes (NS) equations. On the other hand, those equations are cumbersome to integrate over many scales, that is for large values of the Reynolds number and for long times. The reason for this difficulty is readily apparent from Eq. (2.8), which implies that a turbulent field has *many* degrees of freedom. Specifically, the number of required

---

[1]The numerical pre-factor $\sqrt{15}$ is conventional but not arbitrary. It stems from the usual definition of the Taylor-scale Reynolds number as $Re_\lambda = U\lambda/\nu$ using the Taylor scale $\lambda = U/\langle(\partial_i u_i)^2\rangle_{\mathcal{D}}$ with $i = x, y$ or z. The two definitions coincide for isotropic turbulence (Frisch, 1995).

collocation points is $N^3 \sim (L/\eta)^3 \sim Re^{9/4} \sim Re_\lambda^{9/2}$, and this fundamentally prevents numerical methods to reach gigantic Reynolds numbers.

The largest Reynolds number achieved through a direct numerical simulation of the Navier-Stokes equations is to this day $Re_\lambda \approx 1300$ (Iyer et al., 2017) using 16384^3 collocation points. This corresponds to a macro-scale Reynolds number of the order $Re \approx 10^5$, that of a small washing-machine. For such values, the turbulence is expected to be fully developed, as observed in controlled studies of hydrodynamic turbulence using the Von-Kármán experiment (Dubrulle, 2019). While current controlled experimental realizations of such flows track the fluid over thousands of integral times, numerics however only manage to produce turbulent dynamics at such Reynolds number over a few integral times.

For our purpose, where we are interested in analyzing ensembles of solutions rather than a single realization, we will deal with more modest resolutions, involving anything in between 512^3 and 4096^3 points. Still, achieving long time integration of the NS equations remains a formidable task, and we rely on a numerical solver implementing massive parallelization of the dynamics. At this point, let us point out that besides computing time availability, storing full turbulent fields entails huge memory cost. To give a rough idea, storing a field every few τ_η for a few integral time-scales requires a storage $C \propto Re_\lambda N^3 \propto N^{11/3} \propto Re_\lambda^{11/2}$. This means that doubling resolution produces data approximately 13 times as voluminous.

2.3.2 Spectral space and LaTu solver

LaTu solver. The use of Fourier space in turbulence simulations is a powerful tool that produces highly accurate schemes compared to other methods such as finite-difference, finite-volume or finite-element methods (see the book by Ferziger et al. (2002)). Besides, it provides a well-controlled approximation of the NS dynamics that relies on the concept of Galerkin projection (Orszag, 1973).

In the present thesis, we rely on the specific **LaTu** numerical solver, developed in the recent years by H. Homann, in order to numerically solve the NS equations. The LaTu solver solves the NS equations in a triply periodic cubic domain with edge 2π. It relies on a massive parallelisation through a pseudo-spectral scheme using fast-Fourier transforms to bridge physical space to Fourier space. We recall that pseudo-spectral codes efficiently combine calculation methods in spectral and physical space to produce fast schemes while retaining the power of Fourier projections. On the one hand, the spatial derivatives are easily calculated in spectral space by pointwise multiplication of the Fourier transformed fields with the wavevectors **k**. On the other hand, the quadratic non-linearity involving cumbersome convolution in spectral space is computed using point-wise multiplication in physical space. As such, the cost of a single time step requires $O(N^3 \log N)$ operations. This is way more efficient than the $O(N^6)$ operations that would be required if the code was purely spectral (Anderson and Wendt, 1995).

We typically use a forcing scheme which prescribes the kinetic energy in the first two Fourier shells, as described by Homann et al. (2007). We here describe the turbulence obtained using three different resolutions, namely 512^3, 1024^3 and 4096^3, which respectively achieve a Re_λ of 199, 325 and 731. Because of the finite resolution, there is a maximal wavenumber k_{max} which characterizes the smallest structures that the simulation can produce. In many simulations, $k_{max} = [N/3]$ and this corresponds to the so-called 2/3 de-aliasing rule which guarantees conservation of energy in the limit $\mathbf{f} = 0, \nu = 0$ (Orszag, 1971). In our simulations, we rely on another de-aliasing scheme known as Hou smoothing that was introduced by Hou and Li (2007), for which $k_{max} = [N/2]$. While Hou smoothing does not conserve energy in the inviscid limit, it is considered a safe method by computational fluid dynamicists, which allows to solve for a slightly extended inertial range compared to the standard 2/3-rule. Those are the simulations which we rely on the course of this manuscript, and we summarize the main parameters of our simulations in Table 2.1. Finally, note that the integral scale L yield to the wavenumber $K_L = 2\pi/L \sim 4$, which coincides with the forcing scale.

A rule of thumb to estimate the accuracy of a Fourier solver is the quantity $k_{max}\eta$ that should be of order unity or larger. In our simulations, $k_{max} = 2N/5$ (instead of $N/3$ if we had not used Hou smoothing but rather the 2/3-rule), and the value of η are summarized in Table 2.1. For the 512^3 and 1024^3 runs, we get $k_{max}\eta \simeq 0.86$, and for the 4096^3 run, we get $k_{max}\eta \simeq 1.2$. Those numbers mean that the 4096^3 run is slightly better resolved than the other two.

N^3	ν	Δt	ε	η	τ_η	u_{rms}	L	τ_L	R_λ
512^3	$5\ 10^{-4}$	10^{-3}	0.4083	0.0042	0.035	0.8564	1.54	1.80	199
1024^3	$2\ 10^{-4}$	$5\ 10^{-4}$	0.431	0.0021	0.022	0.87	1.52	1.753	315
4096^3	10^{-5}	$6\ 10^{-4}$	$3.8\ 10^{-3}$	$7.16\ 10^{-4}$	0.051	0.19	1.86	9.68	731

Table 2.1: Numerical and physical parameters of the direct numerical simulation: N^3 number of collocation points, ν kinematic viscosity, Δt time step, ε average kinetic energy dissipation rate, $\eta = \nu^{3/4}/\varepsilon^{1/4}$ Kolmogorov dissipative scale, $\tau_\eta = \nu^{1/2}/\varepsilon^{1/2}$ Kolmogorov time, u_{rms} root-mean square velocity, $L = u_{\text{rms}}^3/\varepsilon$ large-eddy length scale, $\tau_L = L/u_{\text{rms}}$ large-eddy turnover time, $R_\lambda = \sqrt{15}\, u_{\text{rms}}^2/(\nu^{1/2}\varepsilon^{1/2})$ Taylor-based Reynolds number.

Energy budget.   In the light of the K41 theory, let us now characterize some of its essential features. To do so, we first rely on the spectral space representation of the velocity field. Specifically, writing

$$\mathbf{u}(\mathbf{x}, t) = \sum_{\mathbf{k}} \hat{\mathbf{u}}(\mathbf{k}, t)\, e^{i\mathbf{k}\cdot\mathbf{x}}\,, \quad \text{where} \quad \hat{\mathbf{u}}(\mathbf{k}, t) := \frac{1}{(2\pi)^3} \int_{\mathcal{D}} \mathrm{d}\mathbf{x}\, \mathbf{u}(\mathbf{x}, t)\, e^{-i\mathbf{k}\cdot\mathbf{x}}, \tag{2.9}$$

one defines the isotropic energy spectrum $E(k, t)$ as:

$$E(k, t) := \frac{1}{2} \sum_{\mathbf{k}} |\hat{\mathbf{u}}(\mathbf{k}, t)|^2 \text{ with } \quad k - \frac{1}{2} < |\mathbf{k}| \le k + \frac{1}{2}. \tag{2.10}$$

The latter quantity allows to compute the total kinetic energy as $E := \sum_{k=1}^{k_{max}} E(k, t)$ and provides the estimate $\Omega := \sum_{k=1}^{k_{max}} k^2\, E(k, t)$ for the enstrophy. In addition, the non-linear energy flux is defined as

$$\Pi(k, t) = \sum_{|\mathbf{k}| \ge k} T(\mathbf{k}, t), \quad \text{where} \quad T(\mathbf{k}, t) := \Re\left\{ \sum_{i,j=1,2,3} \hat{u_i^\star}(\mathbf{k}, t)\, \mathbb{P}_{i,j}(\mathbf{k})[\mathbf{u} \times \widehat{(\nabla \times \mathbf{u})}]_j(\mathbf{k}, t) \right\} \tag{2.11}$$

is the energy transfer function. Those quantities appears in the scale-by-scale energy budget:

$$\partial_t \mathcal{E}(k, t) + \Pi(k, t) = \mathcal{F}(k, t) + \mathcal{D}(k, t), \tag{2.12}$$

where $\mathcal{E}_k$, Π_k, $\mathcal{D}_k$ and $\mathcal{F}_k$ respectively represent the energy contained in wavenumbers $\le k$, the energy flux (2.11) from modes $\le k$ to modes $\ge k$, the energy dissipation and the energy injection rate. Explicit formula for those quantities are :

$$\mathcal{E}(k, t) = \frac{1}{2} \sum_{|\mathbf{k}| \le k} |\hat{\mathbf{u}}(\mathbf{k}, t)|^2, \quad \mathcal{D}(k, t) = -\nu \sum_{|\mathbf{k}| \le k} |\mathbf{k}|^2\, |\hat{\mathbf{u}}(\mathbf{k}, t)|^2 \quad \text{and} \quad \mathcal{F}(k, t) = \sum_{|\mathbf{k}| \le k} \hat{f}_k \cdot \hat{\mathbf{u}}(-\mathbf{k}, t). \tag{2.13}$$

K41 theory relates to the statistically steady state of turbulence, formally described by averaging both sides of Eq. (2.12). The scale-by-scale energy budget then becomes
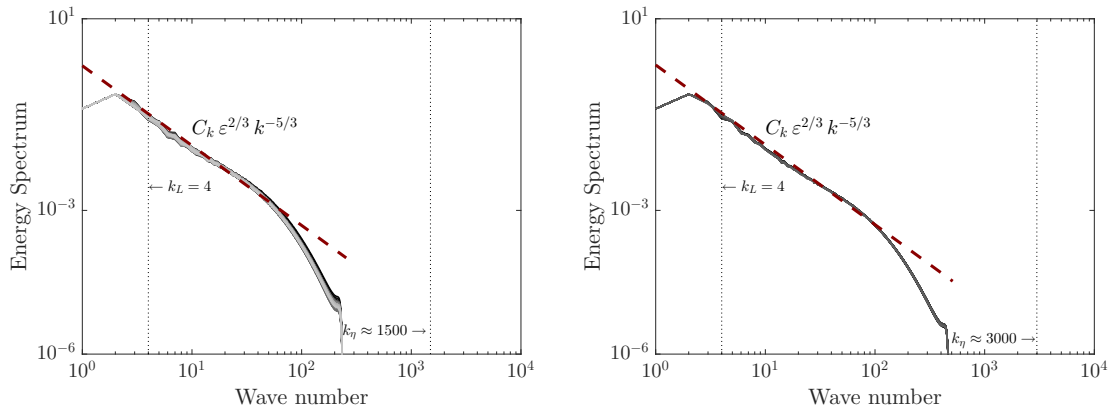
$$\Pi(k) = \mathcal{F}(k) + \mathcal{D}(k), \tag{2.14}$$

with the short-hand notation $\Pi(k) = \langle \Pi(k, t) \rangle$, $\mathcal{F}(k) = \langle \mathcal{F}(k, t) \rangle$, etc.

The Wiener-Khinchin theorem ties the scaling of the energy spectrum to the Fourier transform of the two-point correlation. As such, the K41 theory entails scaling of the velocity increments as $E(k) = C_K \varepsilon^{2/3} k^{-5/3}$ with C_K a pre-factor known as the Kolmogorov constant. Inertial range statistics then feature constancy of the stationary energy flux for $\eta \ll \ell \ll L$.

Numerics.   In Fig. 2.2, we indeed observe the Kolmogorov $-5/3$ spectrum for two different resolutions of the flow: In the left panel, the simulation employs 512^3 collocation points and in the right panel 1024^3 points. In both pictures, the scaling range extends over more than a decade. It is delimited by $k_L = 4$ on the infra-red side, determined by forcing scale. The difference in Reynolds numbers materializes in the 1024^3 simulation having larger extent on the ultra-violet side in contrast to the 512^3 run, because the small scales are better resolved, hence allowing smaller value for the viscosity.

As anticipated, we observe that the Kolmogorov scale $k_\eta = 2\pi/\eta$ is not a sharp delimiter of the dissipative range. Formula (2.5) estimates $k_\eta \approx 1500$ for the 512 run and $k_\eta \approx 3000$ for the 1024 run (see Fig. 2.2)... this is much larger than k_{max}! [2] In both cases, the spectrum within the inertial range is well fitted by the formula $E(k) = C_K\, \varepsilon^{2/3}\, k^{-5/3}$ (red dash-line), where the constant $C_K \approx 1.5$ is in good agreement with the values usually reported in experimental studies Pope (2001); Sreenivasan (1995).
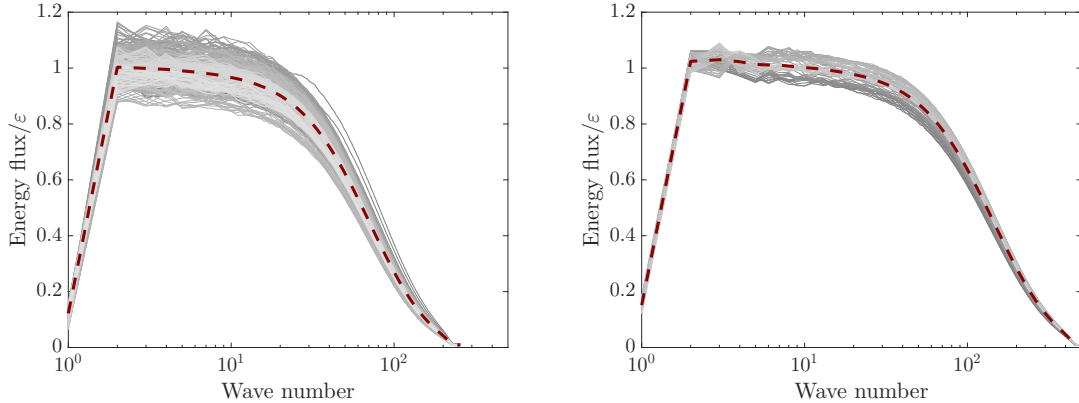
Figure 2.2: Turbulent spectrum of energy for two different resolutions of the flow. On the left side the simulation employs 512^3 collocation points and in the right side 1024^3 points. Gray lines show the energy spectrum at different times and the red dash-line shows the Kolmogorov spectrum $E(k) = C_K\, \varepsilon^{2/3}k^{-5/3}$ with $C_K \approx 1.5$. The two vertical dash-lines display the forcing scale k_L and the Kolmogorov scale k_η.

Fig. 2.3 shows the normalized energy flux as a function of the wavenumber for both simulations. The energy flux is clearly not constant over the full inertial range $k_\eta \gg k \gg k_L$, and exhibits strong fluctuations in time, as shown by the spread of the light grey lines, showing different simulation times. The average of those is shown in red. Upon normalization by the mean dissipation rate, the flux is approximately a constant on the scales $2 < k \lesssim 20$ for the 512^3 simulation and $2 < k \lesssim 50$ for the 1024^3 simulation. Note that the plateau behavior only holds for wavenumber k much lower than the dissipative wavenumber k_η (see Fig 2.2). The observation that the energy flux essentially behaves as a constant over a wide range of scales illustrates the concept of cascade, *e.g.* the observation that within this range, identified as the inertial range, the scale-to-scale energy transfer matches the energy dissipation rate. In other words, we expect that in the limit of vanishing viscosity

$$\Pi(k) = const = \varepsilon \quad \text{for all } k \gg k_L. \tag{2.15}$$

---

[2]This value of k_η corresponds to a physical dissipative scale $\eta \approx \Delta x/3$. This rather small value is allowed thanks to our use of Hou smoothing. If we had relied on the usual 2/3 de-aliasing rule, we would have tuned the parameters so that $\eta \approx \Delta x/2$.
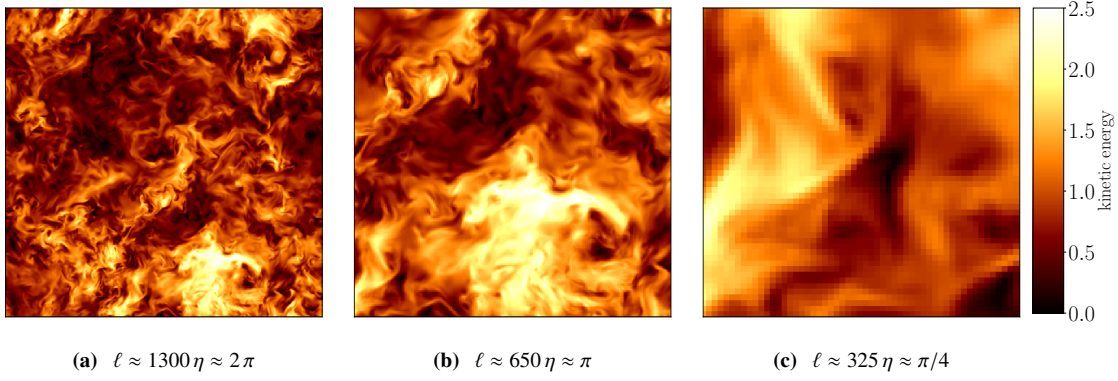
Figure 2.3: Energy flux normalized by the mean dissipation rate ε for two different resolutions of the flow. The left panel displays a resolution of 512^3 collocation points and the right panel a resolution of 1024^3 collocation points. The gray lines show the instantaneous energy flux at different times, and the red dash-line the time-average.

2.4 Turbulence in physical space

2.4.1 K41 theory
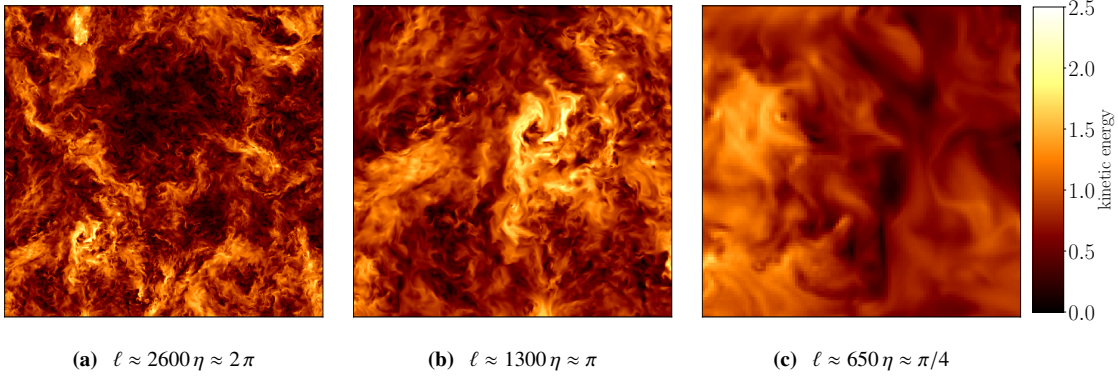
The use of a pseudo-spectral method to solve the NS equations seemingly ties the analysis to spectral space. However, the latter only provides limited advantage compared to physical space. While the second order moment of the increments is directly linked to the energy spectrum, it is cumbersome to access higher order moments of the velocity field in spectral space. For that matter, it remains insightful to study high-order statistics in physical space, in spite of the periodic boundary conditions.

Fig. 2.4 and Fig. 2.5 respectively display three snapshots of the kinetic energy density $e(\mathbf{x}, t) = 1/2|\mathbf{u}|^2(\mathbf{x}, t)$; projected in the plane $x - y$ of the fluid. In order to appreciate the variety of scales participating in the field, various levels of zoom have been chosen: 2π, π and $\pi/4$. Those respectively correspond to the integral scale, the inertial range and the onset of small scales. We observe that the fluid displays complex patterns throughout those scales, possibly representative of a self-similar behavior. In addition, the right panels of Fig. 2.4 and Fig. 2.5 allow to appreciate the resolution limits inherent to the use of numerical simulations, zooming into the structures of the order of the dissipation scale. On those scales, the energy field is smooth and does not ressemble the large-scale pattern shown in the left panel: the self-similarity is clearly lost. It will be readily seen that this multi-scale physics does not fit within the framework of K41 theory, and that a better description is provided by the so-called K62 theory, which takes into account the spatial fluctuations of the dissipation.

(a) $\ell \approx 1300\,\eta \approx 2\pi$ **(b)** $\ell \approx 650\,\eta \approx \pi$ **(c)** $\ell \approx 325\,\eta \approx \pi/4$

Figure 2.4: Snapshots of the energy density $e(\mathbf{x}, t) = 1/2|\mathbf{u}|^2(\mathbf{x}, t)$ for different levels of zoom in the $x - y$ plane, using the 3D simulation with 512^3 collocation points.

In order to compare the two different resolutions, we show in Fig. 2.4 and Fig. 2.5 the energy field using the same zoom level ℓ when expressed in terms of the large-scale L. Note that because one resolution is twice the other the dissipative scales are $\eta_{1024} = \eta_{512}/2$. We indeed observe that 1024^3 run has a better resolution and better resolves smaller structures. At fixed level of zoom, the energy field is less blurry.

(a) $\ell \approx 2600\,\eta \approx 2\pi$ **(b)** $\ell \approx 1300\,\eta \approx \pi$ **(c)** $\ell \approx 650\,\eta \approx \pi/4$

Figure 2.5: Snapshots of the energy density $e(\mathbf{x}, t) = 1/2|\mathbf{u}|^2(\mathbf{x}, t)$ for different levels of zoom in the $x - y$ plane, using the 3D simulation with 1024^3 collocation points.

K41 theory is formally meant to describe fluids at infinite Reynolds numbers. A natural question to ask is whether the fluid flows generated by direct numerical simulations of the Navier-Stokes equations fit into that framework, at least approximately. To address this issue, convenient objects to introduce are the structure functions. Those objects prove very useful in highlighting the self-similar nature of the velocity field and appear in the 4/5 law of turbulence, one of the few exact results known to physicists on the NS equations.

Structure functions characterize the statistical distribution of the turbulent velocity field by measuring its statistical moments. Specifically, structure functions measure the moments of the velocity difference between two points $\mathbf{x}' = \mathbf{x} + \ell\mathbf{r}$ and $\mathbf{x}$, with $\mathbf{r}$ a prescribed unit vector. It is then customary to introduce the parallel and the perpendicular structure functions, respectively defined as
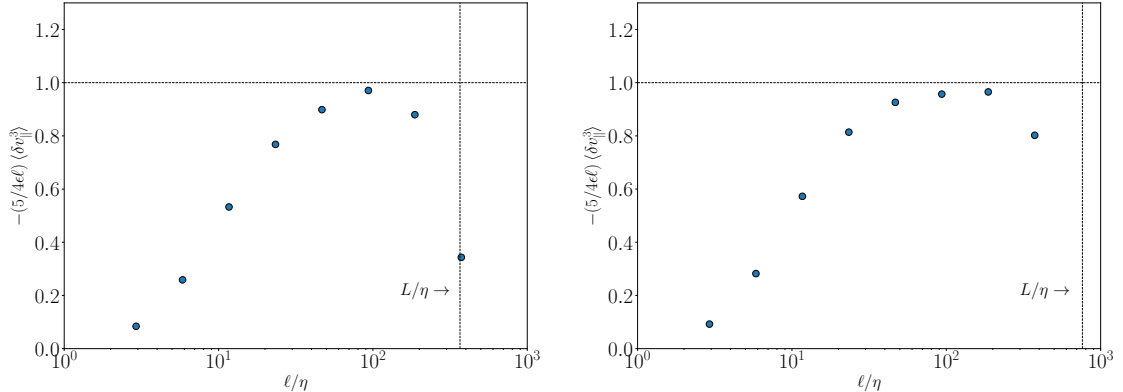
$$S_{p,\parallel}(\ell) = \langle((\mathbf{u}(\mathbf{x} + \ell\mathbf{r}) - \mathbf{u}(\mathbf{x})) \cdot \mathbf{r})^p\rangle \quad \text{and} \quad S_{p,\perp} = \langle((\mathbf{u}(\mathbf{x} + \ell\mathbf{r}) - \mathbf{u}(\mathbf{x})) \cdot \mathbf{r}_\perp)^p\rangle, \tag{2.16}$$

where $\langle \cdot \rangle$ denotes an average over both space and angular sectors, and $\mathbf{r}_\perp$ is a unit vector perpendicular to $\mathbf{r}$ [3]. The first moment is the expected value, the second moment is the variance, the third relates to the skewness and the fourth to the kurtosis. Among those, the third-order moment has a peculiar status as the K41 hypothesis (and more precisely the combination of H1 and H3) yield the

4/5 Law: *In the limit of infinite Reynolds number, the third order parallel structure function of homogeneous isotropic turbulence, evaluated for increments ℓ small compared to the integral scale, is given in terms of the mean energy dissipation per unit mass ε (assumed to remain finite and non-vanishing) by*

$$S_{3,\|} = -\frac{4}{5}\varepsilon\ell. \tag{2.17}$$

While an exact result, one may still ponder upon the universality of this law, and its relevance when it comes to describing finite-Reynolds simulations. Fig. 2.6 shows the third-order parallel structure function as a function of the physical scale ℓ, normalized by the Kolmogorov scale η. We normalize the structure function with the pre-factor $-\frac{5}{4\varepsilon\ell}$, so that it is 1 when the 4/5 law is valid. As in Fig. 2.2 and in Fig. 2.3, two different resolutions are shown, using either 512^3 (left) or 1024^3 (right) collocation points. For scales of the order of $10\,\eta$ and up to $\sim 500\,\eta$, deviations to the 4/5 law are clearly visible. The universality of inertial range statistics is there polluted by finite-size effects (dissipative scales or injection scales). Still, the 4/5 law holds approximately over a narrow range of scales. In the larger simulation, with a higher Reynolds number, this range extends over almost one decade. This behavior is the physical space counterpart to the energy flux observed in Fig 2.3.

Figure 2.6: Illustration of the 4/5 law: The normalized parallel third order moment as a function of the length ℓ normalized by the dissipation scale η. The horizontal dash-line shows the 4/5 behavior and the vertical one the normalized integral scale L/η. Two turbulent resolutions are resolved: 512^3 collocation points in the left side and 1024^3 points in the right.
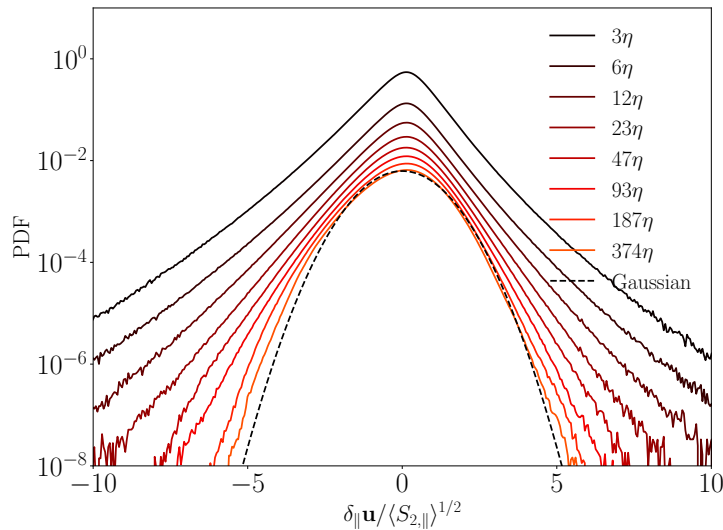
2.4.2 Failure of K41 theory

In the K41 description, the turbulent velocity field is assumed to have mono-fractal statistics, characterized by the scaling exponent $h = 1/3$. In principle, this should imply Gaussian statistics for the velocity field. Let us indeed fix ℓ within the inertial range, and a unit vector $\mathbf{r}$. The parallel increments along the unit vector can be decomposed as

$$\delta\mathbf{u}_\|(\mathbf{x}, \ell\mathbf{r}) = (\mathbf{u}(\mathbf{x} + \ell\mathbf{r}) - \mathbf{u}(\mathbf{x})) \cdot \mathbf{r} = \sum_{i=0}^{K-1} \delta_\|\mathbf{u}(\mathbf{x}_i, \mathbf{r}\ell/K), \text{ with } \mathbf{x}_i = \mathbf{x} + i\mathbf{r}\ell/K \tag{2.18}$$

---

[3] specifically $\mathbf{r}_\perp := \mathbf{e} \times \mathbf{r}$ with $\mathbf{e}$ a prescribed unit vector.

for some prescribed $K \gg 1$ such that $\ell/K \gg \eta$. By homogeneity, the increments at positions $\mathbf{x}_i$, e.g. $\delta_\parallel \mathbf{u}(\mathbf{x}_i, \ell/K)$, are identically distributed and have finite variance $\propto \varepsilon^{2/3}(\ell/K)^{2/3}$. Assuming statistical independence of the velocity increments intervening in the summation of the rhs of Eq. (2.18), and invoking the central limit theorem should then yield Gaussian statistics for the velocity $\delta_\parallel \mathbf{u}(\mathbf{x}, \ell)$. Besides independence, this arguments requires K to be large enough. Now, if the statistics are Gaussian at a prescribed scale, even large, then they have to be Gaussian at all scales from the H2 self-similarity hypothesis. However, this conclusion is erroneous and not supported by observation. Indeed, Fig. 2.7 shows the distributions of the parallel structure functions at various scales throughout the inertial range for the 1024^3 simulation. Approximate Gaussian behavior is seen for the large separations hinting at the validity of the above argument. Yet, as one monitors the distributions of velocity increments separated by smaller and smaller separations, one observes clear deviation from Gaussianity. In fact, it is apparent from Fig. 2.7 that the tails become fatter upon moving down the scales, revealing clear breakdown of scale-invariance and failure of the K41 picture to account for the turbulent statistics.

Figure 2.7: Probability density function of the parallel velocity increments $\delta_\parallel u$ for various separations represented by different colors and rescaled by their variances. The distributions are shifted vertically to enhance visibility. The dashed line represents the centered Gaussian distribution with unit variance, defined through $P(x) = exp(-x^2/2)/\sqrt{2\pi}$. The data is obtained from a 3D simulation with 1024^3 collocation points.

The breakdown of self-similarity can be traced back to the behavior of the structure functions. For simplicity, let us discuss the case of the parallel structure functions. Due to scale invariance, we expect that the structure functions follow a power law:

$$S_{p,\parallel}(\ell) \sim \ell^{\xi_p} \tag{2.19}$$

The scaling of the second-order structure function relates to the correlation of the velocity field. It is the physical space counterpart to the energy spectrum. For this quantity, one expects scaling close to 2/3 following the K41 axioms. As seen in the left side of Fig. 2.8, scaling is present but highly depleted by the presence of the dissipative scales. This finite-size effect produces high uncertainty when it comes to measuring a scaling exponent. To patch this undesirable feature, we rely on the **extended** self-similarity (ESS) approach (Benzi et al., 1993), which can be seen as a technical way to accomodate dissipation.
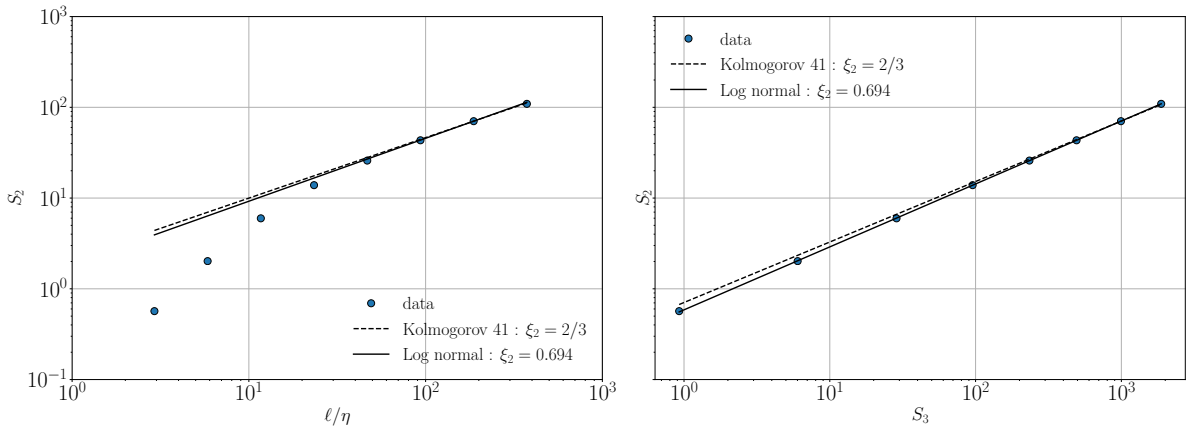
Our ESS analysis employs the two following rather standard tricks:

1. Instead of Eq. (2.16), we monitor the scaling behavior of the structure functions:

$$S_p(\ell) = \langle |(\mathbf{u}(\mathbf{x} + \ell\mathbf{r}) - \mathbf{u}(\mathbf{x})) \cdot \mathbf{r}|^p \rangle. \tag{2.20}$$

Note that the difference with the previously defined parallel structure function is the presence of the absolute value inside the average. Hence, we are putting the analysis of odd and even structure functions on the same footage.

2. According to the 4/5 law, we know that the third order structure function is proportional to ℓ. Thus, instead of ℓ, the scaling of S_p is analysed as a function of S_3, hence allowing an extended scaling range down to the dissipative scale. This analysis allows to spot even small deviations to the K41 scaling as shown for instance in the left panel of Fig. 2.8.

Figure 2.8: Second order structure function. On the left side as a function of the length ℓ normalized by the dissipation scale τ_η and on the right side as a function of the third order structure function. The blue dots display the numerical data obtained from the 1024 run. The dash and solid lines respectively show the exponents obtained from the Kolmogorov $K41$ and an arbitrary model used in ESS, in our case it is a log-normal function.
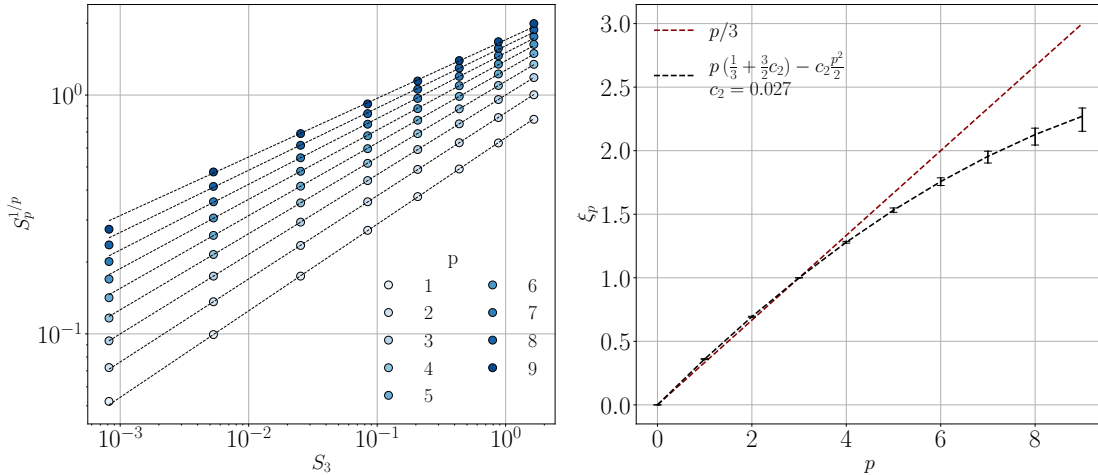
Through extended self-similarity, we characterize deviations from mono-fractal statistics (K41) by estimating the scaling exponents of the structure functions. The left side of Fig. 2.9 shows the relation between $S_p^{1/p}$ and S_3. If the mono-fractal behavior was to hold, the lines would be parallel between them and would follow the relation $S_p^{1/p}/S_3 \sim 1/3$. Clearly, this is not the case and numerics display a multi-fractal behavior, as the curves seem to converge towards each other on their right-ends. This observation is substantiated by the right panel of Fig. 2.9, where the scaling exponents are reported. The red dash-line shows the K41 behavior characterized by the scaling $\xi_p = p/3$. Obviously, the numerical data (delimited by the black error bars) do not follow this law, and deviations are particularly apparent from $p \geq 4$. Conversely, we observe that numerics are in good agreement with the quadratic fit:

$$\xi_p = c_1 p - c_2 \frac{p^2}{2}. \tag{2.21}$$

The coefficients c_1 and c_2 are related through the 4/5 law (2.17), which prescribes $\xi_3 = 1$, and hence:

$$c_1 = \frac{1}{3} + \frac{3}{2} c_2. \tag{2.22}$$
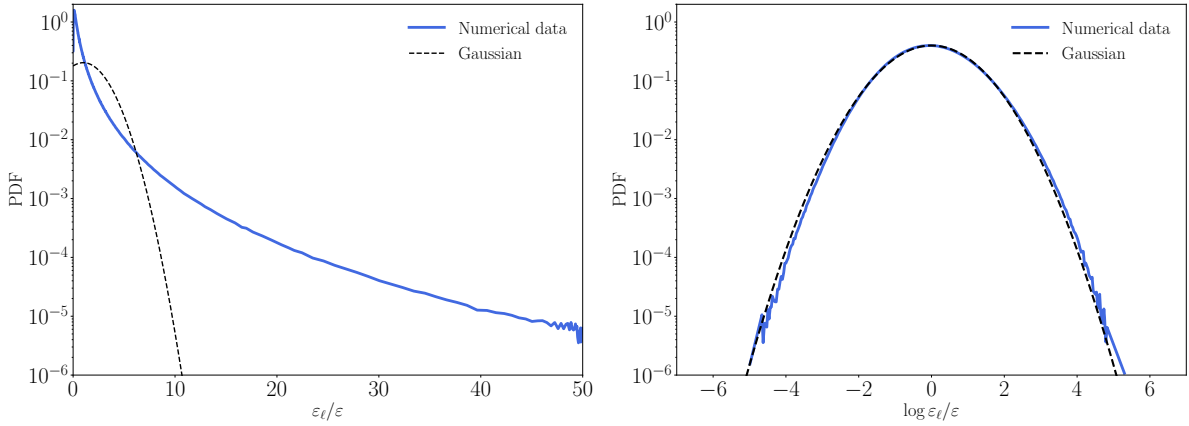
The relations (2.21) and (2.22) provide a parametric formula for the scaling exponent ξ_p, which depends on a single parameter c_2. This empirical fit gives an excellent description of the data, provided that $c_2 \approx 0.03$. Please note that this value of c_2 matches that found in previous experimental and numerical studies (Chanal et al., 2000; Arneodo et al., 1996, 1998; Delour et al., 2001). In fact, the deviation from linear behavior described by Eq. (2.21) can be traced back to the fluctuations of the dissipation field, as we explain in the next section.

Figure 2.9: Illustration of the extended self-similarity analysis. The left panel displays the relation between the structures function $S_p^{1/p}$ and S_3. The right panel displays the exponents ξ_p of the structure functions as a function of the moment order p. The red dashed line shows the K41 behavior characterized by the scaling $\xi_p = p/3$. The black dashed line shows the quadratic fit defined by Eq. (2.21). Finally, the error bars display the maximal and minimal values measured for p using our data points. The results are obtained from the numerical simulation with 1024^3 collocation points.

2.4.3 K62 theory and statistics of the dissipation field

Naturally, our invocation of the central limit theorem in the previous section was conditioned on two assumptions: statistical independence and identical distribution for the increments involved in Eq. (2.18). In fact, it is unclear whether any of those two assumptions hold true. Assuming that the increments are identically distributed is actually a pretty crude assumption, based on a mean-field treatment for the dissipation field. Yet, the analysis of Fig. 2.3 revealed that the fluxes and therefore the energy dissipation are highly fluctuating quantities. This observation is true when one looks at fluctuations in time, but also fluctuations in space.
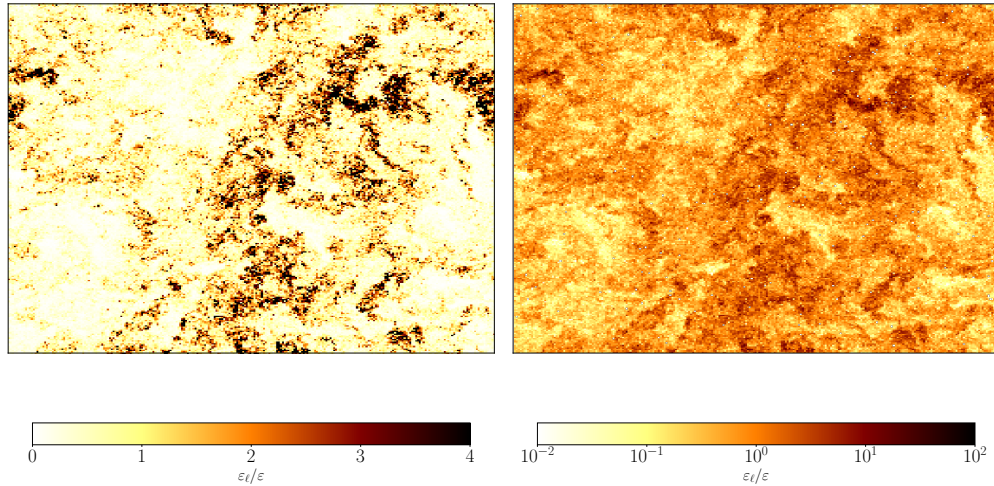
Figure 2.10: Probability distribution function (PDF) of the energy dissipation rate normalized by its mean value (left side), and of the logarithm of the energy dissipation rate (right side). In both panels the Gaussian function is plotted in a dark dash-line. Numerics are obtained from the numerical simulation with 4096^3 collocation points.

Defining $e(x, t) = \|\mathbf{u}(x, t)\|^2/2$ as the local density of energy, one can derive from the NS equations

the local energy budget (Frisch, 1995; Duchon and Robert, 2000):

$$\partial_t e + \nabla \cdot (\mathbf{u}(e + p)) - \nu \Delta(e + p) = -\varepsilon(\mathbf{x}) + \mathbf{f} \cdot \mathbf{u}. \tag{2.23}$$

The negative rhs of this equation is the dissipation due to the *local* dissipation field $\varepsilon(\mathbf{x}) := \nu \|\nabla u + \nabla u^T\|^2/2$. It is an experimental fact, that the dissipation field is actually highly non-Gaussian, and rather displays log-normal statistics (Kolmogorov, 1962; Obukhov, 1962). This holds true also in our numerics, at least to a good approximation, as shown in Fig. 2.10. We observe that compared to a Gaussian function the dissipation density function has very slowly decaying tails, reaching large values (see left panel of Fig. 2.10). The log-normal statistics in fact appear when one considers the logarithm of the dissipation field instead of the dissipation field itself. The right panel of Fig. 2.10 shows that the former is extremely close to a Gaussian, although it is very slightly positively skewed.

Figure 2.11: Illustration of one slice of the coarse-grained dissipation field normalized by its mean value in the plane $x - y$, using a coarse-graining scale $\ell \approx 34\eta$. The left panel displays a linear scale and the right panel displays a logarithmic scale. Numerics are obtained from the numerical simulation with 4096^3 collocation points.

The essence of the K62 theory is the **refined self-similarity** hypothesis, namely the assumption that the statistics of the velocity field relate to the local dissipation field. Specifically, the assumption ties the statistics of the velocity field to the coarse-grained dissipation field as

$$S_{p,\|} \sim \left\langle \varepsilon_\ell(\mathbf{x})^{p/3} \right\rangle \ell^{p/3}, \tag{2.24}$$

where the coarse-grained dissipation field is
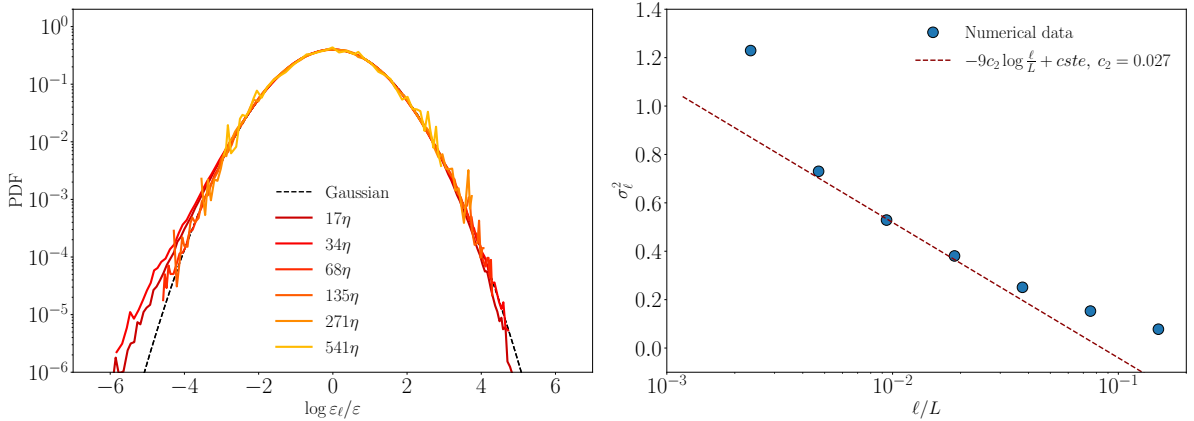
$$\varepsilon_\ell(\mathbf{x}) = \frac{3}{4\pi\ell^3} \int_{|\mathbf{x}'-\mathbf{x}|<\ell} \varepsilon(\mathbf{x}') \, d^3 x', \tag{2.25}$$

namely the dissipation averaged over a ball of radius ℓ.

From numerics and observations, it is known that such quantity is accurately described by log-normal statistics. Fig. 2.11 shows a slice of this field using a coarse-graining at scale $\ell = 34\eta$. It is readily seen from Fig. 2.12 that the log-normal modeling is a very good approximation. This explicitly means that for ℓ within the inertial range, $\log(\varepsilon_\ell/\varepsilon) \sim \mathrm{N}(\mu_\ell, \sigma_\ell)$, *e.g.* the statistics of the coarse-grained dissipation field are prescribed by the log-normal distribution with a mean value equal to μ_ℓ and a variance equal to σ_l.

Mathematically,

$$\mathcal{P}_{\varepsilon_\ell}(\varepsilon_\ell)\,\mathrm{d}\,\varepsilon_\ell = \mathcal{P}_{\ln\varepsilon_\ell}(\ln\varepsilon_\ell)\,\mathrm{d}\ln\varepsilon_\ell = \frac{1}{\sqrt{2\pi\sigma_\ell^2}}\exp\left[\frac{(\ln\varepsilon_\ell - \mu_\ell)^2}{2\sigma_\ell^2}\right]\mathrm{d}\ln\varepsilon_\ell. \tag{2.26}$$

Figure 2.12: Left panel: distributions of the logarithmic values of the coarse-grained dissipation for different scales ℓ (colored lines), together with a Gaussian distribution (black dash-line). The distributions are centered and normalized by their standard deviations σ_ℓ. Right panel: Relation between the variance σ_ℓ^2 as a function of the length ℓ/L (blue points). The relation $\sigma_\ell^2 = 9c_2\ln(L/\ell)$ is plotted with $c_2 = 0.027$ (red dash-line). Numerics are obtained from the numerical simulation with 4096^3 collocation points.

Log-normal distributions have finite moments which are explicitly known. The correction to K41 comes from the discrepancy $\left\langle \varepsilon_\ell(\mathbf{x})^{p/3} \right\rangle \neq \varepsilon^{p/3}$, which can be seen as the origin of the intermittent behavior of the velocity fluctuations. Specifically, the log-normal model (2.26) yields the formula Wikipedia (2020b):

$$\left\langle \left(\frac{\varepsilon_\ell}{\varepsilon}\right)^q \right\rangle = e^{\,q\mu_\ell + q^2\frac{\sigma_\ell^2}{2}}. \tag{2.27}$$

Taking $q = 1$, one obtains the relation $1 = e^{\mu_\ell + \frac{\sigma_\ell^2}{2}}$. From this relation, we can express all the moments in terms of the variance and of the average dissipation ε as

$$\left\langle \varepsilon_\ell^q \right\rangle = \varepsilon^q\, e^{\frac{1}{2}(q^2-q)\sigma_\ell^2}. \tag{2.28}$$

The final step is to relate the variance to the scale ℓ. This is again a heuristic step, obtained from observations, such as in Fig. 2.12. The right panel of Fig. 2.12 shows that the variance approximately scales as

$$\sigma_\ell^2 = 9\,c_2\ln(L/\ell), \tag{2.29}$$

where c_2 can be interpreted as a " coefficient of intermittency". From the data shown in Fig. 2.12, we measure $c_2 = 0.027$ and this characterize deviations from the K41 scaling. Indeed, combining Eq. (2.24), (2.28), (2.29) and (2.27), one obtains the formula

$$\xi_p = \frac{p}{3} + \tau_{p/3}, \quad \text{where } \tau_q = -\frac{9}{2}c_2\,q\,(q-1) \tag{2.30}$$
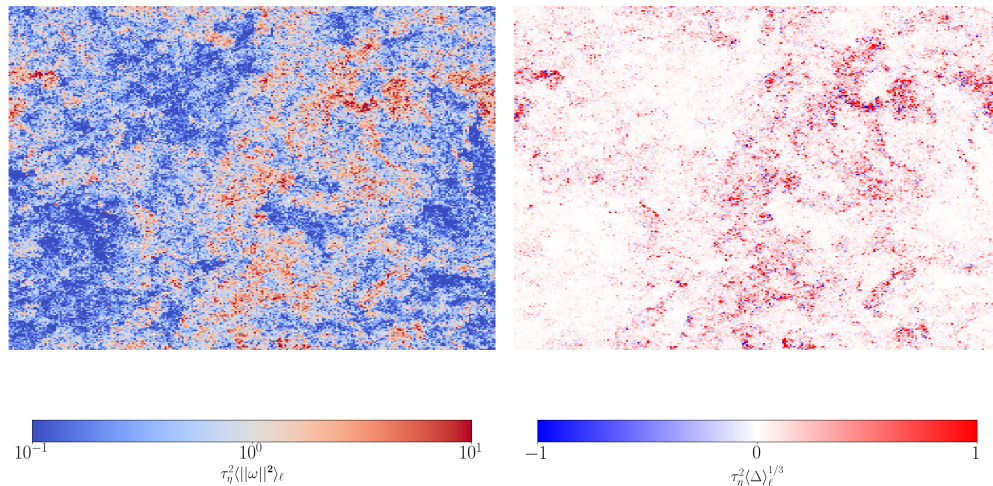
is the scaling exponent of the dissipation field, *e.g.* $\langle \varepsilon_\ell^q \rangle \sim \ell^{\tau_q}$.

We have retrieved the expression (2.21) previously introduced to fit the statistics of the parallel velocity increments. This means that quadratic deviations from linear scaling can indeed be related to fluctuations of the dissipation field, and that $c_2 = 0.027$ indeed characterize deviations from the K41 scaling observed in Fig. 2.9. We note that the log-normal model is only one of the many heuristic approaches that exist in the literature to quantitatively characterize intermittency (Frisch, 1995, Chap. 8). One of the shortcomings of the log-normal approximation is the fact that it becomes non-physical for large values of p: For $p > 1/(3c_2) + 3/2 \simeq 13$, it predicts decreasing behavior for ξ_p, a feature which is known to allow for supersonic velocities, and hence contradicts the hypothesis of incompressibility (Frisch, 1995, Chap. 8). Yet, it remains a useful approximation for values of $p \lesssim 10$ as considered here.

2.4.4 Local structures beyond K62 theory

The K62 framework emphasizes the role of local turbulent structures by tying the intermittent statistics of the velocity field to the local dissipation field, and we expect that those statistics might reflect in the statistics of the transport and mixing of particles. More crucially though, it hints that large-scale properties of turbulence depend on local turbulent structures. This means that without ensemble averaging, we expect that turbulent statistics differ from one region to the other, and that the dissipation field is not the only relevant local field.

Here, we want to illustrate this point, by describing a useful partition of the physical space in terms of strain-dominated and vorticity-dominated regions. This partition is known to be of peculiar relevance in the context of turbulent mixing, as it shapes the patterns of preferential concentrations of inertial particles transported by turbulent fluids, already discussed in Chapter 1 of the introduction and that will be studied in Chapter 3. It is yet only the tip of the iceberg of a vast literature related to the stochastic modeling of the velocity gradients, whose thorough review goes way beyond the scope of this thesis (see for example Meneveau (2011); Chevillard (2015) and references therein).
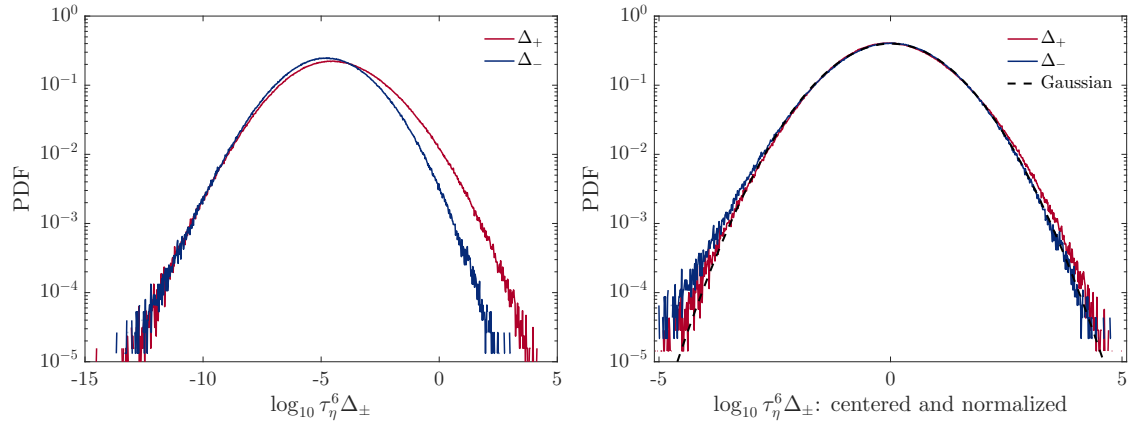
Figure 2.13: Illustration of one slice of the local enstrophy field (left panel) and the coarse-grained 2D-slice of the parameter $\Delta^{1/3}$ (right panel). Both rescaled by τ_η^2 at $\ell \approx 32\eta$. Numerics are obtained from the numerical simulation with 4096^3 collocation points.

For incompressible fluids, the partition between strain and rotating regions is based on the sign of the parameter

$$\Delta = \left(\frac{\det(\boldsymbol{\sigma})}{2} \right)^2 - \left(\frac{\operatorname{tr}(\boldsymbol{\sigma}^2)}{6} \right)^3, \quad \text{where } \boldsymbol{\sigma} = \nabla \mathbf{u} = (\partial_i u_j)_{1 \leq i,j \leq 3}. \tag{2.31}$$
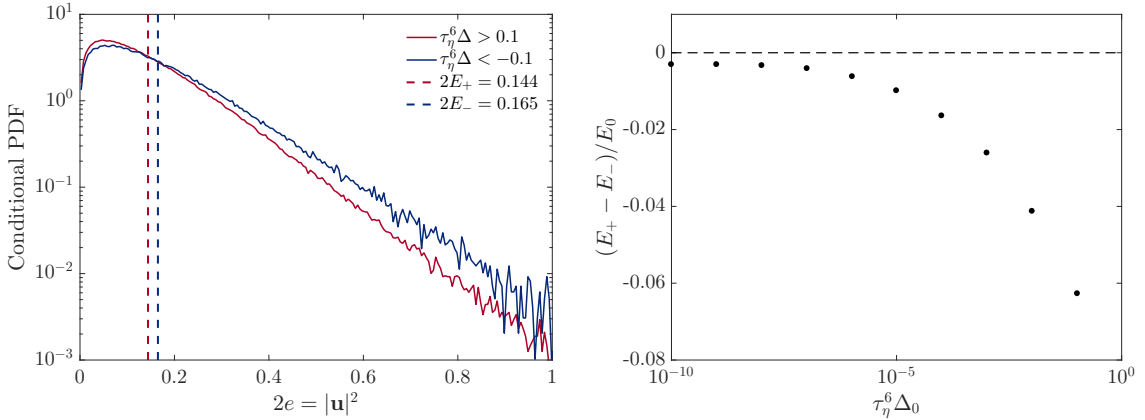
Regions with negative Δ define **hyperbolic** or **strain-dominated** regions, for which the velocity gradient has three real eigenvalues. Regions with positive Δ define **elliptic regions** or **rotation-dominated** regions, for which the velocity gradient has one real and a pair of complex-conjugate eigenvalues (Bec et al., 2005; Bec, 2004; Chong et al., 1990). This parameter can be seen as a 3D version of the Okubo-Weiss parameter traditionally used in 2D flows (Okubo, 1970; Weiss, 1991; Picardo et al., 2018). As an illustration, Fig. 2.13 shows a coarse-grained 2D-slice of the parameter Δ, alongside a slice of the local enstrophy field measuring the level of vorticity. It is readily seen that positive regions for the parameter Δ indeed correlate to regions with a high vorticity.

Similar to the dissipation field, the statistics of the parameters $\Delta_\pm = \pm\Delta\mathbf{1}_{\pm\Delta>0}$ display close to log-normal statistics, as shown in Fig. 2.14.

Figure 2.14: Left panel: Probability distribution function (PDF) of $\log\Delta_\pm$ defined by conditioning the Δ parameter on elliptic regions (in red) or hyperbolic regions (in blue). Right panel: The same distributions but centered and normalized to unit variance, revealing near log-normal behavior of $\Delta_\pm$.

Fig. 2.15 compares the statistics of the local energy field $2e(\mathbf{x}, t) = \|\mathbf{u}\|^2$ conditioned on elliptic and hyperbolic regions. One can see a clear asymmetry, with strain-dominated regions being on average more energetic than rotation-dominated regions. This slightly counterintuitive asymmetry is systematic and amplifies upon further conditioning on regions which are either "very elliptic" ($\delta \gg 1$) or "very hyperbolic" ($\delta \ll -1$). In other words, the partition of the flow between rotation and strain regions is also a partition between "quiet" and "stormy" regions for the turbulence.
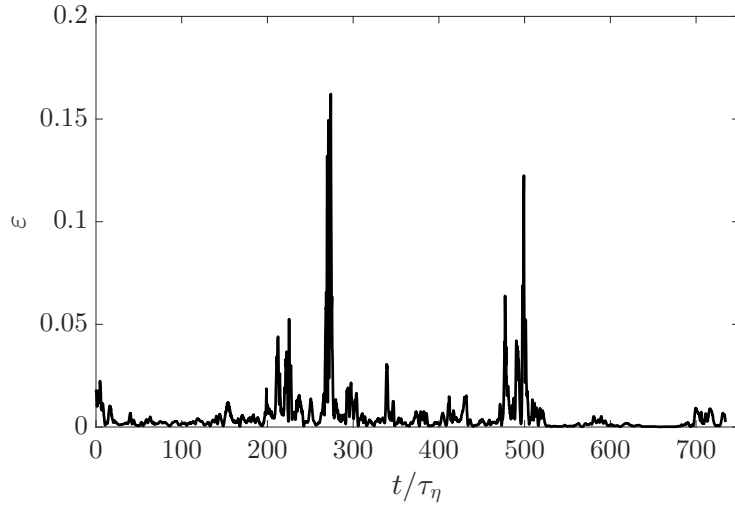
Figure 2.15: Left panel: Statistics of (twice) the local energy $2e = \|\mathbf{u}\|^2$ conditioned on the parameter Δ being either very negative or very positive, depending on a given arbitrary threshold. The two dashed-lines display the average $E_{\pm}$ of the energy over each region. Right panel: difference between those two averages as a function of the threshold Δ_0, revealing that rotation-dominated regions are more "calm" than strain-dominated regions from the point of view of the energy.

2.5 Lagrangian statistics and correlation times

To conclude this chapter on turbulence, we wish to briefly comment on Lagrangian statistics by mentioning some of the important correlation times that will appear in the next chapters. Here, we focus on the statistics along the trajectories of fluid particles (tracers), whose velocities are prescribed by that of the carrier flow.

Dissipation Statistics. In the previous section we introduced the local energy dissipation field as $\varepsilon(\mathbf{x}) := \nu \|\nabla \mathbf{u} + \nabla \mathbf{u}^T\|^2/2$. Fig. 2.16 shows the time evolution of this quantity, along a tracer trajectory. We observe that this quantity is very intermittent, suggesting that the fluid particles visit different turbulent structures along the time. We can qualitatively observe that the extreme events are not isolated events but rather seem to arrive in bursts.
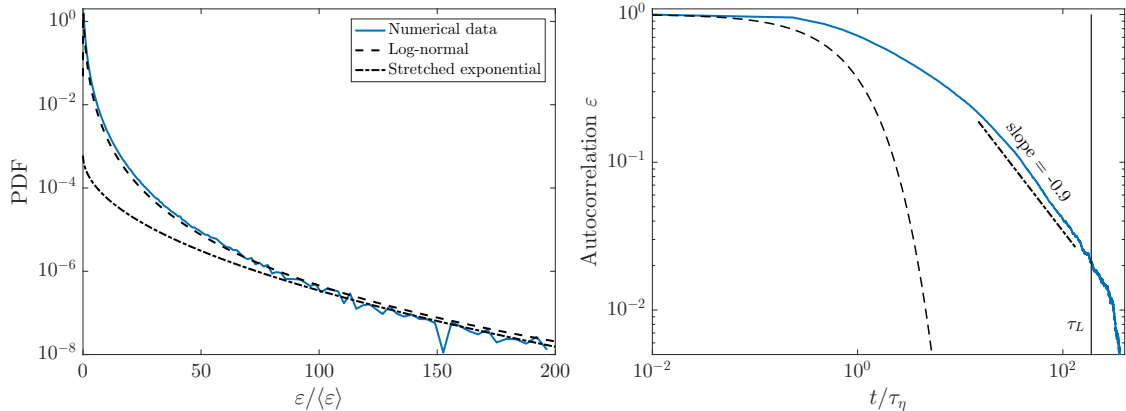
Figure 2.16: Time evolution of the local energy dissipation field $\varepsilon(\mathbf{x}) := \nu \|\nabla \mathbf{u} + \nabla \mathbf{u}^T\|^2/2$ along a Lagrangian tracer. Time is here rescaled by the Kolmogorov timescale τ_η. Numerics are obtained from the numerical simulation with 4096^3 collocation points.

More quantitatively, Fig. 2.17 shows the probability distribution function (PDF) of local dissipation field. As expected, the latter is highly non-Gaussian and displays fat-tails. As we showed in Fig. 2.12 the statistics of the coarse-grained dissipation energy field are prescribed by the log-normal distribution (2.26). The same behaviour is observed with the Lagrangian fluctuations of this quantity, where the PDF fit very well with the log-normal law. In large-Reynolds-number turbulence, this distribution is also well approximated by a stretched exponential law with an exponent $\approx 1/2$ — see, *e.g.*, Meneveau and Sreenivasan (1991); Kailasnath et al. (1992); Chevillard et al. (2003); Donzis et al. (2008)). This means that the dissipation energy have a non-negligible probability of achieving extreme values which are several order of magnitudes above the standard deviation. Along the trajectory, the dissipation field displays long-time correlations, as apparent from the right panel of Fig. 2.17 featuring the Lagrangian autocorrelation $C_\varepsilon(t) = \langle \varepsilon(t)\varepsilon(0) \rangle$. This quantity does not decay following an exponential function. Instead, the autocorrelation decreases slowly and remains correlated on times of the order of the integral timescale. Specifically, we estimate the integral correlation time as

$$\tau_\varepsilon = \frac{\int_0^\infty C_\varepsilon(t)dt}{C_\varepsilon(0)} \approx 0.58\tau_L, \tag{2.32}$$

which is indeed of the order of the integral time scale. In addition, we observe that for times t within the inertial range, the correlation follows a power-law behavior $\propto t^{-\beta}$, with $\beta \approx 0.9 \pm 0.1$.
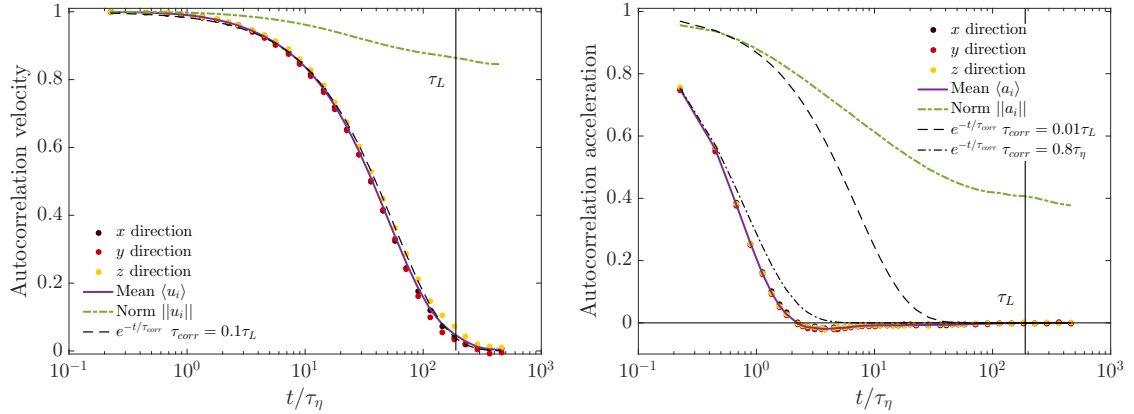
Figure 2.17: Left panel: Probability distribution function (PDF) of the local dissipation field ε, averaged by their mean value $\langle \varepsilon \rangle \approx 0.0037$. Together with a log-normal fit (dashed line) and a stretched exponential fit (dot-dashed line). Right panel: Autocorrelation of the energy dissipation field ε. The large-eddy turnover time is shown with the vertical solid line. The dashed-dotted line stands for $\exp(-t/\tau_\eta)$. The time is here rescaled by the Kolmogorov timescale τ_η.

Velocity and acceleration statistics. We finally wish to comment on the correlation times associated to the Lagrangian velocities and accelerations. Fig. 2.18 shows the autocorrelation of the velocity and of the acceleration along tracer trajectories, defined as

$$\frac{\langle u_i(t)u_i(0)\rangle}{\langle u_i(0)^2\rangle}, \quad \frac{\langle \|\mathbf{u}(t)\|\|\mathbf{u}(0)\|\rangle}{\langle \|\mathbf{u}(0)\|^2\rangle}, \quad \text{etc.} \tag{2.33}$$

For each of these quantities, different behaviors are observed depending on whether one monitors the correlation of the components u_i's and a_i's for $i = x, y, z$ or one measures the correlation of the norms; This type of behavior was previously found from experimental observations (Mordant et al., 2001, 2004). Specifically, the velocity components decorrelate over a timescale $\sim \tau_L$, and the acceleration components decorrelate almost instantaneously over a timescale $\sim \tau_\eta$. Yet, in both cases, the norms remain correlated on timescales larger than the integral scale, and this presumably reflects the conservation of energy.

Figure 2.18: Left panel: Autocorrelation of the velocity components u_i and of the velocity norms along fluid tracers. Right panel: Same quantity for the acceleration. In both panels the dashed-dotted line stands for fits $\propto \exp(-t/\tau_{corr})$, where τ_{corr} is a correlation time. Time is here rescaled by the Kolmogorov timescale τ_η.

2.6 Concluding remarks

In this chapter, we have described a few of the salient features of the Navier-Stokes equations and illustrated the multi-scale nature of turbulent velocity fields. In particular, we highlighted the role of a few local quantities, such as the energy, the dissipation field and a 3D analog of the Okubo-Weiss parameter in shaping the turbulence statistics throughout the scales. We also described a few key Lagrangian properties. Fluctuations play a crucial role in determining the statistics of small complex objects immersed in turbulent fluids. This observation will be substantiated in the next three chapters, involving either small inertial and elongated spheroids (Chapter 3) or small elongated and flexible fibers (Chapter 4 and 5).

3 | Inertial spheroids in turbulent flows

Contents

This chapter focuses on the turbulent motion of small inertial and non-deformable ellipsoids in turbulent flows, in order to quantify the effects of non-sphericity. For simplicity, we focus on the case of spheroids, namely ellipsoids of revolution whose shape is entirely prescribed by their aspect ratio. We present the results of massive numerical simulations of the non-overdamped Jeffery's equations, that provide a parametric study of the statistics of the spheroids, depending on their shape and on their mass. We quantify in details the Lagrangian statistics of the translational and rotational dynamics. In brief, we find that the translational dynamics can be almost fully described in terms of a **harmonic Stokes number** $St^\star$: Deviations from the spherical case can be described in terms of an effective radius built as a harmonic average. The orientation statistics are yet more intricate: The harmonic Stokes number is relevant only for particles with small values of their response time. For large values of the particle response time, the influence of the shape cannot be simply related to the spherical case, and this also proves true for the patterns of preferential concentration observed in our numerical experiments. The chapter is organized as follows. §3.1 provides details on the modeling of the spheroid dynamics. §3.2 give details on our numerical strategy. §3.3 shows the outcome of our numerical simulations along with their detailed analysis. We finally provide some perspectives for future work in §3.4.

3.1 The dynamics of small inertial spheroids

The aim of this section is to recall the governing equations of motion of inertial spheroids immersed in a fluid environment. The general equations valid for arbitrary ellipsoids are listed in Appendix A; We here specialize to the case of spheroids. A spheroid, or ellipsoid of revolution, is defined as a solid surface with a principal axis c and two equal semi-axes a and b (Jeffery, 1922; Weisstein, 2002). The aspect ratio $\lambda = c/a$ characterizes the shape of the spheroid; $\lambda \gg 1$ describes a prolate particle, $\lambda = 1$ describes a sphere and $\lambda \ll 1$ describes an oblate particle. Those three cases are represented in Fig. 3.1.

3.1.1 Kinematics

The motion of the spheroids is obtained by describing both their rotational and their translational dynamics. This involves the position of the ellipsoid center of gravity $\mathbf{X}_p$, the velocity $\mathbf{V}_p$, the orientation $\mathbf{p}_p$ (later

Figure 3.1: Representation of the three different types of spheroids depending on the value of their aspect ratio. From left to right: oblate ($0 < \lambda < 1$), sphere ($\lambda = 1$) and prolate ($\lambda > 1$). The third semiaxis c is always aligned with the z-axis of the particle fixed coordinate system.

prescribed by **p**) and the angular velocity $\mathbf{\Omega}_p$. While translational dynamics is defined in the laboratory frame $(\mathbf{e}_x, \mathbf{e}_y, \mathbf{e}_z)$, the rotational dynamics is defined in the particle frame $(\mathbf{e}_{\hat{x}}, \mathbf{e}_{\hat{y}}, \mathbf{e}_{\hat{z}})$.

The particle frame associated to the spheroid is most conveniently defined in terms of two quantities, namely the unit vector **p** tracking the (oriented) axis of symmetry, and the angle θ measuring the amount of rotation about the vector **p** (see Fig. 3.2). The pair of parameters $(\mathbf{p}, \theta)$ prescribes four scalar quantities known as the Euler parameters (η, ϵ_1, ϵ_2, ϵ_3) defined by

$$
\begin{pmatrix} \eta \\ \epsilon_1 \\ \epsilon_2 \\ \epsilon_3 \end{pmatrix} = \begin{pmatrix} \cos{(\theta/2)} \\ p_x \, \sin{(\theta/2)} \\ p_y \, \sin{(\theta/2)} \\ p_z \, \sin{(\theta/2)} \end{pmatrix}.
\tag{3.1}
$$

Using the Euler parameters, one can express the transformation from the laboratory frame towards the particle frame in terms of the rotation matrix (Goldstein et al., 1980) [4]

$$
\mathbb{A} = \begin{pmatrix} 1 - 2\left(\epsilon_2^2 + \epsilon_3^2\right) & 2\left(\epsilon_1\,\epsilon_2 + \epsilon_3\,\eta\right) & 2\left(\epsilon_1\,\epsilon_3 - \epsilon_2\,\eta\right) \\ 2\left(\epsilon_2\,\epsilon_1 - \epsilon_3\,\eta\right) & 1 - 2\left(\epsilon_1^2 + \epsilon_3^2\right) & 2\left(\epsilon_2\,\epsilon_3 + \epsilon_1\,\eta\right) \\ 2\left(\epsilon_3\,\epsilon_1 + \epsilon_2\,\eta\right) & 2\left(\epsilon_3\,\epsilon_2 - \epsilon_1\,\eta\right) & 1 - 2\left(\epsilon_1^2 + \epsilon_2^2\right) \end{pmatrix}.
\tag{3.2}
$$

As a side remark, we note that the choice of Euler parameters to parametrize three-dimensional rotations has at least two chief advantages compared to other parametrizations, such as the so-called Euler angles. First, it is free of any "gimbal lock " phenomenon, where one degree of freedom disappears when two axes of rotation become parallel (Vince, 2011). Second, the transformation matrix is simple and can be efficiently computed numerically.
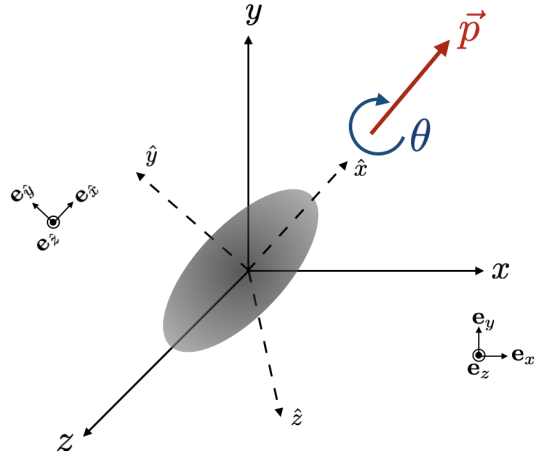
The ellipsoid orientation evolves with time according to the angular velocity $\mathbf{\Omega}_p = (\Omega_{\hat{x}}, \Omega_{\hat{y}}, \Omega_{\hat{z}})$. In

---

[4]This complicated looking rotation matrix is usually deduced using quaternion calculus. The Euler parameters are then represented in terms of the unitary quaternion $q = e^{(\theta/2)(p_x\mathbf{i}+p_y\mathbf{j}+p_z\mathbf{k})}$, and three-dimensional rotations are computed as the transformations $u \to quq^{-1}$, with u a vector-quaternion with $\theta = \pi$ (Wikipedia, 2020c).

terms of the Euler parameters, this translates into

$$\frac{d}{dt}\begin{pmatrix}\eta\\\epsilon_1\\\epsilon_2\\\epsilon_3\end{pmatrix} = \frac{1}{2}\begin{pmatrix}-\epsilon_1 & -\epsilon_2 & -\epsilon_3\\\eta & -\epsilon_3 & \epsilon_2\\\epsilon_3 & \eta & -\epsilon_1\\-\epsilon_2 & \epsilon_1 & \eta\end{pmatrix}\begin{pmatrix}\Omega_{\hat{x}}\\\Omega_{\hat{y}}\\\Omega_{\hat{z}}\end{pmatrix} \tag{3.3}$$

One observes that these kinematic equations preserve the norm of the Euler parameters, that is $\eta^2 + \epsilon_1^2 + \epsilon_2^2 + \epsilon_3^2 = 1$ for all t.

Figure 3.2: Illustration of the components of the Euler parameters used to switch the particle coordinates between the inertial frame $(\mathbf{e}_x, \mathbf{e}_y, \mathbf{e}_z)$ and the particle frame $(\mathbf{e}_{\hat{x}}, \mathbf{e}_{\hat{y}}, \mathbf{e}_{\hat{z}})$.

3.1.2 Dynamics

To determine the dynamics of the ellipsoids, we now restrict our attention to the behavior of spheroids smaller than the Kolmogorov scale τ_η. The spheroids are yet considered heavy enough, so that their motion is unaffected by thermal fluctuations, and fully deterministic. The dynamics is therefore prescribed by Newton's equations, where the only forces acting on the spheroid are the gravity and the hydrodynamic forces.

Translational motion. Further neglecting the effect of gravity, the dynamics of the center of mass, *e.g.* the translational motion, is then described by the linear momentum equations:

$$\frac{d\mathbf{X}_p}{dt} = \mathbf{V}_p$$
$$\frac{d\mathbf{V}_p}{dt} = \frac{\nu\rho}{m_p}\mathbb{A}^T\hat{\mathbb{K}}\mathbb{A}\left(\mathbf{V}_f - \mathbf{V}_p\right) \tag{3.4}$$

where ν is the fluid viscosity, ρ fluid density, $m_p = 4\rho_p\pi abc/3$ the particle mass (with ρ_p the particle density), $\hat{\mathbb{K}}$ the resistance tensor and $\mathbf{V}_f$ the fluid velocity at the particle position. The resistance tensor is

here expressed in the particle frame. It is the diagonal matrix (Oberbeck, 1876):

$$
\hat{\mathbb{K}} = 16\pi a\lambda
\begin{pmatrix}
(\chi_0/a^2 + \chi_1)^{-1} & 0 & 0 \\
0 & (\chi_0/a^2 + \chi_2)^{-1} & 0 \\
0 & 0 & (\chi_0/a^2 + \lambda^2\chi_3)^{-1}
\end{pmatrix}
\tag{3.5}
$$

The shape parameters χ_0, χ_1, χ_2 and χ_3 have been computed by Brenner (1964) as

$$
\chi_0 = a^3\lambda \int_0^\infty \frac{d\beta}{\Delta} \quad \text{with} \quad \Delta(\beta) = \sqrt{(a^2 + \beta)^2((a\lambda)^2 + \beta)},
$$

$$
\text{and} \quad \chi_1 = a^3\lambda \int_0^\infty \frac{d\beta}{(a^2 + \beta)\Delta}, \qquad \chi_2 = a^3\lambda \int_0^\infty \frac{d\beta}{(a^2 + \beta)\Delta}, \qquad \chi_3 = a^3\lambda \int_0^\infty \frac{d\beta}{((a\lambda)^2 + \beta)\Delta}.
\tag{3.6}
$$

Note that the shape parameters χ_1, χ_2 and χ_3 are dimensionless while the shape parameter χ_0 has dimension [length]^2. This implies that the resistance tensor $\hat{\mathbb{K}}$ also has the dimension of a length. Expressions for these shape factors are explicitly known for the spheroids of various shapes, and are summarized in Table 3.1.

	$\lambda > 1$	$\lambda = 1$	$0 < \lambda < 1$
χ_0	$-\kappa\dfrac{a^2\lambda}{\sqrt{\lambda^2 - 1}}$	$2a^2\kappa$	$(\pi - \kappa)\dfrac{a^2\lambda}{\sqrt{1 - \lambda^2}}$
$\chi_1 = \chi_2$	$\dfrac{\lambda^2}{\lambda^2 - 1} + \kappa\dfrac{\lambda}{2(\lambda^2 - 1)^{3/2}}$	$\dfrac{2}{3}\kappa$	$-\dfrac{\lambda}{2(\lambda^2 - 1)^{3/2}}\left(\kappa - \pi + 2\lambda\sqrt{1 - \lambda^2}\right)$
χ_3	$-\dfrac{2}{\lambda^2 - 1} - \kappa\dfrac{\lambda}{(\lambda^2 - 1)^{3/2}}$	$\dfrac{2}{3}\kappa$	$\dfrac{1}{(1 - \lambda^2)^{3/2}}\left(\lambda\kappa - \lambda\pi + 2\sqrt{1 - \lambda^2}\right)$
κ	$\log\left(\dfrac{\lambda - \sqrt{\lambda^2 - 1}}{\lambda + \sqrt{\lambda^2 + 1}}\right)$	1	$2\arctan\left(\dfrac{\lambda}{\sqrt{1 - \lambda^2}}\right)$

Table 3.1: Expressions for the shape factors in the case of ellipsoids of revolution with $a = b$ and $c = a\lambda$ for the three cases: prolates ($\lambda > 1$), spheres ($\lambda = 1$) and oblates ($\lambda < 1$) (Happel and Brenner, 2012).

Rotational dynamics. In the particle frame, the angular velocity of the ellipsoid is given by

$$
\frac{d(\mathbf{I}\,\boldsymbol{\Omega}_p)}{dt} + \boldsymbol{\Omega}_p \times (\mathbf{I}\,\boldsymbol{\Omega}_p) = \mathbf{T},
\tag{3.7}
$$

where $\mathbf{I} = (I_{\hat{x}}, I_{\hat{y}}, I_{\hat{z}})$ is the moment of inertia of the spheroid and $\mathbf{T} = (T_{\hat{x}}, T_{\hat{y}}, T_{\hat{z}})$ the hydrodynamic torque acting on a spheroid. In full explicit form, Eq. (3.7) reads

$$
\frac{d}{dt}
\begin{pmatrix}
\Omega_{\hat{x}} \\
\Omega_{\hat{y}} \\
\Omega_{\hat{z}}
\end{pmatrix}
=
\begin{pmatrix}
\Omega_{\hat{y}}\,\Omega_{\hat{z}} \times (I_{\hat{y}} - I_{\hat{z}})/I_{\hat{x}} \\
\Omega_{\hat{z}}\,\Omega_{\hat{x}} \times (I_{\hat{z}} - I_{\hat{x}})/I_{\hat{y}} \\
\Omega_{\hat{x}}\,\Omega_{\hat{y}} \times (I_{\hat{x}} - I_{\hat{y}})/I_{\hat{z}}
\end{pmatrix}
+
\begin{pmatrix}
T_{\hat{x}}/I_{\hat{x}} \\
T_{\hat{y}}/I_{\hat{y}} \\
T_{\hat{z}}/I_{\hat{z}}
\end{pmatrix},
\tag{3.8}
$$

where the moment of inertia of the spheroid about its principal axis is the diagonal matrix:

$$
\begin{pmatrix}
I_{\hat{x}} & 0 & 0 \\
0 & I_{\hat{y}} & 0 \\
0 & 0 & I_{\hat{z}}
\end{pmatrix}
= \frac{4}{15} \pi \rho_p a^5 \lambda
\begin{pmatrix}
1 + \lambda^2 & 0 & 0 \\
0 & 1 + \lambda^2 & 0 \\
0 & 0 & 2
\end{pmatrix}.
\tag{3.9}
$$

For the hydrodynamic torque acting on the spheroid, we rely on a standard approximation first computed by Jeffery (1922), which relates the torque to the fluid vorticity $\omega = \nabla \times \mathbf{u}$ and to the strain tensor $\mathbb{S} = (\nabla \mathbf{u} + \nabla \mathbf{u}^T)/2$ as

$$
\begin{pmatrix}
T_{\hat{x}} \\
T_{\hat{y}} \\
T_{\hat{z}}
\end{pmatrix}
= \frac{16}{3} \rho \nu \pi a^3 \lambda
\begin{pmatrix}
\frac{1+\lambda^2}{\chi_2 + \lambda^2 \chi_3} \\
\frac{1+\lambda^2}{\chi_1 + \lambda^2 \chi_3} \\
\frac{1}{\chi_1 + \chi_2}
\end{pmatrix}
\begin{pmatrix}
\frac{1-\lambda^2}{1+\lambda^2} S_{\hat{z}\hat{y}} + \omega_{\hat{x}}/2 - \Omega_{\hat{x}} \\
\frac{\lambda^2-1}{\lambda^2+1} S_{\hat{x}\hat{z}} + \omega_{\hat{y}}/2 - \Omega_{\hat{y}} \\
\omega_{\hat{z}}/2 - \Omega_{\hat{z}}
\end{pmatrix}
\tag{3.10}
$$

The quantities $S_{\hat{i}\hat{j}}$ are the components of the strain-tensor, explicitly

$$
S_{\hat{z}\hat{y}} = \frac{1}{2} (\partial_{\hat{y}} u_{\hat{z}} + \partial_{\hat{z}} u_{\hat{y}}) \qquad
S_{\hat{x}\hat{z}} = \frac{1}{2} (\partial_{\hat{z}} u_{\hat{x}} + \partial_{\hat{x}} u_{\hat{z}}) \qquad
S_{\hat{y}\hat{x}} = \frac{1}{2} (\partial_{\hat{x}} u_{\hat{y}} + \partial_{\hat{y}} u_{\hat{x}})
\tag{3.11}
$$

The approximation leading to Eq. (3.10) assumes that to leading order, the flow past the spheroid is well-approximated by a Stokes flow. This is justified from the assumption that the spheroids are smaller than the Kolmogorov scale, and we observe that this useful approximation is also at the core of the slender-body theory used in the next Chapter.

Full dynamics in terms of τ_p. The volume of the spheroids $(4/3)\pi a^3 \lambda$ is equal to the volume of a sphere with radius $r = a\lambda^{1/3}$. This suggests to define the spheroidal response time in terms of the usual expression for spherical particles as (Saw et al., 2008; Bec et al., 2005)

$$
\tau_p = \frac{2\rho_p r^2}{9\rho\nu} = \frac{2\rho_p a^2 \lambda^{2/3}}{9\rho\nu}.
\tag{3.12}
$$

In terms of τ_p, the translational dynamics then becomes:

$$
\frac{d\mathbf{V}_p}{dt} = \frac{1}{6\pi a \lambda^{1/3}} \frac{1}{\tau_p} \mathbb{A}^T \hat{\mathbb{K}} \mathbb{A} \left(\mathbf{V}_f - \mathbf{V}_p \right),
\tag{3.13}
$$

and the rotational dynamics is:

$$
\frac{d\mathbf{\Omega}_p}{dt} = \left(\frac{\lambda^2 - 1}{\lambda^2 + 1} \right)
\begin{pmatrix}
\Omega_{\hat{y}} \Omega_{\hat{z}} \\
-\Omega_{\hat{x}} \Omega_{\hat{z}} \\
0
\end{pmatrix}
+ \frac{40}{9} \frac{\lambda^{2/3}}{\tau_p}
\begin{pmatrix}
\frac{1}{\chi_2 + \lambda^2 \chi_3} \left(\frac{1-\lambda^2}{1+\lambda^2} \tau_{\hat{z}\hat{y}} + \omega_{\hat{x}}/2 - \Omega_{\hat{x}} \right) \\
\frac{1}{\chi_1 + \lambda^2 \chi_3} \left(\frac{\lambda^2-1}{\lambda^2+1} \tau_{\hat{x}\hat{y}} + \omega_{\hat{y}}/2 - \Omega_{\hat{y}} \right) \\
\frac{1}{2\chi_1} \left(\omega_{\hat{z}}/2 - \Omega_{\hat{z}} \right)
\end{pmatrix}.
\tag{3.14}
$$

Please note that, considering the case of a sphere ($\lambda = 1$) we recover the well known motion of a massive sphere (Maxey and Riley, 1983)

$$
\frac{d\mathbf{V}_p}{dt} = \frac{1}{\tau_p} \left(\mathbf{V}_f - \mathbf{V}_p \right)
$$

$$
\frac{d\mathbf{\Omega}_p}{dt} = \frac{10}{3} \frac{1}{\tau_p}
\begin{pmatrix}
\omega_{\hat{x}}/2 - \Omega_{\hat{x}} \\
\omega_{\hat{y}}/2 - \Omega_{\hat{y}} \\
\omega_{\hat{z}}/2 - \Omega_{\hat{z}}
\end{pmatrix}.
\tag{3.15}
$$

3.2 Numerical methods

To study the motion of inertial spheroids in a fully-developed, stationary, homogeneous, isotropic turbulent flow, we use direct numerical simulations of the three-dimensional incompressible Navier-Stokes equations with 512^3 and 1024^3 collocation points (see details in Chapter 2). For the purpose of the present exposition, we here focus on the largest simulation. The numerical parameters and the relevant physical quantities are recalled in Tab. 3.2. The spheroid equations (3.13) and (3.14) are integrated along particle paths using a third-order Runge–Kutta time marching, together with a description of the orientation making use of the Euler parameters.

In order to span the parameter space for the 1024^3 simulation, we have considered 90 different families of 500 000 particles combining the nine aspect ratio $\lambda = 0.1, 0.1778, 0.3162, 0.5623, 1, 1.7783, 3.1623, 5.6234, 10$ and the ten response times $\tau_p = 0.0022, 0.0035, 0.0055, 0.0087, 0.0138, 0.022, 0.0349, 0.0554, 0.0879, 0.1395$. The spheroids and the fluid velocity gradients along the Lagrangian paths are stored with a period $300\Delta t \approx 6.8\,\tau_\eta$ for a time duration of $17700\,\Delta t \approx 400\,\tau_\eta \approx 5\,\tau_L$. Statistics are gathered over approximately 4 large-eddy turnover times.
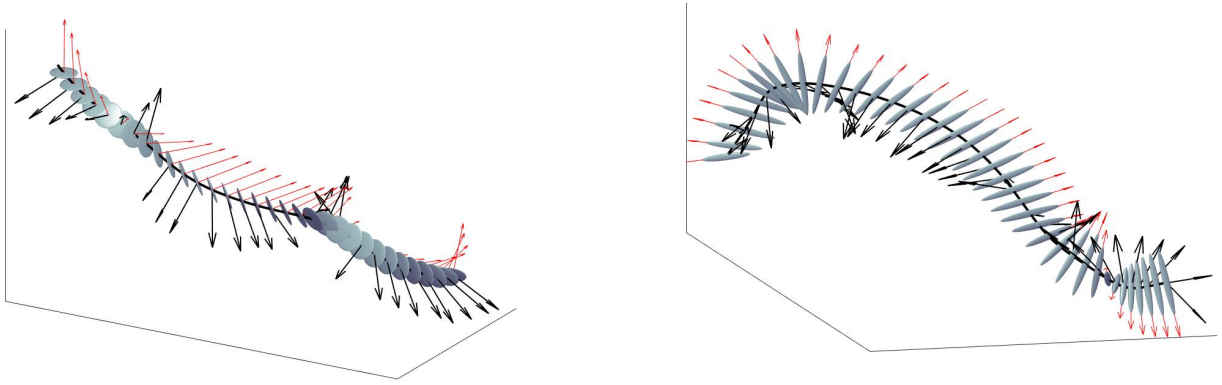
N^3	ν	Δt	ε	η	τ_η	u_{rms}	L	τ_L	R_λ
512^3	$5\,10^{-4}$	10^{-3}	0.4083	0.0042	0.035	0.8564	1.54	1.80	199
1024^3	$2\,10^{-4}$	$5\,10^{-4}$	0.431	0.0021	0.022	0.87	1.52	1.753	315

Table 3.2: Numerical and physical parameters of the direct numerical simulation

3.3 Results and analysis

We now describe our results. There is a wide amount of literature pertaining to the motion of small inertial spherical particles, which in our numerics is recovered for the aspect ratio $\lambda = 1$. Our intention here is to understand how non-sphericity modifies the statistics of small massive particles. We here first study in details the Lagrangian statistics related to the dynamics of the center of mass and of the orientation, hereby providing a full statistical picture of the Lagrangian dynamics of spheroidal particles in turbulence (see Fig. 3.3).

Perhaps, the most spectacular consequence of spherical particles being massive is their tendency to sample the fluid non-uniformly, a phenomenon known as "preferential concentration". We show that the preferential concentration is not a feature specific to spherical particles. However, while the concentration patterns are seemingly independent on their shape for light particles, they become more complicated and possibly non-universal for heavy one. Please note that for us light particles refer to spheroids with a small response time τ_p, and heavy particles to spheroids with a large one.

Figure 3.3: The figure shows two types of spheroids, either oblate (in the left panel) or prolate (in the right panel) following two different tracer trajectory. The red arrows show their orientations and the black ones show their accelerations.

3.3.1   Statistics of the center of mass

Root-mean-square velocity and harmonic Stokes number.   To characterize the translational motion of spheroidal particles, we begin our analysis by measuring the velocity fluctuations of the center of mass along the Lagrangian trajectories. To do so, we introduce the particle root-mean-square velocity (later rms)

$$V_{\mathrm{rms}} = \frac{1}{\sqrt{3}} \left\langle \mathbf{V}_p^2 \right\rangle^{1/2},$$

(3.16)

where we recall that $\mathbf{V}_p = (V_x, V_y, V_z)$ is the velocity vector in the laboratory frame and the operator $\langle \cdot \rangle$ denotes an average over both time and the number of particles. It is natural to relate this quantity to the rms fluid velocity, and the left panel of Fig. 3.4 shows how the ratio between those two rms velocities varies as a function of the Stokes number St $= \tau_p/\tau_\eta$.

For small but non vanishing values of the Stokes number St $\lesssim 0.3 - 0.5$, the rms velocities of the particles are very slightly greater than the fluid rms velocity (see the zoom in the inset of the left panel). This possibly reflects a preferential sampling in the calm strain regions of the flow a feature previously observed by Bec et al. (2005) for spherical particles. Here, this observation remains apparently valid for all the shapes, but the range of Stokes for which this trend is visible depends on the particle shape.

For larger Stokes, say St > 0.5, the effect of non-sphericity ($\lambda \neq 1$) becomes even more apparent. All the particle rms velocities decrease with increasing Stokes numbers, but the sphere is the shape for which this decrease is the most pronounced. In fact, both oblate and prolate particles follow the same trend and the curves are seemingly parallel to each other for St $\gg 1$. This feature suggests a possible universal behavior of the rms velocities with respect to the shapes.
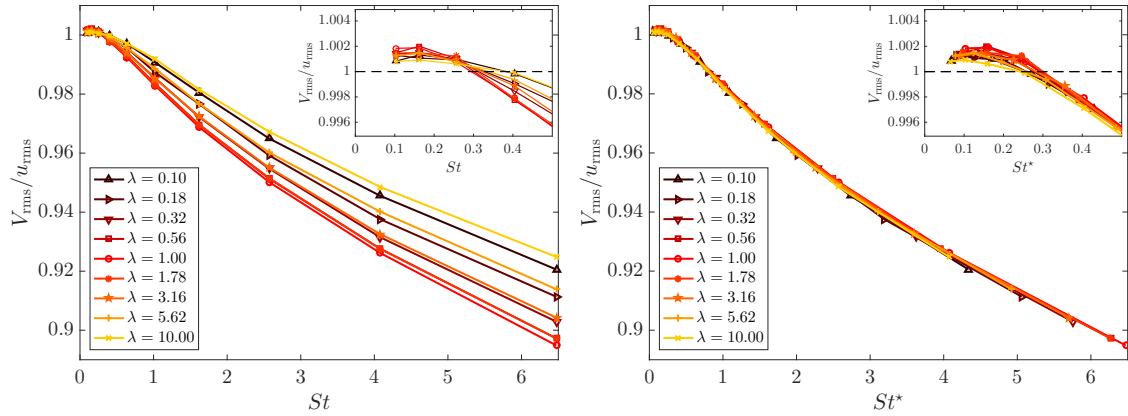
The universality appears in plain sight if following Shapiro and Goldenberg (1993); Zhang et al. (2001), one introduces the **harmonic** Stokes number

$$\mathrm{St}^\star = \frac{3\tau_p \lambda^{-2/3}}{8\tau_\eta \bar{K}}, \quad \text{with } \bar{K} = \frac{1}{3}(K_{\hat{x}\hat{x}} + K_{\hat{y}\hat{y}} + K_{\hat{z}\hat{z}}) = \frac{1}{\overline{\chi_0/a^2 + \theta_i \lambda^2 \chi_i}^{(H)}},$$

(3.17)

where $\theta_{1,2} = 1/\lambda^2$ and $\theta_3 = 1$ and $\overline{\chi_0/a^2 + \theta_i \lambda^2 \chi_i}^{(H)}$ denotes a harmonic mean involving the shape parameters appearing in Eq. (3.13). Note that with this definition, the Stokes number for spheres ($\lambda = 1$) remains unchanged, that is St* = St. Fig. 3.4 shows the root-mean-square velocity of each family as a

function of $St^\star$. One clearly observes that all the curves λ collapse onto a master curve, which is independent on the different aspect ratios, and that solely depends on the dimensionless harmonic Stokes number. This suggests that the relevant response time of the spheroids is not the usual response time defined in terms of a sphere with equal volume, but should be defined as $\tau_p^\star = St^\star \tau_\eta$.

The inset in the right panel of Fig. 3.4 shows that the range over which the particle rms velocities are larger than the fluid velocity is $St^\star \lesssim 0.3$, independent of the shape. Besides, as $St^\star$ decreases towards 0, the rms velocities of the particles tend to decrease towards the fluid rms velocity. This hints that as $St^\star \to 0$, we recover the behavior well established for spherical particles that the rms velocities of the particles and of the fluid coincide. This is the standard limit describing tracer particles uniformly sampling the domain, and our data hint that this limit is also independent of the shape, up to statistical error.
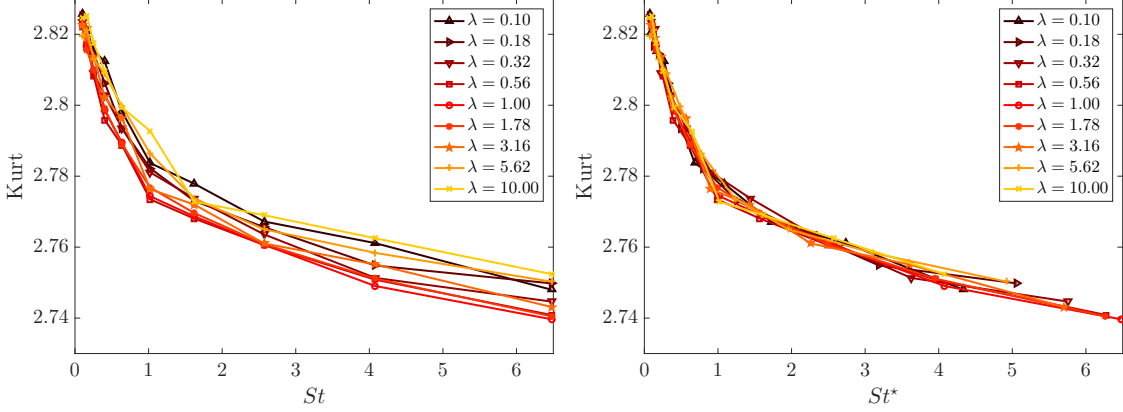
Figure 3.4: Root-mean-square particles velocity $V_{\text{rms}} = \dfrac{1}{\sqrt{3}} \left\langle \mathbf{V}_p^2 \right\rangle^{1/2}$ as a function of the St number (left panel) and $St^\star$ number (right panel) for different families of ellipsoids λ.

Single-time velocity fluctuations. To highlight the relevance of the harmonic Stokes number beyond the root-mean-square velocity, we study higher moments of particles velocity statistics. In particular, we compute the kurtosis defined as:

$$\text{Kurt} = \frac{\langle V_i^4 \rangle}{\langle V_i^2 \rangle^2}.$$
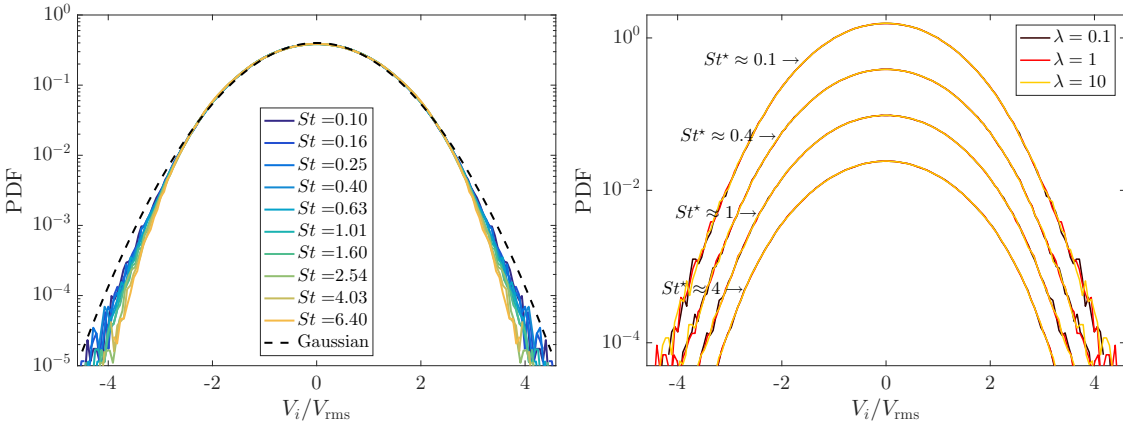
This quantity measures the "flatness" of the probability distribution: if the kurtosis is large, the probability distribution has fat tails and the extreme events are more probable; when the kurtosis decreases the probability to have extreme events also decreases (Pearson, 1905). We recall that a reference value for the kurtosis is Kurt = 3 corresponding to a Gaussian distribution.

The left panel of Fig. 3.5 shows the kurtosis as a function of St. The first observation is that for all Stokes and shapes, the kurtosis is slightly below 3 meaning that the velocity components are sub-Gaussian. We also observe that particles with smaller inertia have a larger kurtosis than heavy one. The right panel of Fig. 3.5 shows the kurtosis now as a function of $St^\star$ and we observe that similarly to the rms velocities, the kurtosis decreases as a function of $St^\star$ and collapses to a unique master curve. This suggests that the harmonic Stokes number not only prescribes the rms average velocities but also the full velocity distribution.

Figure 3.5: Flatness of the particle velocity components $\langle V_i^4 \rangle / \langle V_i^2 \rangle^2$ as a function of St (left panel) and of St* (right panel).

To substantiate this possibility, we measure the fluctuations of the single-time probability distribution of the particles velocity components. The left panel of Fig. 3.6 shows such a probability density function for various values of St, in the case of spherical particles ($\lambda = 1$). As expected from the measurements of the kurtosis, the tails of the distributions deplete when inertia increases. One observes a spreading in the tails of the order of one decade at $V_i = 4\, V_{\rm rms}$ between the smallest and the largest $\tau_{\rm p}$. The right panel of Fig. 3.6 shows the probability distributions of velocity components for $\lambda = 0.1$, 1 and 10, using selected values of the response time chosen such that St* = 0.1, 0.4, 1, and 4. One observes that the distribution associated to different aspect ratios collapse onto master curves that solely depend upon the harmonic Stokes number St*. This shows that the harmonic Stokes number fully accounts for the shape of the particles at the level of one-time velocity fluctuations of the center of mass.

Figure 3.6: Left: Probability density functions (PDF) of the particle velocity components (normalised to unit variance) for $\lambda = 1$ and various St. Right: Same but for different combinations of λ and $\tau_{\rm p}$ associated to four different values of St* (different symbols). Data has been shifted to increase visibility.

Two-time velocity fluctuations. The harmonic Stokes time also proves relevant for multiple-time velocity fluctuations. To illustrate this point, we here characterize the two-time statistics of the particles velocity and define the autocorrelation of the velocity components, as:

$$\mathcal{A}(t) = \frac{\langle V_i(t)\, V_i(0) \rangle}{V_{\rm rms}^2}.$$
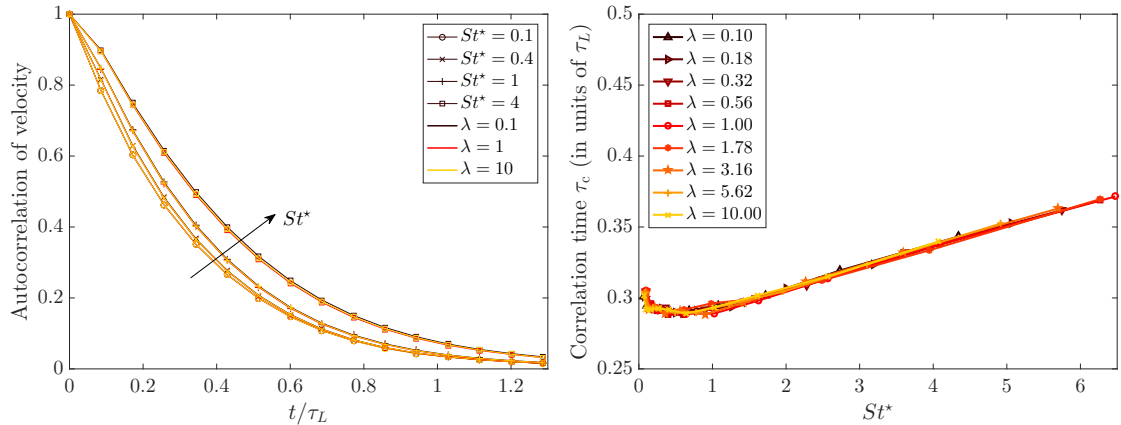
The left panel of Fig. 3.7 shows that such types of correlations decrease over times of the order of the

large-eddy turnover time τ_L. Besides, heavier spheroids decorrelate slower than light ones.

More precisely, we observe that the auto-correlation decays exponentially in the large time limit as

$$\mathcal{A}(t) \simeq \exp(-t/\tau_c),$$

where τ_c is the correlation time. The right panel of Fig. 3.7 shows the behavior of the correlation time as a function of $St^\star$. As expected, particles with large inertia are slightly longer correlated, because the memory effects are more important. One again observes the collapse onto four separated master curves; This suggests that the two-time statistics of the velocity are indeed described in terms of the harmonic Stokes number $St^\star$.
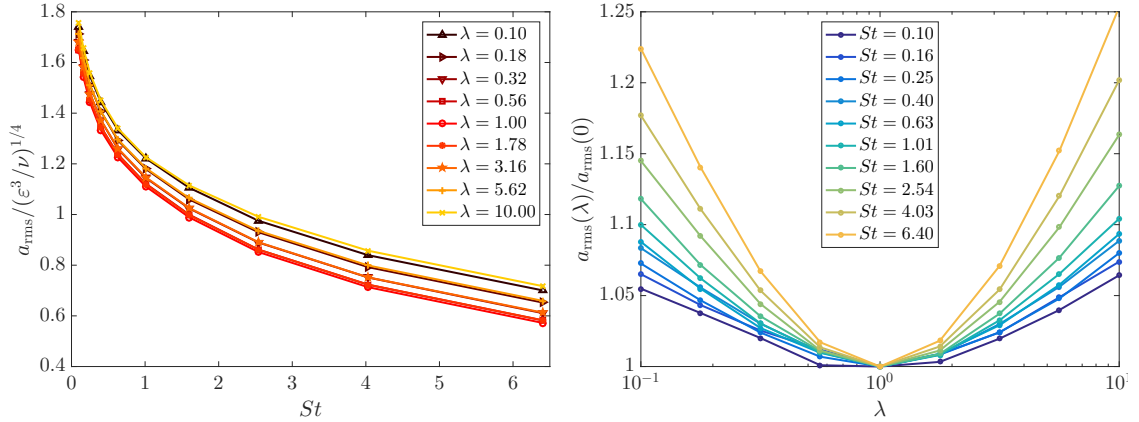
Figure 3.7: Left: Time autocorrelation of the particle velocity components for different combinations of λ and τ_p associated to four different values of $St^\star$ (different symbols). Right: Correlation times obtained from exponential fits of the time autocorrelations, shown here as a function of the harmonic Stokes number.

Acceleration statistics.   The previous results suggest that the harmonic Stokes number $St^\star$ can be used to fully describe the dynamical properties of particles. This behavior describes the dynamics of spheroids as if the orientation of the particles is not correlated with its translational dynamics. However, the fluctuations of the velocity only involve large-scale fluctuations. It could indeed be that on such scales, the orientation is effectively averaged in an isotropic manner. To explore this possibility, one needs to investigate small-scale quantities and this motivates to investigate the statistics of the particle accelerations. We first compute the root-mean-square accelerations, defined as:

$$a_{\text{rms}} = \frac{1}{\sqrt{3}}\langle (\text{d}\mathbf{V}/\text{d}t)^2 \rangle^{1/2} \tag{3.18}$$
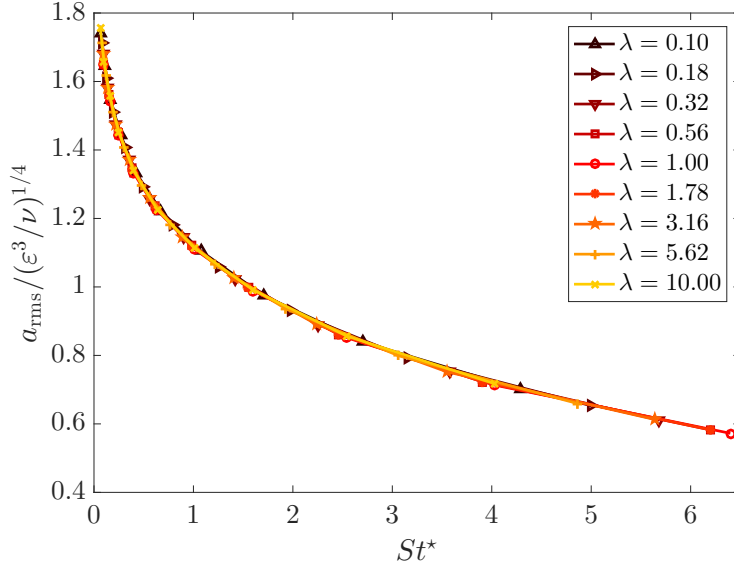
where $\text{d}\mathbf{V}/\text{d}t$ is the particle acceleration in the laboratory frame. Fig. 3.8 shows this quantity as a function of the (usual) Stokes number St. Data is rescaled by what is expected for fluid tracers in a turbulent flow, namely $a_{\text{rms}} \propto \eta/\tau_\eta^2 = (\varepsilon^3/\nu)^{1/4}$. We measure $a_{\text{rms}}/(\varepsilon^3/\nu)^{1/4} \approx 1.8$ in the limit $St \to 0$. This value is consistent with previous measurements reported at $R_\lambda \approx 300$. Note however that this value is not universal; the previous studies by Hill (2002); Biferale et al. (2004); Yeung et al. (2006), showed that the ratio $a_{\text{rms}}/(\varepsilon^3/\nu)^{1/4}$ actually depends on the Reynolds number of the flow, due to the intermittency of turbulent fluctuations.

As the particle inertia increases, we observe a shape-dependent decrease of the root-mean-square acceleration that is consistent to what was for instance reported in Bec et al. (2005) in the spherical case. As can be seen in the right-hand panel of Fig. 3.8, a non-spherical shape of the particles is responsible for an increase of the acceleration when the response time τ_p is fixed.

Figure 3.8: Root-mean-square acceleration a_{rms} as a function of the Stokes number St $= \tau_{\mathrm{p}}/\tau_{\eta}$ for various values of the particle aspect ratio λ. Right: Root-mean-square acceleration a_{rms} normalized to that of a sphere, this time represented as a function of the aspect ratio λ.
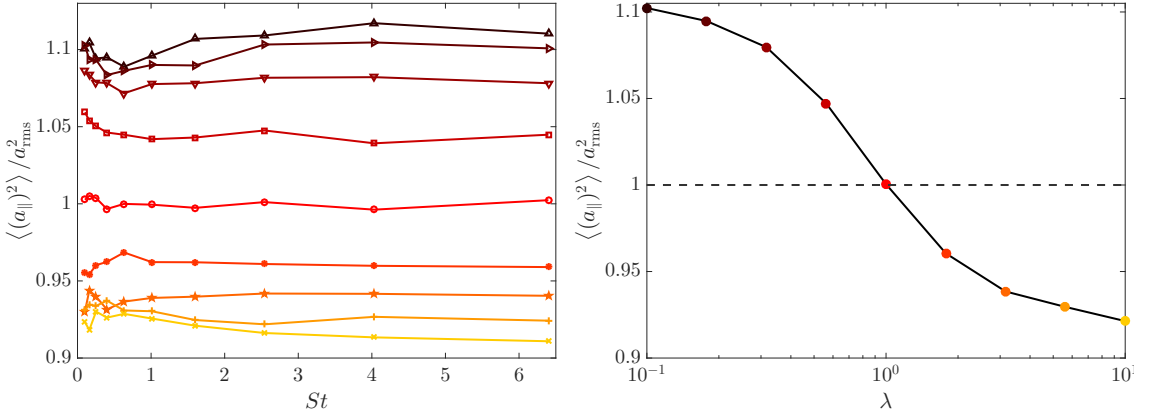
The effect of non-sphericity can in fact be described using the harmonic Stokes number. Fig. 3.9 shows that the root-mean-square acceleration depends solely on the harmonic Stokes number St*, similarly to what was observed for velocity. This means that the acceleration variance of spheroids can be straightforwardly deduced from those of spheres, again suggesting some independence between the particle orientations and the dynamics of the center of mass.
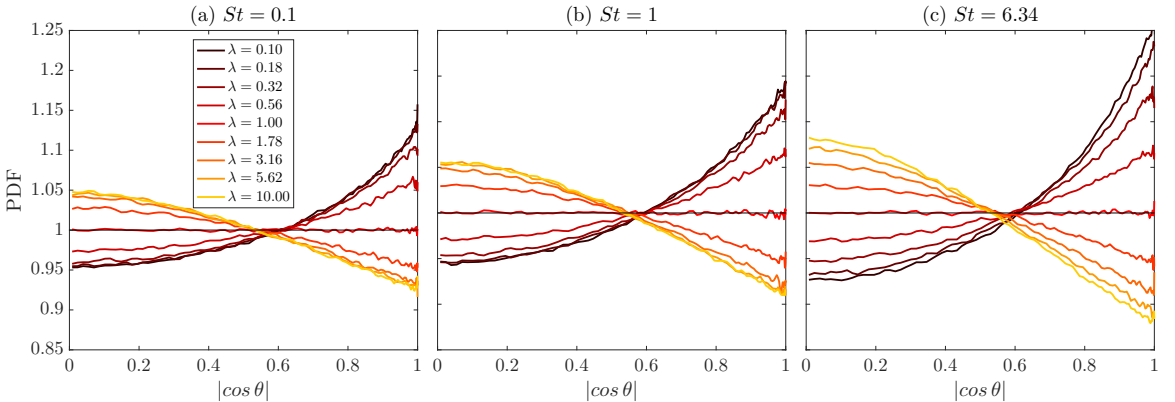
Figure 3.9: Root-mean-square acceleration a_{rms} as a function of the harmonic Stokes number St$^{\star} = \tau_{\mathrm{p}}/\tau_{\eta}^{\star}$ defined in (3.17), shown for various values of the particle aspect ratio λ.

Such a lack of correlations is however not totally true, and this is seen by looking at the statistics of the **parallel acceleration** $a_{\parallel} = \mathbf{p} \cdot \mathbf{a}$, defined as the component of the acceleration along the axis of symmetry of the particles. Indeed, as shown in Fig. 3.10, the variance of the parallel acceleration displays a clear dependence upon the aspect ratio λ. Besides, once normalized to the isotropic variance a_{rms}^2, its contribution seems independent of the particles response time (up to statistical errors). For oblate particles ($\lambda < 1$), accelerations are stronger in the direction of p, while for prolate particles ($\lambda > 1$) accelerations are weaker. This tendency is summarized in the right panel, which shows as a function of λ the value obtained when averaging over the observed plateau. This correlation between the acceleration and the orientation of the

particle can also be appreciated by measuring the distribution of the alignment between the direction of the acceleration $\hat{\mathbf{a}} = \mathbf{a}/|\mathbf{a}|$ and the axis of symmetry $\mathbf{p}$ of the particles. Fig. 3.11 shows that, independently of the response time, oblate particles are more likely to accelerate in the direction of $\mathbf{p}$ while prolate particles are more likely to accelerate in a direction perpendicular to the axis of symmetry.
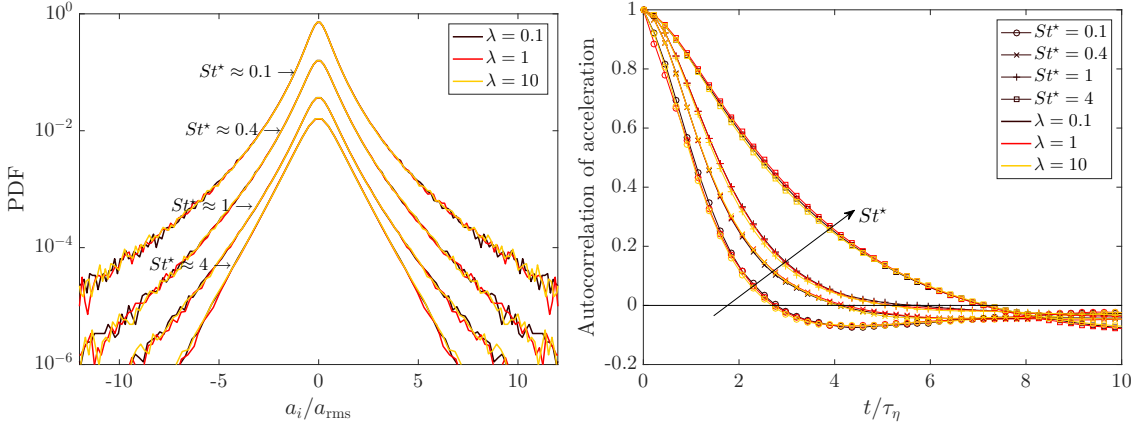
Figure 3.10: Left panel: Mean-square component of the acceleration along the particle axis of symmetry $\mathbf{p}$, normalised by the total root-mean-square value, shown as a function of the Stokes number St for various λ with the same color code as the left-hand panel. Right panel: Values of the observed plateau as a function of the aspect ratio λ

Figure 3.11: Probability density functions of the alignment, defined as the cosine of the angle $\theta \in [0, \pi/2]$ between the particle axis of symmetry and the direction of its acceleration $\hat{\mathbf{a}} = \mathbf{a}/|\mathbf{a}|$ for three different values of the Stokes number and, each time, for various aspect ratios as labeled.
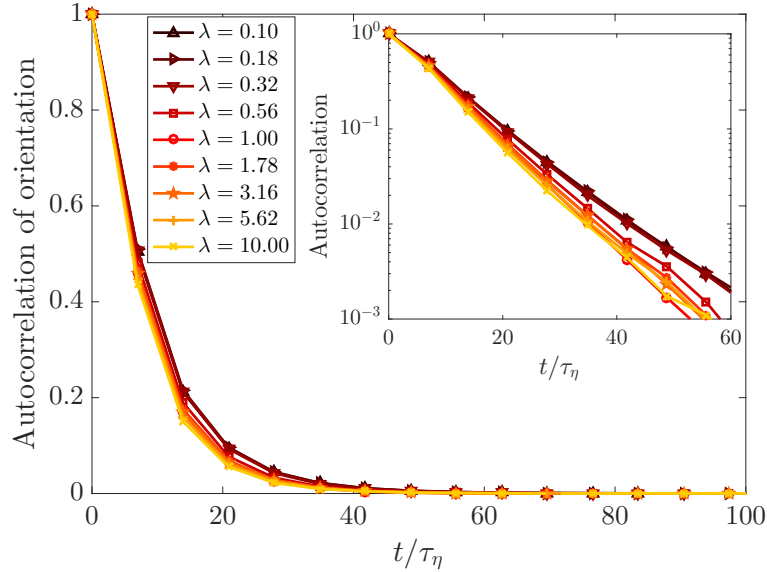
To conclude this discussion on the statistics of the acceleration, we finally show in Fig. 3.12 the probability density functions of the acceleration components (left panel) together with their time autocorrelations (right panel). In both cases, measurements show a harmonious collapse to master curves that solely depend on the harmonic Stokes number. This confirms the general picture for the translational motion of spheroidal particles. As we will see in the next section, the situation is different for the rotational dynamics.
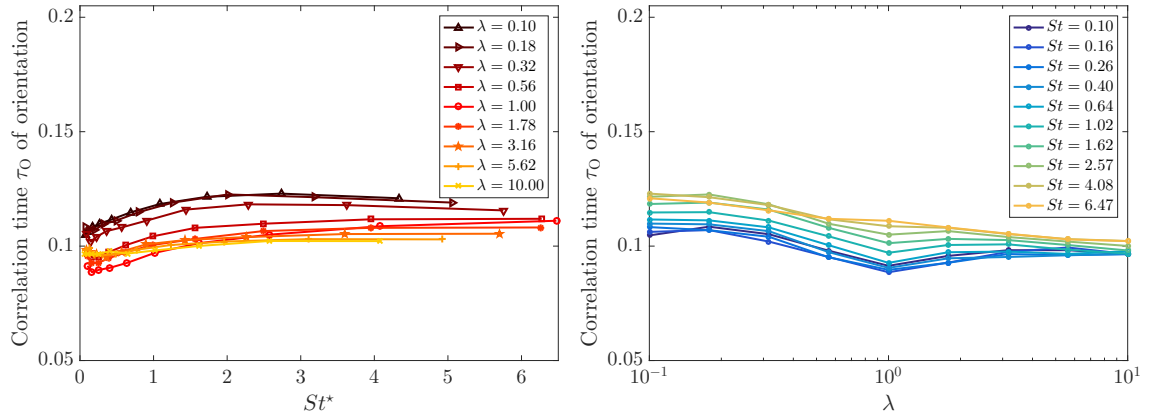
Figure 3.12: Left: Probability density functions of the particle acceleration components $a_i = \mathrm{d}V_i/\mathrm{d}t$, normalized to unit variance and obtained for several aspect ratios (different colors) but with response times chosen to maintain the harmonic Stokes number $St^\star$ to 0.1, 0.4, 1 and 4 (different symbols). Data has been shifted to increase visibility. Right: Time autocorrelation of the particle acceleration $\langle \mathbf{a}(t) \cdot \mathbf{a}(0) \rangle / (3\, a_{\mathrm{rms}}^2)$ for the same aspect ratios and harmonic Stokes numbers.

3.3.2   Statistics of the orientation

Orientation.   We recall that the orientation of the particles is determined by the direction of the unit vector $\mathbf{p}$ aligned with the axis of symmetry. Without further conditioning, the fact that turbulence is homogeneous and isotropic makes the single-time statistics of $\mathbf{p}$ also isotropic and thus not relevant for our statistical analysis. We thus focus on two-time quantities, in order to study how the orientation of the particles decorrelate in time. Fig. 3.13 shows the time autocorrelation $\langle \mathbf{p}(t) \cdot \mathbf{p}(0) \rangle$ as a function of time for $St = 1$ and various λ. Surprisingly, the orientation is correlated over long timescales, much larger than τ_η and rather of the order of the large-eddy turnover time. More precisely, we fit the large-time asymptotics with an exponential law $\propto e^{-t/\tau_\mathrm{O}}$, in order to evaluate the correlation time τ_O of the orientation. The correlation times are displayed in Fig. 3.14, as a function of the harmonic Stokes number $St^\star$ in the left panel and as a function of the aspect ratio in the right panel. They follow a rather intricate behavior and clearly do not collapse on a master curve. This means that the statistics of the orientation do not reduce to the dynamics of a sphere.
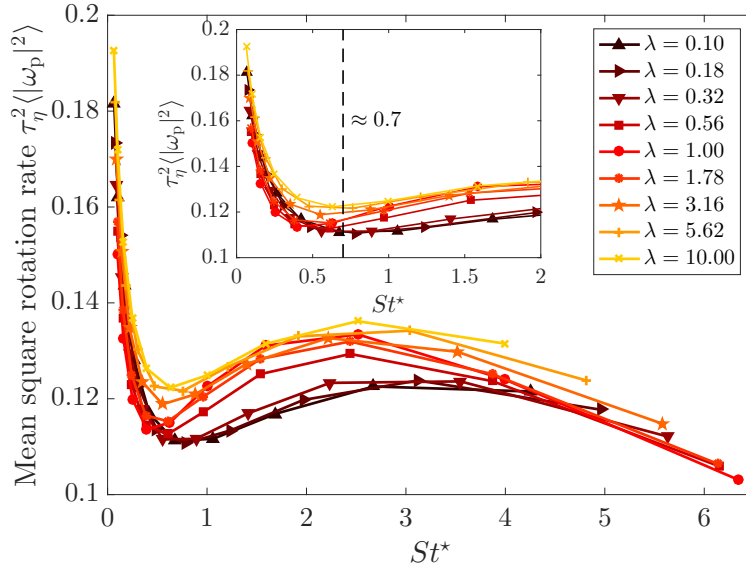
Figure 3.13: Time autocorrelation of the particles orientation for $St = 1$ and various aspect ratios, as labeled. Inset: Same quantities using semilogarithmic axes, hereby revealing the asymptotic exponential decay.
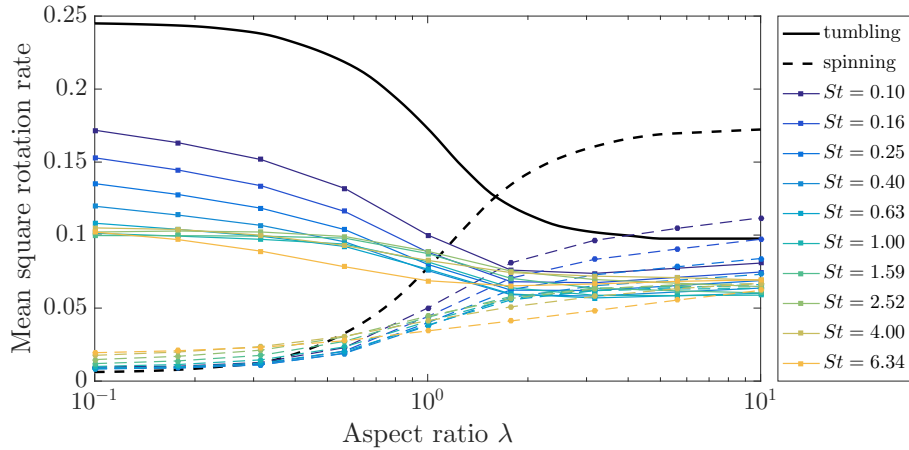
Figure 3.14: Left panel: Correlation time of the particles orientation obtained from an exponential fit of the autocorrelation as a function of $St^\star$. Right panel: Same quantity as a function of the aspect ratio λ.

Rotation rates. The rotation rates of the particles also display non-trivial dependence upon St and λ. Fig. 3.15 shows the total mean-square rotation $\langle|\Omega_p|^2\rangle$, as a function of the harmonic Stokes number $St^\star$. For all values of the aspect ratio, the rotation rate first abruptly decreases when inertia increases, up to $St^\star \approx 0.7$ where it reaches a minimum. It then grows again, reaching a secondary maximum, and finally decreases when $St^\star \gg 1$. Data do not follow a λ-independent behavior, except maybe during the first abrupt decreases, as the zoom in the inset exemplifies. Perhaps, the apparent collapse at small $St^\star$ is due to preferential concentration effects. As argued by Bec et al. (2005), the main mechanism at play at small inertia is the tendency for the particles to non-uniformly sample the flow; This results in the particles being ejected from regions with a high rotation to concentrate in regions with a high strain (and a low vorticity). Such an effect is purely dynamical and relates to the translational motion. It thus likely depends solely on $St^\star$. The behavior observed at larger inertia differs: It couples translational motions, preferential sampling, and the inertial rotational motions. Those behaviors are explained in more details in the next section.

Figure 3.15: Mean-square rotation rate $\langle|\Omega_p|^2\rangle$ as a function of the harmonic Stokes number.

Figure 3.16: Tumbling rate $\langle \Omega_{\hat{x}}^2 + \Omega_{\hat{y}}^2 \rangle$ (solid lines) and spinning rate $\langle \Omega_{\hat{z}}^2 \rangle$ (dashed lines) as a function of the aspect ratio λ (in units of τ_η). The lines without symbols correspond to the data of Byron et al. (2015).
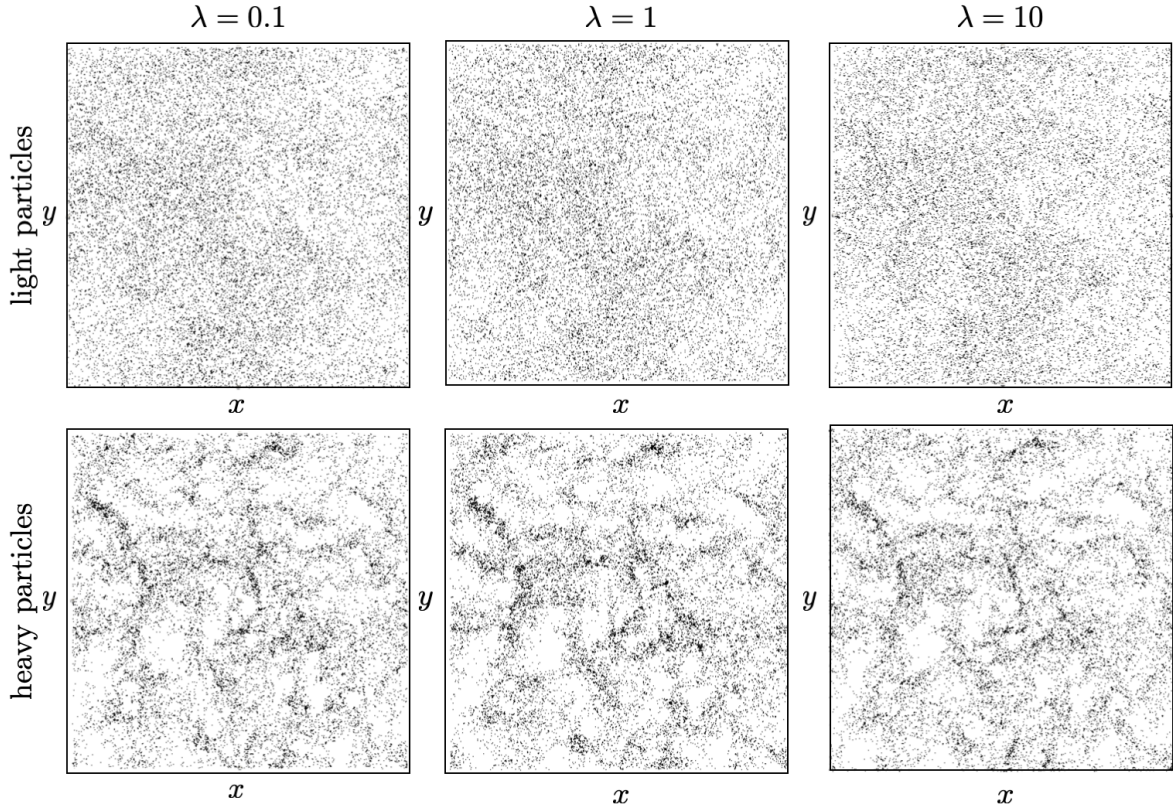
The right panel of Fig. 3.16 represents the decomposition of the rotation rate in spinning (rotation about the $\hat{z}$ direction, parallel to $\mathbf{p}$) and tumbling (sum of rotations about the perpendicular directions $\hat{x}$ and $\hat{y}$). These rates are shown as a function of the aspect ratio, and are compared to the case of inertialess spheroids (shown as lines without symbols) using the data previously published by Byron et al. (2015), and corresponding to a slightly higher Reynolds number $Re_\lambda = 433$ (obtained with 1024^3 resolution points).

Quite generally, one observes that the tumbling and spinning tendencies of inertial spheroids is pretty much akin to that of inertialess ones: In both cases, one observes a higher tumbling of prolate particles and a dominant spinning of oblate ones. Besides, we note that for spheres, the spinning rate is exactly 1/2 of the tumbling rate for every shapes. However, the specific rates of the tumbling and of the spinning rates differ considerably from the inertialess case in at least two ways: *(i)* For every Stokes number, the values of the rates are considerably lower than those obtained by Byron et al. (2015). *(ii)* At higher inertia, the predominance of tumbling over spinning seems to persist at rather large values of the aspect ratio, unlike the inertialess case.
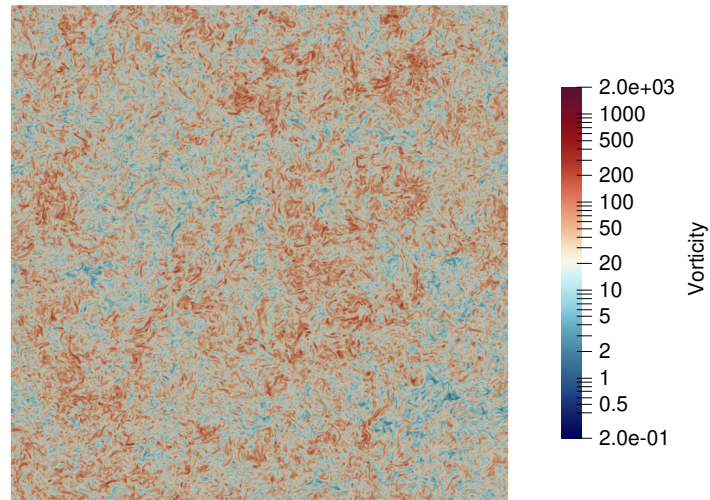
3.3.3 Spatial distributions

To conclude this chapter, and substantiate our previous observations, we finally report results on the clustering properties of inertial spheroids. Qualitatively, a careful observer looking candidly and with rested eyes at the concentration patterns of the particles on 2D slices through the fluid, such as the ones in Fig. 3.17, will notice the following trends:

(i) Very light particles ($St^\star \to 0$) are close to homogeneously distributed over the domain and there are no significant difference between the different shapes.

(ii) Heavier particles (with finite $St^\star$) display inhomogeneous concentration patterns. Those patterns are slightly more visible for the spheres than for either the prolate or the oblate particles.

(iii) The concentration patterns correlate with the corresponding vorticity field, here shown in Fig.3.18: the particles tend to be more clustered in regions where the vorticity field is low.
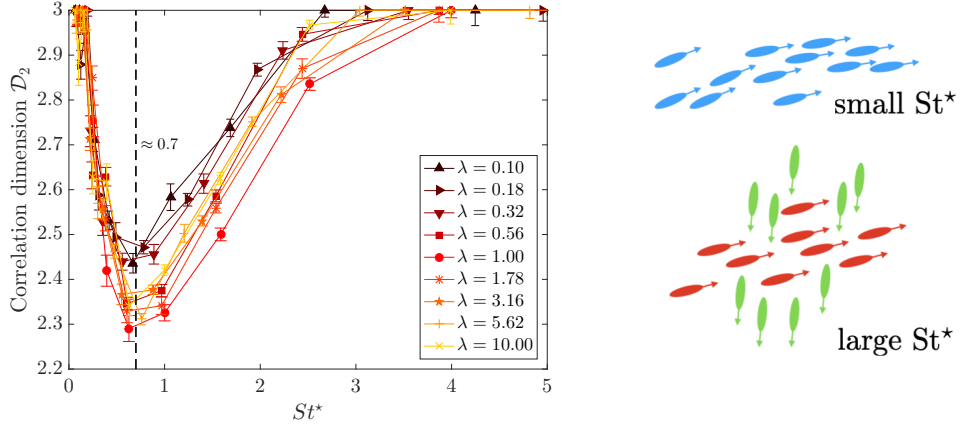
Figure 3.17: Concentration patterns seen in a 2D slice for the three types of spheroids: oblate (left), spherical (middle) and prolate(right). The top row corresponds to light particles with $St^\star \simeq 0.1$ and the bottom row corresponds to heavier particles with $St^\star \simeq 4$.

Figure 3.18: 2D slice of the enstrophy field ω^2 measuring local magnitude of the vorticity. The 2D slice is the same as the one of Fig.3.17.

To measure those effects in a quantitative fashion, we investigate the two-particle statistics, and in particular we compute the probability $P_2^<(r)$ to find two of them at a distance less than r. This quantity is of

particular importance when interested in collisions or coalescences between particles. For separations r in the dissipative range, it is well known that this quantity behave as a power law $P_2^<(r) \propto r^{\mathcal{D}_2}$ where the exponent $\mathcal{D}_2$ is called the correlation dimension (see Chapter 1). At both very small and very large harmonic Stokes numbers, the particles have a uniform distribution and $\mathcal{D}_2 = 3$. At intermediate values, one observes $\mathcal{D}_2 < 3$ with a minimum (maximum of small-scale clustering) reached for $St^\star \approx 0.7$ (see Bec et al. (2007)). We are not aware of any previously published results describing how this picture is changed when accounting for the particle non-sphericity.

Figure 3.19: Left: Correlation dimension $\mathcal{D}_2$ as a function of the harmonic Stokes number $St^\star$ and various aspects ratios, as labeled. Right: Sketch of the small-scale clusters for small $St^\star$ (top, blue) where all particles follow a similar dynamics and are thus aligned with each other and for large $St^\star$ (bottom) where clusters are perturbed by caustics where particles with different orientations meet.

The left panel of Fig. 3.19 shows the behavior of the correlation dimension as a function of the harmonic Stokes number for the various aspect ratios. All curves have similar shapes with a minimum attained at $St^\star \approx 0.7$. For values smaller than this critical point, the correlation dimensions seem to solely depend on $St^\star$. This implies that at small $St^\star$, only translational dynamics is important. Perhaps, this observation can be explained by the fact that time-correlations of the dynamics are small along the trajectories. Hence, it is the effective compressible velocity of the particles which is at play. Clusters are formed by stretching and folding the particle concentration for long times.

For values $\gtrsim 0.7$, the situation is different. We observe a spread of the correlation dimensions at fixed value of the harmonic Stokes number. We note that the spherical shape is the case for which the clustering is the most pronounced. This means that non-sphericity seems to deplete small-scale clustering when $St^\star \gtrsim 0.7$ and is therefore a mechanism that acts towards homogeneization. This effect is possibly explained by the fact that particles with different histories can meet together. Those trajectories are weakly correlated and likely have different orientations. This effect may qualitatively explain why $\mathcal{D}_2 \to 3$ with a shape-dependent rate when $St \gg 1$. This possible scenario of particle clustering is illustrated by the cartoon in the right panel of Fig. 3.19.

3.4 Concluding remarks

Summary.   The results reported here show in a systematic way the effect on the dynamics of the shape of the particles (measured by the aspect ratio λ) and inertia (measured by the Stokes number $St = \tau_p/\tau_\eta$ obtained by non-dimensionalizing their response time by the viscous Kolmogorov timescale). We recovered results from the previous work by Siewert et al. (2014a), performed in the context of particle sedimentation, and we extended the approach in the no-gravity case to provide a detailed characterization of the fluctuations in velocity and in the acceleration. In our view, our most salient result is the evidence that the translation motion and the orientation statistics are only weakly coupled. The translational motion is indeed almost fully prescribed by the motion of an equivalent sphere with response time $\tau_p^\star = \tau_\eta S t^\star$ based on the suitably defined

harmonic Stokes number built from the resistance tensor. The deviations from the motion of a sphere can be spotted at the level of the two-time statistics of the acceleration components, but remain very weak. This decoupling may be of fundamental importance to develop practical Lagrangian stochastic models of light non-spherical particles to be included in industrial codes such as the Saturn Code used by EDF engineers mentioned in the introduction of this thesis. The orientation statistics display more intricate features. While the orientation and rotation rate statistics of light particles seem fully prescribed by St★, this is no longer valid for heavier spheroids. The threshold value is identified as $St^\star \approx 0.7$, above which the statistics become non-universal with respect to the shape. This behavior was found to reflect on the concentration properties of the particles, which we characterized qualitatively and quantitatively. In particular, we recovered and extended the observations of Bec et al. (2005, 2007) made in the spherical case, where the particles concentrate on dynamical fractal sets whose position are correlated with the dissipative structures of the flow. Although not yet fully understood, our study suggests new statistical models to describe how non-sphericity modifies the fractal dimension of these concentrations.

Perspectives.   This study paves the way for future work. Among the perspectives, one could wish to better understand the interplay between the tumbling and the spinning of spheroids. Qualitative insights could probably be obtained from theoretical study of particles within random velocity fields, for example extending a previous approach by Vincenzi (2012) to include inertia. This line of work, along with some more detailed characterization of the dissipative structures based on a Okubo-Weiss -like parametrization, could also serve to better understand the preferential concentration patterns and the depletion of small-scale clustering by non-sphericity.

We also note that including other physical effects could be interesting. We have in mind effects of gravity (Siewert et al., 2014a); which could be easily implemented in our numerics to study gravitational settling and perhaps also effects hydro-dynamical or physical interactions between the particles, in order to model small but finite-size spheroids.

4 | Fibers in a turbulent flow

Contents

The chapter discusses the turbulent dynamics of elongated deformable objects; It specifically focuses on the case of inextensible flexible fibers suspended in turbulent fluids. Such particles are relevant to many industrial applications; our results highlight the crucial role of intermittent fluctuations in the Lagrangian statistics.

The chapter is organized as follows. We first introduce a mathematical model, namely the local slender body theory, that provides a convenient way to address the dynamics of small fibers. The model displays a rich phenomenology, as fibers are likely to experience several kinds of instabilities, from tumbling and buckling to super-buckling. We then described the outcome of highly-resolved numerical simulations. We focus on the buckling statistics of small fibers induced by 3D turbulent fluctuations, and describe two other instabilities due to flexibility, namely misalignments and super-buckling. The analysis was published as a letter in Physical Review Letters, which we attach at the end of the chapter.

4.1 Dynamics of fibers

The objective of this section is to derive a working mathematical model to describe the dynamics of small fibers immersed in a turbulent environment. This involves modeling the fluid/structure coupling between the (rigid) fibers and the (newtonian) fluid. The final result will be the so-called **local slender body theory**.

We here consider elongated inextensible yet flexible objects with rotational symmetry: They are characterized by their length ℓ and circular cross-section of radius a. The aspect ratio is assumed to be smaller than 1, *e.g.* $\epsilon = a/\ell \ll 1$. The fiber dynamics is then fully described in terms of the motion of the center-line curve $s \mapsto \mathbf{X}(s)$, parametrized by the arc-length coordinate $s \in [-\ell/2, \ell/2]$ (see Fig. 4.1). The explicit derivation of the fiber dynamics using the slender body theory relies on several further approximations and modeling assumptions, that we now describe.

Figure 4.1: A typical fiber in free space parametrised by the arc-length coordinate s. Mathematically, the latter describes the local length of the fiber. In the local frame $(\mathbf{e}_1, \mathbf{e}_2, \mathbf{e}_3)$ (also known as Frenet referential frame) the curvature of the fiber is defined as: $\kappa(s) = \frac{d^2\mathbf{X}}{ds^2} \cdot \mathbf{e}_2$.

4.1.1 Fiber without a fluid: mechanical properties
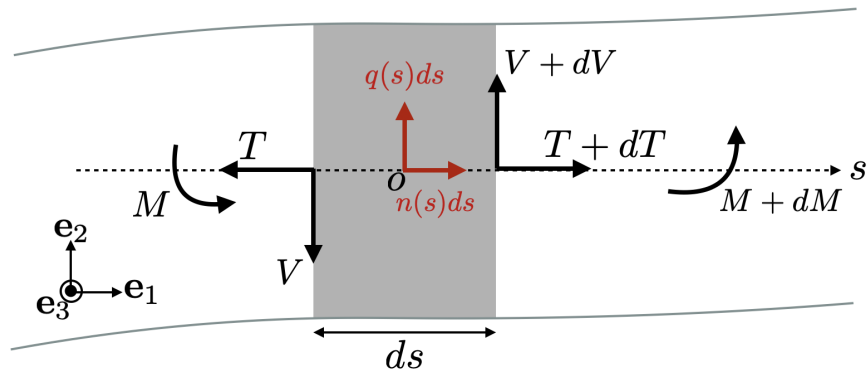
Elongated objects such as fibers are nothing but a specific type of beam, *e.g.* the fundamental atom of civil engineering. In that context, a beam is defined as a solid object with one dimension larger than the two others. To describe our fibers, we consider the simplest model of a beam, given by the **Euler-Bernoulli** theory (see for instance Landau and Lifshitz (1959); Thorin and Forêt (2013) and references therein). The Euler-Bernoulli theory relies on the three following hypothesis:

- the beam only undergoes small deformations,

- the beam is considered in a linear elasticity regime: There exists a linear relation between the stress σ and the strain ϵ,

- the perpendicular section of the beam cannot be deformed by shear stresses.

The dynamics of the beam stems from the balance between the external and the internal forces. Let us consider a small piece of the fiber as the one shown in Fig. 4.2. This small piece is subject to

- the action of the internal tensile forces T (from the left side) and $T + dT$ (from de right side),

- the internal shear forces N (from the left side) and $N + dN$ (from de right side),

- the internal flexural forces M (from the left) and $M + dM$ (from right) acting as torques,

- the external forces $n(x)dx$ and $q(x)dx$.

Please observe, that for simplicity, we here neglect any force likely to *twist* the fiber perpendicular to the cross-section and that would be modelled as torques in the $\mathbf{e}_1$ direction.

Figure 4.2: Forces and torques acting on an infinitesimal slice of beam.

The dynamics of the piece of fiber is then determined from the fundamental principle of mechanics, which reads:

$$\sum F_1 = T + dT - T + n(s)\,ds = \frac{d}{dt}\left(\xi\,ds\,\frac{d\mathbf{X}}{dt}\right)\cdot\mathbf{e}_1,$$
$$\sum F_2 = V + dV - V + q(s)\,ds = \frac{d}{dt}\left(\xi\,ds\,\frac{d\mathbf{X}}{dt}\right)\cdot\mathbf{e}_2, \tag{4.1}$$
$$\sum M_3 = M + dM - M + V\,ds + O(ds^2) = 0,$$

we here non-dimensionalize mass units by the density of the surrounding fluid, so that the fiber's mass per unit length reads $\xi = \sigma/(\rho_f L^2)$ where σ is the linear density of the fiber in kg/m.

To complete the description, we need to specify the rheology of the fibers. We here rely on Hookes law valid for linear elastic materials: assuming small deformations, the theory of elasticity ties the flexural forces to the local curvature $\kappa(s)$ (defined in Fig. 4.1) through:

$$M(s) = E\,\kappa(s) = E\,\frac{d^2\mathbf{X}}{ds^2}\cdot\mathbf{e}_2, \tag{4.2}$$

where E is the bending modulus (also called flexural rigidity). It is defined as $E = YI$, with Y the Young modulus and I the moment of inertia. The latter is computed as $\pi a^4/4$ for a cylinder of radius a (see Appendix B for an explicit derivation). Combining this constitutive behavior to the dynamics of Eq. (4.1), we obtain the final result:

$$\frac{dT}{ds} + n(s) = \frac{d}{dt}\left(\xi\,\frac{d\mathbf{X}}{dt}\right)\cdot\mathbf{e}_1,$$
$$-\frac{d^2M}{ds^2} + q(s) = \frac{d}{dt}\left(\xi\,\frac{d\mathbf{X}}{dt}\right)\cdot\mathbf{e}_2. \tag{4.3}$$

This equation is supplemented with the free-end boundary conditions $\partial_s^2\mathbf{X} = 0$ and $\partial_s^3\mathbf{X} = 0$ at $s = \pm\ell/2$. The equation then entirely prescribes the dynamics of the fiber provided that one can specify the external forces $\mathbf{f}(s) = (q, n)$. In that case, M is prescribed by the curvature and T is prescribed by the inextensibility constraint $|\partial_s\mathbf{X}|^2 = 1$ for all $s \in [-\ell/2, \ell/2]$. We will provide more details on this constraint later on, when we describe the slender body equations.

4.1.2   Fiber within a fluid: the slender body approximations

Let us now immerse our fibers in a fully developed turbulent flow, whose dynamics is governed by the Navier-Stokes equations at high Reynolds number, as previously described in Chapter 2.

A priori, our aim here is to determine the force exerted by the fluid on the fibers in order to model their dynamics. To that end, we use a further modeling assumption and assume that the fiber is not only thin but also small, and in particular smaller than the Kolmogorov scale η. Previous work has exposed the SBT framework with this hypothesis relaxed in a turbulent flow (Gay et al., 2018; Rosti et al., 2018), but this goes beyond the scope of our work, which focuses on the dynamics of sufficiently small particles.

The combination of being small and being thin has two consequences for the fiber:

i) Because it is thin enough, it does not modify the fluid velocity field: In other words it is passive.

ii) Because it is small, it has a well-defined scale, and at the scale of the fiber, the flow is smooth, characterized by a low Reynolds number.

The second consequence means that the linear dissipative term $\nu \nabla^2 \mathbf{u}$ dominates over the non-linear advection term $(\mathbf{u} \cdot \nabla) \mathbf{u}$ and the velocity diffuses. Additionally, a simplifying assumption is to assume that the flow is stationary, *e.g.* $\partial_t \mathbf{u} = 0$. This is justified as the fiber has the fastest timescale of the problem due to its small size. From the fiber point of view, the fluid motion therefore follows a simplified form of the Navier-Stokes equations (2.2), that reduce to the so-called Stokes approximation:
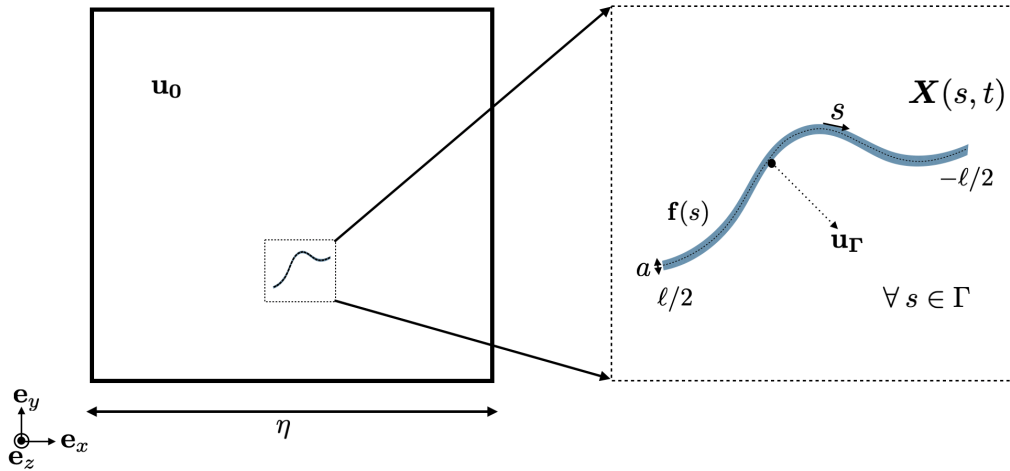
$$-\nabla p + \nu \nabla^2 \mathbf{u} = 0 \quad \text{and} \quad \nabla \cdot \mathbf{u} = 0, \tag{4.4}$$

where ν is the fluid viscosity and p is the pressure field determined from incompressibility[5]. The Stokes equation does not fully specify the coupling between the fiber and the fluid environment. To that end, we need to supplement Eq. (4.4) with boundary conditions, both in the far field away from the fiber and on its surface. Because the fiber is small, it does not affect the far field velocity: the far field velocity is therefore identified to the background velocity field, here denoted by $\mathbf{u}_0$. From the viewpoint of the fiber, the latter is a constant both in space and in time. On the surface of the fiber, we prescribe the standard no-slip boundary conditions for the tangential velocity, together with the impermeability condition for the normal component. Let us now denote as Γ the fiber surface and let $\mathbf{u}_\Gamma$ be the fiber surface velocity. The full boundary conditions for the fluid velocity therefore read:

$$\mathbf{u}(\mathbf{x}) = \mathbf{u}_\Gamma \quad \text{for} \quad \Gamma \quad \text{and} \quad \mathbf{u}(\mathbf{x}) = \mathbf{u}_0 \quad \text{for} \quad \|\mathbf{x}\| \to \infty. \tag{4.5}$$

---

[5]Please recall that we have assumed from Chapter 2 that the fluids have unit densities, so that kinematic and dynamic viscosity coincide.

Figure 4.3: Left panel: small fiber of length ℓ immersed on a fluid parcel of size η (dissipative scale) where $\mathbf{u}_0$ is the background velocity fluid. Right panel: zoom on the fiber. The fiber position $\mathbf{X}(s,t)$ is described along the arc-length $s \in [-\ell/2, \ell/2]$, as well as the force per unity length is $\mathbf{f}(s)$. On all the point of the surface fiber Γ, the velocity is described by $\mathbf{u}_\Gamma$. The aspect ratio is prescribed as $a/\ell \ll 1$, where ℓ is the length of the fiber and a its radius. Note please, that the fibers are very small compared to the Kolmogorov scale η. If we observe the dynamics from this scale, the velocity field is not feeling any effect from the fibers.

In other words, the fluid velocity is equal to $\mathbf{u}_\Gamma$ at the surface of the fiber and far away is equal to the background velocity flow $\mathbf{u}_0$. This is shown in Fig. 4.3, where the fluid background is equal to $\mathbf{u}_0$ for a fluid parcel of the size of the dissipation scale η.

Let us come back to the fiber dynamics. In principle, if one can successfully resolve the Stokes equations with the conditions (4.5), then one can specify the dynamical external forces $\mathbf{f}(s) = (q, n)$, which are the forces exerted by the fluid on the fiber. In that case, the set of Eq. (4.3) previously introduced describes the full dynamics of the fiber. The problem that we face, is that in full generality, the hydrodynamical forces are hard to determine because the boundary-value problem prescribed by Eq. (4.4) and (4.5) is difficult to solve.

In fact, resolving the Stokes equations is only possible when the geometry of the body is "sufficiently simple". The most famous case is when we consider a sphere of radius a. The Stokes velocity past a static sphere is easily computed as:

$$\mathbf{u}(\mathbf{x}) = \mathbf{u}_0 - \frac{3}{4}\frac{a}{x}\left(\mathbf{u}_0 + (\mathbf{u}_0 \cdot \mathbf{x})\frac{\mathbf{x}}{x^2}\right) - \frac{a^3}{4x^3}\left(\mathbf{u}_0 - 3(\mathbf{u}_0 \cdot \mathbf{x})\frac{\mathbf{x}}{x^2}\right),$$

from which one obtains the drag force exerted by the fluid on the sphere $\mathbf{f} = -6\pi\mathbf{u}_0\nu a$ (see for example Pozrikidis and Jankowski (1997)).

Conversely, if the object has a complex geometry such as our fibers, resolving the Stokes equations becomes very cumbersome. For this reason we rely on a standard approach known as **slender body theory**, first introduced by Batchelor (1970a,b). This approach is slightly circumvented but efficient: Rather than determining the force exerted by the fluid, we determine the fluid flow compatible with the local deformation and the far field asymptotics.

The first step is to recast Eq. (4.3) as an expression for the external forces. Explicitly, Eq. (4.3) is equivalent to

$$\mathbf{f}(s) = \partial_t(\xi\partial_t\mathbf{X}) - \partial_s(T\,\partial_s\mathbf{X}) + E\,\partial_s^4\mathbf{X}. \tag{4.6}$$

As a further simplifying approximation, we assume that the inertia of the fiber can be neglected, so that the external forces depend only on the rheology, that is

$$\mathbf{f}(s) = -\partial_s(T \, \partial_s \mathbf{X}) + E \, \partial_s^4 \mathbf{X}. \tag{4.7}$$

Physically, such an approximation is known as an over-damped approximation. Its practical outcome is to relate the external forces $\mathbf{f}(s)$ to the local deformation of the fiber. [6]

The second step is to invoke Newton third law of action-reaction, which implies that the fiber is in turn effectively applying on the fluid a force of opposite direction with equal magnitude $\|\mathbf{f}(s)\|$, and we now want to determine the fiber velocity to which it corresponds. Because of the no-slip boundary condition between the fiber and the fluid, this velocity matches that of the fluid in this region of space. The problem that we need to solve now is to determine the fluid velocity field generated by this force. This is again difficult, unless we rely on the fact that a slender fiber is by definition very thin. Its effect on the fluid can reasonably be modeled by a continuous line of punctual forces:

$$\mathbf{F}_{fiber \to fluid}(\mathbf{x}) = \int_{-\ell/2}^{\ell/2} \mathbf{f}(s)\delta(\mathbf{x} - \mathbf{X}(s))ds, \tag{4.8}$$

where $\mathbf{f}$ is determined by Eq. (4.7), and δ is the Dirac delta function. This methodology allows to replace the boundary value constraint on the fiber by a singular force, which we know how to handle. Indeed, to determine the velocity field, we can now solve the singularly forced Stokes equations

$$\nabla p - \nu \nabla^2 \mathbf{u} = \mathbf{F}_{fiber \to fluid}(\mathbf{x}) \quad \text{and} \quad \nabla \cdot \mathbf{u} = 0,$$
$$\text{with boundary condition} \quad \mathbf{u}(\mathbf{x}) = \mathbf{u}_0 \quad \text{for} \quad \|\mathbf{x}\| \to \infty. \tag{4.9}$$

A wily manner to resolve such linear problem is to use the Stokeslets tensor:

$$\mathbb{G}(\mathbf{x}) = \frac{1}{8\pi\nu} \left(\frac{\mathbb{I}}{|\mathbf{x}|} + \frac{\mathbf{x}\mathbf{x}}{|\mathbf{x}|^3} \right), \tag{4.10}$$

which produces the fundamental solution $\mathbf{u}_{Stokeslets} = \mathbb{G} \cdot \mathbf{f}_0$ to the Stokes equation forced by a punctual force $\mathbf{f}_0$ located at the origin:

$$\nabla p - \nu \nabla^2 \mathbf{u} = \mathbf{f}_0 \delta(\mathbf{x}) \quad \text{and} \quad \nabla \cdot \mathbf{u} = 0,$$
$$\text{with boundary condition } \mathbf{u}(\mathbf{x}) = 0 \quad \text{for} \quad \|\mathbf{x}\| \to \infty. \tag{4.11}$$

The velocity field associated to the problem Eq. (4.9) is then simply and is given by a convolution involving the Stokeslets along the fiber length, superimposed on the background flow:

$$\mathbf{u}(\mathbf{x}) = \mathbf{u}_0 + \int_{-\ell/2}^{\ell/2} \mathbb{G}(\mathbf{x} - \mathbf{X}(s)) \cdot \mathbf{f}(s)ds \tag{4.12}$$

The velocity field generated by the fiber is therefore:

$$\mathbf{u}(\mathbf{x}) = \mathbf{u}_0 + \int_{-\ell/2}^{\ell/2} \frac{\mathbf{f}(s)}{8\pi\nu} \cdot \left(\frac{\mathbb{I}}{|\mathbf{x} - \mathbf{X}(s)|} + \frac{(\mathbf{x} - \mathbf{X}(s))(\mathbf{x} - \mathbf{X}(s))}{|\mathbf{x} - \mathbf{X}(s)|^3} \right) ds, \tag{4.13}$$

where recall that $\mathbf{f}(s)$ represents the forces per unit length acting on the surface of the fiber. As a side remark, we observe that the fundamental solution of Eq. (4.11) exactly matches the leading-order correction to the background flow of the Stokes flow past a sphere given by Eq. (4.1.2), provided $\mathbf{f}$ is the

---
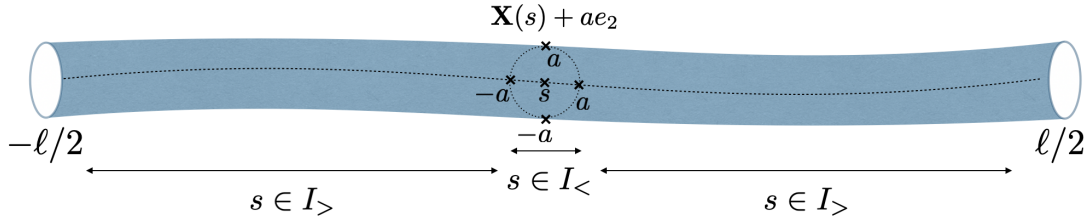
[6]Please observe that the validity of the SBT framework does not rely on the over-damped approximation.

drag force. Hence, since the expression (4.14) relies on the Stokeslets solution, it only considers the leading orders corrections generated by a finite-size fiber on the background flow. To model more accurately the field not too far away from such a fiber, higher-order corrections such as Stokes dipoles could very well be introduced (Johnson, 1980).

To complete our derivation of the slender body equations, we compute the velocity at a distance a away from the line singularity (recall that a is the cross-section radius). The velocity of the fiber elements is then identified to

$$\partial_t \mathbf{X}(s) = \mathbf{u}(\mathbf{X}(s) + ae_2) =$$
$$\mathbf{u}_0 + \int_{-\ell/2}^{\ell/2} \frac{\mathbf{f}(s')}{8\pi\nu} \cdot \left(\frac{\mathbb{I}}{|ae_2 + \mathbf{X}(s) - \mathbf{X}(s')|} + \frac{(ae_2 + \mathbf{X}(s) - \mathbf{X}(s'))(ae_2 + \mathbf{X}(s) - \mathbf{X}(s'))}{|ae_2 + \mathbf{X}(s) - \mathbf{X}(s')|^3} \right) ds'. \tag{4.14}$$

This equation describes a slender body dynamics without any further approximation. It is closed but cumbersome to use as it involves a non-local integral operator on the right-hand side.

Figure 4.4: Illustration of the local approximation invoked in Eq. (4.16) that gives rise to the local slender body theory: The dominant contribution comes from the local region of space $I_<$, and the non-local contribution $I_>$ is negligible.

For the sake of simplicity, we would better have a local model, namely the *local* slender body theory. This motivates a further round of approximations to simplify the integrals appearing in Eq. (4.14), essentially justified by the fact that the fibers are considered in a small deformation regime; this also means that the variation of the internal forces along the fibers are not too strong. Mathematically we therefore make the approximations:

$$\mathbf{X}(s) - \mathbf{X}(s') \approx (s - s')\partial_s \mathbf{X}(s) \quad \text{and} \quad \int \mathbf{f}(s') \cdot \mathbb{G}(s - s') \approx \mathbf{f}(s) \cdot \mathbb{G}(s - s'), \tag{4.15}$$

and split the resulting integral in two parts $I_<$, $I_>$ (see Fig. 4.4) defined as:

$$I_{\lessgtr} = \frac{\mathbf{f}(s)}{8\pi\nu} \cdot \int_{|s-s'|\lessgtr a} \left(\frac{\mathbb{I}}{|ae_2 + (s - s')\partial_s \mathbf{X}(s)|} + \frac{(ae_2 + (s - s')\partial_s \mathbf{X}(s))(ae_2 + (s - s')\partial_s \mathbf{X}(s))}{|ae_2 + (s - s')\partial_s \mathbf{X}(s)|^3} \right) ds'. \tag{4.16}$$

Recalling $a \ll \ell$, it is then straightforward to estimate:

$$I_< \sim O\left(\frac{f(s)}{8\pi\nu} \right) \quad \text{and} \quad I_> \sim -2\log\epsilon \left(\frac{f(s)}{8\pi\nu} \right) \cdot (\mathbb{I} + \partial_s \mathbf{X}(s)\partial_s \mathbf{X}(s)), \tag{4.17}$$

where we recall that $\epsilon = a/\ell$ is the aspect ratio of the fiber. The main contribution to the dynamics is therefore due to the mean-field contribution of the fiber pieces sufficiently far compared to the cross-section radius. We

then obtain the *local* slender body equations [7]:

$$\partial_t \mathbf{X}(s) = \mathbf{u}_0 + \frac{1}{8\pi\nu} \left[b \, \mathbb{D} \, \mathbf{f}(s) + \mathbf{K} \left[\mathbf{f}(s) \right] \right]. \tag{4.18}$$

The presence of the mobility matrix $\mathbb{D} = \mathbb{I} + \partial_s \mathbf{X} \, \partial_s \mathbf{X}^{\mathsf{T}}$ reflects the anisotropic drag exerted by the fluid on the slender fiber and the parameter $b = -\ln(\epsilon^2)$ is much larger than 1. $\mathbf{K} \left[\mathbf{f}(s) \right]$ is a correction term accounting for the non-local effect and here set to 0: As announced, the non-local effects are neglected in the local slender body theory.

4.1.3   Fibers within a turbulent fluid

Background turbulent field.   The local slender body equations (4.18) rely on the validity on the Stokes equations at the scale of the fibers. In a fully developed flow, this approximation certainly holds provided the fibers are smaller than the Kolmogorov dissipative scale η. This property suggests to replace the constant far-field velocity $\mathbf{u}_0$ of Eq. (4.18) by the local turbulent velocity $\mathbf{u}_0(\mathbf{X}, t)$, as represented in Fig. 4.3. As a refinement, the small-fiber approximation then suggests to linearize the fluid velocity along the fibers as $\mathbf{u}_0(\mathbf{X}, t) \approx \mathbf{u}_0(\bar{\mathbf{X}}, t) + \mathbb{A}(\bar{\mathbf{X}}, t) \, (\mathbf{X} - \bar{\mathbf{X}})$ where $\mathbb{A}$ denotes the velocity gradient $\mathbb{A}_{ij}(\mathbf{X}, t) = \partial_j u_i(\mathbf{X}, t)$. Please note, that because of the absence of inertia, the center of mass $\bar{\mathbf{X}}(t)$ follows the dynamics of a simple tracer, namely $d\bar{\mathbf{X}}/dt = \mathbf{u}_0(\bar{\mathbf{X}}, t)$. Eq. (4.18) with the corresponding turbulent background flow $\mathbf{u}_0(\mathbf{X}, t)$ and the external forces applied by the fiber on the fluid $\mathbf{f}(s) = \partial_s(T \, \partial_s \mathbf{X}) - E \, \partial_s^4 \mathbf{X}$, then becomes

$$\partial_t \mathbf{X}(s, t) = \mathbf{u}_0(\bar{\mathbf{X}}, t) + \mathbb{A}(\bar{\mathbf{X}}, t) \, (\mathbf{X} - \bar{\mathbf{X}}) + \frac{b}{8\pi\nu} \, \mathbb{D} \left[\partial_s(T \, \partial_s \mathbf{X}) - E \, \partial_s^4 \mathbf{X} \right]. \tag{4.19}$$

This equation is supplemented with the free-end boundary conditions $\partial_s^2 \mathbf{X} = 0$ and $\partial_s^3 \mathbf{X} = 0$ at $s = \pm \ell/2$.

Tension.   The tension, denoted $T(s, t)$, is the Lagrange multiplier associated to the inextensibility constraint $|\partial_s \mathbf{X}|^2 = 1$. The tension is intrinsically non local. The equation it solves is obtained by observing that $\partial_t |\partial_s \mathbf{X}|^2 = 0$ and a little patience; it reads

$$\partial_s^2 T - \frac{1}{2}|\partial_s^2 \mathbf{X}|^2 \, T = 3 \, E \, |\partial_s^3 \mathbf{X}|^2 + \frac{7}{2} E \, \partial_s^2 \mathbf{X}^{\mathsf{T}} \partial_s^4 \mathbf{X} - \frac{8\pi\nu}{2b} \, \partial_s \mathbf{X}^{\mathsf{T}} \mathbb{A}(\mathbf{X}, t) \, \partial_s \mathbf{X}, \tag{4.20}$$

with the boundary conditions $T = 0$ at $s = \pm \ell/2$. This equation is analogous to the Poisson equation satisfied by the pressure in incompressible fluid dynamics.

From Eq. (4.19), it appears that the dynamics of a given fiber depends on a single dimensionless parameter only; Specifically, the non-dimensional flexibility

$$\mathcal{F} = \frac{8\pi \, \nu \, \ell^4}{b \, E \, \tau_\eta} \tag{4.21}$$

measures the ratio between the elastic relaxation time associated to the fiber/fluid interaction $\tau_{el} = \frac{8\pi \nu \ell^4}{b \, E}$ and the fluid dissipative time-scale τ_η. [8] For small values of $\mathcal{F}$, the fiber is very rigid and behaves as a rod, while for large $\mathcal{F}$, it is very flexible and bends. In this second case, the dynamics is much richer: In particular, small values of E allow the fibers to experience buckling instabilities which alter their geometry. This mechanism is the focus of the next section.

---

[7]For a fluid with non-unit density the rhs should involve the dynamic viscosity instead of the kinematic viscosity, namely the pre-factor $\frac{1}{8\pi\rho\nu}$ instead of $\frac{1}{8\pi\nu}$.

[8]Alternatively, the flexibility is also the fourth power of the ratio between the length of the fiber and the elastic length $\ell_e = (bE\tau_\eta/8\pi\nu)^{1/4}$.

4.2 Numerical methods

To study the dynamics of small inextensible fibers in a fully-developed, stationary, homogeneous, isotropic turbulent flow, we use direct numerical simulations of the three-dimensional incompressible Navier-Stokes equations with 4096^3 grid points, which we described in Chapter 2 and whose essential parameters are summarized in Table 4.1.

N^3	ν	Δt	$\bar{\varepsilon}$	η	τ_η	u_{rms}	L	τ_L	R_λ
4096^3	10^{-5}	6×10^{-4}	3.8×10^{-3}	7.16×10^{-4}	0.051	0.19	1.86	9.68	731

Table 4.1: Numerical and physical parameters of the direct numerical simulation.

Once in a steady state, the flow is seeded with several millions of tracers. The tracer dynamics is then integrated jointly with the fluid, employing the same time step and using a cubic interpolation of the velocity field at the positions of the particles. The trajectories and the fluid velocity gradients along the Lagrangian paths are stored with a period $20\Delta t \approx 0.23\,\tau_\eta$ for a time duration of $63000\,\Delta t \approx 740\,\tau_\eta \approx 3.9\,\tau_L$.

Once the flow is computed and the trajectories are stored, we integrate the local slender body equation (4.19) along the tracer trajectories, using the finite-difference scheme proposed by Tornberg and Shelley (2004). The equation of motion is discretized using a second-order scheme in time, and second-order finite difference scheme in space, to estimate the spatial derivatives. In addition, to avoid temporal stiffness, the bending forces are treated implicitly and the tension equation ensuring that the fibers remain inextensible is treated explicitly. This scheme is also known as the semi-implicit *Adams-Bashforth* scheme (see Butcher and Goodwin (2008)).
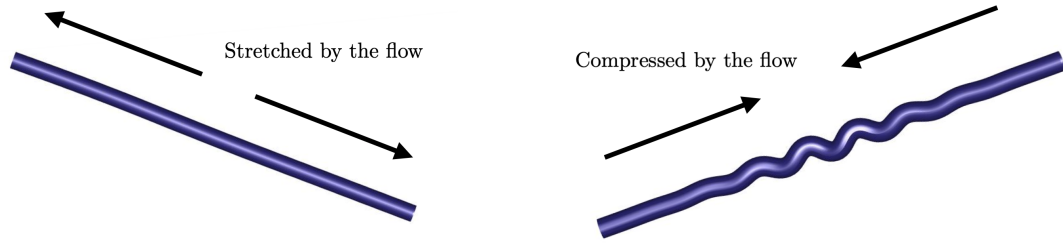
In our numerical simulations, the fiber is discretized with $n = 201$ points along the fiber arc-length s. The inextensibility constraint is enforced by a penalization method (see the details in Appendix C) . Time marching uses a Lagrangian time step $\Delta t_{\mathrm{fib}} = 2.5 \times 10^{-5}$. We use a linear interpolation in time to estimate the velocity gradient at a frequency higher than the output from the fluid simulation. Note that the time step required for the fibers is much smaller than that of the fluid. Indeed, we observed that, even by using a semi-implicit scheme, the problem remains particularly stiff when the bending modulus is small or, equivalently, when the fluid viscosity is large. As we will now see, these values of the parameters are of particular relevance. The full numerical code that integrated small fibers using turbulent data, is presented in Appendix C.

4.3 Results

The main outcome of our numerics is a detailed statistical study of the buckling instability of small inextensible fibers due to the turbulent fluctuations. The analysis is described in the work Allende et al. (2018) (attached at the end of this chapter) and published in *Physical Review Letters* in 2018. Our main observation is that fibers behave most of the time akin to stiff rods. Deviations to this configuration occur through very rare and intermittent buckling events, which we relate to the long-term Lagrangian correlations of the turbulent velocity gradients. We here provide additional statistics to substantiate this relation, and also comment on the dynamics of the fibers beyond the buckling instability.

4.3.1 What is the buckling instability?

The dynamics of the fibers involves the competition between the internal elasticity forces and the drag forces due to the fluid. Most of the time, those forces seem to act concomitantly in order to straighten the fiber, resulting in an unsophisticated stiff rod dynamics. In a turbulent environment, this configuration may however be destabilized because of the violent and intermittent fluctuations of the velocity gradients. In other words, the flow is likely to violently and suddenly compress the fibers, which in turn may buckle. This phenomenon is known as the **buckling instability**.

Figure 4.5: Illustration of the two configurations of the fiber, either stretched as in the left panel or buckled as in the right panel.

When fibers are in the rod-like configuration (see the left panel of Fig. 4.5), the elasticity forces are zero and the tangent vector is constant along the fibers, explicitly:

$$\partial_s \mathbf{X}(s,t) = \mathbf{p}(t) \quad \forall s \in [-\ell/2, \ell/2]. \tag{4.22}$$

In this case, the tension equation (4.20) is solved by the quadratic profile

$$T(s,t) = -\frac{2\pi\nu}{b}\,\dot{\gamma}(t)\left(s^2 - \frac{\ell^2}{4}\right). \tag{4.23}$$

Substituting this expression in the local slender body equation (4.19) yields

$$\frac{\mathrm{d}}{\mathrm{d}t}\mathbf{p} = \mathbb{A}\,\mathbf{p} - \dot{\gamma}\,\mathbf{p}, \quad \text{with} \quad \dot{\gamma}(t) = \mathbf{p}^\mathsf{T}\mathbb{A}(t)\,\mathbf{p}. \tag{4.24}$$

The latter is a specific form of a more general equation known as Jeffery's equation, describing the dynamics of straight inertialess ellipsoidal particles Here, the direction of $\mathbf{p}$ fully describes the configuration of the rod-like fiber. Its dynamics is prescribed by the action of the gradient tensor $\mathbb{A}$. The quantity $\dot{\gamma}$, known as the instantaneous shear rate, measures the stretching/compression of the fluid on the fiber: When $\dot{\gamma} > 0$ the fiber is stretched by the flow, and conversely when $\dot{\gamma} < 0$, the fiber is compressed by the flow. It means that in principle, buckling can only occur when $\dot{\gamma}$ is large and negative.

Note that when fibers are in a buckled state (see the right panel of Fig. 4.5) the elasticity forces become important and the dynamics has to be described by the local SBT model (4.19) in full.

4.3.2 Tracking-down buckling events

To get more quantitative insights about the buckling instability, we need to identify such events. We here discuss two different ways to achieve this task: monitoring either the bending energy along the fiber or the end-to-end length.
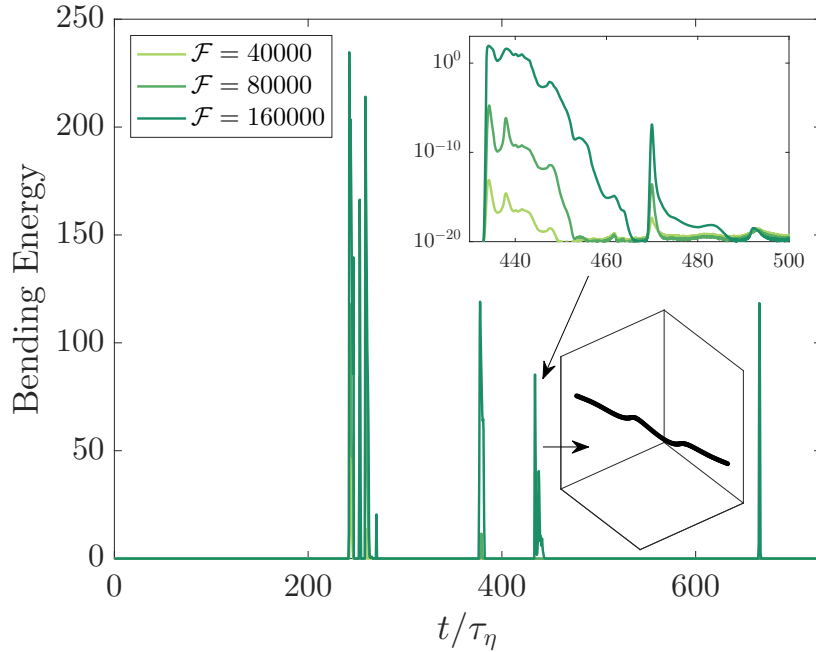
4.3.2.1 Using the bending energy

The bending energy relates to the curvature along the fiber: the curvier, the higher the bending energy. Mathematically, we measure the bending energy as

$$\mathcal{E}_{\text{bend}} = \frac{E}{2}\int_{-\ell/2}^{\ell/2}\kappa^2(s,t)\,\mathrm{d}s = \mathcal{E}_{\text{bend}}^{(0)}\left\langle (\kappa\ell)^2\right\rangle_\ell, \tag{4.25}$$

where $\kappa(s) = |\partial_s^2\mathbf{X}|$ is the fiber curvature, the angular bracket denotes a spatial average along the fiber and $\mathcal{E}_{\text{bend}}^{(0)} = E/(2\ell)$ is a reference energy. When the bending energy is vanishing, the fiber is completely straight; and when it is strictly positive, the fiber is buckled. Buckling instability is thus naturally characterized

by the bending energy becoming very large. We later measure the bending energy in units of $\mathcal{E}_{\text{bend}}^{(0)}$, hereby identifying the bending energy to the average squared curvature $\left\langle (\kappa \ell)^2 \right\rangle_\ell$. This non-dimensional quantity characterizes the buckled configuration of the fiber regardless of the value of its bending modulus E.
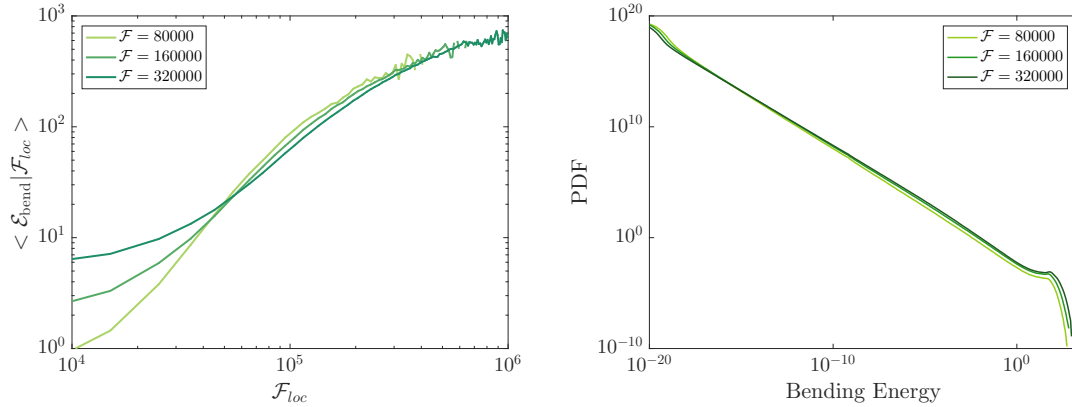
Figure 4.6: Main panel: Time evolution of the bending energy $\mathcal{E}_{\text{bend}}$ computed along a single turbulent tracer trajectory. Inset: Energy bending in a logarithmic scale for a single buckling event between $440 \lesssim t/\tau_\eta \lesssim 500$, together with the fiber shape at $t \approx 440$. The bending energy is expressed in units of $\mathcal{E}_{\text{bend}}^{(0)}$ and time is expressed in units of the Kolmogorov timescale τ_η. In these units, the large-eddy turnover time is $\tau_L \approx 190 \, \tau_\eta$.

Fig. 4.6 shows the time evolution of the bending energy for various arbitrary values of the non-dimensional flexibility $\mathcal{F}$, computed along a specific Lagrangian trajectory. We observe in Fig. 4.6 that bending events are sparse and their statistics are intermittent. Such events are separated by long periods during which the fiber is fully straight, up to numerical precision. For instance, one observes $\mathcal{E}_{\text{bend}} \approx 0$ in the time interval $0 \lesssim t/\tau_\eta \lesssim 200$. The inset of Fig. 4.6 highlights the bending energy for three values of the flexibility $\mathcal{F}$ in a logarithmic scale. Yet, one can also observe that the buckling events themselves depend on the specific value of the flexibility. For example, for the same realisation of the turbulent statistics, the larger the non-dimensional flexibility, the higher the bending energy. Moreover, the increases of energy follow the same trend, with a fast initial growth followed by a slow decay.

The bending energy is non-negative when the flow compresses the fiber and this corresponds to the shear rate $\dot{\gamma}$ taking negative values. To gain statistical insight on those events, a natural quantity to introduce is then the instantaneous flexibility. This positive quantity normalizes the values of the shear rate by the elastic relaxation time τ_{el} as

$$\mathcal{F}_{\text{loc}}(t) = |\dot{\gamma}(t)| \, \tau_{el} = \tau_\eta \, |\dot{\gamma}(t)| \, \mathcal{F}. \tag{4.26}$$

Fig. 4.7 shows the average of the bending energy for different values of the non-dimensional flexibility $\mathcal{F}$, conditioned on the values of $\mathcal{F}_{\text{loc}}$ (and on $\dot{\gamma}$ being negative). As expected, for small values of the compression, that is for small values of $|\mathcal{F}_{\text{loc}}|$, the conditional average bending energy is small and its shape apparently not universal. Beyond a critical value, though, it reaches an asymptotic behavior that is seemingly independent of the flexibility. This feature is apparent through the collapse of the three graphs, corresponding to three different values of the flexibility.

Figure 4.7: Left panel: Mean values of the bending energy conditioned to the negative values of the instantaneous flexibility $\mathcal{F}_{\text{loc}}$ for three different values of the non-dimensional flexibility $\mathcal{F}$. Right panel: Probability distribution function (PDF) of the bending energy for three different values of the non-dimensional flexibility $\mathcal{F}$. The bending energy is expressed in units of $\mathcal{E}_{\text{bend}}^{(0)}$.

One can remark that the average bending energy apparently saturates for high values of the compression. In our understanding, this saturation is the result of the energy balance between the work generated by the internal forces of the fiber and the fluid flow. The total energy of the fiber is not constant in time due to its interaction with the fluid and the work done by the fluid. Since the dynamics of such small fibers is found in the over-damped limit, the kinetic energy can be neglected. Using Eq. (4.3), we therefore obtain the energy balance

$$-\epsilon = \frac{d}{dt}\left(\langle\mathcal{E}_{\text{tension}}\rangle + \langle\mathcal{E}_{\text{bend}}\rangle\right). \tag{4.27}$$

This means that fibers in average give energy to the system, acting as a forcing on the fluid and the injected power exactly balances the energy dissipation rate of the turbulent flow (see Chapter 2). This also implies that the average bending energy cannot exceed the initial average energy of the fiber.

In addition, Fig. 4.7 shows the probability distribution of the bending energy for different values of the non-dimensional flexibility. It is seen that the fluctuations of the bending energy are apparently universal and scale as $P(\mathcal{E}_{\text{bend}}) \sim 1/\mathcal{E}_{\text{bend}}$ over ten decades of $\mathcal{E}_{\text{bend}}$. This scaling is apparently very robust and does not depend on the flexibility, at least when the latter is large enough. We note that the scaling does not prevent normalizability of the PDF. Indeed, for small $\mathcal{E}_{\text{bend}}$, the scaling breaks down and this reflects the non-universality of the onset of the buckling instability. For large $\mathcal{E}_{\text{bend}}$, the scaling needs to break down: From the energy balance (4.27), the average internal energy of the fiber is decreasing with time. Hence, the average bending energy is necessarily finite, and the scaling $P(\mathcal{E}_{\text{bend}}) \sim 1/\mathcal{E}_{\text{bend}}$ cannot hold in the limit $\mathcal{E}_{\text{bend}} \to \infty$.
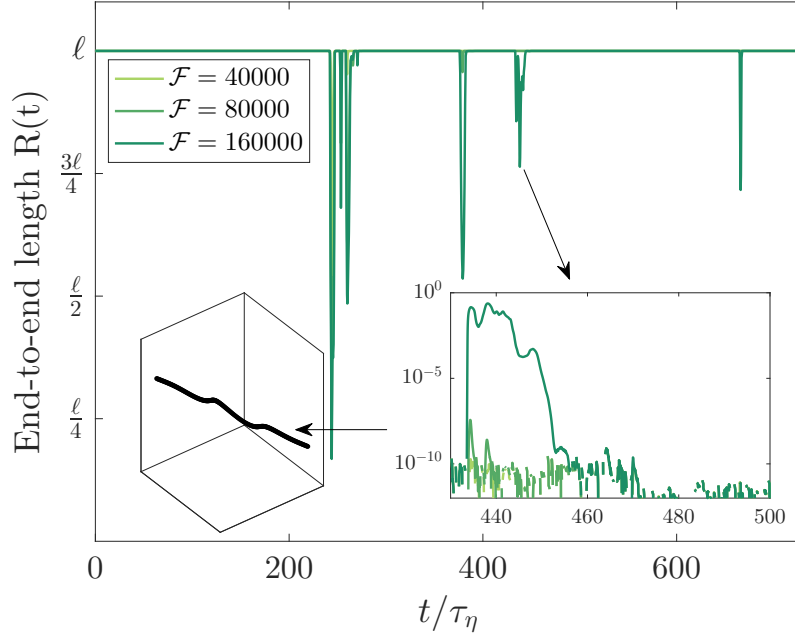
4.3.2.2 Using the end-to-end length

Beyond the bending energy, the end-to-end length is also a very simple manner to measure the buckling of a fiber. This quantity is defined as the distance between the two ends of the fiber, namely

$$R(t) = |\mathbf{X}(\ell/2, t) - \mathbf{X}(-\ell/2, t)|. \tag{4.28}$$
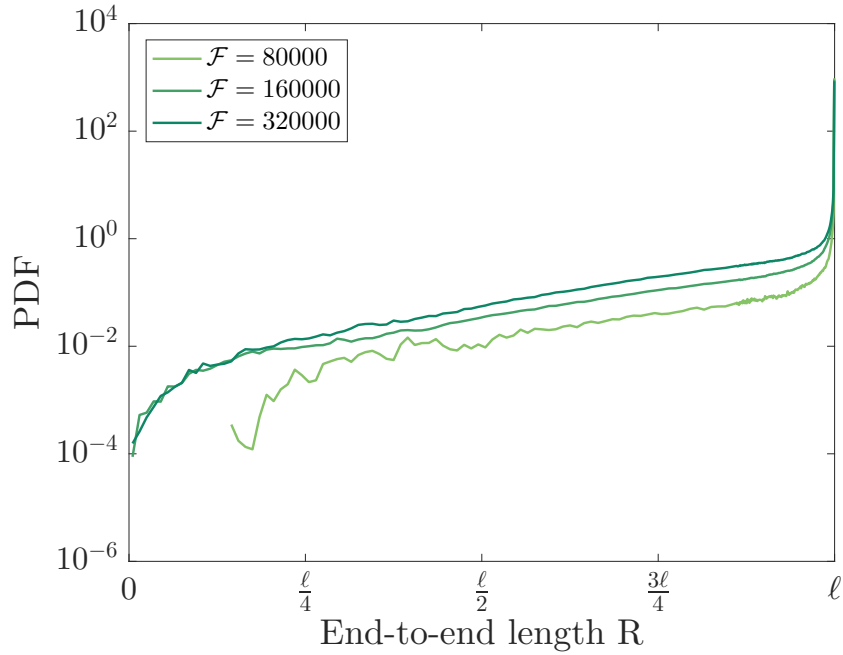
Clearly, when $R = \ell$ the fiber is totally stretched, and it is buckled when $R < \ell$. The main panel of Fig. 4.8 shows the time evolution of the end-to-end length along a single trajectory, for various non-dimensional flexibilities $\mathcal{F}$. This reveals the same phenomenology as previously seen using the bending energy: fibers are most of the time stretched and bending events are sparse and intermittent. The inset of

Fig. 4.8 highlights a single event of buckling, where the length $1 - R(t)$ is now displayed using a logarithmic scale.

Figure 4.8: Time evolution of the end-to-end length $R(t)$ computed along a single turbulent tracer, for three different values of the non-dimensional flexibility $\mathcal{F}$. A single event is represented in the inset, where the length $1 - R(t)$ is plotted for times between $440 \lesssim t/\tau_\eta \lesssim 500$, together with the fiber configuration at $t \approx 440$. Time is here rescaled by the Kolmogorov timescale τ_η. Recall that in these units, the large-eddy turnover time is $\tau_L \approx 190\,\tau_\eta$.

Fig. 4.9 shows the probability distribution of the end-to-end length, obtained by averaging over both time and the fibers, for different values of the non-dimensional flexibility. As expected, the probability is maximal for values equal to the length of the fiber ℓ, because the fibers spend most of their time in a stretched configuration. The probability decreases with the end-to-end length, meaning that the probability of achieving very buckled configurations is small. In addition, and in accordance with the intuition, we observe that it is more likely for fibers with larger flexibilities to attend small values of R.

Figure 4.9: Probability distribution function (PDF) of the end-to-end length R for three different values of the non-dimensional flexibility $\mathcal{F}$.

4.3.3 Buckling in turbulence: an activated process?

In order to relate the statistics of buckling events with the turbulent fluctuations, we need to define buckling in a more quantitative fashion. For simplicity and because it exhibits patterns qualitatively similar to that of the bending energy, we here choose to work with the end-to-end length. To identify the buckling events, we introduce threshold values R_c. The fibers are then unambiguously considered as "buckled" when $R(t) < R_c$, and we define the probability of buckling Φ_c as the fraction of time spent by the fiber in such a state. Left panel of Fig. 4.10 shows the buckling probability as a function of the non-dimensional flexibility for different thresholds R_c. Qualitatively, one can see that choosing different thresholds does not modify the overall behavior of the buckling probability. The main feature displayed in the left panel of Fig. 4.10 is the fact that the buckling probability behaves for large values of the flexibility $\mathcal{F}$ as

$$\Phi_c \propto e^{-(\mathcal{F}_c^\star/\mathcal{F})^\alpha}, \text{with} \quad \alpha \simeq 0.50. \tag{4.29}$$
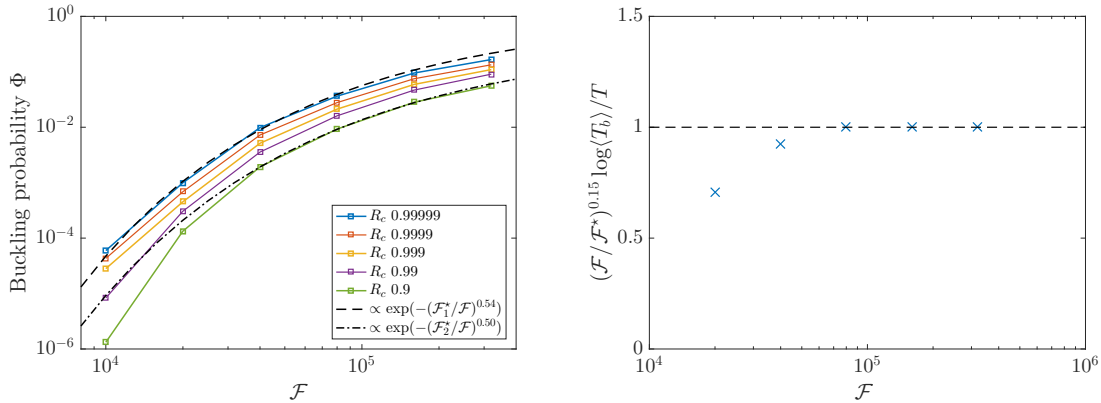
This behavior is very reminiscent of an Arrhenius law (see for example Eyring (1935); Laidler (1984)), which describes the kinetic rate of chemical reactions as being proportional to the factor $e^{-(E_a/k_BT)}$. In this analogy, the quantity $(\mathcal{F}_c^\star)^\alpha$ plays the role of the activation energy and relates to the buckling threshold. The flexibility $\mathcal{F}^\alpha$ has a catalytic role akin to the temperature: high values of $\mathcal{F}^\alpha$ enhance the buckling rate.

While heuristic, this analogy motivates further investigation. In particular it raises the question as to whether the buckling statistics could perhaps be modeled in terms of a (simple) stochastic activated process, similar in flavour to the Kramer's escape problem, which describes the jumping rate of an over-damped Brownian particle in a double-well potential (see Appendix D for more details). The right panel of Fig. 4.10 shows the statistical behavior of the inter-buckling time T_b for the prescribed threshold $R_c = 0.999\,\ell$. It features the behavior:
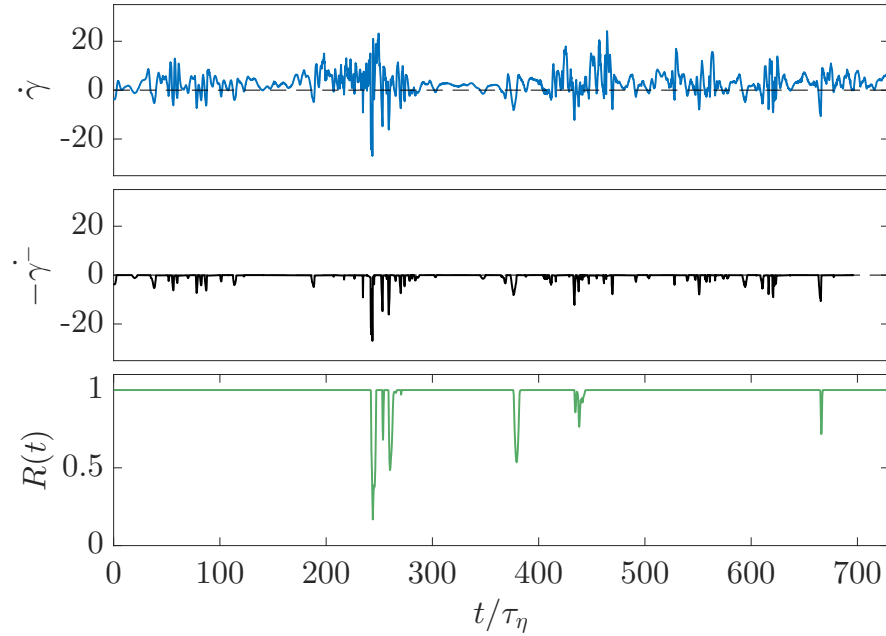
$$\langle T_b \rangle \propto e^{(\mathcal{F}_c^\star/\mathcal{F})^\beta}, \text{with} \beta \simeq 0.15, \tag{4.30}$$

The fact that the exponent $\beta \simeq 0.15$ that stretches the exponential is different from the exponent $\alpha \simeq 0.50$ measured for the buckling rate suggests that buckling by turbulent fluctuations cannot be simply modeled by the standard white-noise Kramer's problem described in Appendix D. Modeling of such anomalous Arrhenius

law requires to understand better the property of the turbulent fluctuations, which here act as an underlying triggering noise with non-trivial time correlations.

Figure 4.10: Left panel: Buckling probability Φ as a function of the non-dimensional flexibility $\mathcal{F}$. The different curves show the fraction of time for which $R(t) < R_c$, together with the fit (4.29) and (4.30) in dashed line. Right panel: Compensated plot for the average time $\langle T_b \rangle$ between two consecutive buckling events, showing the law (4.30).

Figure 4.11: Top panel: instantaneous shear rate along one turbulent tracer trajectory. Middel panel: compressive component of the shear rate $-\dot{\gamma}^-$ along the same trajectory. Bottom panel: End-to-end length along the same trajectory for $\mathcal{F} = 1.6 \times 10^5$.

The natural "turbulent observable" to investigate is the instantaneous shear rate $\dot{\gamma}$ introduced in Eq. (4.24) and which measures how fibers are stretched and compressed by the velocity gradient of the turbulent flow. As shown in Fig. 4.11, the shear rate is a very intermittent quantity. Fig. 4.12 shows the probability distribution function (PDF) of $\dot{\gamma}$: the latter is highly non-Gaussian and displays stretched-exponential tails with exponent ≈ 0.5. This means that the fibers have non zero probability to be subject to extreme shear from the surrounding fluid environment, and in particular to extreme compression. To analyze

the compressive events that may trigger buckling, we define the flow compression as

$$\dot{\gamma}^-(t) = \max(-\dot{\gamma}, 0).$$

It is apparent from Fig. 4.11 that bursts of the compression rate highly correlate with the buckling events as monitored by the end-to-end length.
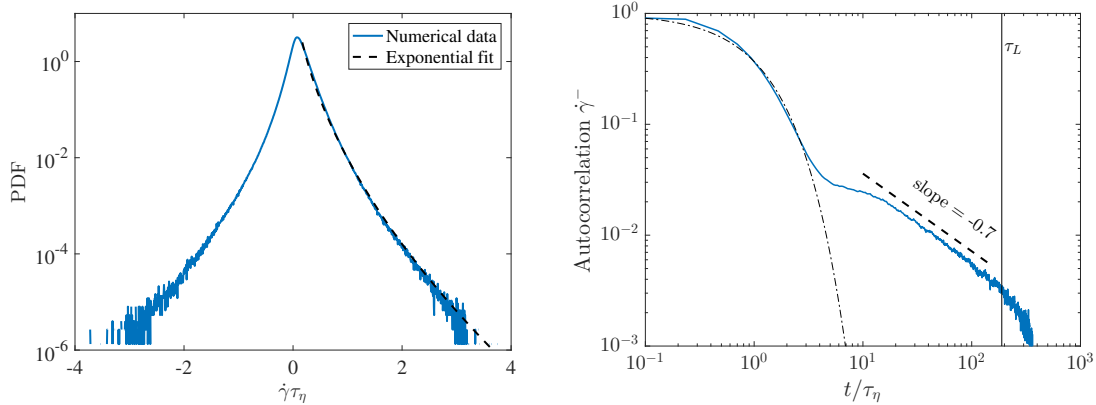
The statistics of the turbulent compression are revealed by computing its auto-correlation

$$\rho(t) = \text{cov}\left(\dot{\gamma}^-(t), \dot{\gamma}^-(0)\right) / \text{Var}(\dot{\gamma}^-). \tag{4.31}$$

This quantity displays two regimes: For times of the order of the Kolmogorov timescale, the auto-correlation is well approximated by an exponential function, and we estimate the corresponding integral correlation time as

$$\tau_- = \int \rho(t)dt \approx 2.8\tau_\eta. \tag{4.32}$$

This describes the correlation between pikes in the same compression burst. At larger times the exponential behavior breaks down, and the autocorrelation regime decreases at a much slower rate, revealing long-time correlation between the different bursts.

Figure 4.12: Left panel: Probability distribution function (PDF) of the instantaneous share rate $\dot{\gamma}$, where its mean value is $\langle\dot{\gamma}\rangle \approx 0.11/\tau_\eta$ and its standard deviation is $\approx 0.2/\tau_\eta$. The dashed line represent the function $\propto exp(A\,(\dot{\gamma}\,\tau_\eta)^{0.54})$ with $A \approx 9$. Right panel: Autocorrelation of the negative components of $\dot{\gamma}$, calculated as $\rho(t) = \text{cov}\left(\dot{\gamma}^-(t), \dot{\gamma}^-(0)\right) / \text{Var}(\dot{\gamma}^-)$. The dashed-dotted line stands for $\exp(-t/\tau_\eta)$. The dashed line shows a slope -0.7. The large-eddy turnover time is shown with the vertical solid line. Time is here rescaled by the Kolmogorov timescale τ_η.

This behavior akin to the so-called on-off intermittency phenomenon (Platt et al., 1993) drives the buckling statistics of fibers involved in a turbulent environment. Therefore, quantitative modeling strategies involving stochastic processes should use this coloured statistics as inputs. This is probably the reason why the Arrhenius law displays anomalous features. While we have not attempted to write down an effective toy model to recover those exponents, this constitues a very natural perspective to go beyond the scope of the present thesis.

4.3.4 Beyond buckling instability
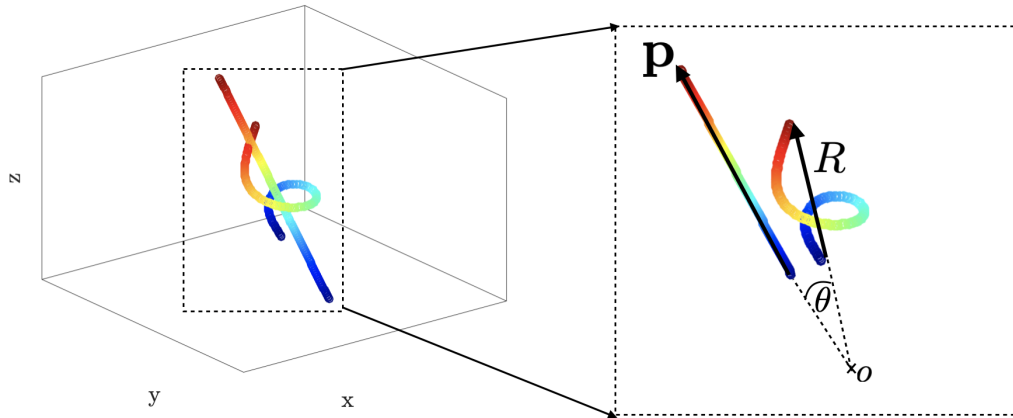
The previous analysis was focused on the buckling instability, which as we will see in the next Chapter is key to understanding the onset of fragmentations. Apart from compressive events, the fiber also experiences effects of vortical motion. This leads to other physical effects, including non-trivial statistics of alignments for the orientations of fibers depending on their flexibility. The combination of flexibility and rotation also yields "super-buckling" events , that allow the fibers to switch their orientations differently than rods. Our aim here is to briefly describe each of those two physical phenomena.

4.3.4.1 Alignement of fibers

We have observed that buckling instabilities are the result of the compression exerted by the flow. As previously described, fibers feel not only the shear but also the rotation induced by the turbulent gradient. Hence, a natural question to ask relates to how the rotation affects the dynamics of our small fibers. It is known from previous work that stiff-rods, have a preferential alignment with the fluid stretching (see Pumir and Wilkinson (2011); Ni et al. (2014)), somewhat similarly to what was also observed for the turbulent vorticity vector $\omega = |\nabla \times \mathbf{u}|$ by Xu et al. (2011). This means that small rod-like particles should be preferentially aligned with the turbulent vorticity vector. To quantify deviations from this behaviour due to the presence of flexibility, it is therefore natural to use rods as a reference dynamics that we can compare to the full fibers'. Since fibers remain most of the time stretched as rods, they are also expected to be preferentially aligned under with the main direction of fluid stretching. In this configuration, both fibers and rods are then rotating with an angular speed given by the vorticity of the turbulent flow. The dynamics of the fiber is then indistinguishable from that of a rod, whose direction $\mathbf{p}(t)$ initially coincides with the direction of the end-to-end vector

$$\mathbf{R}(t) = \mathbf{X}(\ell/\mathbf{2}, \mathbf{t}) - \mathbf{X}(-\ell/\mathbf{2}, \mathbf{t}) \tag{4.33}$$

Such a rod, we later refer to as the tangent rod. Conversely, when fibers buckle the coupling between the two dynamics seems to be lost, and deviations exist between the end-to-end vector and the direction of the tangent rod $\mathbf{p}(t)$, as can be observed in Fig. 4.13.

Figure 4.13: Snapshot of a fiber $\mathbf{X}(s)$ with flexibility $\mathcal{F} = 1.6{\times}10^5$ together with the direction $\mathbf{p}$ of its tangent rod. The end-to-end vector $\mathbf{R}$ and the tangent rod orientation $\mathbf{p}$ have an angle θ between them.

To quantify those, we introduce the **tangent angle** θ between the orientation $\mathbf{p}$ of the tangent rod and the end-to-end vector $\mathbf{R}$ of the fiber, and measured as:

$$\theta = \cos^{-1}\left(\frac{\mathbf{R} \cdot \mathbf{p}}{|R|\,|\mathbf{p}|}\right). \tag{4.34}$$

The probability distribution function of the tangent angle is shown in Fig. 4.14.
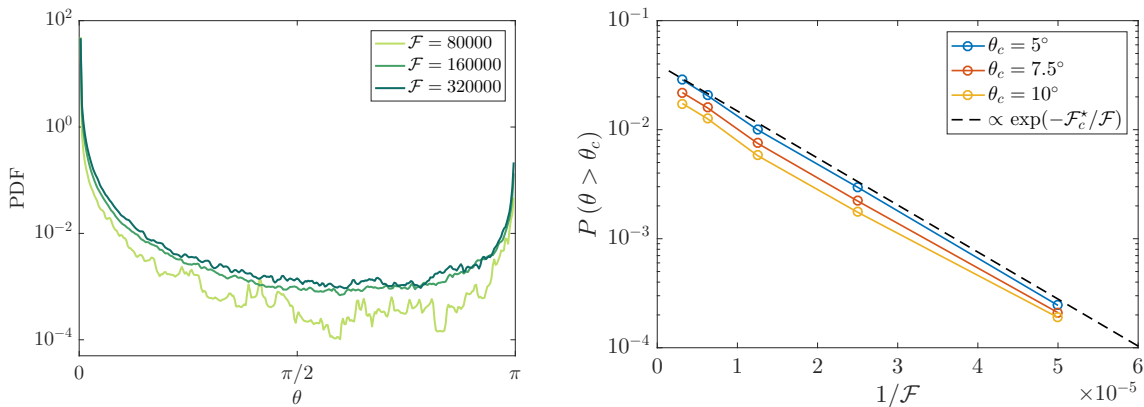
As expected, the peak value of the distribution is found at $\theta = 0$, that is: the fibers and their tangent rods are most of the time perfectly aligned. While the probability sharply decreases as θ increases up to $\pi/2$, the probability of observing "misalignments" is not zero. In addition and quite intuitively, fibers with a small values of the flexibility $\mathcal{F}$ are less likely to achieve large values of θ. The surprising feature of the distribution is however the presence of another sharply pronounced peak at $\theta = \pi$. This means that the fiber has an opposite orientation to its tangent rod. Those events can only be attributed to a mechanism allowing

the fibers to switch direction using their flexibility, and this mechanism we call a **super-buckling event**. We will explore in the next section the statistics of those events more in details.

For now, let us comment slightly further on the statistics of the misalignments of the fibers, by defining the probability $P(\theta > \theta_c)$ that the tangent vector exceeds a prescribed threshold θ_c. Fig. 4.14 shows, that similar to what was previously observed for the buckling statistics, an Arrhenius law appears, that is

$$P(\theta > \theta_c) \propto \exp(-\mathcal{F}_c^\star/\mathcal{F}). \qquad (4.35)$$
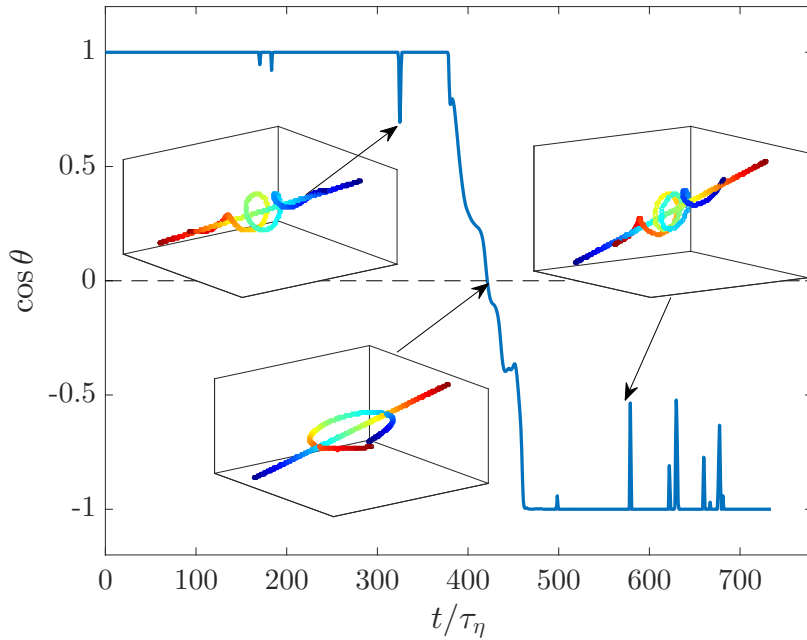
Again the flexibility $\mathcal{F}$ plays the role of a temperature but this time, we point out that the law is NOT anomalous. This means that the misalignment process can probably be modeled as a standard Poisson process, and seems therefore blind to the intermittent correlations of the gradient statistics. This is a surprising observation, that we do not fully explain at this point. This means that the Lagrangian statistics of the rotation rate are very different than that of $\dot{\gamma}^-$.

Figure 4.14: Left panel: Probability density functions of the tangent angle θ, for three values of the non- dimensional flexibility. Right panel: Arrhenius law for probability that the tangent angle exceeds the threshold θ_c as a function of the non-dimensional flexibility $\mathcal{F}$. The fit (dashed line) show the behavior $\propto \exp(-\mathcal{F}_c^\star/\mathcal{F})$, with $\mathcal{F}_c^\star$ a coefficient measured empirically.

4.3.4.2 Super Buckling instability

A super-buckling event is defined as a switch in the fiber direction, measured by the tangent angle exceeding $\pi/2$, obtained through a strong compression by the flow. One can understand this mechanism as follows: When $\dot{\gamma}$ becomes sufficiently strong and negative the fiber is completely buckled and its relaxation then occurs in the opposite direction. Fig. 4.15 shows this behavior, by monitoring the cosine of tangent angle. When $\cos\theta = 1$, the fiber is fully stretched and aligned with the flow; for values between $0 < \cos\theta < 1$ the fiber is buckled but is still aligned with the direction of the tangent rod $\mathbf{p}$; when $\cos\theta < 0$, the fiber is misaligned, and this signals a super-buckling event.

Figure 4.15: Time evolution of the cosine of the tangent angle $\cos\theta$ computed along a single trajectory, using the non-dimensional flexibility $\mathcal{F} = 1.6{\times}10^{5}$. The three small boxes show the instantaneous configurations of the fiber and of the tangent rod. The colormap allows to identify the two ends of the objects: from blue for the initial points to red for the end points along the fibers and rods.
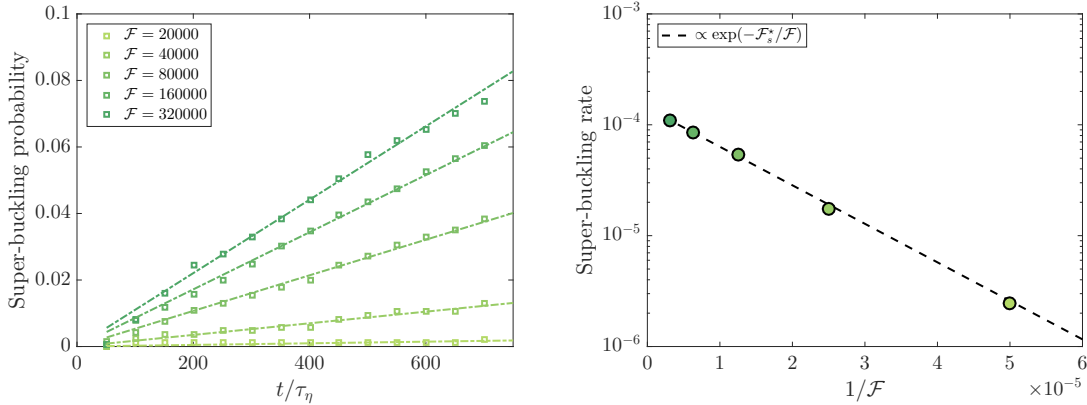
Obviously, the super-buckling events are extremely rare. To give an estimate of their probability of occurence, we show in the left panel of Fig. 4.16 the super-buckling probability, measured as:

$$P_{\circlearrowleft} = \frac{\#\,\text{trajectories for which}\quad \cos\theta < 0 \text{ anytime between } 0 \text{ and } t}{\#\ \text{trajectories}}. \tag{4.36}$$

One observes that $P_{\circlearrowleft}(t)$ grows linearly in time. This means that the rate

$$\lambda_{\circlearrowleft}(\mathcal{F}) = P_{\circlearrowleft}/t \tag{4.37}$$

measures the number of super-buckling event per unit of time. It is a constant in time and depends on the flexibility. The right panel of Fig. 4.16 measures this rate in units of τ_{η}. The first observation is that the rate is very low! For example, for the fibers with the highest flexibility, the chances are less than 0.01% that they will experience a super-buckling event during an interval of time τ_{η}. The second observation, is that this kinetic again follows an Arrhenius law. Similar to the law observed for the misalignments, it is not anomalous. This means again, that while very rare, the super-buckling events can be described stochastically in terms of a standard activated process. The mechanisms that conspire into producing such super-buckling events are still not totally clear, but seems to be the result of a strong misalignement with the vorticity direction of the flow, combined with a strong compression by the flow.
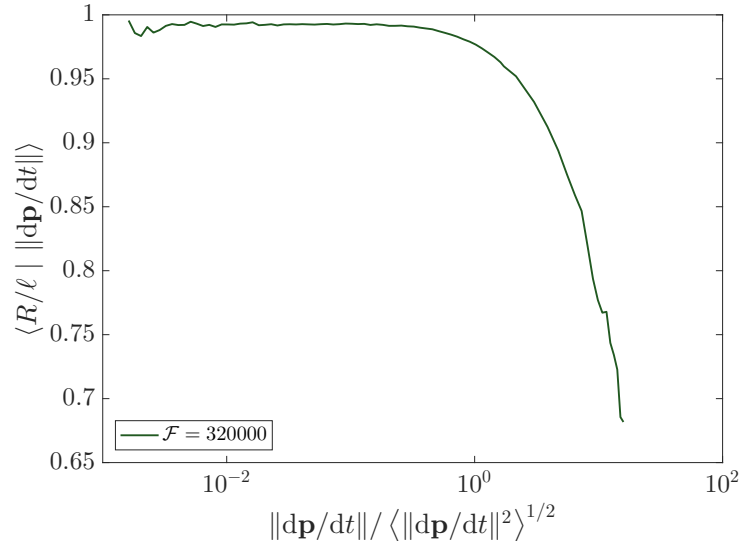
Figure 4.16: Left panel: Super buckling rate $\lambda_{\cup}$ as a function of the time for various values of the flexibility. Right panel: Super buckling time as a function of the flexibility $\mathcal{F}$.

To conclude this section, let us here emphasize that the super-buckling mechanism is very different from the tumbling of rigid rods. From a dynamical point of view, this is confirmed by looking at the values taken by the end-to-end length R, when conditioned on the tumbling rate

$$\dot{\phi} = \left\| \frac{d\mathbf{p}}{dt} \right\|, \tag{4.38}$$

measuring the angular velocity at which the tangent rods rotate.

Fig. 4.17 shows the behaviour of the conditional average of the end-to-end length for one specific value of the flexibility. It is seen, that for small values of the tumbling rate the fibers are stretched. Conversely, when the tumbling rate increases the fiber are in a buckled configuration. As previously mentioned, the rods rotate with an angular velocity given by the vorticity of the flow. High values of the tumbling rate therefore indicate that the fibers inside a high vorticity region, where the fluid is highly fluctuating, and where gradients may conspire to bend the fiber.
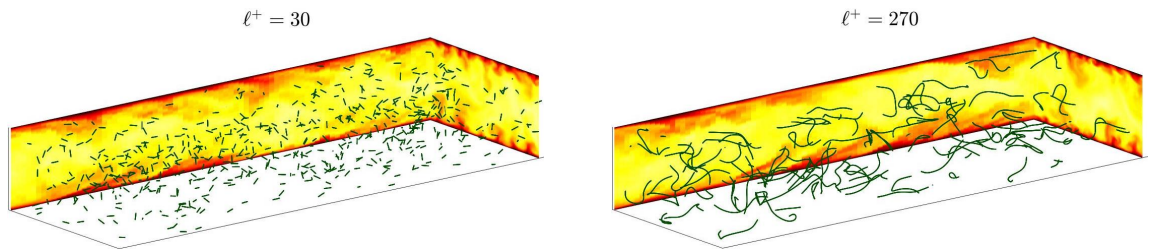
Figure 4.17: End-to-end length conditioned on the tumbling rate of the tangent rod $\mathbf{p}$.

4.4 Perspectives and ongoing work

Remarks.   We have described in details the dynamics of small fibers passively transported by a turbulent flow. We found that the dynamics of such fibers are determined by local turbulent fluctuations. Our most salient observation is that the coupling between the fibers and turbulence can be phenomenologically modeled in terms of various activation processes. This is the case for the buckling instability, where the buckling rate ressembles an anomalous Arrhenius law. This is also the case for the statistics of the misalignments, described through the tangent angle, and the super-buckling rates. The common feature of those laws is the role played by the flexibility of the fibers, which is akin to that of a temperature in chemical kinetics. The origin of the anomalous Arrhenius law featuring a stretched exponential behavior is to our understanding related to the long-time correlations of the compressive shear rate, and more generally to the Lagrangian intermittency of the shear rate. While unexplored in the present thesis, we believe that our work paves the way for stochastic modelling of the buckling instability in terms of non-homogeneous Poisson processes, and or activated processes driven by non-Brownian noise.

For the sake of simplicity, we have focused on one of the simplest framework of fiber-fluid interactions, namely the local slender body theory. As exposed in details in this chapter, this approach relies on a series of approximations, whose validity could be put into question, were we to extend our description beyond the case of small massless inextensible fibers. In order to study influence of flexibility on preferential sampling of fibers, one may for example wish to include inertial response. In principle, and apart from potential issue with numerical timestepping, this would not require too much modeling effort: it would suffice to simply relax the over-damped approximation. In another line of research with obvious range of applications, one could wish to study the properties of long fibers coupled with turbulence. In that case, several approximations might break down including the relevance of the Stokes equations to provide a handful SBT approach. Besides, the use of the local approximation might become questionable if the fibers are allowed to become severely entangled.

Ongoing work.   To explore the interaction between large flexible fibers and walls, we study fibers into a turbulent channel flow configuration. Two snapshots of the fiber distribution with different lengths are shown in Fig. 4.18. At a qualitative level, one observes that short rigid fibers remain very straight, while long flexible fibers bend patter intricate ways. Close to the wall, fibers tend to align with the mean flow close, and long fiber being moreover stretched when they penetrate the viscous layer. In the bulk, short fibers orientate randomly while long fibers seem to weakly display a weak preferential alignment with the mean flow.

$$\ell^+ = 30 \qquad\qquad\qquad\qquad \ell^+ = 270$$
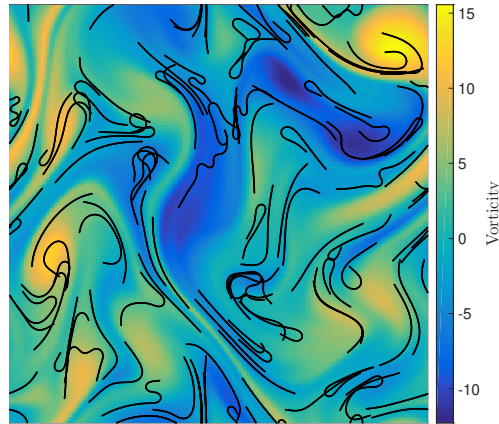
Figure 4.18: Instantaneous distributions of fibers with length $\ell^+ = 30$ (left) and $\ell^+ = 270$ (right). The coloured planes shows the streamwise component of the fluid velocity in the planes $x = L_x$ and $z = 0$. The fluid flows from left to right.

Preliminary results show that fibers drift away from the boundaries and preferentially concentrate in the bulk of the flow. The underlying mechanisms involve strong deformations of the fibers when they are located rather close to the wall, at a distance comparable or smaller than their lengths. During such events, the fibers effectively bounce away from the boundaries and migrate toward the bulk of the flow. As a consequence of this concentration of fibers in the flow bulk, we moreover find that fibers are more efficiently transported by the flow. They indeed spend more times in regions where the mean velocity is larger, leading to higher fluxes than those of the fluid. A fine understanding on the mechanisms at play relating the migration statistics to the rheology of the fibers is still elusive, and in particular when one studies fibers, whose lengths exceed the channel width. Finally, one could consider more realistic scenarios to more faithfully account

for the interactions between the fibers and the wall, including physical effects such as lubrication forces and boundary attachment. A longer-term perspective relates to modeling intra-fiber or fiber-fiber interactions. Experiments show that fibers can knot and form entangled aggregates, suggesting somes effects in their transport properties. The stastical analysis of the topologies of such intricate fibers could probably prove a fruitful and open field of study.

In addition, to explore the relevance of the local SBT beyond the description of small fibers, one could rely on 2D turbulent flows, hereby allowing for some light systematic studies comparing the skills of the local SBT to reproduce the statistics of specific mechanical models of fibers, such as the elastic chains studied by Picardo et al. (2018). To illustrate this possibility, we reproduced the results of Picardo et al. (2018) using a 2D local slender body theory [9], and numerical simulation of a 2D turbulent flow of 256^2 collocation points within a periodic box. Like the elastic chains used in Picardo et al. (2018), our fibers are inertialess and passively transported by the flow and with a fiber length of the order of the inertial range. Fig. 4.19 shows that at a qualitative level the local slender body description reproduces the main physical observation of Picardo et al. (2018): fibers buckle within the vortex zones and stretch outside. The essential differences between our continuous model and the elastic chains is the presence of the inextensibility constraint, and the fact the SBT relies on a small deformation hypothesis.

Figure 4.19: Snapshots of fibers immersed in a two-dimensional turbulent flow. Fibers have an elasticity of $\mathcal{F} = 5000$ and a length of $\ell_{fiber} = 1.5$ equal to one quarter of the domain edge.

While further investigations of quantitative mathematical models of fibers coupled with turbulence is a promising field of possibilities, we here will follow our journey with the local SBT, in order to characterize one of the dramatic consequence of fibers being flexible in a highly fluctuating environment: If brittle, they can break! The characterization of fragmentation is the focus of our next chapter.

---

[9] Naturally the local SBT has to be slightly modified in 2D, because the Stokes paradox prevents even small passive fibers not to alter the background flow, when relying on the Stokes equation for the fluid-fiber interaction. To fix this issue, one needs to replace the 2D Stokeslests by a so-called 2D Oseenlets, solving the singular Oseen equation

$$\nabla p - \nu \nabla^2 \mathbf{u} + \mathbf{u}_0 \cdot \nabla \mathbf{u} = \mathbf{f_0}\delta(\mathbf{x}) \quad \text{and} \quad \nabla \cdot \mathbf{u} = 0,$$
$$\text{with boundary condition } \mathbf{u}(\mathbf{x}) = 0 \quad \text{for} \quad \|\mathbf{x}\| \to \infty. \tag{4.39}$$

4.5   Reproduction of the paper:
"Stretching and Buckling of Small Elastic Fibers in Turbulence"

We here reproduce the paper "Stretching and Buckling of Small Elastic Fibers in Turbulence" published in Physical review letters, that was co-authored with Jérémie Bec and Christophe Henry.

Stretching and Buckling of Small Elastic Fibers in Turbulence

Sofía Allende, Christophe Henry, and Jérémie Bec

Université Côte d'Azur, CNRS, OCA, Laboratoire J.-L. Lagrange, 06300 Nice, France

Small flexible fibers in a turbulent flow are found to be as straight as stiff rods most of the time. This is due to the cooperative action of flexural rigidity and fluid stretching. However, fibers might bend and buckle when they tumble and experience a strong enough local compression. Such events are similar to an activation process, where the role of temperature is played by the inverse of Young's modulus. Numerical simulations show that buckling occurs very intermittently in time. This results from unexpected long-range Lagrangian correlations of the turbulent shear.

Elongated colloidal particles are essentially subject to three forces: bending elasticity, thermal fluctuations, and viscous drag with the suspending flow. An important and well-studied case is that of infinitely flexible polymers for which only two effects compete: coiling promoted by thermal noise and stretching induced by fluid shear. Relaxation to equilibrium is then fast enough to give grounds for adiabatic macroscopic models, such as elastic dumbbells [1,2], often used to investigate the rheology of polymer suspensions [3]. Much less is known about when the thermal fluctuations are negligible but bending elasticity becomes important. This asymptotics is relevant to describe macroscopic particles, such as cellulose fibers in the paper making industry [4], or diatom phytoplankton colonies [5] that significantly participate in the CO_2 oceanic pump [6]. In principle, without molecular diffusion there is no coiling. Furthermore, bending elasticity and flow stretching act concomitantly to straighten the fiber, suggesting an unsophisticated stiff rod dynamics. However, most natural or industrial flows are turbulent. They display violent and intermittent fluctuations of velocity gradients, susceptible of destabilizing a straight configuration by buckling the fiber [7].

We are interested in elongated, deformable, nondiffusive particles passively transported by a turbulent flow. We aim at quantifying two aspects: first, the extent to which their dynamics can be approximated as that of rigid rods and, second, the statistics of buckling. For that purpose, we focus here on the simplest model, the *local* slender-body theory, which describes the motion of an inextensible Euler-Bernoulli beam immersed in a viscous fluid. In the limit of zero inertia, the fiber velocity is obtained by equating the drag, the tension, and the bending elasticity (see, e.g., Ref. [8]). The dynamics of a fiber with cross section a and length ℓ is then

$$\partial_t X = u(X, t) + \frac{c}{8\pi\rho_f\nu}\mathbb{D}[\partial_s(T\partial_s X) - E\partial_s^4 X],$$

$$|\partial_s X|^2 = 1, \quad \text{with} \quad \mathbb{D} = \mathbb{I} + \partial_s X \partial_s X^\mathsf{T}, \qquad (1)$$

in the asymptotics $c = -[1 + 2\log(a/\ell)] \gg 1$. Here, $X(s, t)$ is the spatial position of the point indexed by the arc length coordinate $s \in [-\ell/2, \ell/2]$, u is the velocity field of the fluid, ν its kinematic viscosity, ρ_f its mass density, and E denotes the fiber's Young modulus. The tension $T(s, t)$, which satisfies $T|_{\pm\ell/2} = 0$, is the Lagrange multiplier associated to the fiber's inextensibility constraint. Equation (1) is supplemented by the free-end boundary conditions $\partial_s^2 X|_{\pm\ell/2} = 0$ and $\partial_s^3 X|_{\pm\ell/2} = 0$.

The considered fibers are much smaller than the smallest active scale of the fluid velocity u. In turbulence, this means $\ell \ll \eta$, where $\eta = \nu^{3/4}/\varepsilon^{1/4}$ is the Kolmogorov dissipative scale, $\varepsilon = \nu\langle\|\nabla u\|^2\rangle$ being the turbulent rate of kinetic energy dissipation. In this limit, the particle motion is to leading order that of a tracer and $d\bar{X}/dt = u(\bar{X}, t)$, where $\bar{X}(t)$ denotes its center of gravity. The deformation of the fiber solely depends on the local velocity gradient, so that $u(X, t) \approx u(\bar{X}, t) + \mathbb{A}(t)(X - \bar{X})$, where $\mathbb{A}_{ij}(t) = \partial_j u_i(\bar{X}, t)$. The dynamics is then fully described by two parameters: the fluid flow Reynolds number Re, prescribed very large, and the nondimensional fiber flexibility, defined as

$$\mathcal{F} = \frac{8\pi\rho_f\nu\ell^4}{cE\tau_\eta}, \qquad (2)$$

where $\tau_\eta = \sqrt{\nu/\varepsilon}$ is the Kolmogorov dissipative time and quantifies typical values of the turbulent strain rate. The parameter $\mathcal{F}$ can be understood as the ratio between the timescale of the fiber's elastic stiffness to that of the turbulent velocity gradients. At small $\mathcal{F}$, the fiber is very rigid and always straight. On the contrary, for large $\mathcal{F}$ it is very flexible and might bend. Clearly, if the fiber had inertia, the dynamics would involve its material density and depend on an extra parameter (e.g., the Stokes number). This would probably affect bending properties.

In the straight configuration, the tangent vector is constant along the fiber, i.e., $\partial_s X = \mathbf{p}(t)$, and follows Jeffery's equation for straight ellipsoidal rods [9]:

$$\frac{d\mathbf{p}}{dt} = \mathbb{A}\mathbf{p} - (\mathbf{p}^{\mathsf{T}}\mathbb{A}\mathbf{p})\mathbf{p}. \qquad (3)$$

This specific solution to Eq. (1), which is independent of s, is stable when the fiber is sufficiently rigid. However, it becomes unstable when increasing flexibility, or equivalently for larger fluid strain rates. As shown and observed experimentally in two-dimensional velocity fields, such as linear shear [7,10,11] or extensional flows [12–14], this instability is responsible for a buckling of the fiber. This occurs when the elongated fiber tumbles [15,16] and experiences a strong enough compression along its direction. This compression is measured by projecting the velocity gradient along the rod directions, i.e., by the stretching rate $\dot{\gamma} = \mathbf{p}^{\mathsf{T}}\mathbb{A}\mathbf{p}$. In turbulence, buckling thus occurs when the instantaneous value of $\dot{\gamma}$ becomes large with a negative value (compression).

To substantiate this picture, we have performed direct numerical simulations of three-dimensional homogeneous isotropic turbulence. The flow is obtained by integrating the incompressible Navier-Stokes equations using the LATU spectral solver with 4096^3 collocation points and a force that keeps kinetic energy constant in the two first Fourier shells [17]. Once a statistically steady state is reached with a Taylor microscale Reynolds number, $\mathrm{Re}_\lambda \approx 730$, the flow is seeded with several millions of tracers, along which the full velocity gradient is stored with a period $\approx \tau_\eta/4$ during four large-eddy turnover times (up to $t \simeq 734\tau_\eta$). The local slender-body equation for fibers, Eq. (1), is then integrated *a posteriori* along a subset of 4000 tracer trajectories uniformly distributed in the domain, and eight different values of the flexibility. We use the semi-implicit, finite-difference scheme of Ref. [9], with the inextensibility constraint enforced by penalization. $N = 201$ grid points are used along the fiber arc length, with a time step $5 \times 10^{-4}\tau_\eta$. We use linear interpolation in time to access the velocity gradient at a higher frequency than the output from the fluid simulation.

Numerics confirm that fibers much smaller than the Kolmogorov scale are almost always straight. This can be measured from the end-to-end length $R(t) = |\mathbf{X}(\ell/2, t) - \mathbf{X}(-\ell/2, t)|$. When $R = \ell$, the fiber has a rod shape. Buckling occurs when $R < \ell$. The upper panel of Fig. 1 shows the time evolution of the end-to-end length along a single trajectory for various nondimensional flexibilities $\mathcal{F}$. Clearly, bending is sparse and intermittent. Buckling events are separated by long periods during which $R \equiv \ell$, up to numerical precision. For instance, one observes $|1 - R(t)/\ell| < 10^{-13}$ in the time interval $100 < t/\tau_\eta < 180$. In the lower panel of Fig. 1, we have shown the time evolution of the stretching rate $\dot{\gamma}$ along the same Lagrangian trajectory. As expected, buckling events are associated with strong negative fluctuations of $\dot{\gamma}$. Note that, because $\mathbf{p}$ is preferentially aligned with the fluid stretching [18], the rate $\dot{\gamma}$ has a positive mean $\langle \dot{\gamma} \rangle \approx 0.11/\tau_\eta$. Its standard deviation is $\approx 0.2/\tau_\eta$.
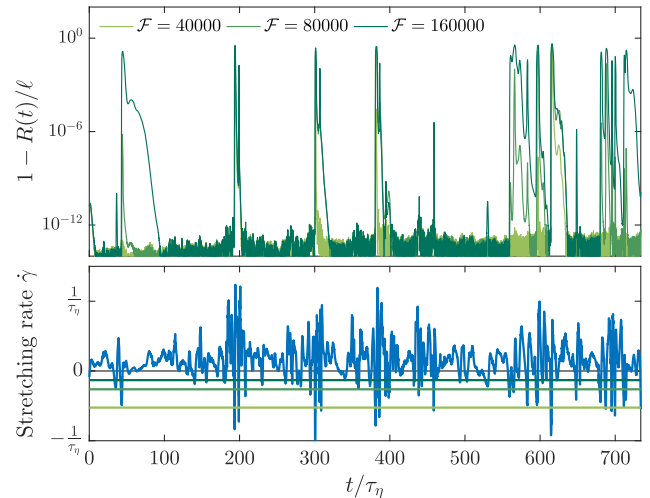
FIG. 1. Top: Time evolution of the end-to-end length $R(t)$ for a specific turbulent tracer trajectory and three different values of the nondimensional flexibility $\mathcal{F}$, as labeled. Bottom: Evolution of the instantaneous stretching rate $\dot{\gamma}$ along the same trajectory. The solid lines correspond to $\tau_\eta \dot{\gamma} = 0, -0.13, -0.26$, and -0.52. Note that time is rescaled by the Kolmogorov timescale τ_η. In these units, the large-eddy turnover time is $\tau_L \approx 190\tau_\eta$.

To get more quantitative insight, we define buckling events as times when $R(t)/\ell$ is below a prescribed threshold (we have used 0.999). Figure 2 shows the probability of buckling as a function of the flexibility $\mathcal{F}$. This quantity, denoted Φ, is defined as the fraction of time spent by the end-to-end length below this threshold. Conversely to
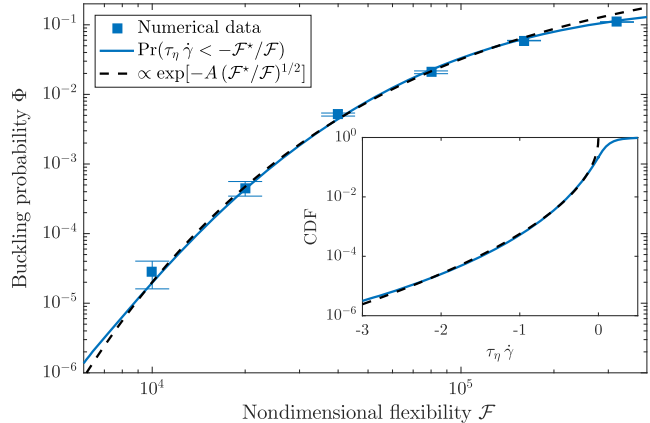
FIG. 2. Probability of buckling Φ as a function of $\mathcal{F}$. The squares come from numerical simulations and were calculated as the fraction of time during which $R(t)/\ell < 0.999$. Error bars show the standard deviation of these estimates, obtained when assuming that buckling events are uncorrelated. The bold line is the probability that the stretching rate $\dot{\gamma}$ is less than $-\mathcal{F}^\star/(\tau_\eta\mathcal{F})$ with $\mathcal{F}^\star = 2.1 \times 10^4$. The corresponding cumulative distribution function (CDF) is shown in the inset, together with a fit (dashed line) of the form $\propto \exp[-A(\tau_\eta|\dot{\gamma}|)^{1/2}]$, where $A = 1.69$. The same approximation is used in the main panel to fit Φ (dashed line).

simple steady shear flows (see, e.g., Ref. [8]), and differently from what is observed for long fibers in turbulence [19,20], here we find that there is no critical value of the flexibility above which buckling occurs. Fibers bending is similar to an activated process with $\Phi \propto \exp(-C/\mathcal{F}^\alpha)$ and where the flexibility $\mathcal{F}$ plays a role resembling that of temperature in chemical reactions. Indeed, the fiber is found to buckle when its instantaneous flexibility $\mathcal{F}_{\mathrm{loc}}(t) = \tau_\eta |\dot{\gamma}(t)|\mathcal{F}$ is larger than a critical value $\mathcal{F}^\star$, with $\dot{\gamma}(t) < 0$. This leads to

$$\Phi = \mathrm{Pr}\left(\tau_\eta \dot{\gamma} < -\mathcal{F}^\star/\mathcal{F}\right). \tag{4}$$

As can be seen in Fig. 2, the cumulative probability of the stretching rate can indeed be used to reproduce the numerical measurements of Φ by choosing $\mathcal{F}^\star = 2.1 \times 10^4$. This value, which just corresponds to a fit, is much larger than those observed in time-independent shear flows [11] where buckling occurs for $\mathcal{F} \gtrsim 300$. A first reason comes from using the Kolmogorov dissipative timescale when defining $\mathcal{F}$. This is a natural but arbitrary choice in turbulence. However, τ_η is significantly smaller than typical values of $\dot{\gamma}^{-1}$, so that effective flexibilities could be smaller than $\mathcal{F}$. This is similar to choosing τ_η rather than the Lyapunov exponent to define the Weissenberg number for the coil-stretch transition of dumbbells in turbulent flow [21]. Another explanation for a large $\mathcal{F}^\star$ could be the intricate relation in turbulence between the amplitude of velocity gradients and their dynamical timescales, which implies in principle that the stronger $\dot{\gamma}$ is, the shorter the lifetime of the associated velocity gradient.

Fibers with a small flexibility buckle only when the instantaneous stretching rate is sufficiently violent. Moreover, it is known that at large Reynolds numbers [22], the probability distribution of velocity gradients has stretched-exponential tails with exponent $\approx 1/2$. This behavior is also present in the cumulative probability of $\dot{\gamma}$, as seen in the inset of Fig. 2. This leads to the prediction that

$$\Phi \propto e^{-A(\mathcal{F}^\star/\mathcal{F})^{1/2}} \quad \text{for } \mathcal{F} \ll \mathcal{F}^\star. \tag{5}$$

This asymptotic behavior is shown as a dashed line in the main panel of Fig. 2. It gives a rather good fit of the data, up to $\mathcal{F} \approx 1.6 \times 10^5$. At larger values, this activationlike asymptotics and relation to the tail of the distribution is no longer valid. At very small values (or equivalently large negative $\dot{\gamma}$'s), one observes tiny deviations from the stretched exponential, certainly resulting from numerical errors overpredicting extreme gradients [23].

The relevance to buckling of an instantaneous flexibility larger than $\mathcal{F}^\star$ can be seen in Fig. 1. The dashed lines in the bottom panel are the critical values $\tau_\eta \dot{\gamma} = -\mathcal{F}^\star/\mathcal{F}$ associated to the three flexibilities of the top panel. We indeed observe that buckling occurs when the instantaneous stretching rate underpasses these values. In some cases

(e.g., for times between 400 and $500\tau_\eta$), it seems that the fiber is straight, even if $\dot{\gamma}$ is below the threshold. Still, buckling occurs but with an amplitude so small that it cannot be detected from the top panel. This threshold therefore provides information on the occurrence of buckling, but not on the strength of the associated bending.

Another qualitative assessment that can be drawn from Fig. 1 is that large excursions of $\dot{\gamma}$ are not isolated events but form clumps. This is a manifestation of the Lagrangian intermittency of velocity gradients. Tracers might indeed be trapped for long times in excited regions of the flow, leading to fluctuations correlated over much longer times than τ_η. This can be quantified from the autocorrelation $\rho(t)$ of the negative part $\dot{\gamma}^- = \max(-\dot{\gamma}, 0)$ of the stretching rate, which is represented in the inset of Fig. 3. The corresponding integral correlation time is $\int \rho(t)dt \approx 2.8\tau_\eta$. This can be explained by the abrupt decrease of the autocorrelation at times of the order of the Kolmogorov timescale. This behavior is essentially a kinematic effect due to fast rotations. Remember that $\dot{\gamma}$ is obtained by projecting the velocity shear on the direction $\mathbf{p}$ of a rigid rod. This direction rotates with an angular speed given by the vorticity $\omega = |\nabla \times \boldsymbol{u}|$, so that $\dot{\gamma}$ can alternate from expansion to compression, on timescales of the order of $\omega^{-1} \sim \tau_\eta$. Surprisingly, at longer times $t \gtrsim 4\tau_\eta$, the autocorrelation of $\dot{\gamma}^-$ changes regime and decreases much slower than an exponential. This contradicts the classical phenomenological vision that velocity gradients are purely a small-scale quantity with correlations spanning only the dissipative scales. For more than a decade in t within the
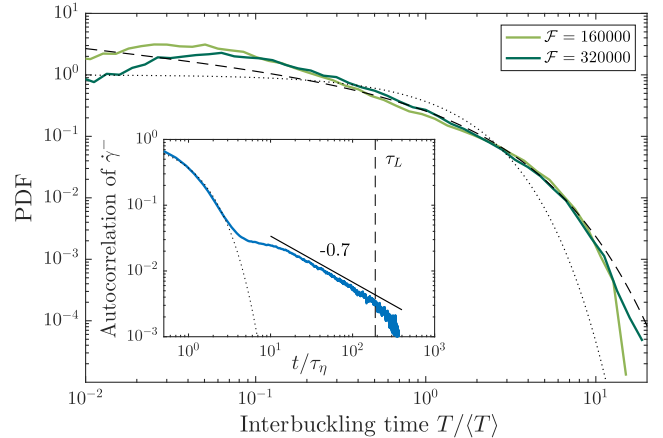
FIG. 3. Probability density functions [PDF (solid lines)] of the time T between successive buckling events, normalized to its average $\langle T \rangle \approx 52\tau_\eta$ for $\mathcal{F} = 1.6 \times 10^5$, and $\langle T \rangle \approx 36\tau_\eta$ for $\mathcal{F} = 3.2 \times 10^5$. The dotted line represents the exponential distribution. The dashed line is a Weibull distribution, Eq. (6), with shape $\beta = 0.7$ and scale parameter $\lambda = 1$. Inset: Autocorrelation $\rho(t) = \mathrm{cov}(\dot{\gamma}^-(t), \dot{\gamma}^-(0))/\mathrm{Var}(\dot{\gamma}^-)$ of the negative part of the stretching rate. The dotted line stands for $\exp(-t/\tau_\eta)$. The vertical dashed line indicates the large-eddy turnover time $t = \tau_L$. The solid line shows a slope -0.7.

inertial range, we indeed find a power-law behavior $\rho(t) \propto t^{-\beta}$, with $\beta \approx 0.7 \pm 0.1$. To our knowledge, this is the first time such a long-range behavior is observed for turbulent Lagrangian correlations.

These intricate correlations have important consequences on the incidence of buckling. Memory effects are present, as the fiber is likely to bend several times when in a clump of violent, high-frequency fluctuations of $\dot{\gamma}$. Consequently, the probability distribution $p(T)$ of the time T between successive buckling events is not exponential. This is clear from the main panel of Fig. 3, where this distribution is shown for $\mathcal{F} = 1.6 \times 10^5$ and 3.2×10^5. One observes deviations from the exponential distribution (dotted line). They relate to the two regimes discussed above for the time correlations of $\dot{\gamma}^-$. First, the distribution of interbuckling times is maximal for T of the order of τ_η. This corresponds to rapid oscillations of the sign of $\dot{\gamma}$. The fiber experiences several tumblings in an almost-constant velocity gradient and is alternatively compressed and pulled out by the flow due to fast rotations. This leads to a rapid succession of bucklings and straightenings. Second, strong deviations to the exponential distribution also occur for interbuckling times T in the inertial range. As seen in Fig. 3, the distribution of interbuckling times in the intermediate range $0.5 \lesssim T/\langle T \rangle \lesssim 5$ is well approximated by a Weibull distribution with shape β and scale parameter λ:

$$p(T) \approx \frac{\beta T^{\beta-1}}{\lambda^\beta} e^{-(T/\lambda)^\beta}. \tag{6}$$

This decade exactly matches the time lags for which $\dot{\gamma}$ displays long-range correlations, that is, $\rho(t) \sim t^{-\beta}$. The return statistics of processes with power-law correlations is indeed expected to be well approximated by a Weibull distribution [24]. Longer times correspond to $t \gtrsim \tau_L$, for which $p(T)$ is expected to ultimately approach an exponential tail.

To characterize further buckling events and in particular their geometry, we show in Fig. 4 the joint probability density of the end-to-end length R and of the fiber's mean curvature, $\bar{\kappa} = (1/\ell) \int |\partial_s^2 X| ds$. The distribution is supported in a thin strip aligned with $\bar{\kappa} \propto (1 - R/\ell)^{1/2}$. Bucklings correspond to loops in this plane. Trajectories typically start such excursions with a larger curvature (upper part of the strip) than the one they have when relaxing back to a straight configuration (lower part). The orange curve corresponds to the first buckling event of the trajectory shown in Fig. 1. The curvature increases concomitantly to a decrease of the end-to-end length. Right before reaching a maximal bending, the fiber displays several coils (top left inset). This configuration depends on the most unstable mode excited with the current value of the instantaneous flexibility $\mathcal{F}_{\text{loc}}$. It is indeed known that buckling fibers in steady shear flows can experience several
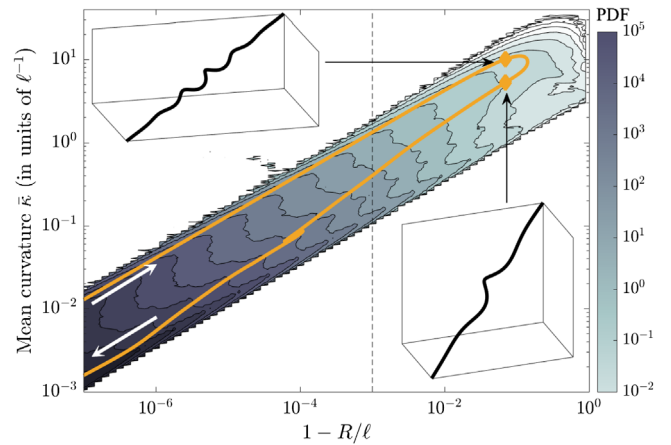
FIG. 4. Contour levels of the joint distribution of the end-to-end length R and of the mean curvature $\bar{\kappa}$ for $\mathcal{F} = 1.6 \times 10^5$. The vertical dashed line shows the threshold $R/\ell = 0.999$. An excursion of the same trajectory as Fig. 1 is shown for $43 < t/\tau_\eta < 77$ (orange). Also, two instantaneous configurations of the fiber are represented for $t = 43\tau_\eta$ (top left inset) and $t = 45\tau_\eta$ (bottom right inset).

bifurcations, depending on their elasticity [7]. Once the fiber has again aligned with $\dot{\gamma} > 0$, that is, a couple of τ_η's later, these coils unfold (bottom right inset), the curvature decreases, and the fiber relaxes back to a straight configuration. This specific event has been chosen for its simplicity and representativity. Still, it experiences a nontrivial episode at $1 - R \approx 10^{-4}$, during which the fiber configuration seems frozen. This event corresponds to the plateau observed in the top of Fig. 1 for $50\tau_\eta < t < \approx 80\tau_\eta$, right after the maximum of buckling. At these instants of time, $\dot{\gamma}$ is weakly oscillating around zero and the fiber is neither compressed nor stretched by the flow.

To conclude, recall that we have focused on passively transported fibers. In several applications, they actually have an important feedback on the flow and might even reduce turbulent drag. We found here that the dynamics of flexible fibers strongly depends on the shear strength: In calm regions, they just behave as stiff rods; in violent, intermittent regions, they can buckle, providing an effective transfer of kinetic energy toward bending elasticity. Such nonuniform, shear-dependent effects likely lead to intricate flow modifications, where the presence of small fibers affects not only the amplitude of turbulent fluctuations but also their very nature. Such complex non-Newtonian effects undoubtedly lead to novel mechanisms of turbulence modulation.

---

[1] P.-G. de Gennes, *Scaling Concepts in Polymer Physics* (Cornell University Press, Ithaca, NY, 1979).

[2] T. Watanabe and T. Gotoh, Phys. Rev. E **81**, 066301 (2010).

[3] A. S. Pereira, G. Mompean, L. Thais, E. J. Soares, and R. L. Thompson, Phys. Rev. Fluids **2**, 084605 (2017).

[4] F. Lundell, L. D. Söderberg, and P. H. Alfredsson, Annu. Rev. Fluid Mech. **43**, 195 (2011).

[5] M. N. Ardekani, G. Sardina, L. Brandt, L. Karp-Boss, R. Bearon, and E. Variano, J. Fluid Mech. **831**, 655 (2017).

[6] V. Smetacek, Protistologica **150**, 25 (1999).

[7] L. E. Becker and M. J. Shelley, Phys. Rev. Lett. **87**, 198301 (2001).

[8] A. Lindner and M. Shelley, *Fluid-Structure Interactions in Low-Reynolds-Number Flows* (Royal Society of Chemistry, London, 2015), pp. 168–192.

[9] A.-K. Tornberg and M. J. Shelley, J. Comput. Phys. **196**, 8 (2004).

[10] M. Harasim, B. Wunderlich, O. Peleg, M. Kröger, and A. R. Bausch, Phys. Rev. Lett. **110**, 108302 (2013).

[11] Y. Liu, B. Chakrabarti, D. Saintillan, A. Lindner, and O. du Roure, Proc. Natl. Acad. Sci. U.S.A. **115**, 9438 (2018).

[12] Y.-N. Young and M. J. Shelley, Phys. Rev. Lett. **99**, 058303 (2007).

[13] E. Wandersman, N. Quennouz, M. Fermigier, A. Lindner, and O. Du Roure, Soft Matter **6**, 5715 (2010).

[14] V. Kantsler and R. E. Goldstein, Phys. Rev. Lett. **108**, 038103 (2012).

[15] C. M. Schroeder, R. E. Teixeira, E. S. G. Shaqfeh, and S. Chu, Phys. Rev. Lett. **95**, 018301 (2005).

[16] E. Plan and D. Vincenzi, Proc. R. Soc. A **472**, 20160226 (2016).

[17] H. Homann, J. Dreher, and R. Grauer, Comput. Phys. Commun. **177**, 560 (2007).

[18] R. Ni, N. T. Ouellette, and G. A. Voth, J. Fluid Mech. **743** R3 (2014).

[19] C. Brouzet, G. Verhille, and P. Le Gal, Phys. Rev. Lett. **112**, 074501 (2014).

[20] M. Rosti, A. Banaei, L. Brandt, and A. Mazzino, Phys. Rev. Lett. **121**, 044501 (2018).

[21] G. Boffetta, A. Celani, and S. Musacchio, Phys. Rev. Lett. **91**, 034501 (2003).

[22] P. Kailasnath, K. R. Sreenivasan, and G. Stolovitzky, Phys. Rev. Lett. **68**, 2766 (1992).

[23] D. Buaria, A. Pumir, E. Bodenschatz, and P. Yeung, in *APS Meeting Abstracts* (American Physical Society, New York, 2017).

[24] J. F. Eichner, J. W. Kantelhardt, A. Bunde, and S. Havlin, Phys. Rev. E **75**, 011128 (2007).

5 | Fragmentation of fibers by turbulence

Contents

The rheological response of suspended objects induced by the violent intermittent fluctuations of turbulent fluid flows may have crucial consequences in physical world phenomena. This is particularly true if one has in mind the fate of genuine physical fibers: Being brittle, they are susceptible to break when they undergo strong stress. It is thus extremely natural to include fragmentation processes in our modeling of small fibers, and study how the turbulent fluctuations trigger and shape the fragmentation statistics as a function of time. The fundamental questions are simple: How many fragments? What are their size? Answering those questions is the scope of the present chapter, where we address both the microscopic and the statistical modeling of such fragmentation process.

The modeling of fragmentation processes is key to understanding natural and industrial phenomena (Beysens et al., 1995; Bertoin, 2006). Salient examples include break-up of DNA chains (Nagata, 2000; Yan et al., 2006; Cristiano et al., 2019); fragmentation of meteors in space (Hüfner and Mukhopadhyay, 1986; Keil et al., 1994; Khrennikov et al., 2020) and study of the outcome of explosions in a military context (Mott, 2006; Gold and Baker, 2008). We note that this latter field of application, following the work of Griffith and Mott (Griffith, 1943; Mott, 1947) is at the origin of a systematic approach to fragmentation, combining statistical studies and microphysics modeling (Horn and Merrill, 1984). The statistical description can rely on various mathematical frameworks, from mean field population models based on ordinary differential equations and stochastic processes to reaction diffusion system based on partial differential equations (Bortolussi and Gast, 2016). Quite generally, such models require information on two quantities: the fragmentation rate (*i.e.* the frequency of the breakup events) and a modeling of the outcome of one fragmentation event, for instance in terms of number of fragments or in terms of the distribution of sizes. Here, we will show how an appropriate stochastic Lagrangian population model can be used in combination to microscopic simulations to provide faithful estimates on the statistics of the fragments.
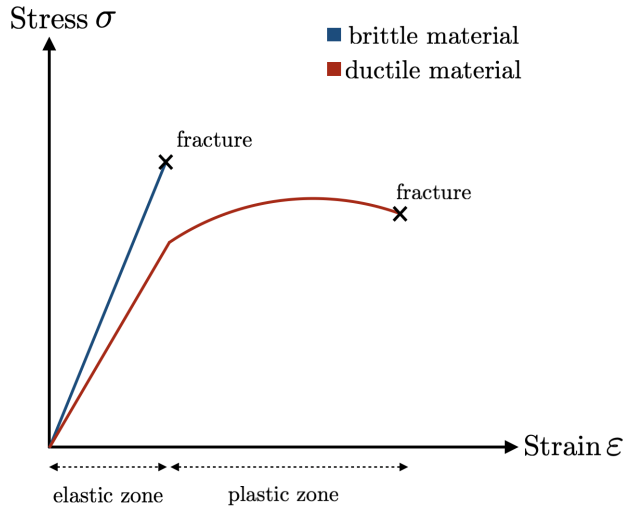
The chapter is organized as follows. We first detail our numerical simulations of the mechanisms of fragmentation for small fibers involved in a turbulent flow. Second, we propose a statistical framework, that upon calibration using our numerical experiments, can be used to predict the statistics of small-fiber fragmentation within turbulence. We finally discuss some of the shortcomings of our modeling approach and suggest perspectives for future work.

Our exposition is a spin-off to the paper "Dynamics and fragmentation of small inextensible fibers in turbulence" published in Philosophical transactions A, that was co-authored with Jérémie Bec and Christophe Henry. The paper is reproduced at the end of the chapter.

5.1 How to model fragmentation in numerical simulations?

5.1.1 The physics of brittle materials

To study fragmentation from our direct numerical simulations (DNS), we model the fibers as a brittle material. This means that the regime of linear elasticity remains valid all the way until a certain critical fracturation point is reached, at which the material breaks. This constitutes a simplifying assumption, as real-world materials typically undergo a regime of plastic deformation before they actually break. When this plastic regime extends way beyond the elastic regime, the material is called ductile. When this plastic regime is non or close to non-existant, the material is called fragile or brittle. In practice, the brittle approximation allows to rely on the SBT equations all the way until fracturation. This means that fracturation simply consists of reaching an imposed limit of validity for the constitutive equation of state of the fiber; in other words all the way until fracture, the fiber follows a Hooke's law, tying the topology of the fiber to the internal efforts and internal energy (see Fig.5.1).
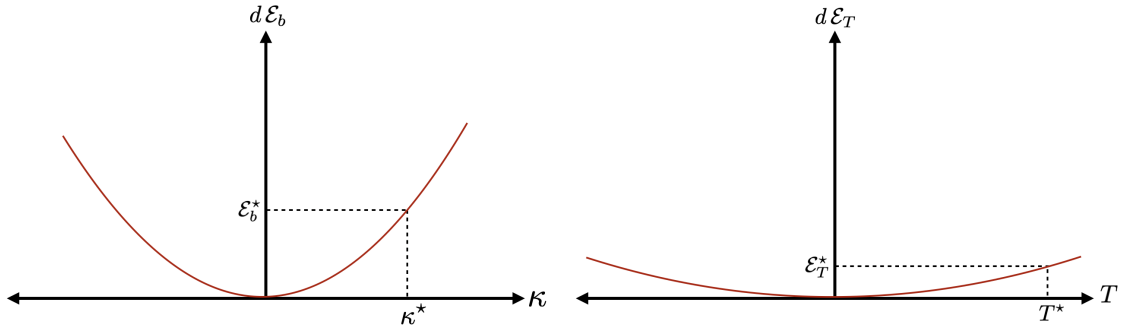
Figure 5.1: Stress σ as a function of the strain ε for two different materials, either brittle (in blue) or ductile (in red), together with their fracture point.

In terms of energy, this means that the fiber cannot reach an infinite elastic energy and will break when the latter reaches a given critical value $\mathcal{E}_b^\star$. In particular, when the fibers buckle, the increase of the local curvature leads to the increase of the local bending energy $d\mathcal{E}_b(s) = (E/2)\,\kappa(s)^2 ds$, where E is the bending modulus defined in the previous chapter. Hence, the fiber will break when its curvature becomes too high. Such a mechanism is referred to as a **flexural failure** (see the left panel of Fig. 5.2) and provides the mechanism for fragmentation when the fiber undergoes strong compression stress.

In the case of an extensional stress, our assumptions that the fibers are inextensible imply that, strictly speaking, the fibers are not elastic. In fact, what inextensibility really means is that physically, the fibers are

characterized by a very large Young modulus $Y = E/I$. Mathematically, our inextensible fibers can be seen as the formal limit obtained as $Y = E/I \to \infty$, with $E = O(1)$, implying $I \to 0$ where I is cross-sectional moment of inertia (see previous chapter). This means that the extensional potential energy of an inextensible fiber is formally 0. In other words, we need an infinite stress to have a small strain. In the case of a large, but finite Y, the elastic energy associated to local stretching in the axial direction is the extensional energy $d\mathcal{E}_T(s) = T(s)^2/(2Y)ds$ (Landau and Lifshitz, 1959) in terms of the local tension T. Hence, a fragile fiber will break when the extensional energy reaches a prescribed threshold, or equivalently when the tension becomes locally too high (see the right panel of Fig. 5.2). In order to implement a mechanism allowing failure due to strong stretching in the inextensible case, it is therefore possible to impose a threshold on the local tension [10]. We refer to such mechanism as a **tensile failure**.

Figure 5.2: Illustration of the relation between the local bending energy $d\mathcal{E}_b(s)$ and the curvature κ in the left side and the local extensional energy $d\mathcal{E}_T(s)$ and the tension T in the right side. The respective critical values $\kappa^\star$ and $T^\star$ are given by the physical properties of the material.

To summarize,

- Fibers can break through **tensile failure**, when undergoing stretching efforts. The internal tension is then likely to become very high, leading to fragmentation if it supersedes a prescribed threshold that depends on its material properties.

- Another way to break fibers is to compress them, in order to trigger a buckling instability and provoke a **flexural failure**. In that case, the fibers break because the local curvature becomes too high. In other words, fibers cannot exceed a prescribed curvature without breaking.

Let us now describe practical details on the numerical implementation of those two fragmentation processes in our DNS.

5.1.2   Numerical implementation

With those two mechanisms at hand, we can now incorporate fragmentation processes in our numerics, depending on the two threshold parameters $\kappa^\star$ and $T^\star$. Following the tracer trajectories along which the SBT are integrated, fragmentation processes are triggered whenever either the local tension or the local curvature reach the threshold values. In that case the fiber breaks into two pieces.

For simplicity, we make the three following modeling assumptions:

i the threshold parameters $\kappa^\star$ and $T^\star$ can be chosen independently from each other;

ii the breaking is instantaneous, *e.g.* faster than any timescale in the problem;

iii the daugther fragments follow the same Lagrangian trajectory as their parents. This means that a given fiber will generate a full dynasty of fragments, which do not feel any sort of relative dispersion. This assumption has the chief advantage to drastically simplify the numerics! However, it will produce

---

[10]which is not vanishing, contrarily to the extensional energy!

a strong statistical correlation between the fragment sizes that needs to be taken into account in the statistical description.

5.2 Outcome of turbulent fluctuations

Let us now describe in more details the outcome of stretching and buckling events triggering the two kinds of failures in terms of fragmentation statistics.

5.2.1 Stretching by the flow: tensural failure
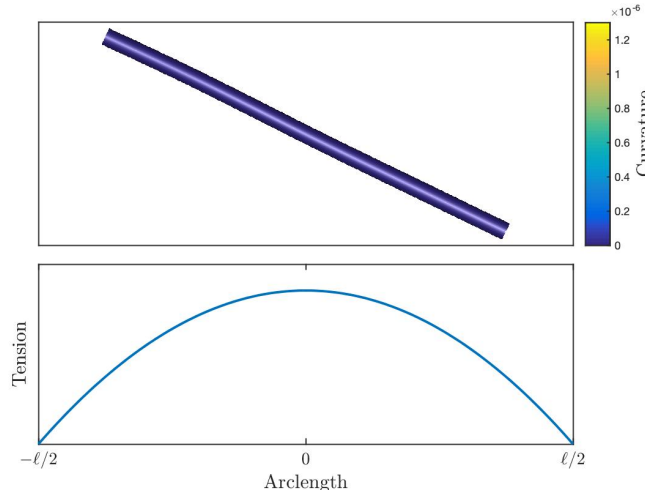
Large tensions are reached when the fiber experiences a strong stretching along its main axis and is thus generally in a fully straight state. In this case the tension is given by

$$T(s, t) = -\frac{\mu}{4} \dot{\gamma}(t) \left(s^2 - \frac{\ell^2}{4} \right),$$ (5.1)

where $\mu = 8\pi \nu / b$ (see previous chapter for more details). We observe that Eq. (5.1) follows a parabolic shape with the arc-length coordinate s and its maximum is

$$T_{\max} = \frac{\mu \dot{\gamma} \ell^2}{16}$$ (5.2)

reached at the middle of the fiber (see the bottom panel of Fig. 5.3).

Figure 5.3: Top panel: Straight fiber with a flexibility $\mathcal{F} = 1.6 \times 10^5$. The color rendering shows the fiber curvature. Bottom panel: tension as a function of the arc-length at the same instant of time

As a consequence, a tensile failure occurs when the shear rate reaches the critical value

$$\dot{\gamma}_T^{\star}(\ell) = 16 \, T^{\star} / (\mu \ell^2),$$

in which case the fiber breaks into two daughter fragments of size $\ell/2$. Note that the critical value depends on the fiber length ℓ and in its physical properties by $T^{\star}$. This implies that a stretching event will not systematically generate only two pieces: It may in fact generate a sequence of tensile failures for the fragments. The final number and sizes of the pieces at the end of the event depends on the maximal positive value $\dot{\gamma}_m$ reached by the shear rate.
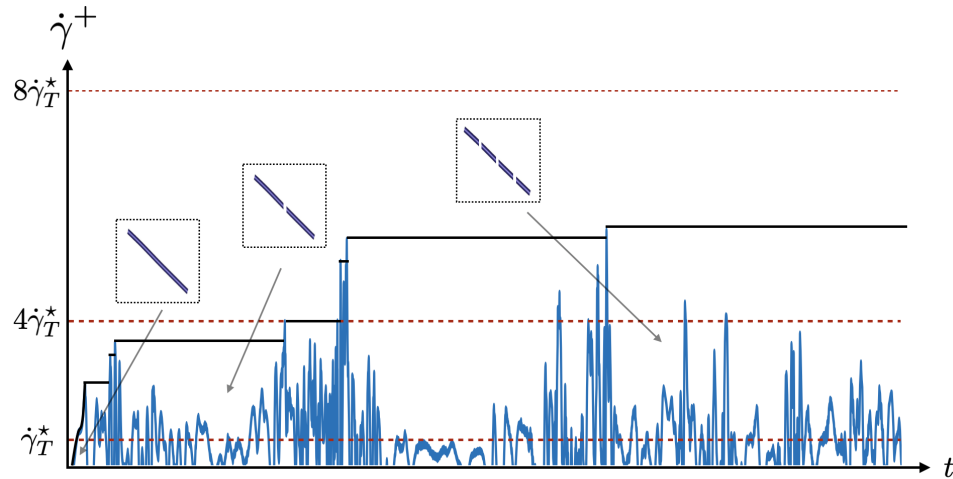
Specifically,

- If $\dot{\gamma}_m < \dot{\gamma}_T^\star(\ell)$, then the fiber does not break. It can be considered as one daughter fragment of size ℓ.

- If $\dot{\gamma}_T^\star(\ell) \leq \dot{\gamma}_m < \dot{\gamma}_T^\star(\ell/2)$, the fiber breaks into two daughter fragments of equal sizes $\ell/2$.

- If $\dot{\gamma}_T^\star(\ell/2) \leq \dot{\gamma}_m < \dot{\gamma}_T^\star(\ell/4)$, the fiber breaks into two daughter fragments of equal sizes $\ell/2$, which in turn break into two grand-daughter fragments of equal sizes $\ell/4$. The final number of pieces is 4.

- If $\dot{\gamma}_T^\star(\ell/4) \leq \dot{\gamma}_m < \dot{\gamma}_T^\star(\ell/8)$, the fiber breaks into two daughter fragments of equal sizes $\ell/2$, which in turn break into two grand-daughter fragments of equal sizes $\ell/4$, which in turn break into two grand-grand-daughter fragments of equal sizes $\ell/8$. The final number of pieces is 8.

- If $\dot{\gamma}_T^\star(\ell/2^n) \leq \dot{\gamma}_m < \dot{\gamma}_T^\star(\ell/2^{n+1})$, the fiber breaks into two daughter fragments [...] which in turn break into two grand-[...]-grand-daughter fragments of equal sizes $\ell/2^{n+1}$. The final number of pieces is 2^{n+1}.

More generally, the number of successive failures is:

$$n_T = \left\lceil \frac{1}{2} \log_2 \frac{\dot{\gamma}_m}{\dot{\gamma}^\star(\ell)} \right\rceil + 1,$$

and the total number of pieces is: 2^{n_T} provided $n_T \geq 0$. Fig. 5.4 illustrates this scenario.

Figure 5.4: Evolution of the positive values of the shear rate as a function of the time t and the illustration of the different levels given a critical value of tensile failure. Each time that fibers supersede a red dashed-lines they breaks into two more pieces illustrates in small boxes.
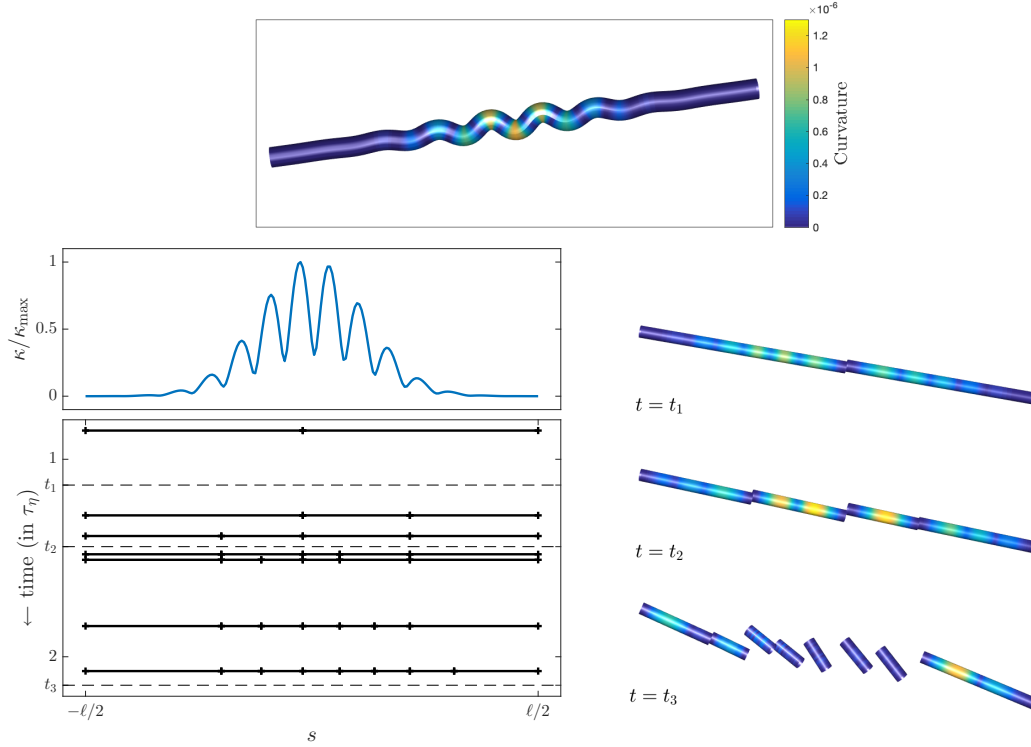
We observe that if tensile failure is the only mechanism involved in the fragmentation (*e.g.* , not considering flexural failure) then the number of pieces present at time t along a Lagrangian trajectory is fully specified by the Lagrangian statistics of $\max_{[0,t]}(\dot{\gamma})$. Specifically,

$$\mathcal{P}(\# = 2^n, t) = \mathcal{P}(\max_{[0,t]}(\dot{\gamma}) \in [2^{2n}\, \dot{\gamma}^\star(\ell)\, ; \, 2^{2n+2}\, \dot{\gamma}^\star(\ell)]). \tag{5.3}$$

5.2.2 Compressing by the flow: flexural failure

Now we focus on the flexural failure mechanism, which we implement in our numerics by imposing a critical value for the curvature $\kappa^\star$. Fig. 5.5 shows this mechanism at play during one of the buckling events. We observe not one but a sequence of flexural failures, resulting in the formation of many fragments at the end of the event. The scenario goes as follows: When it achieves a local curvature $\kappa^\star$ for the first time, the fiber breaks in two pieces. Unlike the parabolic tension profile which precedes tensural failure, the curvature profile when the fiber first breaks by flexural failure is wavy, characterized by a mode with a certain wavenumber k_{b*} and modulated by an apparently Gaussian enveloppe. Along the fiber, the curvature therefore displays a

number $n_b \sim 2k_b*$ of local maxima, likely to be very close to the critical threshold. After the initial failure, the fragments are still compressed by the flow, and this may bring the local peaks of the curvature to reach the threshold $\kappa^\star$. This heuristic view explains why single buckling event trigger a sequence of flexural failures and may produce a non-trivial number of fragments.

Figure 5.5: Top panel: Buckled fiber with a flexibility $\mathcal{F} = 1.6 \times 10^5$. The color rendering shows the fiber curvature. Bottom left panel: tension as a function of the arc-length at the same instant of time. Left bottom panel: Evolution of a fiber during fragmentation. The curvature of the growing mode is displayed at the time of the first breakup, as a function of the arc-length s. Together with the time evolution of the size distribution (time growing from top to down); Each horizontal plain line is a break-up event and segments correspond to fiber fragments. Right panel: Three instantaneous configurations of the fragments at time t_1, t_2 and t_3. Colors code the values of curvature (from zero in dark blue to $\kappa^\star$ in yellow). Note that in this pseudo 3D representation, the arc-length s runs from right to left.

It turns out that quantitative estimates on the number of fragments can be obtained from the linear stability analysis of the local SBT equation, by considering the outcome of a slightly perturbed rod. The full calculation is not immediate and the details are discussed in 5.5. The outcome of the analysis is the fact that the most unstable mode can be characterized as a function of the negative values of the instantaneous shear rate $\dot{\gamma}^- \propto \mathcal{F}_{loc}$. The mode has a profile that matches the observation of the DNS; it is characterized by an oscillating function with a wavenumber k_b and a Gaussian envelope with a spatial variance $\ell^2/2c_b$, such that:

$$k_b \simeq \sqrt{\mathcal{F}_{\text{loc}}}/(2\pi \sqrt{32}) \quad \text{and} \quad c_b \simeq \sqrt{\mathcal{F}_{\text{loc}}}/8. \tag{5.4}$$

The wavenumber provides an estimate for the expected number of pieces as:

$$n_b \simeq 2k_b \propto \left[\ell^2 \sqrt{-\dot{\gamma}}\right].$$

Because of the Gaussian modulation, this number most probably over-estimates the total number of fragments. Conversely to tensile failure, the position s where the curvature is maximal is not necessarily constant in time, and depends on the growth stage of the most unstable mode.

5.3 Stochastic approach to turbulent fragmentation

In our turbulent environment, fibers are exposed to fluctuating events that exercise strong external constraints on the fiber, and are likely to trigger a fragmentation process. The scope of the present section is to analyze the effects of such fluctuations on the statistics of fragments. To that end, we sketch a general framework based on probabilities defined at the level of Lagrangian trajectories. We then illustrate the applicability of this approach, by focusing on the fragmentation by buckling events.

5.3.1 General framework: Lagrangian population model

We here describe a statistical approach to model the fragmentation process, which can be seen as a stochastic Lagrangian population model, and can be described in full generality using the theory of renewal processes (Hughes, 1995, Chap. 5) (Karlin, 2014, Chap. 3) (Shlesinger and Hughes, 1981; Shlesinger, 1974; Pyke, 1961). The idea is to estimate the statistics of the "dynasty" of fragments generated by an initial fiber of size ℓ. In our numerics, we assume that every daughter fragments follow the same Lagrangian trajectory, prescribed by the Lagrangian trajectory of a reference tracer. This tracer can be thought of as the center of mass of the dynasty; the statistics of the fragments evolve through time, as the center of mass of the dynasty encounters dangerous events leading to fiber break-ups.
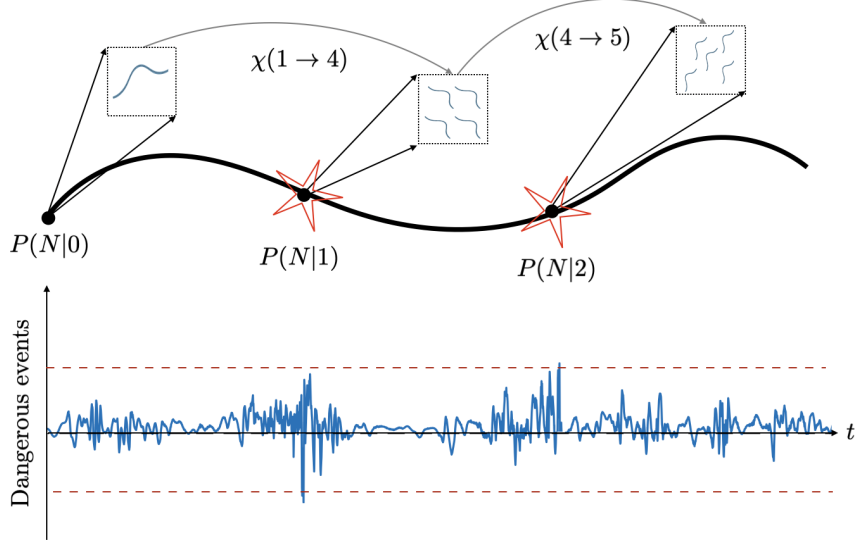
Our approach is based on a discrete description, using master equations to model the evolution of the fiber fragmentation. In full generality, the evolution of the population of fragments along a Lagrangian trajectory can be described statistically by the quantity:

$$
\begin{aligned}
P_t(N, \{\ell_k\}_{k=1,...,N}) = \mathcal{P}(\text{number of fragments } &= N \\
& \& \ \forall k \in [1;N] \text{ the } k^{th} \text{ fragment has size } = \ell_k \\
& \text{at time t}).
\end{aligned}
\tag{5.5}
$$

This quantity is a very detailed fine-grained probability distribution in the sense that it provides the full information on the statistics of the fragments. However it is cumbersome to manipulate, and it is also cumbersome to compute from numerics. For this reason we turn our attention to the modeling of coarse-grained quantities, such as $P_t(N)$ and $P_t(\ell)$, respectively describing the evolution of the number of fragments and the evolution of the average fragment size. Such quantities give us relevant mean-field information about the evolution of the fragmentation process, and can be studied more easily in terms of a stochastic dynamics. For simplicity, we here further restrict our analysis to the evolution of the number of fragments given by the quantity $P_t(N)$.

Fig. 5.6 illustrates the general idea: the evolution of the fragmentation process is measured along a prescribed Lagrangian trajectory, as well as its dynamics. During their lives, fibers experience dangerous events that can trigger their fragmentation. Those dangerous events are either the strong compressive events leading to buckling and flexural failure, or the strong stretching events leading to tensile failure. As described in the previous section, actual breaking of the fibers require the events to be strong enough. In our turbulent environment, such dangerous events are extremely short; they are characterized by a negative or positive peak of the shear rate or an extremely time-localized incursion of the shear rate below or above threshold values.

Because of the presence of non-trivial time correlations between the dangerous events, one cannot in full generality rely on standard Poisson processes to describe the dynamics of the the resulting number of fragments N. To account for those correlations, we therefore use a description in terms of more general **renewal process** ((Hughes, 1995). The process will be fully determined by the rheological response of the fiber according to the magnitude of the events and to their signs (negative for flexural failure and positive for tensile failure).

Figure 5.6: Illustration of a statistical framework describing the statistical evolution of the number of fragments $P_t(N)$. Top panel: the evolution of a "fiber dynasty" along a Lagrangian trajectory, where the red stars represent the break-up events, where the fibers break and the population increases. Bottom panel: time evolution of the shear rate along the trajectory. The dangerous events are identified with incursions of the shear rate above (below) prescribed positive (negative) thresholds, here represented by the red dashed-lines. The probabilities $P(N|k)$ is the probability to have N pieces given k dangerous events and is assumed to be independent of time. The transition probability $\chi(N' \to N)$ is the probability that a dangerous event creates N pieces out of N'.

We model the dynamics of $P_t(N)$ by introducing the joint probability

$$P_t(N,k) = \mathcal{P}(\text{number of fragments } = N$$
$$\& \text{ number of dangerous events} = k \tag{5.6}$$
$$\text{at time } t$$

which represents the joint probability to find N pieces and k dangerous events at time t along the Lagrangian trajectory of the dynasty. From the fundamental postulate of probability, this joint probability can be expressed as

$$P_t(N) = P_t(N|k)\rho_t(k), \tag{5.7}$$

in terms of the conditional probability $P_t(N|k)$ that N fragments are found given that k dangerous events at time t, and in terms of the probability $\rho_t(k)$ to have exactly k dangerous events at time t. The probability $P_t(N|k)$, depends on the physical properties of the fiber, and we will here assume that it is independent from time, *e.g.* $P_t(N|k) = P(N|k)$. Physically, this models the property that fibers do not age with time. The time correlations between the dangerous events are encoded in the quantities $\rho_t(k)$.

We can now write the dynamics of $P_t(N)$ in terms of the master equation:

$$P_t(N) = \sum_k P_t(N,k) = \sum_k P(N|k)\rho_t(k), \tag{5.8}$$

The rheological response of the daughter fragments $P(N|k)$ can be determined from the time-independent recurrence relation

$$P(N|k) = \sum_{N'} P(N'|k-1)\chi(N' \to N), \tag{5.9}$$

where $P(N'|k-1)$ is the probability to have N' pieces given $k-1$ dangerous events, and $\chi(N' \to N)$, is the transition probability that a dangerous event creates N pieces out of N'. This probability is described by the rheological response of the fibers to dangerous events and physical mechanisms at play in the breaking process.

5.3.2 Stochastic modeling of fragmentation by flexural failure

To see how the framework applies, and understand the interplay between the turbulence statistics $\rho_t(k)$ and the rheology of the fibers $\chi(N' \to N)$, let us now focus on the stochastic modeling of the fragmentation of fibers due to the flexural failure events only.

The master equation (5.8) for the evolution of the number of fragments $P_t(N)$ then specifically involves

- $\rho_t(k)$, which represents the probability to have k *buckling events* between 0 and t,

- $P(N|k)$, which is the probability to have N fragments out of k buckling events and depends on the rheology.

Modeling of the rheology. The transition kernel χ determining $P(N|k)$ can be partially obtained from the considerations of the previous section, where we argued that the number of fragments is a non-linear function of $\dot{\gamma}^-$, and the size ℓ. This provides the estimate

$$\chi(1 \to N) = \chi_\ell(1 \to N) = \int d\dot{\gamma}\, p_b(\dot{\gamma}) \chi(1 \to N|\dot{\gamma})$$

$$\text{with } \chi(1 \to N|\dot{\gamma}) = \delta_{N n_b} \text{ and } n_b \propto \left[|\dot{\gamma}^-|^{1/2}\ell^2\right],$$

(5.10)

where $[a]$ is the floor of a, and p_b denotes the probability density of the shear rate conditioned on the buckling events.

Full modeling of the quantities $\chi(N \to N')$ requires additional assumptions on the rheology. Possible models include the following:
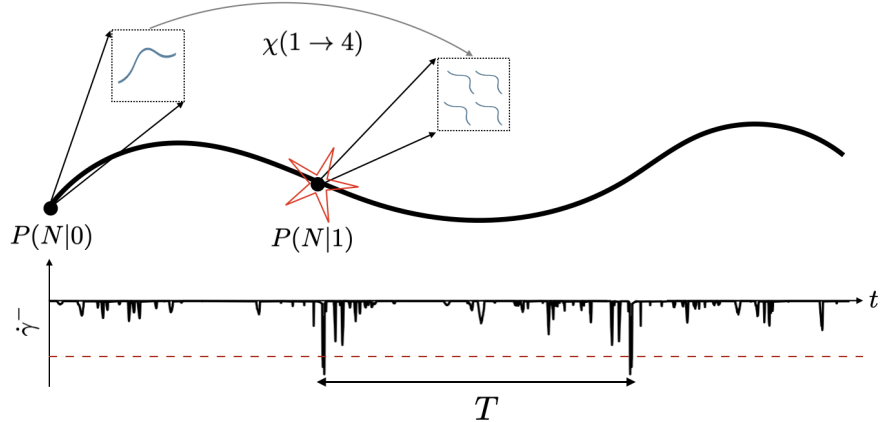
1. Daughter fragments are too small to break again: a fiber can only break if its size is ℓ (see Fig. 5.7), in that case

$$\chi(N' \to N) = \delta_{N'N} \text{ if } N' > 1.$$

2. Daughter fragments have all the same size at each step, and break collectively. In that case, one could use the modeling

$$\chi(N' \to N) = \chi_{\ell/N'}(1 \to N/N') \propto N'^{-2}\chi(1 \to N/N'),$$

which relates the transition kernel $\chi(N' \to N)$ to the probability to creating N/N' daughter fragments out of an initial fiber of size ℓ/N'. The second relation stems from 5.10. This fully prescribes the rheological response of the daughter fragments.

Figure 5.7: Illustration of a statistical framework describing the statistical evolution of the number of fragments $P_t(N)$ due to flexural failure. Top panel: the evolution of a "fiber dynasty" along a Lagrangian trajectory. The red star represents the break-up event, where the fiber breaks and the population increases. Bottom panel: time evolution of the negative part of the shear rate along the trajectory $\dot{\gamma}^-$. The dangerous events are identified as buckling events characterized by incursions of the shear rate below a prescribed negative thresholds, here represented by the red dashed-line. The parameter T represents the inter-buckling time. The quantity $P(N|k)$ is the probability to have N pieces given k dangerous events and is assumed to be independent of time. The transition probability $\chi(N' \to N)$ is the probability that a dangerous event creates N pieces out of N'.
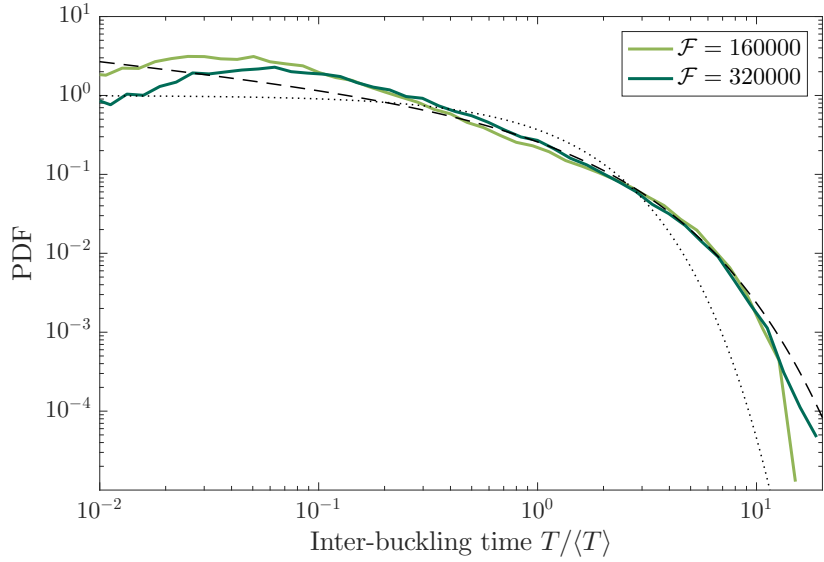
Modeling of turbulent fluctuations. Turbulent fluctuations are modeled in terms of the probability $\rho_t(k)$, which in turn is fully determined by the waiting time statistics between two consecutive buckling events, namely the "inter-buckling time" $\Psi(T)$ defined as

$$\rho_t(k) = \rho(k, t) = \int_0^t \rho(k-1, t')\Psi(t-t')dt'$$
$$= \Psi \otimes \rho(k-1),$$
$$= \Psi^{\otimes k} \otimes \rho(0).$$
(5.11)

where $\Psi(T)$ represents the distribution of inter-buckling times T (see Fig. 5.7). This probability has been found in our precedent chapter 4 to be different from an exponential and rather follow the Weibull distribution (see Appendix E)

$$\Psi(T) \approx \frac{\beta T^{\beta-1}}{\lambda^\beta} e^{-(T/\lambda)^\beta},$$
(5.12)

with a mean value $\tau = \langle T \rangle \approx 52\,\tau_\eta \approx 0.3\,\tau_L$ and $\beta \approx 0.7$. This behavior is illustrated in Fig. 5.8 and suggests the presence of memory effects due to the correlations between the strong and negative events of the shear rate $\dot{\gamma}$. This also means that fibers are bending several times when they come into a clump of strong and violent fluctuations of $\dot{\gamma}$.

Figure 5.8: Probability density functions (solid lines) of the time T between successive buckling events, normalized to its average $\langle T \rangle \approx 52\,\tau_\eta$ for $\mathcal{F} = 1.6 \times 10^5$, and $\langle T \rangle \approx 36\,\tau_\eta$ for $\mathcal{F} = 3.2 \times 10^5$. The dotted line represents the exponential distribution. The dashed line is a Weibull distribution (E.1) with shape $\beta = 0.7$ and scale parameter $\lambda = 1$.

Interplay between turbulence and rheology. The natural question that arises is: Does the Weibull distribution has a specific impact in the statistical modeling of the number of fragments ? To address this question, let us comment on the short-time and the long-time asymptotics of our model.

Large-time asymptotics. Large-time asymptotics can be estimated by the means of the Laplace transform, a common tool in the theory of renewal processes. Defining $\hat{\rho}(k, s) = \int_0^\infty \mathrm{d}t\, e^{-st}\rho(k, t)$ and $\hat{\Psi}(k, s) = \int_0^\infty \mathrm{d}t\, e^{-st}\Psi(k, t)$, one obtains from Eq. (5.11) the relation

$$\hat{\rho}(k, s) = \hat{\Psi}(s)^k \, \frac{1 - \hat{\Psi}(s)}{s}$$

The Weibull distribution has a finite mean $\tau \approx 0.3\tau_L$. This means that $\Psi(s) = 1 - s\tau + o(s)$ and $\hat{\rho}(k, \tau) = \tau e^{-ks\tau}(1 + o(1))$ as $s \to 0$. This implies that on times $t \gg \tau$, the distribution $\rho(k, t)$ is akin to that derived from exponential waiting times, and

$$\rho_t(k) \approx \tau\delta(t - k\tau) \quad \text{as} \quad t \gg \tau \tag{5.13}$$

The effect of turbulence and of the large-time correlation of the shear rate is then fully prescribed by the average waiting time τ. The fact that the inter-buckling time is a Weibull distribution rather than an exponential function does not play a specific role. For the modeling, this means that we can rely on continuous time approximation using the relation $P(N, k\tau) \approx P(N|k)$ for large times $k\tau$; This justifies the use of practical kinetic description, as described in Appendix F, where we characterize the fragmentation process using the various fragmentation rates estimated in the paper attached in §5.5.

Short-time asymptotics. To comment on this case, let us consider the case where daughter fragments are assumed to be too small to break again, and make the following further approximation: every buckling event identified as dangerous is a breaking event, that is all "dangerous buckling events" would trigger a fiber fragmentation for the original fiber of size ℓ, so that $\chi(1 \to 1) = 0$. In that case, one obtains

$$P_t(N) = \begin{cases} 1 - \int_0^t \Psi & \text{if } N = 1 \\ \chi(1 \to N)\int_0^t \Psi & \text{otherwise .} \end{cases} \tag{5.14}$$

In this case, the effect of turbulent fluctuations through the Weibull inter-buckling statistics is important. The probability of short waiting times is enhanced compared to a Brownian environment that would be characterized by an exponential distribution of waiting times with the same average. This observation concludes our analysis.

5.4 Perspectives
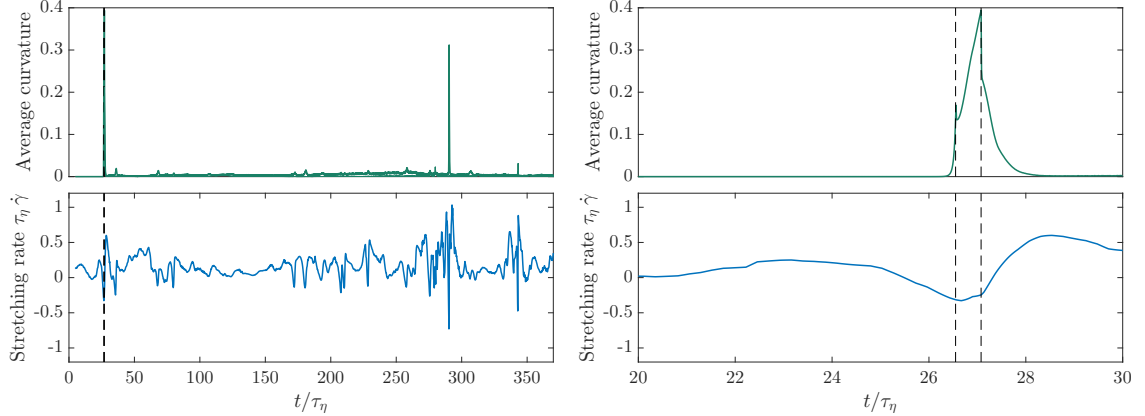
In this chapter, we have described two fundamental mechanisms leading to fragmentation of small brittle fibers in a turbulent flow. We presented a way to implement them in DNS, and sketched a stochastic framework to account for the full fragmentation process, depending on the Lagrangian statistics of the shear rate.

To summarize, the first mechanism is due to a compressive effort, for which the fiber achieves large values of the curvature and breaks by flexural failure. The second mechanism is due to an extensional effort, for which the fiber achieves large values of the tension and breaks by tensile failure.

The outcomes of those two mechanisms are very different, resulting in different sizes and numbers of the daughter fragments. Through tensile failure, fibers break into two pieces of equal length, each time that their internal tension supersedes a threshold $T^\star$. In our approach, those events are directly related to the shear rate reaching values $\propto T^\star/\ell^2$. This means that the stochastic modeling of tensile failure relates to the Lagrangian statistics of the maxima of the shear rate, and this fully prescribes not only the number but also the sizes of the daughter fragments. This observation clearly suggests that refined modeling of the extremal statistics of the shear rate is key to accurate account of fragmentation.
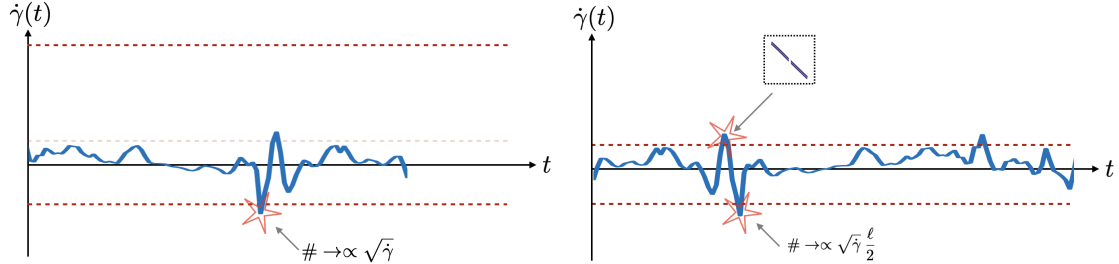
At this point, a natural question could also be: Is this result fully realistic? Anyone who ever tried to break an elongated body in two equal pieces by pulling it on both sides may object that it is very hard to obtain exactly two pieces of equal size! The reason comes from the fact that in our daily environment material objects have microscopic internal defects that favor the fragmentation near their neighborhood. Hence, a step toward a more realistic description of tensile failure could involve a random distribution of defects along the fiber, whose specific properties may depend on the type of material and on the corresponding physics of the so-called fragile rupture (Landau and Lifshitz, 1959).

We implemented the flexural failure mechanisms in our numerics by breaking at positions along the fibers where the local curvature is larger than a critical value $\kappa^\star$. We observe that this simple mechanism is likely to trigger an effect reminiscent of a "random cascade" of successive flexural failures. Hence, the number of pieces that a buckling event produces is not necessarily two. In the SBT framework, we argued that such a fragmentation process produces a number of pieces $\propto \dot{\gamma}^{1/2}\ell^2$; This number is determined from linear analysis, and relates to the most unstable buckling mode developed, given by the specific instantaneous negative shear rate $\dot{\gamma}$. This estimate provides a convenient way to estimate the rate of flexural failures in our stochastic framework. This rate probably overestimate the number of pieces produced by a dangerous event, and could be further substantiated by precisely tracking down the flexural failures along Lagrangian trajectories as illustrated in Fig. 5.9.

Figure 5.9: Top panel: evolution of the bending energy along the fiber trajectory. Bottom panel: evolution of the shear rate, together with the critical value to going down a buckling instability of fibers with a flexibility of $\mathcal{F} = 3.2 \times 10^5$. In both panels the dash-point lines show the times of fragmentation on the fiber.

Another issue relates to accurate statistical modeling of the interplay between the two fragmentation mechanisms beyond the mean-field. We here studied the flexural and tensile fragmentation processes independently from one another, but we appreciate that those processes do not commute: Both mechanisms have their outcomes depend non-linearly on the sizes of the fiber. Fig. 5.10 shows an explicit example that a tensile failure followed by a flexural failure does not yield the same number of pieces as a flexural failure followed by a tensile failure of same magnitudes. Hence, the time-ordering of the sequences is a crucial parameter when it comes to determine the statistics of the fragmentation.

Figure 5.10: Illustration of the non commutativity of flexural and tensile failure. In the left panel a flexural failure initiates the fragmentation processa and in the right panel a tensile failure.

Finally, let us here point out that our analysis relied on several important simplifying modeling assumptions. Relaxing them could constitute interesting exercises, in order to analize how much those simplifications impact the modeling of fragmentation processes within turbulence. In our numerics, we did not implement any kind of relative dispersion between the daughter fragments coming from a same ancestor. This approximation greatly simplified our numerics, but constitutes an obvious shortcoming to accurately describe long-time statistics of the fragmentation. In reality, the chaotic exponentiation followed by the explosive separation of trajectories known to occur in turbulent flows should tend to separate them apart in the long term. In the stochastic modeling, this phenomenon could be reflected at the level of the transition kernels.

In our practical use of our stochastic framework, we also restricted ourselves to the description of the first dangerous event leading to break-up, assuming that initial size is so small that the daughter fragments have sizes and corresponding flexibilities which in practice prevent them from being broken again by turbulent fluctuations. This is also quite a crude approximation, which would for example not hold were we to study the statistics of long fibers, *e.g.* longer than the Kolmogorov scale.

Finally, our most salient observation is perhaps the fact that fibers undergo a process very reminiscent of a cascade of fragments, but without inertia. It has been long argued in the scientific literature that when genuine massive fibers breaks, flexural waves propagate which carry the flexural failure from the initial breaking point throughout one end of the fiber, and produce highly non-homogeneous fragmentation distributions. Studying fragmentation of massive fibers within turbulence is therefore another natural perspective that could build on the present work.

5.5 Reproduction of the paper: "Dynamics and fragmentation of small inextensible fibers in turbulence"

We here reproduce the paper "Dynamics and fragmentation of small inextensible fibers in turbulence" published in Philosophical transactions A, that was co-authored with Jérémie Bec and Christophe Henry.

Research

Author for correspondence:
Jérémie Bec
e-mail: jeremie.bec@mines-paristech.fr

Dynamics and fragmentation of small inextensible fibres in turbulence

Sofía Allende[1], Christophe Henry[2] and Jérémie Bec[1]

[1]MINES ParisTech, PSL Research University, CNRS, CEMEF, Sophia-Antipolis, France
[2]Université Côte d'Azur, INRIA, Team TOSCA, Sophia-Antipolis, France

JB, 0000-0002-3618-5743

The fragmentation of small, brittle, flexible, inextensible fibres is investigated in a fully developed, homogeneous, isotropic turbulent flow. Such small fibres spend most of their time fully stretched and their dynamics follows that of stiff rods. They can then break through tensile failure, i.e. when the tension is higher than a given threshold. Fibres bend when experiencing a strong compression. During these rare and intermittent buckling events, they can break under flexural failure, i.e. when the curvature exceeds a threshold. Fine-scale massive simulations of both the fluid flow and the fibre dynamics are performed to provide statistics on these two fragmentation processes. This gives ingredients for the development of accurate macroscopic models, namely the fragmentation rate and daughter-size distributions, which can be used to predict the time evolution of the fibre size distribution. Evidence is provided for the generic nature of turbulent fragmentation and of the resulting population dynamics. It is indeed shown that the statistics of break-up is fully determined by the probability distribution of Lagrangian fluid velocity gradients. This approach singles out that the only relevant dimensionless parameter is a local flexibility which balances flow stretching to the fibre elastic forces.

This article is part of the theme issue 'Fluid dynamics, soft matter and complex systems: recent results and new methods'.

1. Introduction

The fragmentation process, which consists in breaking a body in different pieces, is very common and relevant to a wide range of phenomena in science and technology [1,2]. Natural examples occurring at different length scales are numerous, from break-up in DNA chains [3,4] to meteors in space [5]. Moreover, a precise understanding of the material properties involved in the breaking process proves fundamental in several industrial applications, as in combustion [6] or in wastewater treatment [7]. Traditionally, fragmentation is modelled from a macroscopic point of view using statistical approaches (e.g. [8–11]) to predict the time evolution of fragment size distributions from empirical observations. It relies on population balance models, which are based on a set of PDEs giving the mean-field behaviour of a population of objects. Such models require information on two quantities: the fragmentation rate (i.e. the frequency of the break-up events) and the daughter size distribution (i.e. the size of all fragments generated by a break-up event). New models for these two quantities are needed to account for the effects of fluctuations and fine physical phenomena occurring during break-up.

We focus here on the fragmentation of brittle elongated particles with a constant length, which will be called inextensible fibres in the following. From the point of view of material sciences, a brittle material breaks under the action of an external force with little elastic deformation and without plastic deformation [12]. In essence, break-up at the molecular level occurs when the local stress overcomes the internal cohesion between molecules. In the case of brittle fragmentation, the fracture induced by this rupture of equilibrium is assumed to propagate instantaneously at the material level leading to the fragmentation of the whole object [10,13]. At the scale of the fibre, this fragmentation can occur due to three different actions: tensile failure occurs when the external force acts to stretch the fibre along its main axis; flexural failure happens when an external torque induces a flexion perpendicular to the fibre main axis; torsional failure occurs when the fibre is twisted by an applied torque. In the present case of brittle materials, we consider the simplest approximation of the fragmentation process where failure happens as soon as a given threshold is reached. In that case, three thresholds are defined for each failure mechanism: a stretch force in tensile failure, a bending angle in flexural failure and a twisting angle in torsional failure. These three thresholds are actually related to each other since they all depend on the material properties and geometry (which govern fragmentation at the molecular level).

This study addresses more specifically the case of inextensible fibres immersed in a fluid. Such situations are found in a number of applications. For example, in the paper industry, cellulose fibres have been investigated in [14]. In a biological context, fibre dynamics have been used to model diatom phytoplankton colonies in the ocean [15] and organic matter at fresh water intakes [16]. Besides, we consider the case of fibres that are smaller compared with the smallest fluid scale (the Kolmogorov scale in turbulent flows). In that case, the dynamics of a fibre is determined by the action of three forces: bending elasticity, viscous drag and internal tension. The fibre will mostly experience tensile and flexural failures due to its stretching or compression by the flow, while torsional failure is negligible due to the fluid flow linearity at such small scales. Bending elasticity and viscous drag act together to stretch the fibre, making it akin to a stiff rod. Tensile failure then occurs when the local tension reaches values above a threshold. However, when fibres change their directions and experience strong-enough compression, their configurations can become buckled [17]: this is known as the buckling instability. The instability has been well documented for simple steady shear flows [18], in which there exists a critical value of the flexibility above which buckling occurs. Clearly, flexural failure can only occur when the fibre buckles and the curvature overcomes a threshold.

The problem of turbulent fragmentation has been essentially addressed for droplets [19,20], fractal flocs [21] and microscopic polymers [22,23]. The break-up of macroscopic fibres has been essentially addressed in laminar flow [24]. Accurate predictions in turbulent flows require extending such work to strongly fluctuating environments and interpreting them within a statistical framework. Remarkably, a similar dynamics holds true for fibres immersed in highly fluctuating environments. For instance, it was shown in [25], that the dynamics of inextensible

Table 1. Numerical and physical parameters of the direct numerical simulation: N^3 number of collocation points, ν kinematic viscosity, Δt time step, $\bar{\varepsilon}$ average kinetic energy dissipation rate, $\eta = \nu^{3/4}/\bar{\varepsilon}^{1/4}$ Kolmogorov dissipative scale, $\tau_\eta = \nu^{1/2}/\bar{\varepsilon}^{1/2}$ Kolmogorov time, u_{rms} root-mean square velocity, $L = u_{\mathrm{rms}}^3/\bar{\varepsilon}$ large-eddy length scale, $\tau_L = L/u_{\mathrm{rms}}$ large-eddy turnover time, $R_\lambda = \sqrt{15}\, u_{\mathrm{rms}}^2/(\nu^{1/2}\bar{\varepsilon}^{1/2})$ Taylor-based Reynolds number.

N^3	ν	Δt	$\bar{\varepsilon}$	η	τ_η	u_{rms}	L	τ_L	R_λ
4096^3	10^{-5}	6×10^{-4}	3.8×10^{-3}	7.16×10^{-4}	0.051	0.19	1.86	9.68	731

fibres that are smaller than the Kolmogorov scale in turbulent flow follow most of the time that of stiff rods. Deviations occur when the fibres experience strong-enough local compression, making them buckle. Such events are very rare and intermittent, because of the long-term Lagrangian correlations of turbulent velocity gradients. During these events, the stresses experienced by the particles can be strong enough to lead to their break-up. In fact, turbulent flows are known to generate very large velocity gradients, and those, in turn, may initiate a fragmentation process. Our aim here is to provide such statistics on the mechanisms of fibre break-up in a turbulent flow with dilute fibre suspensions, and specifically to characterize the statistics of the extrema of both the tension and the curvature. Those statistics obtained with fine-scale simulations of individual fibres are used as the basic ingredients, in order to develop accurate macroscopic models, relevant for the above-mentioned natural and industrial applications. Such models predict the time evolution of the fibre size distribution. A question that we want to address relates to the generic nature of turbulent fragmentation processes and of the resulting population dynamics. Turbulent fluctuations are indeed expected to be sufficiently generic to ensure universal behaviours, as for instance observed in [26] for the fragmentation of cracking solids.

To address this problem, we resort to numerical approaches that couple highly resolved turbulent flow simulations to fibre dynamics simulations using the slender-body equation (see below). We focus on the case of inextensible fibres that are brittle, smaller than the Kolmogorov scale and that do not have an effect on the fluid.

This paper is organized as follows. In §2, we give a brief description of our settings, including the slender body theory used to model fibres and the numerical tools used to simulate their dynamics in turbulent flow. We moreover give an overview of the mechanisms pertaining to fibre fragmentation (tensile failure and flexural failure). In §3, we investigate tensile failure and show that it occurs when the fibre is straight. Consequently, the tension is always maximal at its middle and the fibre always breaks in two equal pieces. We also give predictions on the rate at which such failures happen and compare them to numerics. In §4, we turn to flexural failure that happens when the fibre buckles. Thanks to a linear analysis of this instability, we obtain predictions on the associated break-up rates and on the resulting size distribution. Finally, in §5 we summarize our findings and draw some perspectives.

2. Model and numerical method

The objective is to investigate fragmentation processes in a fully developed, homogeneous, isotropic turbulent flow. To that aim, we use direct numerical simulations of the three-dimensional incompressible Navier–Stokes equation. We use the pseudo-spectral solver *LaTu* with 4096^3 collocation points and a third-order Runge–Kutta time marching [27]. A force is added at each time step to keep the kinetic energy constant in the two first Fourier shells. This leads the velocity field to reach a statistically stationary, homogeneous, isotropic turbulent state. The Eulerian parameters of the simulation are summarized in table 1.

Once in a statistical steady state, the flow is seeded with several millions of tracers. Their dynamics is integrated with the same time marching as the fluid and using a cubic interpolation of the velocity field at their location. Their trajectories together with the fluid velocity gradients

at their location are stored with a period $20\Delta t \approx 0.23\,\tau_\eta$ for a time duration of $63\,000\,\Delta t \approx 740\,\tau_\eta \approx 3.9\,\tau_L$). These data are used *a posteriori* to integrate the dynamics of flexible fibres.

We consider very thin fibres that can be approximated as inextensible Euler–Bernoulli beams immersed in a viscous fluid and whose dynamics is thus given by the *local* slender-body theory (e.g. [18]). This model employs fibres with length ℓ and circular cross-section with radius a; the aspect ratio is $\epsilon = a/\ell \ll 1$. The position and conformation of a given fibre is then described by a curve $s \mapsto \mathbf{X}(s,t)$, parametrized by the arc-length coordinate $s \in [-\ell/2, \ell/2]$. We moreover assume that the fibre's inertia is negligible, so that its dynamics is obtained by balancing locally the viscous drag with the fluid to tension and bending elasticity, so that

$$\partial_t \mathbf{X} = \mathbf{u}(\mathbf{X},t) + \frac{1}{\mu}\,\mathbb{D}\left[\partial_s(T\,\partial_s\mathbf{X}) - E\,\partial_s^4\mathbf{X}\right], \quad \text{with } |\partial_s\mathbf{X}|^2 = 1 \tag{2.1}$$

where

$$\mu = \frac{8\pi\,\rho_f\,\nu}{b} \quad \text{and} \quad \mathbb{D} = \mathbb{I} + \partial_s\mathbf{X}\,\partial_s\mathbf{X}^{\mathsf{T}},$$

where the specific form of the mobility matrix $\mathbb{D}$ arises from the anisotropic drag exerted by the fluid on the slender fibre. This equation is supplemented with the free-end boundary conditions $\partial_s^2\mathbf{X} = 0$ and $\partial_s^3\mathbf{X} = 0$ at $s = \pm\ell/2$. In the above equations, ρ_f is the fluid mass density, E is the fibre's bending modulus (also called flexural rigidity) defined as $E = YI$ (with Y the Young modulus and I the fibre's moment of inertia) and the parameter $b = -\ln(\epsilon^2 e)$ is much larger than 1. The fluid velocity field is denoted by $\mathbf{u}$. We focus on situations where fibres have a very low volume concentration. In this very diluted regime, they are passively transported by the fluid flow, and hence do not influence the dynamics of the advecting velocity field $\mathbf{u}$. The tension, denoted $T(s,t)$, is the Lagrange multiplier associated with the inextensibility constraint $|\partial_s\mathbf{X}|^2 = 1$. The tension is intrinsically non-local. The equation it solves is obtained by requiring that $\partial_t|\partial_s\mathbf{X}|^2 = 0$ and reads

$$\partial_s^2 T - \frac{1}{2}|\partial_s^2\mathbf{X}|^2\,T = 3\,E\,|\partial_s^3\mathbf{X}|^2 + \frac{7}{2}E\,\partial_s^2\mathbf{X}^{\mathsf{T}}\partial_s^4\mathbf{X} - \frac{\mu}{2}\,\partial_s\mathbf{X}^{\mathsf{T}}\mathbb{A}(\mathbf{X},t)\,\partial_s\mathbf{X}, \tag{2.2}$$
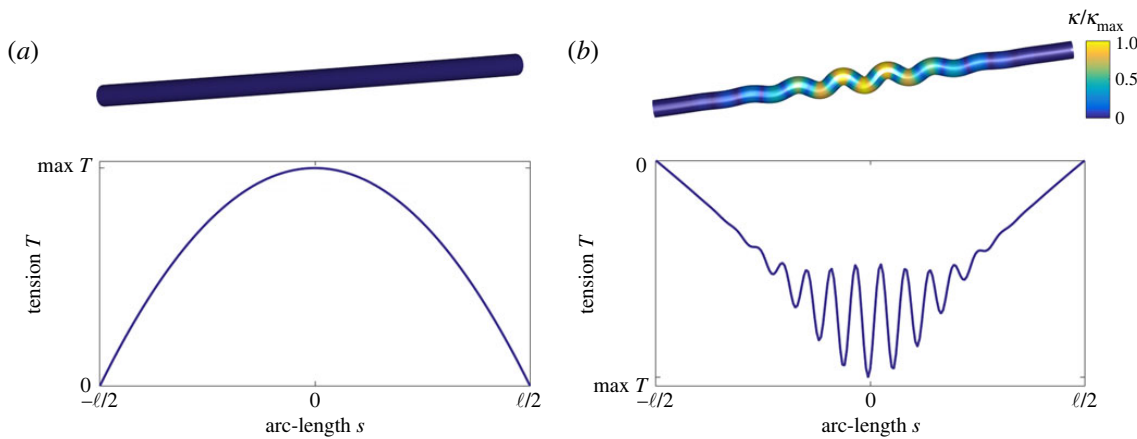
with the boundary conditions $T = 0$ at $s = \pm\ell/2$. Here $\mathbb{A}$ denotes the velocity gradient $\mathbb{A}_{ij}(\mathbf{X},t) = \partial_j u_i(\mathbf{X},t)$. This equation is equivalent to the Poisson equation satisfied by pressure in incompressible fluid dynamics.

We assume that the fibres have a length ℓ much smaller than the Kolmogorov dissipative scale η. It is easily checked that their centre of mass $\bar{\mathbf{X}}(t)$ then follow the dynamics of simple tracers, namely $d\bar{\mathbf{X}}/dt = \mathbf{u}(\bar{\mathbf{X}},t)$. Moreover, the fluid velocity variations along the fibres can be linearized, $\mathbf{u}(\mathbf{X},t) \approx \mathbf{u}(\bar{\mathbf{X}},t) + \mathbb{A}(\bar{\mathbf{X}},t)(\mathbf{X} - \bar{\mathbf{X}})$ with a local velocity gradient $\mathbb{A}$ that is constant along the fibre. Under these assumptions, we integrate the local slender-body equation (2.1) along the above-mentioned tracer trajectories, using the finite-difference scheme of [28] with $N = 201$ grid points along the fibre arc-length. The inextensibility constraint is enforced by a penalization method. Time marching uses a semi-implicit Adams–Bashforth scheme with a Lagrangian time step $\Delta t_{\text{fib}} = 2.5 \times 10^{-5}$. We use a linear interpolation in time to estimate the velocity gradient at a frequency higher than the output from the fluid simulation. Note that the time step required for the fibres is much smaller than that of the fluid. Indeed, we observe that, even by using a semi-implicit scheme, the problem remains particularly stiff when E is small or, equivalently, μ is large. As we will now see, these values of the parameters are of particular relevance.

In addition to the Reynolds number R_λ of the fluid flow, which is prescribed very large, the dynamics of a given fibre depends on a single dimensionless parameter only: the non-dimensional flexibility

$$\mathcal{F} = \frac{8\pi\,\rho_f\,\nu\,\ell^4}{b\,E\,\tau_\eta}. \tag{2.3}$$

This parameter appears when non-dimensionalizing equation (2.1) with the two relevant scales entering the dynamics and deformation of small fibres, namely their length ℓ and the Kolmogorov dissipative time τ_η. The non-dimensional flexibility can be understood as the ratio between the time scale of the fibre elastic stiffness to that of the turbulent velocity gradients. For small values of $\mathcal{F}$, the fibre is very rigid and behaves as a rod, while for large $\mathcal{F}$, it is very flexible and bends.

Figure 1. Instantaneous configuration of a fibre with non-dimensional flexibility $\mathcal{F} = 1.6 \times 10^5$ during a buckling event (b) and as a stiff rod (a). Top: the colour rendering shows the fibre curvature. Bottom: tension as a function of the arc-length at the same instant of time. (Online version in colour.)

In this second case, which corresponds to long fibres (small values of E or large values of μ), the dynamics is much richer and the fibre develop into non-trivial geometrical configurations (see top panels of figure 1).

When the fibre is in a fully straight state (figure 1a), one can assume that the tangent vector is constant, i.e. $\partial_s \mathbf{X}(s, t) = \mathbf{p}(t)$ at all values of s. As shown in [28], its direction $\mathbf{p}$ is then a solution of Jeffery's equation for straight inertialess ellipsoidal rods

$$\frac{\mathrm{d}}{\mathrm{d}t}\mathbf{p} = \mathbb{A}\,\mathbf{p} - \dot{\gamma}\,\mathbf{p}, \quad \text{with} \quad \dot{\gamma}(t) = \mathbf{p}^{\mathsf{T}}\mathbb{A}(t)\,\mathbf{p}. \tag{2.4}$$

The orientation $\mathbf{p}$ is sheared and rotated by the velocity gradient tensor $\mathbb{A}$, and the stretching/compression component given by $\dot{\gamma}$ is removed in order to fulfill the constraint $|\mathbf{p}| = 1$. The corresponding term in the right-hand side of (2.4) indeed originates from the tension in the slender-body equation (2.1). The later is obtained by from (2.2) with $\partial_s \mathbf{X} = \mathbf{p}$, leading to

$$T(s, t) = -\frac{\mu}{4}\,\dot{\gamma}(t)\left(s^2 - \frac{\ell^2}{4}\right), \tag{2.5}$$

meaning that the tension is maximal in the middle of the fibre and follows a parabolic shape with the arc-length coordinate s (figure 1a). When the fibre is strongly compressed ($\dot{\gamma} < 0$), the straight configuration might become unstable, leading to buckling (figure 1b). In that case, the tension can display several local extrema (this will be discussed later in §a).

In turbulence, fibres are most of the time in a straight state and very rarely buckle [25]. It was shown there that the buckling instability develops when the instantaneous value of $\dot{\gamma}$ takes large negative values. Besides, velocity gradients in turbulent flows can experience arbitrarily large fluctuations. This impacts the dynamics of the fibre, and in particular the transition rates between the straight and the buckled configurations. Explicitly, the fibres behave as stiff rods in calm regions, and fibres bend/stretch more frequently in very fluctuating regions.

Large turbulent fluctuations may then initiate a break-up process. Indeed, strong stretching and compression by the flow produces large values of the tension and curvature, respectively. As anticipated, two mechanisms can then initiate a fragmentation: *tensile failure* when the fibre breaks because the local tension is too high, and *flexural failure* when the fibre breaks due its curvature being too large. Large positive values of the tension leading to tensile failure are attained when the fibre is in a fully straight configuration and experiences a strong shear from the flow, as shown in figure 1a. In this configuration, the bending energy is zero, thus the tension balance the stretching due to velocity gradients. The solution of the tension is then a parabola, where the maximum is attained in the middle of the fibre—as transpires from equation (2.5).

Conversely, as is illustrated on the top panel of figure 1b, the curvature becomes very large during buckling. Such large values of the curvature could lead to fragmentation through flexural failure. These instabilities are typically dominated by a single mode with symmetric properties. Such modes depends on the flexibility of the fibre and on the magnitude of the compression by the flow. Depending on which of these two mechanisms is predominant, the fibres might break at different locations. This could imply very different evolutions of the distribution evolution of the fibre size distribution [29].

3. Fragmentation through tensile failure

We here start by investigating fragmentation due to large values of the tension. This occurs when the maximal tension along the fibre is larger than a critical value $T^\star$ that depends on its material properties. To estimate the contribution of this mechanism to the fragmentation process, we need to study both the rate $\lambda_T(T^\star)$ at which a large tension is attained and the location where the maximum is located on the fibre.

Large tensions are reached when the fibre experiences a strong stretching along its main axis and is thus generally in a fully straight state. In that case, we have seen in the previous section (cf. equation (2.5)) that the tension is a concave parabola with its maximum

$$T_{\max} = \frac{\mu\,\dot{\gamma}\,\ell^2}{16},\tag{3.1}$$

reached at the middle of the fibre. As a consequence, a tensile failure will always break short fibres in two equal pieces, giving a trivial daughter distribution. It should be noted here that this is true for fibres without molecular defects (i.e. $T^\star$ is constant along the fibre length).

Another consequence is that tensile failure occurs when the stretching rate along the fibre exceeds a critical value, namely $\dot{\gamma} > 16\,T^\star/(\mu\ell^2)$, and thus when the velocity gradient reaches strong positive values. Turbulent gradients along the Lagrangian path are known to display very sharp fluctuations and oscillations. This implies that the rate at which a large value of $\dot{\gamma}$ is exceeded, is approximately proportional to the probability distribution at this value, so that
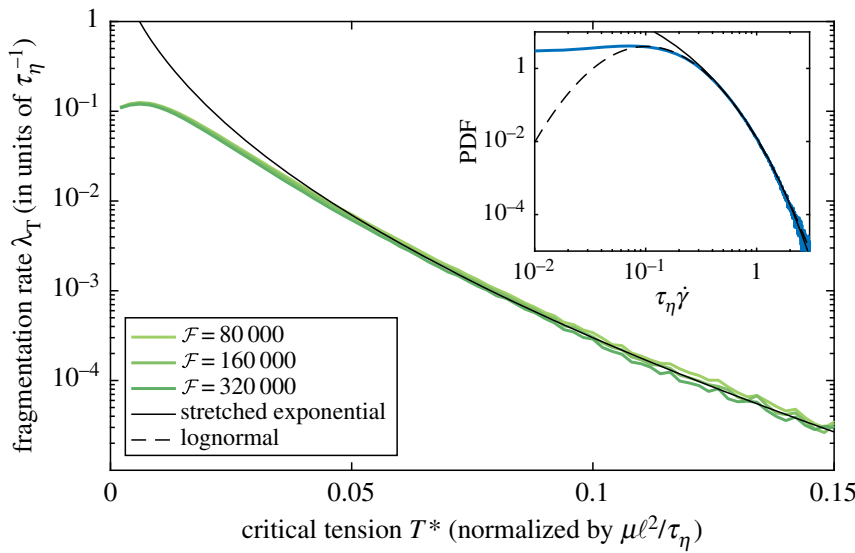
$$\lambda_T(T^\star) \propto \Pr\left(\dot{\gamma} > \frac{16\,T^\star}{(\mu\ell^2)}\right).\tag{3.2}$$

The right-hand side involves the distribution of $\dot{\gamma}$ and thus that of fluid velocity gradients. In large-Reynolds-number turbulence, this distribution is fairly approximated by a lognormal with far tails which are actually closer to a stretched exponential with an exponent $\approx 1/2$—e.g. [30–33]). Either of these two behaviours are compatible with our observations: For large values of the tension it is not possible to distinguish one from the other. The inset of figure 2 shows the probability density function of the stretching rate $\dot{\gamma}$. Its behaviour at positive values is well represented by a lognormal distribution when $\dot{\gamma}$ is of the order of τ_η^{-1} with a far tail at $\dot{\gamma} \gg \tau_\eta^{-1}$ that rather approach a stretched exponential behaviour. As stressed in [34], the coefficients used in fits have a non-trivial dependence upon the Reynolds number. From now on, we focus on the case $R_\lambda = 731$, as chosen in our simulation. We will come back to this dependence in the conclusions.

These considerations suggest to use these two possibles forms to fit the tensile fragmentation rate λ_T as a function of the physical parameters of the fibre. When $T^\star/(\mu\ell^2) \gg \tau_\eta^{-1}$, a stretched-exponential form is expected to be more relevant, so that

$$\lambda_T(T^\star) \approx \lambda_0\,\exp\left[-a\left(\frac{\tau_\eta\,T^\star}{\mu\ell^2}\right)^{1/2}\right],\tag{3.3}$$

with fitting parameters a frequency, λ_0, and a dimensionless constant a. As can be seen in figure 2, such a formula gives indeed a good approximation to numerical calculations of the tensile fragmentation rates.

Figure 2. Tensile fragmentation rate λ_T as a function of the critical tension $T^\star$ for various values of the non-dimensional flexibility $\mathcal{F}$. The rate has been non-dimensionalized by τ_η^{-1} while the x axis displays $\tau_\eta T^\star/(\mu\ell^2)$. The solid line is the stretched-exponential fit (3.3) with $\lambda_0 = 14/\tau_\eta$, $a = 34$ and $\tau \approx \tau_\eta$. The dashed line is the lognormal fit (3.4) with $\lambda_0' = 0.13/\tau_\eta$, $a' = 1.12$ and $\tau = 102\,\tau_\eta$. Inset: Probability density function (PDF) of the stretching rate $\dot\gamma$ at positive values (blue bold solid line, blue online), together with a stretched exponential fit (thin line) and a lognormal fit (dashed line). (Online version in colour.)

At $T^\star/(\mu\ell^2) \sim \tau_\eta^{-1}$, as can be seen in figure 2, the tensile fragmentation rate behaves as a lognormal, namely

$$\lambda_T(T^\star) \approx \lambda_0' \exp\left[-a'\left(\log\frac{\tau T^\star}{\mu\ell^2}\right)^2\right], \tag{3.4}$$
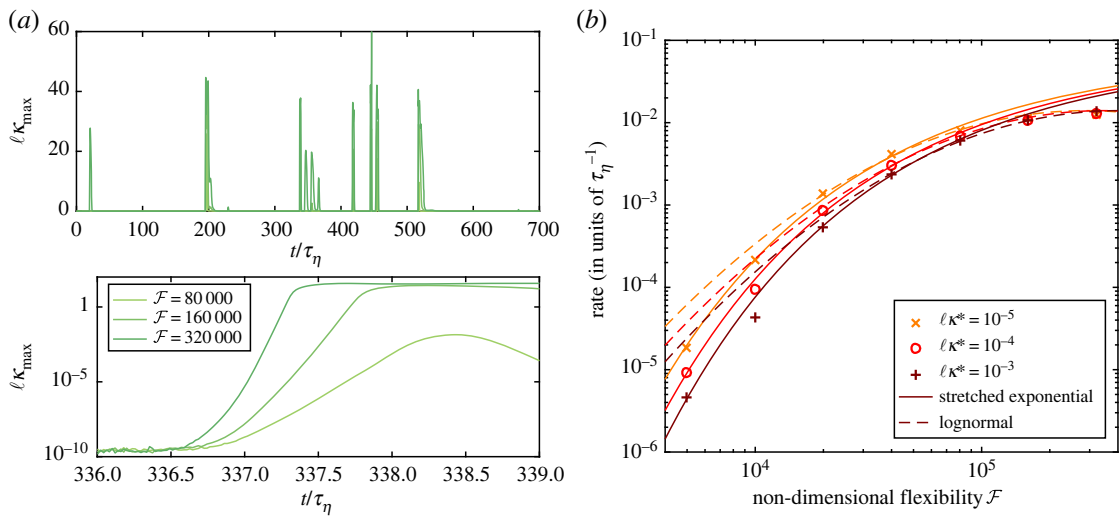
where a' is a dimensionless fitting constant, and λ_0' and τ are fitting parameters with dimensions of a frequency and a time, respectively. The values of these parameters reported in the caption suggest that, while λ_0' is of the order of the Kolmogorov time scale τ_η, the time τ is 100 times larger. This can be explained by the fact that $T_{\max}(\mu\ell^2) \sim \dot\gamma/16$ and in turn, as seen in [25], typical values of $\dot\gamma$ are of the order of $0.1/\tau_\eta$ leading to a factor of the order of 100.

To summarize this section, let us stress that tensile failure is here entirely prescribed by the (intermittent) statistics of the velocity gradients. This is a stylized feature of our approach, and provides a simplified framework to study fragmentation. Note that this assumption holds true only for small fibres. When considering fibres larger than the Kolmogorov length scale, the velocity gradient will not be uniform along the fibre. This implies in particular that the fibre could be locally stretched and compressed at the same time and breaks in pieces of arbitrary sizes.

Also, it is important to notice that reaching large values of the tension requires $\dot\gamma$ to locally exceed a critical value that is $\propto \ell^{-2}$. Tensile failure thus becomes rarer and rarer when fibres become smaller. In addition, the daughter population is typically centred over the half of the mother size. This implies that a fragmentation process involving only tensile failure cannot efficiently lead to the fast formation of small fragments. As we will see in the next section, this strongly differs when flexural failure is involved. In that case, many small segments can be created during a single event.

4. Fragmentation through flexural failure

Conversely to tensile failure, flexural failure displays a much more complicated behaviour. Such break-ups happen when the fibre is bent and, more precisely, when the curvature becomes larger than a given threshold. Then, there exists a location s along the fibre such that, at the

Figure 3. (*a*) Time evolution of the maximal curvature $\kappa_{\max}$ along a single turbulent tracer trajectory but for three different values of the non-dimensional flexibility $\mathcal{F}$. The upper part shows the full trajectory, while the lower is a semilogarithmic time zoom on the buckling event occurring at time $t \approx 337\,\tau_\eta$. (*b*) Rates at which the maximal curvature exceeds given values $\kappa^\star$ (as labelled) as a function of the non-dimensional flexibility. Each dataset is fitted by both a stretched exponential (solid curves) and by a lognormal (dashed curves). (Online version in colour.)

break-up time $t^\star$, one has $|\partial_s^2 \mathbf{X}(s, t^\star)| \geq \kappa^\star$. Clearly, as the curvature is continuous with respect to arc-length and time, such a break-up occurs at the first time when the maximum of curvature $\kappa_{\max} = \max_s |\partial_s^2 \mathbf{X}|$ exceeds $\kappa^\star$. As anticipated in §2, these events happen when the fibre undergo a buckling. Such an instability occurs when the instantaneous value of the stretching rate $\dot{\gamma}$ defined in equation (2.4) becomes large negative (compression). Figure 3*a* shows the time evolution of the fibre's maximal curvature along a Lagrangian trajectory for different values of $\mathcal{F}$. It can be seen that buckling events, for which $\kappa_{\max} \neq 0$, are very sparse and intermittent. Such events are separated by long periods, which can be of the order of the large-eddy turnover time, during which the fibre is fully straight, up to numerical precision. It is shown in [25] that in turbulence, the rate at which buckling appears is similar to an activation process. More precisely, it was found that the fibre buckles when its instantaneous flexibility $\mathcal{F}_{\mathrm{loc}}(t) = \tau_\eta\, |\dot{\gamma}(t)|\, \mathcal{F}$ becomes larger than a critical value $\mathcal{F}^\star$, provided that $\dot{\gamma}(t) < 0$. This leads to estimate the buckling rate as

$$\lambda_{\mathrm{Buckl}} \propto \mathrm{Pr}\left(\dot{\gamma} < -\frac{\mathcal{F}^\star}{(\tau_\eta\, \mathcal{F})} \right). \tag{4.1}$$

As in the case of tensile failure rates, the distribution of the stretching rate $\dot{\gamma}$ can be approximated either by a lognormal or by a stretched exponential, leading to approximations of the above formula. We expect the rate of flexural failure to be upper bounded by this buckling rate.

However, for break-up to occur, we additionally require that the maximum curvature exceeds $\kappa^\star$. The corresponding rates are shown in figure 3*b* as a function of the non-dimensional flexibility $\mathcal{F}$ and for various values of the threshold $\kappa^\star$. Lognormal and stretched exponential functional forms give good approximations with fitting parameters that depend on $\kappa^\star$. Understanding this dependence requires investigating more closely the development of the instability. Figure 3*c* shows the time growth of the maximum of curvature during one of these events for various values of the non-dimensional flexibility. One observes that the increase is approximately exponential with a rate that depends on $\mathcal{F}$. Small values of $\kappa^\star$ are reached during the instability growth and it is thus needed to characterize further this regime in order to quantify how this affect rates. The development of the buckling instability is furthermore of importance as flexural failure will actually not happen when the threshold is exceeded but rather when it is for the first time. At difference with tension that has fast fluctuations, the curvature has an on–off behaviour.

As can be seen in figure 3*c*, the growth of κ_{max} can be followed by a period during which it remains at finite values for quite some time. This indicates that the rates shown in figure 3*b* are actually overestimating the actual flexural failure rates. In the following, we provide more accurate estimates.

(a) Linear analysis and relevance to turbulent flows

The buckling instability occurs when the fibre, initially in a straight configuration $\partial_s \mathbf{X} \equiv \mathbf{p}$, experiences a strong compression by the flow. This is likely to happen when the flow locally displays a violent shear, so that the rodlike fibre is like a Jeffery orbit [35]: in that case, the rod rotates and is not aligned with the flow. During such event, the fibre alternatively experience stretching and compression along its main axis, giving it the opportunity to buckle. Performing a linear stability analysis for such orbits is however complex. Indeed, upon buckling, the initially straight fibre picks a specific trajectory among an infinite family. The selected trajectory depends on the initial perturbation and is very sensitive to fine sub-leading details, such as thermal noise [36], fibre or fluid inertia [37,38], or, as in our turbulent settings, the fact that the flow is not a pure shear.
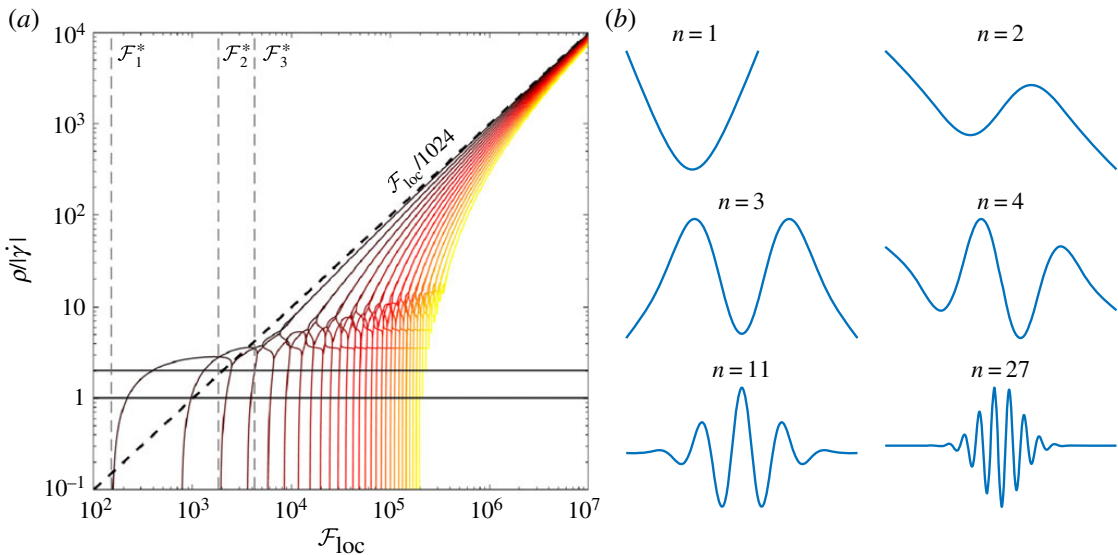
As we will see in the sequel, a simplified linear stability analysis already fairly describes buckling events, meaning that we can avoid delving into the complicated context of Jeffery orbits. Let us consider that the fibre experiences a time-constant compression $\dot{\gamma} = \mathbf{p}^{\mathsf{T}} \mathbb{A} \, \mathbf{p} < 0$ along its direction. The base solution $\mathbf{p}(t)$ describes a rod-like solution to the slender body equation (2.1). We introduce a perturbed solution as $\mathbf{X}(s, t) = \bar{\mathbf{X}}(t) + s \, \mathbf{p}(t) + \boldsymbol{\chi}(s, t)$, where $\bar{\mathbf{X}}(t)$ is the average position of the fibre centre of mass and the perturbation $\boldsymbol{\chi}$ is of small amplitude (i.e. $|\boldsymbol{\chi}| \ll \ell$). For buckling, we are interested in perturbations that grow perpendicularly to the fibre direction. The two transverse components of $\boldsymbol{\chi}$ are decoupled and evolve as (e.g. [18])

$$\frac{1}{|\dot{\gamma}|} \, \partial_t \chi = \chi + s \, \partial_s \chi + \frac{1}{4} \left(s^2 - \frac{\ell^2}{4} \right) \partial_s^2 \chi - \frac{E}{\mu \, |\dot{\gamma}|} \, \partial_s^4 \chi, \tag{4.2}$$

with the free-end boundary conditions $\partial_s^2 \chi = 0$ and $\partial_s^3 \chi = 0$ at $s = \pm \ell/2$. This linear equation admits solutions of the form $\chi(s, t) = e^{\rho t} \hat{\chi}(s)$, where $\hat{\chi}$ is the eigenfunction of the right-hand side of (4.2) associated with the eigenvalue ρ. Once time is rescaled by $\dot{\gamma}^{-1}$ and arc-length by ℓ, this eigenvalue problem depends on a unique non-dimensional parameter $\mathcal{F}_{loc} = \mu \, |\dot{\gamma}| \, \ell^4 / E$, which measures the ratio between the fluid compression and the elastic force. Because of the presence of non-constant coefficients, there is no straightforward way to obtain the full spectrum of eigenmodes as a function of the dimensionless flexibility $\mathcal{F}_{loc}$. Still, there are two trivial solutions given by $\rho / \dot{\gamma} = 1$ with $\hat{\chi} = \text{const.}$ and $\rho / \dot{\gamma} = 2$ with $\hat{\chi} = a \, s$ and a constant. For these two unstable modes, the fibre remains straight and does not buckle. To access more complicated configurations, we rely on integrating numerically equation (4.2).

Figure 4*a* represents the 30 most unstable eigenvalues as a function of the non-dimensional flexibility. A first non-straight mode becomes unstable when $\mathcal{F}_{loc} > \mathcal{F}_1^\star \approx 153$. This threshold is in agreement with [18]. This first growing mode, labelled as $n = 1$, is shown in figure 4*b*. When $\mathcal{F}_{loc}$ increases, there is a sequence of bifurcations with a change of the most unstable eigenfunction. We label these modes with the number n of extrema that $\hat{\chi}$ contains (see panel *b*). The first bifurcation is between order $n = 1$ and $n = 2$, which occurs at $\mathcal{F}_{loc} = \mathcal{F}_2^\star \approx 1840$. When $\mathcal{F}_{loc}$ further increases, the most unstable modes are of higher order n. It also appears from figure 4*b* that the amplitude of fluctuations decreases very fast as the arc-length coordinate s gets further from the fibre centre. One finally observes that when $\mathcal{F}_{loc} \to \infty$, the most unstable eigenvalues grow as $\rho / \dot{\gamma} \propto \mathcal{F}_{loc}$.

In this asymptotics of large dimensionless flexibility, the small parameter $\mathcal{F}_{loc}^{-1}$ multiplies the highest-order derivatives. This indicates that the limit is singular but could actually be tackled using a WKB (Wentzel, Kramers, Brillouin) perturbative approach (e.g. [39]). The WKB method

Figure 4. (*a*) Thirty largest eigenvalues associated with the linear evolution (4.2) as a function of $\mathcal{F}_{\mathrm{loc}}$. The two horizontal lines at $\rho = \dot{\gamma}$ and $\rho = 2\dot{\gamma}$ show the two unstable straight modes. The three vertical lines at $\mathcal{F}_{\mathrm{loc}} = \mathcal{F}_1^\star$, $\mathcal{F}_2^\star$ and $\mathcal{F}_3^\star$ are bifurcations above which the most unstable non-straight mode is $n = 1$, 2 and 3, respectively. The dashed line represents the asymptotic behaviour $\rho/\dot{\gamma} \simeq \mathcal{F}_{\mathrm{loc}}/1024$ reached at large values. (*b*) Illustrations of the fibre geometric state in eigenmodes of various orders n. (Online version in colour.)

suggests writing the solution as the exponential of an asymptotic series expansion

$$\hat{\chi}(s) \sim \exp\left(\frac{1}{\varepsilon}\sum_{p\geq 0}\varepsilon^p \varphi_p(s)\right), \tag{4.3}$$
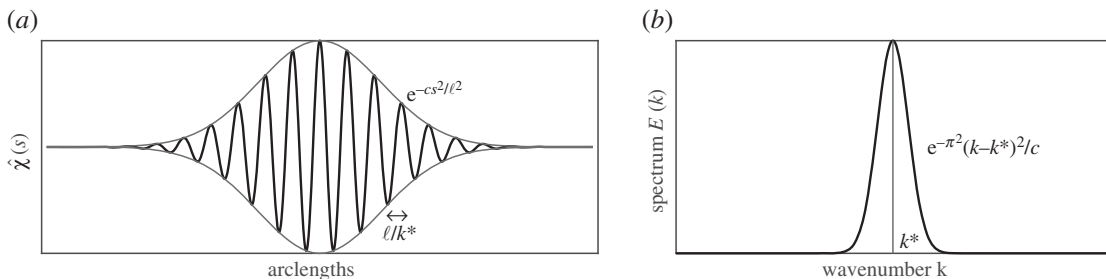
where $\varepsilon = \mathcal{F}_{\mathrm{loc}}^{-\delta}$ is a small parameter and $\varphi_p(s)$ are terms in the expansion. The exponent $\delta > 0$ is obtained by substituting the expansion (4.3) in (4.2) and balancing the leading-order terms. Far from the fibre's ends, one has

$$\frac{\rho}{|\dot{\gamma}|} = \frac{1}{4\,\varepsilon^2}\left(s'^2 - \frac{1}{4}\right)(\partial_{s'}\varphi_0)^2 - \frac{1}{\mathcal{F}_{\mathrm{loc}}\,\varepsilon^4}\,(\partial_{s'}\varphi_0)^4, \tag{4.4}$$

with $s' = s/\ell$. This gives $\varepsilon = \mathcal{F}_{\mathrm{loc}}^{-1/2}$ and $\rho/|\dot{\gamma}| \sim \mathcal{F}_{\mathrm{loc}}$, meaning that $\delta = 1/2$ and confirming the observed linear behaviour of the eigenvalues in the asymptotics of $\mathcal{F}_{\mathrm{loc}} \to \infty$. Besides, when $\mathcal{F}_{\mathrm{loc}}$ increases, the order n of the dominant mode becomes larger and the eigenfunction gets more localized at $|s'| \ll 1$. This suggests expressing the dominant term as $\varphi_0(s') = a_0 + a_1 s' + a_2 s'^2 + a_3 s'^3 + \cdots$. Now, using this expansion in (4.4) and balancing equal powers of s', one obtains to leading order

$$\frac{\rho}{|\dot{\gamma}|} = -\frac{\mathcal{F}_{\mathrm{loc}}}{16}\,a_1^2 - \mathcal{F}_{\mathrm{loc}}\,a_1^4, \quad \text{so that } a_1^2 = -\frac{1}{32} \pm \sqrt{\frac{1}{1024} - \frac{\rho}{|\dot{\gamma}|\,\mathcal{F}_{\mathrm{loc}}}}. \tag{4.5}$$

This leading term contributes an exponential behaviour $\propto \exp(\pm\sqrt{\mathcal{F}_{\mathrm{loc}}}\,a_1)$ at $s' = \pm 1$ in the eigenfunction $\hat{\chi}$. When the real part of b is non-zero, this term diverges as a function of $\mathcal{F}_{\mathrm{loc}}$ and this is incompatible with the imposed free-end boundary conditions. a_1 should thus be a pure imaginary number. This means that a_1^2 is real negative, and with (4.5), we get necessarily $\rho/\dot{\gamma} < \mathcal{F}_{\mathrm{loc}}/1024$, the maximal eigenvalue corresponding to the case when the bound is reached. This prediction gives the value $1/1024$ for the constant of the linear behaviour of ρ, in agreement with the measurements reported in figure 4. Note that for this specific eigenvalue, one obtains $a_1 = \mathrm{i}/\sqrt{32}$ (i being the imaginary unit).

Figure 5. (a) Typical asymptotic shape of the eigenfunctions consisting of a fast oscillation with a Gaussian envelope. (b) Spectrum $E(k) = |\mathbb{F}[\hat{\chi}](k)|^2$ of the same function, where $\mathbb{F}[\hat{\chi}]$ designates the Fourier transform of $\hat{\chi}$. It is a Gaussian centred at $k = k^\star$ with variance $c/(2\pi^2)$.

Moving on to higher-order terms, one can easily check that contributions of the order of s' vanish for the above value of a_1. As to the terms $\propto s'^2$, they give

$$0 = \frac{1}{4}a_1^2 - \frac{1}{16}(4\,a_2^2 + 6\,a_1 a_3) - \left(24\,a_1^2 a_2^2 + 12\,a_1^3 a_3\right). \tag{4.6}$$

Using $a_1 = i/\sqrt{32}$, we get $a_2 = -1/8$. This finally leads to writing $\varphi_0 \approx a_0 + i\,s'/\sqrt{32} - s'^2/8$.

This asymptotic analysis suggest to write the eigenfunction of order n as
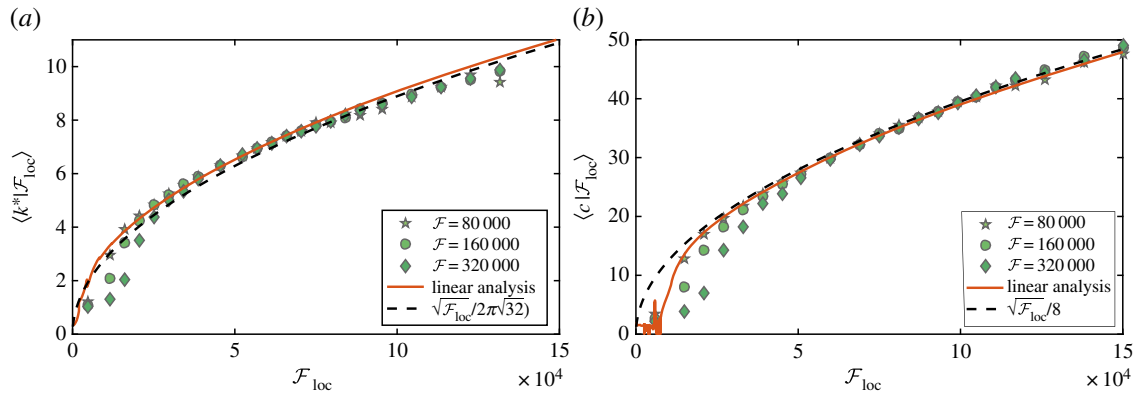
$$\hat{\chi}(s) = \begin{cases} e^{-c\,(s/\ell)^2}\cos(2\pi\,k^\star s/\ell) & \text{for } n = 2k^\star + 1 \text{ odd}, \\ e^{-c\,(s/\ell)^2}\sin(2\pi\,k^\star s/\ell) & \text{for } n = 2k^\star \text{ even}, \end{cases} \tag{4.7}$$

whose typical shape is represented in figure 5a. The above asymptotic analysis shows that the most unstable mode is characterized by an oscillating function with a wavelength $k^\star$ and a Gaussian envelope with a coefficient c. These two parameters are given by

$$k^\star \simeq \frac{\sqrt{\mathcal{F}_{\text{loc}}}}{2\pi\sqrt{32}} \quad \text{and} \quad c \simeq \frac{\sqrt{\mathcal{F}_{\text{loc}}}}{8}. \tag{4.8}$$

To estimate numerically $k^\star$ and c, we use the Fourier spectrum of the eigenfunction. It is defined as the squared modulus of the coefficients of the Fourier transform of $\hat{\chi}$. As illustrated in figure 5b, the spectrum of the asymptotic form (4.7) is a Gaussian function of k. The wavenumber $k^\star$ is approximated as the mean associated with this distribution, while the coefficient c is deduced from its variance. We use this approach to measure $k^\star$ and c as a function of $\mathcal{F}_{\text{loc}}$ for the eigenfunctions obtained numerically from the integration of the linear system (4.2). The results are displayed as solid curves on figure 6, together with the asymptotic predictions (4.8) displayed as black dashed curves. The good agreement between these curves confirm the relevance of the asymptotic analysis at large values of $\mathcal{F}_{\text{loc}}$ that we consider here.

Following this linear analysis, we then perform the same kind of analysis to the case of fibres that follow turbulent trajectories. To capture the dawn of the instability, we track fibres whose curvature, after having almost relaxed to zero, grows again and exceeds a given threshold. We use the fibre's shape at the instant of time when the threshold is first reached as an estimate of the growing mode. In such fluctuating settings, we make use of the instantaneous non-dimensional flexibility $\mathcal{F}_{\text{loc}} = \tau_\eta |\dot{\gamma}|\,\mathcal{F}$. For each event, we measure $k^\star$ and c from the Fourier spectrum of the fibre shape. We then compute their average value conditioned on the observed value of $\mathcal{F}_{\text{loc}}$. The resulting estimates are shown as symbols in figure 6 for three different values of $\mathcal{F}$. Clearly, these measurements show that the linear analysis reported above is able to describe the growth of buckling modes in turbulent flows, assuming that the relevant parameter is given by the instantaneous value of the non-dimensional flexibility.

Figure 6. Numerical estimates of the wavenumber $k^\star$ (*a*) and of the coefficient c of the Gaussian envelope (*b*) characterizing the most unstable mode. Results are shown both for the numerical integration of the linearized dynamics (solid curves) and for turbulent data (symbols associated with various $\mathcal{F}$, as labelled). The asymptotic predictions (4.8) are shown as black dashed curves. (Online version in colour.)

(b) Estimates for flexural fragmentation rates in turbulence

We now apply the above considerations to determine both the rate at which flexural failure occurs and the resulting daughter size distribution upon fragmentation. We assume that the fibres are brittle, so that they break as soon as their curvature exceeds a critical value $\kappa^\star$, which is relatively small. Because of that, break-up happens while the fibre is still at the beginning of a buckling event that can be described within the linear approximation. We moreover assume that the instability growth is given by eigenvalues and eigenfunctions that are properly described by the large-flexibility asymptotics of the previous subsection (this assumption is only valid if the growth rate is large enough to consider that the shear $\dot{\gamma}$ is constant during the instability and so $\mathcal{F}$ is large).
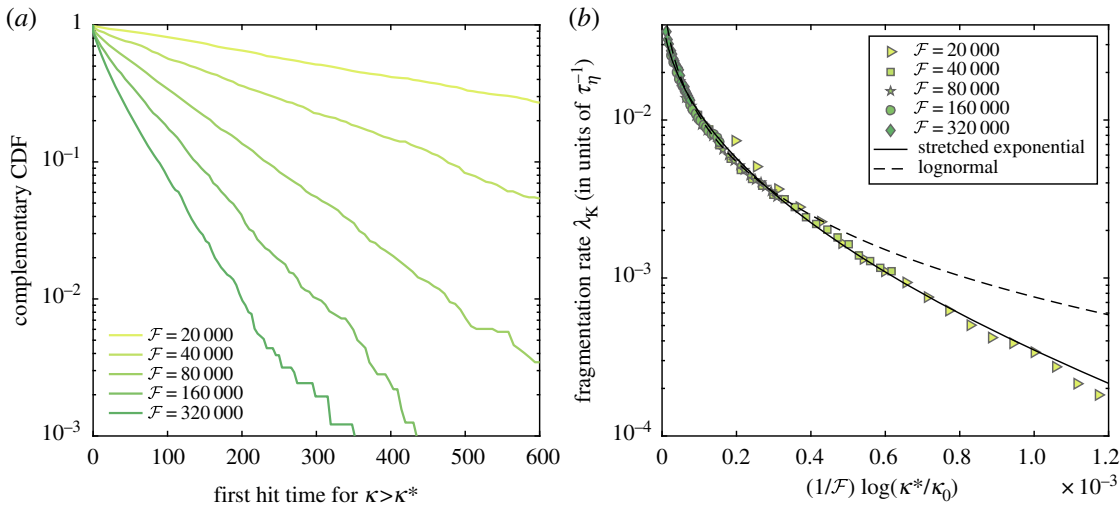
(i) Fragmentation rate

The rate at which flexural failure occurs is the rate at which the maximal curvature along a fibre exceeds for the first time the critical value $\kappa^\star$. A first condition for this to happen is to have the fibre developing a buckling: this requires $\mathcal{F}_{\mathrm{loc}} = \tau_\eta \, |\dot{\gamma}| \, \mathcal{F}$ becoming larger than a critical value $\mathcal{F}^\star$ at time t_0, which marks the beginning of the event. After that, the instability grows exponentially with a rate $\rho \simeq |\dot{\gamma}| \, \mathcal{F}_{\mathrm{loc}}/1024$. The maximal curvature also follows this growth, so that

$$\kappa_{\max}(t) \simeq \kappa_{\max}(t_0) \exp\left[\frac{\tau_\eta \, |\dot{\gamma}|^2 \, \mathcal{F}}{1024} \, (t - t_0)\right]. \tag{4.9}$$

Of course, without an initial curvature nothing would happen. It is indeed required to have initially a small deviation to the base state for the instability to develop. In physical situations, several effects give such perturbations, including thermal noise, material inhomogeneities along the fibres, a small extensibility, the fluid flow modifications due to the fibre, and more importantly, the sub-leading turbulent fluctuations that are neglected when we assume that the fibre samples a space-independent fluid velocity gradient. Such effects are clearly not in the model we use. Still, in our simulations, the instability is triggered by a small numerical noise that comes either from the accuracy of the method, from roundoff errors, or from the penalty approach that is used to enforce inextensibility. This error is visible in figure 3*c* where, before the buckling starts, one has $\kappa_{\max} \approx \kappa_0 \approx 2 \times 10^{-10} \, \ell^{-1}$.

No matter how small they are, arbitrary values of curvature are not necessarily reached by all buckling events. For instance, during the specific event shown in figure 3*c*, the maximal curvature barely reaches $\kappa_{\max} = 10^{-2} \, \ell^{-1}$ in the case of the fibre with the smallest flexibility. The growth rate

Figure 7. (a) Complementary Cumulative Distribution Function (CDF) of the first time at which the fibres curvature hits a value $\kappa^\star = 10^{-6}$, shown for various values of the flexibility, as labelled. (Time is here in units of τ_η.) (b) Fragmentation rate λ_K as a function of the dimensionless parameter $(1/\mathcal{F}) \log(\kappa^\star/\kappa_0)$, with a reference curvature set to $\kappa_0 = 2 \times 10^{-10}$. Symbols correspond to different values of $\kappa^\star$ and $\mathcal{F}$. The solid line is the stretched-exponential fit (4.12) with $\lambda_0 = 0.055 \, \tau_\eta^{-1}$ and $a = 160$. The dashed line is the lognormal fit (4.13) with $\lambda_0' = 0.06 \, \tau_\eta^{-1}, a' = 0.11$, and $b' = 13.12$. (Online version in colour.)

is there too small or, equivalently, compression does not last long enough. During this very event, the two other more flexible fibres reach much larger curvatures and saturate at $\kappa_{\max} \approx 30\ell^{-1}$. These distinct behaviours originate from large differences in the instability growth rates. The time during which the fibre is compressed is completely determined, either by the fluid flow through the Lagrangian persistence time of velocity gradients, or by the evolution of the base orientation $\mathbf{p}(t)$, which for instance perform a Jeffery orbit and tumbles. In both cases, the relevant time scale during which the fibre is compressed is of the order of $|\dot{\gamma}|^{-1}$.

A necessary condition for the fibre to break is thus that it reaches curvatures larger than $\kappa^\star$ on a time smaller than the compression duration $\simeq \alpha \, |\dot{\gamma}|^{-1}$, where α is an order-unity constant. Using the exponential law (4.9), one should thus have

$$t - t_0 \simeq \frac{1024}{\tau_\eta \, |\dot{\gamma}|^2 \, \mathcal{F}} \, \log\left(\frac{\kappa^\star}{\kappa_0}\right) < \alpha \, |\dot{\gamma}|^{-1}. \tag{4.10}$$

This leads to the following estimate for the rate at which flexural failure occurs:

$$\lambda_K(\kappa^\star) \propto \mathrm{Pr}\left(\dot{\gamma} < -\frac{\left[(1024/\alpha) \, \log(\kappa^\star/\kappa_0)\right]}{(\tau_\eta \, \mathcal{F})}\right). \tag{4.11}$$

This formula is similar to the buckling rate of equation (4.1) except that, this time, the critical non-dimensional flexibility depends on $\kappa^\star$. Also, it suggests that λ_K is simply a function of the dimensionless parameter $(1/\mathcal{F}) \log(\kappa^\star/\kappa_0)$ that can be fitted, as before, by either a stretched exponential or a lognormal.

To test this prediction numerically, the main difficulty is to estimate this rate from finite-time simulations. Depending on the values of the fibre flexibility and of the critical curvature, the typical time needed for the curvature to become larger than $\kappa^\star$ can be longer than the simulation duration. Hence, to estimate this rate, we have rather measured the probability distribution of the first time at which $\kappa_{\max}$ hits $\kappa^\star$. The complementary cumulative distribution function is shown in figure 7a for different flexibilities and a fixed value of the critical curvature. Clearly, one observes that the first-hit time follows an exponential law. Fitting such laws gives a straightforward way to estimate λ_K as a function of the two parameters $\mathcal{F}$ and $\kappa^\star$. The results are shown in figure 7b.

One finds that when $\mathcal{F}$ is large enough, all data indeed collapse when represented as a function of the non-dimensional parameter $(1/\mathcal{F}) \log(\kappa^\star/\kappa_0)$.

To propose fitting formulae for this rate, we rely on approximating the distribution of turbulent velocity gradients by either a stretched exponential or a lognormal law, as was done for tensile failure. In the first case, we write

$$\lambda_K(\kappa^\star) \approx \lambda_0 \, \exp\left[-a \left(\frac{\log(\kappa^\star/\kappa_0)}{\mathcal{F}} \right)^{1/2} \right], \tag{4.12}$$

with fitting parameters λ_0 (with the dimension of a frequency) and a (dimensionless). As can be seen in figure 7a, this a formula gives a rather good approximation. As to the lognormal fit, it reads
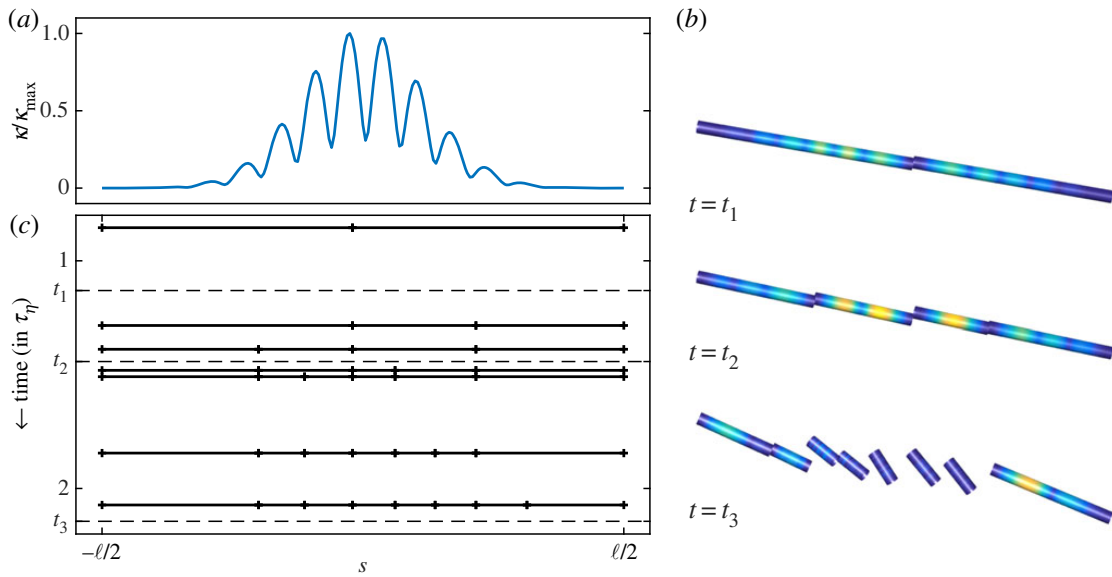
$$\lambda_K(\kappa^\star) \approx \lambda_0' \, \exp\left[-a' \left[\log\left(\frac{\log(\kappa^\star/\kappa_0)}{\mathcal{F}} \right) + b' \right]^2 \right], \tag{4.13}$$

where the fitting parameters are this time a frequency λ_0' and two dimensionless parameters a' and b'. As for tension, the lognormal fit does not describe well data associated to the tail of the distribution, that is small values of $\mathcal{F}$ or, equivalently, large values of $\kappa^\star$. These two fits provide estimates of the rate at which flexural failure occurs as a function of all physical parameters, including the fibre length, aspect ratio, Young modulus, the fluid velocity and mass density that enter the definition of the non-dimensional flexibility $\mathcal{F}$ given in equation (2.3).

(ii) Daughter size distribution

We next turn our attention to understand the resulting sizes of the fragments obtained due to flexural failure during buckling. Up to now, by focusing on the flexural failure rate, we have addressed only a single (the first) break-up event. Because the fibre is curved according to a given buckling mode of order n, the location where break-up occurs clearly depends on n. When n is is odd, the break-up occurs at the centre of the fibre, which breaks in two equal pieces. When n is even, the two resulting fragments have approximately sizes $\ell \times (n/2)/(n+1)$ and $\ell \times (n/2+1)/(n+1)$. Actually, this primary break-up is sometimes followed by successive fragmentations. We indeed find that, because of the continuing compression by the flow, the unstable mode keeps on bending the small secondary pieces, so that their curvature still grows and can reach again the critical value. This is illustrated for a specific buckling event in figure 8 where we have implemented in the numerical simulation the break-up process and the follow-up of resulting fragments. In this case, the instability triggers the growth of a mode of order $n = 14$ (figure 8a). A first break-up occurs at $s \approx -0.02\,\ell$, but the resulting fragments undergo successive fragmentations. This process finally leads to the formation of eight pieces. In this daughter distribution, six fragments have sizes of the order of $\ell/(n+1) \approx 0.07\,\ell$, the two remaining being associated with the ends of the original fibre (figure 8c). As can be followed in figure 8b, the locations where new break-ups occur follow the structures of the initial bending. Note that the full process occurs on time scales of the order of τ_η, confirming that this corresponds to a single buckling event. Note that for this specific event, we have tested how the fragmentation process depends upon the numerical scheme, and in particular on the choice of the time step size Δt. Our results indicate that stability and convergence are ensured only when Δt is much smaller than the local time scale prescribed by the instability growth rate. In order to maintain a reasonable computational cost, we have thus implemented a time-adaptive strategy that accounts for such a constraint.

A single buckling event can hence lead to the creation of several small pieces, depending on which wavenumber is excited. The selection of the most unstable mode depends on the local value of the non-dimensional flexibility $\mathcal{F}_{\rm loc} = \tau_\eta \, |\dot{\gamma}| \, \mathcal{F}$, which fluctuates with $\dot{\gamma}$. Following the results of previous section, we expect for a given value of $\mathcal{F}_{\rm loc}$ that the most unstable mode is of order $n \simeq 2k^\star \simeq \sqrt{\mathcal{F}_{\rm loc}}/(\pi\sqrt{32})$. In that case, the daughter distribution will be peaked at $\ell' = \ell/(n+1) \simeq \pi\sqrt{32}\,\ell/\sqrt{\mathcal{F}_{\rm loc}}$. Assuming that each buckling event leads to break the fibre in $(n+1)$ fragments of equal size ℓ', we can draw an approximation for the daughter size distribution. Hence, the

Figure 8. Evolution of a fibre during fragmentation. Panel (*a*) shows the growing mode by displaying, at the time of the first break-up, the fibre's curvature as a function of the arc-length *s*. Panel (*c*) represents the time evolution of the size distribution (time growing from top to down); each horizontal plain line is a break-up event and segments correspond to fibre fragments. (*b*) Three instantaneous configurations of the fragments at time t_1, t_2 and t_3. Dark regions (blue online) correspond to a zero curvature and light (yellow online) to values close to $\kappa^\star$. Note that on this pseudo three-dimensional representation, the arc-length *s* runs from right to left. (Online version in colour.)

probability that a fibre of length ℓ breaks in ℓ/ℓ' fragments of size ℓ' reads

$$\Pr(\ell \to \ell') \propto \frac{\ell/\ell'}{\tau_\eta \, \mathcal{F}} \; p_{\dot\gamma}\left(-\frac{32\,\pi^2 (\ell/\ell')^2}{\tau_\eta \, \mathcal{F}}\right), \tag{4.14}$$

where $p_{\dot\gamma}(\cdot)$ denotes the probability density function of the stretching rate $\dot\gamma$. Assuming as previously that the later follows a stretched-exponential law, one obtains
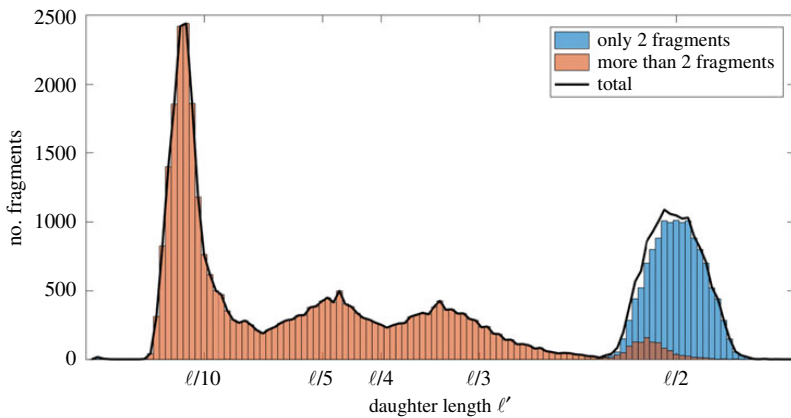
$$\Pr(\ell \to \ell') \propto \frac{\ell/\ell'}{\mathcal{F}} \; \mathrm{e}^{-a\,(\ell/\ell')/\sqrt{\mathcal{F}}}, \tag{4.15}$$

where a is a positive constant. This particularly simple form suggests that the creation of small-length fragments follows an activation-like distribution. In practical terms, this implies that fragment sizes below $a\ell/\sqrt{F}$ are statistically irrelevant and almost never observed. An equivalent form can be written for lognormal statistics of $\dot\gamma$, namely

$$\Pr(\ell \to \ell') \propto \frac{\ell/\ell'}{\mathcal{F}} \; \mathrm{e}^{-a'\left[\log((\ell/\ell')^2/\mathcal{F})+b'\right]^2}, \tag{4.16}$$

with a' and b' constants. This second leads to the same qualitative considerations as above.

Finally, to illustrate the complexity of this process, we show in figure 9, the fibre length distribution of fibres after the first fragmentation series. All fibres have initially the same length ℓ and the same non-dimensional flexibility $\mathcal{F} = 32\,000$. The simulation is done for a specific value of the critical curvature ($\kappa^\star = 10^{-6}\ell^{-1}$), above which these fibres break. A fragmentation series is defined as the set of break-ups occurring during the same buckling event, that is in a time lag going from the initial development of the buckling instability to the time when all fragments have relaxed to a fully straight configuration. The resulting distribution is clearly multi-modal. It develops a peak at sizes ℓ' of the order of $\ell/2$, corresponding to fibres that broke only once during this series. Such events represent approximately one half of the fragmentations. Another marked peak is present at $\ell' \approx \ell/12$. This other maximum is an artefact of the representation, as smaller are the segment, more numerous they are. Clearly, the number of fragments sharply tends to zero

Figure 9. Histogram of the length ℓ' of fragments stemming from the first fragmentation event encountered by 12 000 fibres with initial length ℓ and a flexibility $\mathcal{F} = 320\,000$. (Online version in colour.)

when their size becomes very small. Finally, the distribution displays finite values at intermediate sizes, contributing a significative probability of obtaining fragments of sizes $\ell/3$, $\ell/4$, $\ell/5$, etc.

5. Conclusion and perspectives

We have studied the fragmentation processes undergone by small, inextensible, inertialess fibres in turbulent flow, focusing on tensile and flexural failures. In both cases, we have shown that break-up occurs when the fibre runs into a flow region of high strain, where it is either stretched above internal cohesive forces or compressed, buckles and fractures under excessive bending. By assuming an idealized description for internal fragmentation processes, we found that the fragmentation rates can be expressed through the distribution of turbulent stretching rates. Using standard functional approximations for such probability laws, we proposed fits for both the tensile failure and the flexural failure rates that are calibrated and validated against the results of direct numerical simulations in a high-Reynolds-number flow. Our analysis emphasizes the central role played by the fibres non-dimensional flexibility in understanding how frequently fragmentation occurs.

Besides rates, we reported results on daughter size distributions upon fragmentation. Tensile failure always occurs when the fibre is stretched by the flow and thus has a fully straight configuration. The tension is then maximal at its centre, so that this type of break-up always produces two fragments with equal sizes. We found that the situation is more intricate in the case of flexural failure. Fragmentation occurs when the fibre develops a buckling instability and the resulting break-up process produces a size distribution that depends on the details of the most unstable buckling mode. By performing a linear stability analysis, we provided estimates of this size distribution that depend on the instantaneous fluid strain experienced by the fibre. This approach indicates that the number of fragments produced upon break-up becomes larger when the fibres experiences more violent compressions. Our analysis builds upon the results of Vandenberghe & Villermaux [13] on how buckling affects the fragmentation of elastic slender bodies. Specifically, they studied the fragmentation of elongated bodies considering the effect of inertia (which has been neglected in this paper). They show the existence of an additional effect in the fragmentation process: the propagation of elastic waves after a first break-up. The released energy is able to increase further the curvature in the newly separated parts of the fibre, possibly leading to successive secondary break-ups and to the formation of many small-size fragments. In our work, we unveil another, possibly complementary mechanism where the smaller fragments appear as fingerprints of the initial most-unstable growing mode. The case of inertial fibres with a size that can be larger than the Kolmogorov scale will be studied in the future.

An appealing prospective to our work concerns the Reynolds-number dependence of fragmentation rates and processes. While our numerics limited themselves to a single level of turbulence, our analysis can be easily extended to encompass intermittent descriptions of turbulent statistics. At a qualitative level, one expects more violent fluctuations as the Reynolds number increases. This implies that the rare events leading to the production of many small fragments should have an increasing statistical relevance. At a quantitative level, one can for instance apply the recent work of Buaria *et al.* [34], who carefully investigated the Reynolds-number dependence of the probability distributions of velocity gradients. Their findings can be straightforwardly used in our approach to write an explicit Reynolds-number dependence of the fragmentation rates and associated daughter size distributions.

Finally, it is important to stress again that, in this work, we have oversimplified the microscopical break-up processes by considering that the fibres material is brittle and that fibres are free of any molecular defects. In most realistic settings, the threshold value for each break-up mechanism may vary along the fibre length while plastic effect cannot be neglected, meaning that flexural failure may occur at locations that have been bended several times in the fibre's history. Even if they involve an extra parametrization, such effects can be easily implemented and investigated numerically (e.g. [40]). We expect in particular interesting impacts of the non-trivial time distribution of violent fluctuations. The turbulent fluid strain that is experienced by a fibre along its Lagrangian trajectory is typically very intermittent in time, so that buckling events are strongly correlated among each other. Nevertheless, generalizing to such settings the analysis that has been developed here represents a real challenge. The strongest bending is indeed expected to occur when the buckling instability has saturated, questioning in that case the relevance of the linear analysis. Besides, the more general case of prolate/oblate particles with a finite aspect ratio requires more subtle fragmentation scenario since it can occur along two-dimensional planes, leading to fragments that can quickly display a more complex shape.

References

1. Beysens D, Campi X, Pefferkorn E. 1995 *Fragmentation phenomena*. Singapore: World Scientific.
2. Hüfner J, Mukhopadhyay D. 1986 Fragmentation of nuclei, stones and asteroids. *Phys. Lett. B* **4**, 373–376. (doi:10.1016/0370-2693(86)90397-7)
3. Nagata S. 2000 Apoptotic DNA fragmentation. *Exp. Cell Res.* **256**, 12–18. (doi:10.1006/excr.2000.4834)
4. Yan B *et al.* 2006 A unique role of the DNA fragmentation factor in maintaining genomic stability. *Proc. Natl Acad. Sci. USA* **103**, 1504–1509. (doi:10.1073/pnas.0507779103)
5. Keil K, Haack H, Scott ERD. 1994 Catastrophic fragmentation of asteroids: evidence from meteorites. *Planet. Space Sci.* **42**, 1109–1122. (doi:10.1016/0032-0633(94)90011-6)
6. Seames WS. 2003 An initial study of the fine fragmentation fly ash particle mode generated during pulverized coal combustion. *Fuel Proc. Tech.* **81**, 109–125. (doi:10.1016/S0378-3820(03)00006-7)

7. Verawaty M, Tait S, Pijuan M, Yuan Z, Bond PL. 2013 Breakage and growth towards a stable aerobic granule size during the treatment of wastewater. *Water Res.* **47**, 5338–5349. (doi:10.1016/j.watres.2013.06.012)

8. Griffith L. 1943 A theory of the size distribution of particles in a comminuted system. *Can. J. Res.* **21**, 57–64. (doi:10.1139/cjr43a-005)

9. Horn AF, Merrill EW. 1984 Midpoint scission of macromolecules in dilute solution in turbulent flow. *Nature* **312**, 140–141. (doi:10.1038/312140a0)

10. Åström JA. 2006 Statistical models of brittle fragmentation. *Adv. Phys.* **55**, 247–278. (doi:10.1080/00018730600731907)

11. Babler MU, Biferale L, Lanotte AS. 2012 Breakup of small aggregates driven by turbulent hydrodynamical stress. *Phys. Rev. E* **85**, 025301. (doi:10.1103/PhysRevE.85.025301)

12. Rösler J, Harders H, Baeker M. 2007 *Mechanical behaviour of engineering materials: metals, ceramics, polymers, and composites*. Berlin, Germany: Springer.

13. Vandenberghe N, Villermaux E. 2013 Geometry and fragmentation of soft brittle impacted bodies. *Soft Matter* **9**, 8162–8176. (doi:10.1039/c3sm50789k)

14. Lundell F, Söderberg L, Alfredsson P. 2011 Fluid mechanics of papermaking. *Annu. Rev. Fluid Mech.* **43**, 195–217. (doi:10.1146/annurev-fluid-122109-160700)

15. Ardekani N, Sardina G, Brandt L, Karp-Boss L, Bearon RN, Variano EA. 2017 Sedimentation of inertia-less prolate spheroids in homogenous isotropic turbulence with application to non-motile phytoplankton. *J. Fluid Mech.* **831**, 655–674. (doi:10.1017/jfm.2017.670)

16. Santoso A, Ilmi B. 2018 Analysis of erosion rate on discharge slurry HDPE pipe in canal water intake PLTGU Grati using CFD simulation. *Int. J. Marine Eng. Innov. Res.* **2**, 253–260. (doi:10.12962/j25481479.v2i4.4063)

17. Becker L, Shelley M. 2001 Instability of elastic filaments in shear flow yields first-normal-stress differences. *Phys. Rev. Lett.* **87**, 198301. (doi:10.1103/PhysRevLett.87.198301)

18. Lindner A, Shelley M. 2016 Elastic fibers in flows. In *Fluid-structure interactions in low-Reynolds-number flows* (eds C Duprat, H Stone), ch. 5, pp. 168–192. Cambridge, UK: The Royal Society of Chemistry. (doi.org/10.1039/9781782628491-00168).

19. Biferale L, Meneveau C, Verzicco R. 2014 Deformation statistics of sub-Kolmogorov-scale ellipsoidal neutrally buoyant drops in isotropic turbulence. *J. Fluid Mech.* **754**, 184–207. (doi:10.1017/jfm.2014.366)

20. Ray SS, Vincenzi D. 2018 Droplets in isotropic turbulence: deformation and breakup statistics. *J. Fluid Mech.* **852**, 313–328. (doi:10.1017/jfm.2018.453)

21. Kobayashi M, Adachi Y, Ooi S. 1999 Breakup of fractal flocs in a turbulent flow. *Langmuir* **15**, 4351–4356. (doi:10.1021/la980763o)

22. Vanapalli SA, Ceccio SL, Solomon MJ. 2006 Universal scaling for polymer chain scission in turbulence. *Proc. Natl Acad. Sci. USA* **103**, 16 660–16 665. (doi:10.1073/pnas.0607933103)

23. Pereira AS, Soares EJ. 2012 Polymer degradation of dilute solutions in turbulent drag reducing flows in a cylindrical double gap rheometer device. *J. Non-Newtonian Fluid Mech.* **179**, 9–22. (doi:10.1016/j.jnnfm.2012.05.001)

24. Odell JA, Keller A. 1986 Flow-induced chain fracture of isolated linear macromolecules in solution. *J. Polym. Sci.* **24**, 1889–1916. (doi:10.1002/polb.1986.090240901)

25. Allende S, Henry C, Bec J. 2018 Stretching and buckling of small elastic fibers in turbulence. *Phys. Rev. Lett.* **121**, 154501. (doi:10.1103/PhysRevLett.121.154501)

26. Domokos G, Kun F, Sipos AA, Szabó T. 2015 Universality of fragment shapes. *Sci. Rep.* **5**, 9147. (doi:10.1038/srep09147)

27. Homann H, Dreher J, Grauer R. 2007 Impact of the floating-point precision and interpolation scheme on the results of DNS of turbulence by pseudo-spectral codes. *Comput. Phys. Commun.* **177**, 560–565. (doi:10.1016/j.cpc.2007.05.019)

28. Tornberg A, Shelley M. 2004 Simulating the dynamics and interactions of flexible fibers in Stokes flows. *J. Comput. Phys.* **196**, 8–40. (doi:10.1016/j.jcp.2003.10.017)

29. Grady D. 2010 Length scales and size distributions in dynamic fragmentation. *Int. J. Fracture* **163**, 85–99. (doi:10.1007/s10704-009-9418-4)

30. Chevillard L, Roux SG, Lévêque E, Mordant N, Pinton J-F, Arnéodo A. 2003 Lagrangian velocity statistics in turbulent flows: effects of dissipation. *Phys. Rev. Lett.* **91**, 214502. (doi:10.1103/PhysRevLett.91.214502)

31. Kailasnath P, Sreenivasan KR, Stolovitzky G. 1992 Probability density of velocity increments in turbulent flows. *Phys. Rev. Lett.* **68**, 2766. (doi:10.1103/PhysRevLett.68.2766)

32. Meneveau C, Sreenivasan K R. 1991 The multifractal nature of turbulent energy dissipation. *J. Fluid Mech.* **224**, 429–484. (doi:10.1017/S0022112091001830)

33. Donzis DA, Yeung PK, Sreenivasan KR. 2008 Dissipation and enstrophy in isotropic turbulence: resolution effects and scaling in direct numerical simulations. *Phys. Fluids* **20**, 045108. (doi:10.1063/1.2907227)

34. Buaria D, Pumir A, Bodenschatz E, Yeung PK. 2019 Extreme velocity gradients in turbulent flows. *New J. Phys.* **21**, 043004. (doi:10.1088/1367-2630/ab0756)

35. Jeffery GB. 1922 The motion of ellipsoidal particles immersed in a viscous fluid. *Proc. R. Soc. Lond. A* **102**, 161–179. (doi:10.1098/rspa.1922.0078)

36. Munk T, Hallatschek O, Wiggins CH, Frey E. 2006 Dynamics of semiflexible polymers in a flow field. *Phys. Rev. E* **74**, 041911. (doi:10.1103/PhysRevE.74.041911)

37. Subramanian G, Koch DL. 2005 Inertial effects on fibre motion in simple shear flow. *J. Fluid Mech.* **535**, 383–414. (doi:10.1017/S0022112005004829)

38. Einarsson J, Candelier F, Lundell F, Angilella JR, Mehlig B. 2015 Rotation of a spheroid in a simple shear at small Reynolds number. *Phys. Fluids* **27**, 063301. (doi:10.1063/1.4921543)

39. Bender CM, Orszag SA. 1999 *Advanced mathematical methods for scientists and engineers I: asymptotic methods and perturbation theory*. New York, NY: Springer.

40. Marchioli C, Soldati A. 2015 Turbulent breakage of ductile aggregates. *Phys. Rev. E* **91**, 053003. (doi:10.1103/PhysRevE.91.053003)

19

royalsocietypublishing.org/journal/rsta   *Phil. Trans. R. Soc. A* **378**: 20190398

6 | Concluding remarks

We reported troughout this manuscript new results pertaining to the dynamics and the fluctuations of small complex particles in a turbulent flow. As discussed in the introduction, our definition of a complex particle emcompasses any particle which is not a tracer, and possesses non-trivial properties impacting their dynamics, among them non-trivial shapes, response times, sizes or rheologies. To build quantitative insights about the interplay between such properties and turbulence, we focused on two specific cases, namely small inertial spheroids and small flexible fibers, for which we used massive numerical simulations of the Navier-Stokes equations to generate high Reynolds homogeneous isotropic turbulence, and to our knowledge unprecedented statistical datasets.

Those datasets allowed to address in a quantitative fashion the three questions formulated in the introduction:

- *How do turbulent flows prescribe the dynamics of complex particles?*
- *How do turbulent flows prescribe the concentration patterns of complex particles?*
- *How to model fragmentation processes caused by turbulence?*

Beyond constituting a guideline in the exposition of our results, those three questions also allowed us to formulate new perspectives related to the modeling of complex particles in turbulence.

Summary of our results. Our first stream of results relates to the interplay between shape, mass and turbulence, and to that end we studied heavy spheroids in a homogeneous isotropic turbulent flow. In this approach, where we ignore the effects of gravity and buoyancy, mass only prescribes the response times, either larger (for "heavy" particles) or smaller (for "light" particles) than the viscous Kolmogorov timescale τ_η. The coupling with turbulence is then fully determined by their shapes, through the aspect ratio λ, and by response time, through the Stokes number St $= \tau_p/\tau_\eta$. We showed that the translation motion and the orientation statistics are only weakly coupled. The translational motion is almost fully prescribed by the motion of an equivalent sphere with response time $\tau_p^\star = \tau_\eta \, \mathrm{St}^\star$ based on a suitably defined *harmonic Stokes number* built from the resistance tensor. While the harmonic Stokes number does not fully account for fine-scale statistics such as the two-time statistics of the acceleration components, the deviations remain very weak, and the description in terms of an effective sphere proves very efficient. On the other hand, the orientation statistics display more intricate features. While the statistics of the orientation and of the rotation rate of light particles seem fully prescribed by St*, this is no longer the case for heavy spheroids. The threshold value is identified as St$^\star \approx 0.7$, above which the statistics become non-universal with respect to the shape. This behavior was found to be reflected on the concentration properties of the particles. In particular, we recovered and extended the observations of Bec et al. (2005, 2007) made in the spherical case, where the particles concentrate on dynamic fractal sets whose position is correlated with the dissipative structures of the flow. Our study shows that deviations are small but measurable, and this means that new statistical models should be developed to account for non-sphericity in the concentration patterns of heavy particles.

Our second stream of results relates to the interplay between shape and rheology, and this led us to study small flexible fibers without inertia, passively transported by a turbulent flow. To generate the relevant statistical dataset, we relied on the local slender body theory (SBT) in the overdamped approximation, which is the simplest but still highly-non trivial continuous framework to tackle the dynamics of flexible fibers. Our

data shows that fibers are stretched and compressed by the turbulent velocity gradient. We observed that fibers spend most of the time stretched as stiff rods, where their dynamics is fully described by the Jeffery's equations of rods. Fluctuations appear when the fibers are strongly compressed by the flow. In such cases, the fibers go into a buckling instability. These events are very rare and intermitent, and are determined by the turbulent fluctuations. We found that the buckling rate can be phenomenologically modeled in terms of an activation process, and an anomalous Arrhenius law. Such is also the case for other statistics related to the orientation dynamics, such as the statistics of misalignments, described through a suitably defined tangent angle, and the super-buckling rates, describing events where the fibers switch their orientations following buckling events.

Finally, we described two fundamental mechanisms leading to fragmentation of small brittle fibers in a turbulent flow: tensile failure when fibers break by an extensional effort, for which the internal tension achieves high values; and flexural failure when fibers break by a compressive effort, for which the fiber achieves large values of the curvature. The outcomes of those two mechanisms are very different, resulting in different sizes and numbers of the daughter fragments. Through tensile failure, fibers break into two pieces of equal length, each time that their internal tension supersedes a threshold $T^\star$. In our approach, those events are directly related to the shear rate reaching values $\propto T^\star/\ell^2$. This means that the stochastic modeling of tensile failure relates to the Lagrangian statistics of the maxima of the shear rate, and this fully prescribes not only the number but also the sizes of the daughter fragments. The flexural failure mechanism is more complex. In the SBT framework, we argued that the number of pieces generated by a buckling instability can be expected to go $\propto \dot{\gamma}^{1/2}\ell^2$; This number is determined from linear analysis, and relates to the most unstable buckling mode developed, given by the specific instantaneous negative shear rate $\dot{\gamma}$. We observed that the flexural failure mechanism is likely to trigger an effect reminiscent of a "random cascade" of successive flexural failures, as observed in the fragmentation of inertial elongated particles.

Perspectives. In our view, these different series of results pave the way for future work and new challenges in the description of complex particles in a turbulent flow. In relation to spheroids in a turbulent flow, we can think of refining the description of the orientation rate, and in particular of the interplay between tumbling and spinning of spheroids. Qualitative insights could probably be obtained from theoretical study of particles within random velocity fields, for example extending a previous approach by Vincenzi (2012) to include inertia. This setting could also possibly be used to provide qualitative insights about the preferential concentration patterns and the depletion of small-scale clustering by non-sphericity.

Related to shapes, one could want to understand the dynamics induced by more complex shapes, such as non-symmetrical ellipsoids. We believe, that lack of symmetry should not impact the translation dynamics and the relevance of the harmonic Stokes numbers, but would probably produces non-trivial deviations for the rotational dynamics and the concentration properties if combined with high response times. Finally, one could wish to implement in our numerics the effects of gravity. This modification would require only minor modifications of our codes, and might lead to interesting interplay between gravitational settling and preferential concentrations. Among other effects, but that would possibly require more work, one could also think about implementing hydro-dynamical or physical interactions between the particles, in order to model small but finite-size spheroids.

In relation to fibers, one could wish to explore the relevance of the local slender body theory beyond the description of small fibers in homogeneous isotropic turbulence. To that end, one development relates to the implementation of large flexible fibers in 2D turbulence and large fibers immersed in a channel flow. Preliminary results show that the local slender body theory in 2D turbulent flows reproduces the statistics of specific mechanical models of fibers, such as the elastic chains studied by Picardo et al. (2018), at least at a qualitative level, showing fibers buckling within the vortex zones and stretching outside. Again, one could wish to refine the description by considering massive fibers and to study how preferential concentration patterns are or not altered (Singh et al., 2020) and how fragmentation occurs. Another natural development is the behavior of fibers within a channel flow rather than within a homogeneous isotropic turbulent fluid. Preliminary results considering long and flexible fibers transported within a turbulent channel flow show fibers qualitatively drifting close from the boundaries and preferentially concentrate in the bulk of the flow. A fine understanding on the mechanisms at play relating the migration statistics to the rheology of the fibers is

yet elusive. A longer-term perspective relates to modeling intra-fiber or fiber-fiber interactions. Experiments show that long fibers can get knotted and form entangled aggregates; and this physics certainly reflects on their transport. The statistical analysis of the topologies of such intricate fibers could probably prove a fruitful and open field of study.

A | Dynamics for an ellipsoid of arbitrary shape

In Chapter 3, we presented the equations describing the dynamics of an ellipsoid of revolution, also known as a spheroid. Those equations are in fact deduced from a general set of equations valid for ellipsoids characterized by arbitrary values for their axes a, b and c (Jeffery, 1922; Fan and Ahmadi, 1995). Please recall that the translational dynamics is defined in the laboratory frame $(\mathbf{e}_x, \mathbf{e}_y, \mathbf{e}_z)$ and the rotational dynamics is defined in the particle frame $(\mathbf{e}_{\hat{x}}, \mathbf{e}_{\hat{y}}, \mathbf{e}_{\hat{z}})$. We list below the relevants quantities from which the equations of Chapter 3 are deduced.

Resistance tensor. The resistance tensor is expressed in the particle frame. It is the diagonal matrix (Oberbeck, 1876):

$$\hat{\mathbb{K}} = 16\,\pi a\lambda \begin{pmatrix} (\chi_0/a^2 + \chi_1)^{-1} & 0 & 0 \\ 0 & (\chi_0/a^2 + \chi_2)^{-1} & 0 \\ 0 & 0 & (\chi_0/a^2 + \lambda^2\chi_3)^{-1} \end{pmatrix} \tag{A.1}$$

Shape parameters. The shape parameters χ_0, χ_1, χ_2 and χ_3 have been computed by Brenner (1964) as

$$\chi_0 = abc \int_0^\infty \frac{\mathrm{d}\beta}{\Delta}, \qquad \Delta(\beta) = \sqrt{(a^2 + \beta)(b^2 + \beta)(c^2 + \beta)},$$

$$\chi_1 = abc \int_0^\infty \frac{\mathrm{d}\beta}{(a^2 + \beta)\Delta}, \qquad \chi_2 = abc \int_0^\infty \frac{\mathrm{d}\beta}{(b^2 + \beta)\Delta}, \qquad \chi_3 = abc \int_0^\infty \frac{\mathrm{d}\beta}{(c^2 + \beta)\Delta}. \tag{A.2}$$

Moment of inertia. The moment of inertia of an ellipsoid about its principal axis is a diagonal matrix:

$$\begin{pmatrix} I_{\hat{x}} & 0 & 0 \\ 0 & I_{\hat{y}} & 0 \\ 0 & 0 & I_{\hat{z}} \end{pmatrix} = \frac{m_p}{5} \begin{pmatrix} b^2 + c^2 & 0 & 0 \\ 0 & a^2 + c^2 & 0 \\ 0 & 0 & b^2 + a^2 \end{pmatrix} = \frac{4}{15}\pi\rho_p abc \begin{pmatrix} b^2 + c^2 & 0 & 0 \\ 0 & a^2 + c^2 & 0 \\ 0 & 0 & b^2 + a^2 \end{pmatrix} \tag{A.3}$$

Hydrodynamic torque. The hydrodynamic torque acting on an ellipsoid in the limit of a Stokes flow (see Jeffery (1922)) is

$$
\begin{pmatrix} T_{\hat{x}} \\ T_{\hat{y}} \\ T_{\hat{z}} \end{pmatrix} = \frac{16}{3} \rho \nu \pi a b c \begin{pmatrix} \frac{b^2+c^2}{b^2\chi_2+c^2\chi_3} \\ \frac{a^2+c^2}{a^2\chi_1+c^2\chi_3} \\ \frac{a^2+b^2}{a^2\chi_1+b^2\chi_2} \end{pmatrix} \begin{pmatrix} \frac{b^2-c^2}{b^2+c^2}\,\tau_{\hat{z}\hat{y}} + (\omega_{\hat{z}\hat{y}} - \Omega_{\hat{x}}) \\ \frac{c^2-a^2}{c^2+a^2}\,\tau_{\hat{x}\hat{z}} + (\omega_{\hat{x}\hat{z}} - \Omega_{\hat{y}}) \\ \frac{a^2-b^2}{a^2+b^2}\,\tau_{\hat{y}\hat{x}} + (\omega_{\hat{y}\hat{x}} - \Omega_{\hat{z}}) \end{pmatrix}, \tag{A.4}
$$

where
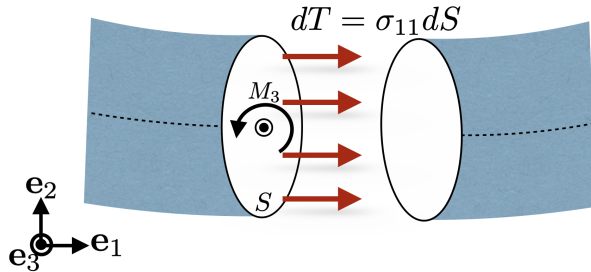
$$
\begin{aligned}
\tau_{\hat{z}\hat{y}} &= \frac{1}{2}\left(\partial_{\hat{y}} u_{\hat{z}} + \partial_{\hat{z}} u_{\hat{y}}\right), & \tau_{\hat{x}\hat{z}} &= \frac{1}{2}\left(\partial_{\hat{z}} u_{\hat{x}} + \partial_{\hat{x}} u_{\hat{z}}\right), & \tau_{\hat{y}\hat{x}} &= \frac{1}{2}\left(\partial_{\hat{x}} u_{\hat{y}} + \partial_{\hat{y}} u_{\hat{x}}\right), \\
\omega_{\hat{z}\hat{y}} &= \frac{1}{2}\left(\partial_{\hat{y}} u_{\hat{z}} - \partial_{\hat{z}} u_{\hat{y}}\right), & \omega_{\hat{x}\hat{z}} &= \frac{1}{2}\left(\partial_{\hat{z}} u_{\hat{x}} - \partial_{\hat{x}} u_{\hat{z}}\right), & \omega_{\hat{y}\hat{x}} &= \frac{1}{2}\left(\partial_{\hat{x}} u_{\hat{y}} - \partial_{\hat{y}} u_{\hat{x}}\right).
\end{aligned} \tag{A.5}
$$

B | Derivation of the flexural forces

In Chapter 4, we described the forces involved in a beam using the Euler-Bernoulli theory. Here, we describe an explicit derivation of the internal flexural forces of the beam. From a mechanical point of view, the flexural torque of the fiber acting at the central point of a cross-section (with normal vector $n = e_1$) is:

$$
\begin{aligned}
M_3 = M &= \int_S -y\,(\sigma \cdot n)\cdot e_1 dS \\
&= -\int_S y\,\sigma_{11}\,dS
\end{aligned}
\tag{B.1}
$$

where y here denotes the coordinate in the second-direction (e_2) and σ_{11} represents the perpendicular stress to the surface S acting on this surface. As shown in Fig. B.1, the flexural torque is a vector aligned with the third-direction e_3, and is generated by the fact that the perpendicular force T stems from surface tensural efforts integrated in the direction e_2.
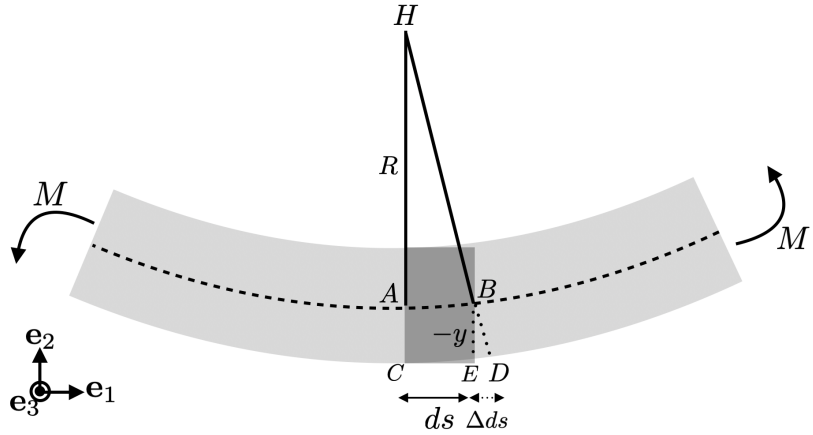
Figure B.1: Scheme of the forces acting on a piece of beam, along with the flexural torque acting in the third-direction.

Hookes law for linear elastic material ties the stress σ and the strain ε as $\sigma = Y\varepsilon$. The strain is a local quantity, defined as the relative expansion or contration of the small piece. Explicitly and using the notations of Fig. B.2, this quantity is identified as $\varepsilon = \Delta ds/ds$.

Indeed, and again referring to Fig. B.2, we observe that the triangles $\triangle HAB$, $\triangle HCD$ and $\triangle BED$ are similar. Using Thales theorem:

$$
\frac{HA}{AB} = \frac{BE}{ED} \quad \Rightarrow \quad \frac{R}{ds} = \frac{-y}{\Delta ds} \quad \Rightarrow \quad \epsilon = \frac{\Delta ds}{ds} = \frac{-y}{R} = -y\chi
$$

Figure B.2: A geometrical view of the flexural deformation in a small piece ds of a beam. Here, R is the radius of curvature and the curvature is defined as $\chi = \frac{1}{R}$.

Hence, the torque due to flexural forces is:

$$
\begin{aligned}
M &= \int_S Y - y^2 \chi dS \\
&= -Y\chi \int_S y^2 dS \\
&= -YI\chi
\end{aligned}
\tag{B.2}
$$

with Y the Young modulus and I the moment of inertia. Observe for example that $I = \pi a^4/4$ for a cylinder of radius a.

C | Numerical scheme to integrate the local slender body theory

Fibers have been numerically integrated along turbulent tracers using either MATLAB code or a C++ code. All the details about the flow integration are shown in Chapter 2 and the numerical and physical parameters of this specific data base are found in Table (4.1).

We work with several values of the non-dimensional flexibility $\mathcal{F}$ and millions of turbulent tracers. The code integrates at the same time the dynamics of fibers and the dynamics of a stiff rod. The fiber position $\mathbf{X}(s,t)$ is discretized into $n = 201$ grid points along the fiber arc-length s, so that the grid size is $\Delta s = L/n$.

Following the approach of Tornberg and Shelley (2004), a second-order accurate centered finite difference scheme is used. Spatial derivatives are discretized by accounting for the free-end boundary conditions $\partial_s^2 \mathbf{X} = 0$ and $\partial_s^3 \mathbf{X} = 0$ at $s = \pm \ell/2$. The explicit operators of the path derivative D_p and the discret fiber position X_j are:

1. Fot the first derivative:

$$D_1 X_j = \begin{cases} (-X_{j+2} + 4X_{j+1} - 3X_j)/(2\Delta s) & j = 0 \\ (X_{j+1} - X_{j-1})/(2\Delta s) & 1 \leq j \leq N - 1 \\ (3X_j - 4X_{j-1} + X_{j-2})/(2\Delta s) & j = N \end{cases} \tag{C.1}$$

2. Fot the second derivative:

$$D_2 X_j = \begin{cases} (-X_{j+3} + 4X_{j+2} - 5X_{j+1} + 2X_j)/(\Delta s^2) & j = 0 \\ (X_{j+1} - 2X_j + X_{j-1})/(\Delta s^2) & 1 \leq j \leq N - 1 \\ (2X_j - 5X_{j-1} + 4X_{j-2} - X_{j-3})/(\Delta s^2) & j = N \end{cases} \tag{C.2}$$

3. Fot the third derivative:

$$D_3 X_j = \begin{cases} (-3X_{j+4} + 14X_{j+3} - 24X_{j+2} + 18X_{j+1} - 5X_j)/(2\Delta s^3) & j = 0 \\ (-X_{j+3} + 6X_{j+2} - 12X_{j+1} + 10X_j - 3X_{j-1})/(2\Delta s^3) & j = 1 \\ (X_{j+2} - 2X_{j+1} + 2X_{j-1} - X_{j-2})/(2\Delta s^3) & 2 \leq j \leq N - 2 \\ (3X_{j+1} - 10X_j + 12X_{j-1} - 6X_{j-2} + X_{j-3})/(2\Delta s^3) & j = N - 1 \\ (5X_j - 18X_{j-1} + 24X_{j-2} - 14X_{j-3} + 3X_{j-4})/(2\Delta s^3) & j = N \end{cases} \tag{C.3}$$

4. Fot the fourth derivative:

$$D_4 X_j = \begin{cases} (-2X_{j+5} + 11X_{j+4} - 24X_{j+3} + 26X_{j+2} - 14X_{j+1} + 3X_j)/(\Delta s^4) & j = 0 \\ (-1X_{j+4} + 6X_{j+3} - 14X_{j+2} + 16X_{j+1} - 9X_j + 2X_{j-1})/(\Delta s^4) & j = 1 \\ (X_{j+2} - 4X_{j+1} + 6X_j - 4X_{j-1} + X_{j-2})/(\Delta s^4) & 2 \leq j \leq N - 2 \\ (2X_{j+1} - 9X_j + 16X_{j-1} - 14X_{j-2} + 6X_{j-3} - X_{j-4})/(\Delta s^4) & j = N - 1 \\ (3X_j - 14X_{j-1} + 26X_{j-2} - 24X_{j-3} + 11X_{j-4} - 2X_{j-5})/(\Delta s^4) & j = N \end{cases} \tag{C.4}$$

The code is composed by the following steps:

1. compute the derivatives of $\mathbf{X}$ using the operator D_p,

2. compute the velocity along the fiber as:

$$\mathbb{A}_{ij}(\mathbf{X}, t) = \partial_j u_i(\mathbf{X}, t), \tag{C.5}$$

3. resolve the tension $\bar{T} = T/E$ in the units of the bending modulus E, ensuring the inextensibility constraint $|\partial_s \mathbf{X}|^2 = 1$ by the penalization method

$$2\partial_s^2 \bar{T} - |\partial_s^2 \mathbf{X}|^2 \, \bar{T} = 6|\partial_s^3 \mathbf{X}|^2 + 7\partial_s^2 \mathbf{X}^\mathsf{T} \partial_s^4 \mathbf{X} - \frac{1}{\mathcal{F}} \, \partial_s \mathbf{X}^\mathsf{T} \mathbb{A}(\mathbf{X}, t)\, \partial_s \mathbf{X}, + \frac{1}{\mathcal{F}} \beta (1 - |\partial_s \mathbf{X}|^2) \tag{C.6}$$

where β is a coefficient of penalization prescribed to be very small.

4. compute the time evolution of $\mathbf{X}$ with the semi-implicit Adams-Bashforth scheme.

5. update the position and orientation of the fiber.

We reproduce below the Matlab script that we used:

```matlab
%% MATLAB SCRIPT: INTEGRATION OF FIBERS ALONG TURBULENT TRACER
%   The gradient along a trajectory is supposed to be stored in the
      array
%   Sig which as a dimension 3 x 3 x Nt

tau_eta = 0.0513;       % Kolmogorov time scale
F = 2.5e3;              % non?dimentional flexibility
L = 1;                  % fiber's length
Nt = 1000;              % number of time step
dt = 2.5e-4*tau_eta;    % time?step size
N = 200;                % number of grid points along the fibers'
      arclength
delta_s = L/N;          % arc?length discretization
beta = 400/tau_eta ;    % coefficient of the penalization method

%% INITIAL CONDITIONS
mu = F*tau_eta; % flexibility in units of the Kolmogorov timescale
%   Fibers initialized as straight segments along the x direction
X = [linspace(0,L,N+1)' zeros(N+1,2)];
%   Rod initialized with the end-to-end direction of the fiber
P = (X(end,:)-X(1,:))'; % direction
P = P/sqrt(sum(P.^2)) ; % normalization

%% FINITE-DIFFERENCES OPERATORS
%   FIRST-ORDER DERIVATIVE
D1 = spdiags([-ones(N+1,1),zeros(N+1,1),ones(N+1,1)],[-1 0 1],N+1,N+1);
D1(1,1)=-3; D1(1,2)=4; D1(1,3)=-1;
D1(N+1,N+1)=3; D1(N+1,N)=-4; D1(N+1,N-1)=1;
D1 = D1/(2*delta_s);
%   SECOND-ORDER DERIVATIVE
%   with free-end BC:
D2 = spdiags([ones(N+1,1),-2*ones(N+1,1),ones(N+1,1)],[-1 0 1],N+1,N+1)
     ;
D2(1,1)=2; D2(1,2)=-5; D2(1,3)=4; D2(1,4)=-1;
D2(N+1,N+1)=2; D2(N+1,N)=-5; D2(N+1,N-1)=4; D2(N+1,N-2)=-1;
```

```matlab
33   D2 = D2/delta_s^2;
34   %  with Dirichlet BC:
35   LaplDirichlet = spdiags([ones(N-1,1),-2*ones(N-1,1),ones(N-1,1)],[-1 0
        1],N-1,N-1);
36   LaplDirichlet = LaplDirichlet/delta_s^2;
37   %  THIRD-ORDER DERIVATIVE
38   D3 = spdiags([-ones(N+1,1),2*ones(N+1,1),zeros(N+1,1),-2*ones(N+1,1),
        ones(N+1,1)],[-2 -1 0 1 2],N+1,N+1);
39   D3(1,1)=-5; D3(1,2)=18; D3(1,3)=-24; D3(1,4)=14; D3(1,5)=-3;
40   D3(2,1)=-3; D3(2,2)=10; D3(2,3)=-12; D3(2,4)=6; D3(2,5)=-1;
41   D3(N+1,N+1)=5; D3(N+1,N)=-18; D3(N+1,N-1)=24; D3(N+1,N-2)=-14; D3(N+1,N
        -3)=3;
42   D3(N,N+1)=3; D3(N,N)=-10; D3(N,N-1)=12; D3(N,N-2)=-6; D3(N,N-3)=1;
43   D3 = D3/(2*delta_s^3) ;
44   %  FOURTH-ORDER DERIVATIVE (when treated explicitly)
45   D4 = spdiags([ones(N+1,1),-4*ones(N+1,1),6*ones(N+1,1),-4*ones(N+1,1),
        ones(N+1,1)],[-2 -1 0 1 2],N+1,N+1);
46   D4(1,1)=3; D4(1,2)=-14; D4(1,3)=26; D4(1,4)=-24; D4(1,5)=11; D4(1,6)
        =-2;
47   D4(2,1)=2; D4(2,2)=-9; D4(2,3)=16; D4(2,4)=-14; D4(2,5)=6; D4(2,6)=-1;
48   D4(N+1,N+1)=3; D4(N+1,N)=-14; D4(N+1,N-1)=26; D4(N+1,N-2)=-24; D4(N+1,N
        -3)=11; D4(N+1,N-4)=-2;
49   D4(N,N+1)=2; D4(N,N)=-9; D4(N,N-1)=16; D4(N,N-2)=-14; D4(N,N-3)=6; D4(N
        ,N-4)=-1;
50   D4 = D4/delta_s^4;
51   %  FOURTH-ORDER DERIVATIVE (when treated implicitly)
52   Op4 = spdiags([ones(N-3,1),-4*ones(N-3,1),6*ones(N-3,1),-4*ones(N-3,1),
        ones(N-3,1)],[-2 -1 0 1 2],N-3,N-3);
53   Op4(1,1)=2/11; Op4(1,2)=-4/11; Op4(1,3)=2/11;
54   Op4(2,1)=-16/11; Op4(2,2)=43/11; Op4(2,3)=-38/11;
55   Op4(N-4,N-3)=-16/11; Op4(N-4,N-4)=43/11; Op4(N-4,N-5)=-38/11;
56   Op4(N-3,N-3)=2/11; Op4(N-3,N-4)=-4/11; Op4(N-3,N-5)=2/11;
57   Op4 = Op4/delta_s^4;
58
59   %% TIME LOOP
60
61   for it=1:Nt
62
63       % 1st step: compute the derivatives of X
64       D1X = [D1*X(:,1), D1*X(:,2), D1*X(:,3)];
65       D2X = [D2*X(:,1), D2*X(:,2), D2*X(:,3)];
66       D3X = [D3*X(:,1), D3*X(:,2), D3*X(:,3)];
67       D4X = [D4*X(:,1), D4*X(:,2), D4*X(:,3)];
68
69       % 2nd step: compute the fluid velocity along the fiber
70       DU(:,1) = Sig(1,1,it)*D1X(:,1)+Sig(1,2,it)*D1X(:,2)+Sig(1,3,it)*D1X
            (:,3);
71       DU(:,2) = Sig(2,1,it)*D1X(:,1)+Sig(2,2,it)*D1X(:,2)+Sig(2,3,it)*D1X
            (:,3);
72       DU(:,3) = Sig(3,1,it)*D1X(:,1)+Sig(3,2,it)*D1X(:,2)+Sig(3,3,it)*D1X
            (:,3);
73
74       % 3rd step: compute the tension
75       NormXs = sum(D1X.^2,2);
```

```
76      A = -mu*sum(D1X.*DU,2); % fluid contribution
77      A = A + (7*sum(D2X.*D4X,2)+6*sum(D3X.*D3X,2)); % bending
           contribution
78      A = A + (mu*beta)*(1-NormXs); % penalization term
79      M = 2*LaplDirichlet-spdiags(sum((D2X(2:N,:)).^2,2),0,N-1,N-1);
80      T = [0; M\A(2:N); 0];
81
82      % 4th step: computing the r.h.s. of time evolution
83      D1T = D1*T;
84      Ufib = cumsum(DU,1)*delta_s ...
85          + (2/mu)*[D1T.*D1X(:,1),D1T.*D1X(:,2),D1T.*D1X(:,3)] ...
86          + (1/mu)*[T.*D2X(:,1),T.*D2X(:,2),T.*D2X(:,3)];
87      DP = Sig(:,:,it)*P-(P'*Sig*P)*P;
88      if t==0 % 1st step = Euler
89          RHS_X = X(3:(N-1),:)+dt*Ufib(3:(N-1),:);
90          XXi = D1X(3:(N-1),:);
91          Pnew = P+dt*DP;
92      else % otherwise = Adams-Bashforth
93          RHS_X = (4/3)*X(3:(N-1),:)-(1/3)*Xold+(2*dt/3)*(2*Ufib(3:(N-1)
               ,:)-Ufib_old);
94          XXi = D1*(2*X-Xold); XXi = XXi(3:(N-1),:);
95          Pnew = (4/3)*P-(1/3)*Pold+(2*dt/3)*(2*DP-DPold);
96      end
97
98      % 5th step: implicit treatment of the bending elasticity
99      Axy = spdiags(XXi(:,1).*XXi(:,2),0,N-3,N-3)*Op4;
100     Axz = spdiags(XXi(:,1).*XXi(:,3),0,N-3,N-3)*Op4;
101     Ayz = spdiags(XXi(:,2).*XXi(:,3),0,N-3,N-3)*Op4;
102     DD4 = [ spdiags(1+XXi(:,1).^2,0,N-3,N-3)*Op4 Axy Axz; ...
103         Axy spdiags(1+XXi(:,2).^2,0,N-3,N-3)*Op4 Ayz; ...
104         Axz Ayz spdiags(1+XXi(:,3).^2,0,N-3,N-3)*Op4];
105     MM = speye(3*(N-3),3*(N-3))+(2/3)*(dt/mu)*DD4;
106     Xnew = MM\reshape(RHS_X,[3*(N-3),1]);
107     Xnew = reshape(Xnew,[N-3,3]);
108     Xnew = [(48/11)*Xnew(1,:)-(52/11)*Xnew(2,:)+(15/11)*Xnew(3,:);...
109         (28/11)*Xnew(1,:)-(23/11)*Xnew(2,:)+(6/11)*Xnew(3,:);...
110         Xnew ;
111         (28/11)*Xnew(end,:)-(23/11)*Xnew(end-1,:)+(6/11)*Xnew(end-2,:)
               ;...
112         (48/11)*Xnew(end,:)-(52/11)*Xnew(end-1,:)+(15/11)*Xnew(end-2,:)
               ];
113
114     % 6th step: update
115     Xold = X(3:(N-1),:);
116     X = Xnew;
117     Ufib_old = Ufib(3:(N-1),:);
118     Pold = P;
119     P = Pnew;
120     DPold = DP;
121 end
```
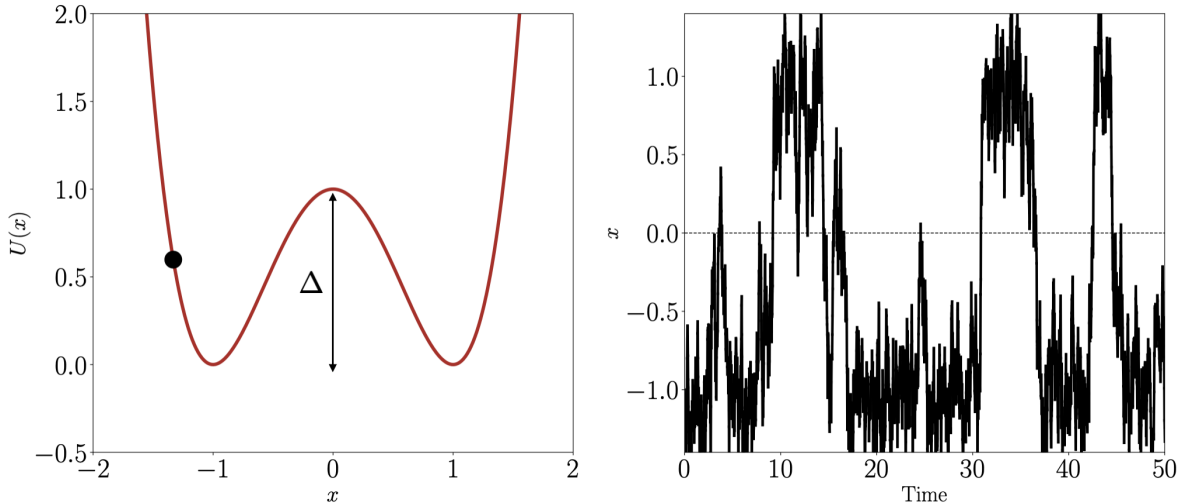
D | Activated process

A thermally activated process is a process that overcomes an energy barrier to pass from an initial state to a final state due to thermal fluctuations. A standard example refers to the minimal energy required for a chemical reaction to occur (Kaufmyn, 2005; Van Kampen, 2007). Typically, the kinetic rate of a reaction for any thermally activated process is given by the Arrhenius law:

$$k = A e^{-E_a/(k_b T)}, \tag{D.1}$$

where E_a is the activation energy, k_b is the Boltzmann constant, T is the temperature in Kelvin and A is a prescribed coefficient also known as pre-exponential factor or Arrhenius factor. The ratio k can be understood as the probability that any given collision will result in a reaction. The energy of activation is the amount of energy needed so that the reaction occurs: the larger the energy, the less probable the reaction. Conversely, at high temperature, the molecules are more excited and the level of energy of the system is higher. Hence, the probability that the reaction effectively happens increases.

Figure D.1: Left panel: the double-well potential energy of a the brownian particle as a function of its position. Right panel: time evolution of the particle position.

The most simple mathematical modeling of an activation process is formulated in terms of a stochastic equation known as the Kramers problem (Gardiner, 1985; Pavliotis, 2014; Risken, 1996, Chap. 5, Chap. 4). This problem considers an over-damped Brownian particle within a double-well potential, whose dynamics obeys the stochastic equation

$$\frac{dX(t)}{dt} = -U'(X(t)) + \sqrt{2\kappa}\, \eta(t), \tag{D.2}$$
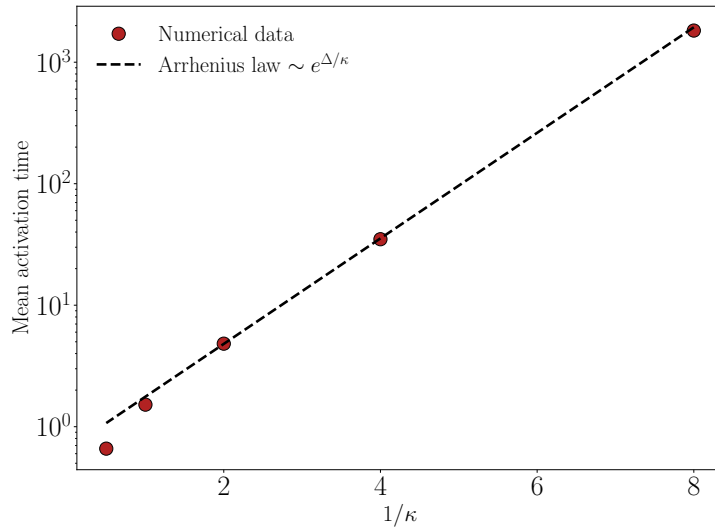
where $\kappa = k_b T$ represents the thermal energy, η is the white noise, characterized by $\langle \eta(t) \rangle = 0$ and $\langle \eta(t) \eta(t') \rangle = \delta(t - t')$, and U is the double-well potential represented in Fig. D.1, characterized by an energy barrier Δ separating the two wells.

Due to the presence of noise, the particles have non zero probability to jump from one well to the other, even in the limit of a very small temperature. More precisely, standard textbook calculations show that the timelaps between two consecutive jumps follows an exponential distribution: $p(t) = \tau e^{-t/\tau}$. τ is the mean waiting time to pass from one well to the other well, and can be evaluated as

$$\tau = \pi/(2\sqrt{2\Delta})\, e^{\Delta/\kappa}, \tag{D.3}$$

the inverse of which is the jumping rate, analogous to the kinetic rate of chemical reactions.

Expression (D.3) can therefore be interpreted as an Arrhenius law, and can indeed be verified numerically using Monte-Carlo simulations of the stochastic dynamics (D.2), as shown in Fig. D.2.

Figure D.2: Mean activation time as a function of $1/\kappa$. The numerical data is setting with red circles and the Arrhenius law is showing in the dash-line.
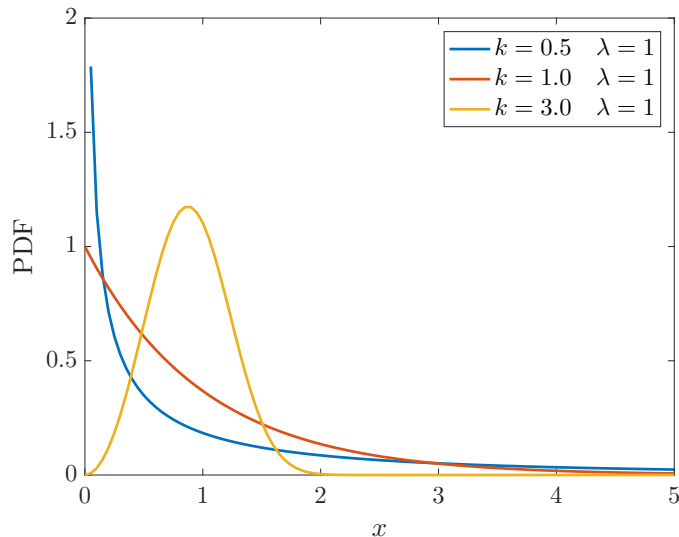
E | Weibull probabilistic distribution

Several random processes are described by a Weibull law (Rinne, 2008; Murthy et al., 2004). It is for instance, used in industrial engineering to represent manufacturing and delivery times or failures manufacturing systems.

The Weibull probability density function is

$$
f(x; \lambda, k) = \begin{cases} \frac{k}{\lambda} \left(\frac{x}{\lambda} \right)^{k-1} e^{(-x/\lambda)^k} & x \geq 0 \\ 0 & x < 0, \end{cases} \tag{E.1}
$$

where $k > 0$ is the shape parameter and $\lambda > 0$ is the scale parameter of the distribution.

Figure E.1: Probability density function of a Weibull random variable

Generally, this distribution is used to model the "time-to-failure". In this case, the shape parameter leads to the following interpretation:

- When $0 < k < 1$ the rate decreases in the time.

- When $k = 1$ the rate is contant over time. In this case the Weibull distribution is reduced to an exponential distribution.

- When $k \geq 1$ the rate increases with time.

Fig.E.1 shows the probability density function of a Weibull ramdom variable x for three different values of the shape parameter k.

This law corresponds to the waiting times between successive events distributed as a non-homogeneous Poisson process with rate x^{k-1}/λ^k. Conversely to a classical Poisson process (corresponding to $k = 0$) which has a constant rate, the process considered here has a rate which decreases with the waiting time x when $k \geq 1$. It thus has memory: the longer we wait, the less likely it is to observe a new event.

F | Derivation of a kinetic equation for the fragmentation of fibers

Relevance of a kinetic description. We here derive a kinetic model for the dynamics of the population of fibers, to account for the statistical measurements on fragmentation made along single trajectories, and the two kinds of failures that the fibers undergo. The kinetic description relies on the number density $n(\ell, t)$, which we introduce as the average number of fragments of length ℓ at time t per unit volume. It has the dimension of Length^{-3}.

For a fixed length ℓ, the kinetic evolution of this quantity between time t and $t + \Delta t$ involves two terms: a sink term Δn^-, which corresponds to the number of fragmentations involving a fiber of initial size ℓ that has occurred in this time interval, and a source term Δn^+, which comes from all fragmentations of size $\ell' > \ell$ that lead to a fragment of size ℓ. We assume that the time lag Δt over which we sample this time evolution is longer than the typical duration of a single fragmentation event, but shorter than the time between two successive fragmentations.

This means, that the validity of this approach relies on two assumptions. First, it requires a clear timescale separation between the duration of a single fragmentation event and the time separating two of them. Second, it requires that fragmentation events are memoryless, so that they can be considered as a Poissonian process. The latter point may seem restrictive, as we know from our data that fragmentation has memory, as there are long-term correlations in the violent events encountered along tracer trajectories. Yet, as explained in details in Chapter 5, the specific type of correlation between dangerous events involve waiting time statistics that follow Weibull distributions. For this kind of distributions, the population dynamics can be described in terms of rates in the large-time asymptotics, exactly as if the waiting times were standard exponentials, and this is the correct physical justification beneath the use of kinetic equations. Further comments on this point in a context of transport by turbulent flows can also be found in Krstulovic et al. (2013); Bec et al. (2016).

Modeling failures. We now specify our model by implementing the two types of fragmentation processes. Those associated to a tensile failure take place when the tension exceeds a critical value $T^\star$. They occur with a rate $\lambda_{\mathrm{T}}(\ell; T^\star)$ that can be estimated either from Eq. (3.3) or from Eq. (3.4) of § 5.5. [11] A single event of tensile failure always leads to the formation of two daughter fragments of equal lengths. As explained in Chapter 5, this process can moreover cascade and lead to the formation of 2^n fragments with $n \geq 1$, each with a length equal to $\ell/2^n$. This leads to write the probability that a fiber of size ℓ breaks in ℓ/ℓ' fragments of size ℓ' as $\mathrm{P}_{\mathrm{T}}(\ell'|\ell) = p_n \, \delta(\log_2 \ell/\ell' - n)$.

The fragmentations associated to flexural failure happen when the curvature exceeds a critical value $\kappa^\star$. This occurs with a rate $\lambda_{\mathrm{K}}(\ell; \kappa^\star)$ that account for the probability of observing a buckling event. The rates are estimated in Eq. (4.12) and (4.13) of § 5.5. The resulting daughter size distribution is also estimated in the paper and reads $\mathrm{Pr}(\ell \to \ell')$ in Eq. (4.15) and (4.16) of § 5.5. For clarity, we denote it as $\mathrm{P}_{\mathrm{K}}(\ell'|\ell)$ to single out the contribution of flexural failures. As in the case of tensile failure, this daughter size distribution is only

---

[11]As explained in § 5.5, faithfully estimating the rate $\lambda_{\mathrm{T}}(\ell; T^\star)$ requires modeling the statistics of the velocity gradients, and this can be heuristically achieved either using a stretched exponential or a log-normal distribution, leading to two possible models for $\lambda_{\mathrm{T}}(\ell; T^\star)$.

defined for discrete values of ℓ/ℓ'. Note that the two rates λ_{T} and λ_{K} have the dimension of the inverse of time.

Sources and sinks.   We now estimate the source terms and the sink terms associated to the two fragmentation processes. The sinks are easy to write: They correspond to the number of fragments of size ℓ that have disappeared by fragmentation between times t and $t + \Delta t$:

$$\Delta n^- = -\lambda_{\mathrm{T}}(\ell)\,\Delta t\,n(\ell, t) - \lambda_{\mathrm{K}}(\ell)\,\Delta t\,n(\ell, t). \tag{F.1}$$

The source terms are obtained by summing over all possible mother lengths ℓ' that break in a fragment of size ℓ. They read

$$\Delta n^+ = \sum_{\ell' > \ell} \frac{\ell'}{\ell}\,\lambda_{\mathrm{T}}(\ell')\Delta t\,\mathrm{P}_{\mathrm{T}}(\ell|\ell')\,n(\ell', t) + \sum_{\ell' > \ell} \frac{\ell'}{\ell}\,\lambda_{\mathrm{K}}(\ell')\Delta t\,\mathrm{P}_{\mathrm{K}}(\ell|\ell')\,n(\ell', t). \tag{F.2}$$

The fact that these terms are $\propto (\ell'/\ell)$ comes from the fact that each time a fragment of size ℓ' breaks, it creates ℓ'/ℓ fragments of sizes ℓ. Finally by writing $n(\ell, t + \Delta t) - n(\ell, t) = \Delta n^- + \Delta n^+ \approx \Delta t\,\partial_t n(\ell, t)$, we get the integro-differential equation

$$\partial_t n = -\left[\lambda_{\mathrm{T}}(\ell) + \lambda_{\mathrm{K}}(\ell)\right] n + \sum_{\ell' > \ell} \frac{\ell'}{\ell}\left[\lambda_{\mathrm{T}}(\ell')\,\mathrm{P}_{\mathrm{T}}(\ell|\ell') + \lambda_{\mathrm{K}}(\ell')\,\mathrm{P}_{\mathrm{K}}(\ell|\ell')\right] n(\ell', t). \tag{F.3}$$

One can easily check that this equation conserves the total length of fibers $\mathcal{L} = \sum_\ell \ell\,n(\ell, t) = \mathrm{const}$. This is a consequence of the normalisation of the daughter size distribution $\sum_\ell \mathrm{P}_{\mathrm{K}}(\ell|\ell') = \sum_\ell \mathrm{P}_{\mathrm{T}}(\ell|\ell') = 1$.

Perspectives.   The kinetic equation (F.3) is a kind of Smoluchowski equation (Smoluchowski, 1917; Gardiner and Chaturvedi, 1977; Gardiner, 1985). To further substantiate its relevance to describe our data we could follow the tentative workplan:

- Integrate the full microscopic fragmentation process from DNS, including or not both the tensural and the flexural failures for specific choices of $T^\star$ and $\kappa^\star$, and construct a reference database for the mean number of fragments $n(\ell, t)$.

- Use the fitting formule described in the paper § 5.5 for the rates and the daughter size distribution, in order to integrate (F.3) and obtain kinetic predictions that could be compared to DNS.

- Identify discrepancies and the mechanisms that might be responsible of them. Are differences present only in the tail of $n(\ell, t)$? Are they present at all times? It could be that only some violent events lead to deviations. It could also be that the kinetic approach works well only for asymptotic values of the parameter $\mathcal{F}$, $T^\star$, and $\kappa^\star$.

- Propose possible improvements of the kinetic approach that would account for the effect of long-term correlations. Such deviations can be described using the more general population model described in Chapter 5, which does not rely on validity of Poisson-type approximations.

List of Tables

List of Figures

Bibliography

Abraham, E. (1998). The generation of plankton patchiness by turbulent stirring. Nature, 391(6667):577–580. 1.1, 1.4.2

Ahmad, A. and Vincenzi, D. (2016). Polymer stretching in the inertial range of turbulence. Phys. Rev. E, 93(5):052605. 1.4.2

Ali, A., Plan, E., Ray, S., and Vincenzi, D. (2015). Bending dynamics of semi-flexible particles in turbulent flows. 1.4.2

Ali, A., Plan, E., Ray, S., and Vincenzi, D. (2016). Semiflexible particles in isotropic turbulence. Phys. Rev. Fluids, 1(8):082402. 1.4

Aliseda, A., Cartellier, A., Hainaux, F., and Lasheras, J. (2002). Effect of preferential concentration on the settling velocity of heavy particles in homogeneous isotropic turbulence. J. Fluid Mech., 468:77–105. 1.3.1, 1.3.1

Allende, S., Henry, C., and Bec, J. (2018). Stretching and buckling of small elastic fibers in turbulence. Phys. Rev. Lett., 121(15):154501. 4.3

Anderson, J. and Wendt, J. (1995). Computational fluid dynamics, volume 206. Springer. 2.3.2

APS-physics (2006). Physical review letter on breaking spaghetti leads to 2006 ig nobel award. [Online; accessed November 1, 2020]. 1.5

Ardekani, M., Sardina, G., Brandt, L., Karp-Boss, L., Bearon, R., and Variano, E. (2017). Sedimentation of inertia-less prolate spheroids in homogenous isotropic turbulence with application to non-motile phytoplankton. J. Fluid Mech., 831:655–674. 1.3.2, 1.4

Arneodo, A., Baudet, C., Belin, F., Benzi, R., Castaing, B., Chabaud, B., Chavarria, R., Ciliberto, S., Camussi, R., and Chilla, F. (1996). Structure functions in turbulence, in various flow configurations, at reynolds number between 30 and 5000, using extended self-similarity. EPL, 34(6):411. 2.3.1, 2.4.2

Arneodo, A., Manneville, S., and Muzy, J. (1998). Towards log-normal statistics in high reynolds number turbulence. Eur. Phys. J. B, 1(1):129–140. 2.4.2

Arrigo, K., Perovich, D., Pickart, R., Brown, Z., Van Dijken, G., Lowry, K., Mills, M., Palmer, M., Balch, W., and Bahr, F. (2012). Massive phytoplankton blooms under arctic sea ice. Science, 336(6087):1408–1408. 1.1

Audoly, B. and Neukirch, S. (2005). Fragmentation of rods by cascading cracks: why spaghetti does not break in half. Phys. Rev. Lett., 95(9):095505. 1.5, 1.19, F

Balkovsky, E., Falkovich, G., and Fouxon, A. (2001). Intermittent distribution of inertial particles in turbulent flows. Phys. Rev. Lett., 86(13):2790. 1.3.1

Ballent, A., Purser, A., de Jesus Mendes, P., Pando, S., and Thomsen, L. (2012). Physical transport properties of marine microplastic pollution. Biogeosci. Discuss., 9(12). 1.1

Barton, A., Ward, B., Williams, R., and Follows, M. (2014). The impact of fine-scale turbulence on phytoplankton community structure. LOFE, 4(1):34–49. 1.1

Batchelor, G. (1970a). Slender-body theory for particles of arbitrary cross-section in stokes flow. J. Fluid Mech., 44(3):419–440. 4.1.2

Batchelor, G. (1970b). The stress system in a suspension of force-free particles. J. Fluid Mech., 41(3):545–570. 4.1.2

Baudet, C., Bon-Mardion, M., Bonnay, P., Braslau, A., Castaing, B., Chillà, F., Chevillard, L., Daviaud, F., Diribarne, P., and Dubrulle, B. (2015). Local velocity measurements in the shrek experiment at high reynolds number. 2.3.1

Bec, J. (2004). Multifractal concentrations of inertial particles in smooth random flows. arXiv preprint nlin/0402024. 2.4.4

Bec, J., Biferale, L., Boffetta, G., Celani, A., Cencini, M., Lanotte, A., Musacchio, S., and Toschi, F. (2005). Acceleration statistics of heavy particles in turbulence. arXiv preprint nlin/0508012. 1.1, 1.3.1, 1.9, 2.4.4, 3.1.2, 3.3.1, 3.3.1, 3.3.2, 3.4, 6, F

Bec, J., Biferale, L., Cencini, M., Lanotte, A., Musacchio, S., and Toschi, F. (2007). Heavy particle concentration in turbulence at dissipative and inertial scales. Phys. Rev. lett., 98(8):084502. 1.3.1, 1.9, 3.3.3, 3.4, 6, F

Bec, J., Biferale, L., Cencini, M., Lanotte, A., and Toschi, F. (2011). Spatial and velocity statistics of inertial particles in turbulent flows. In Journal of Physics-Conference Series, volume 333, page 012003. 1.3.1

Bec, J., Ray, S., Saw, E., and Homann, H. (2016). Abrupt growth of large aggregates by correlated coalescences in turbulent flow. Phys. Rev. E, 93(3):031102. F

Becker, L. and Shelley, M. (2001). Instability of elastic filaments in shear flow yields first-normal-stress differences. Phys. Rev. lett., 87(19):198301. 1.15, 1.4.1, F

Benzi, R., Ciliberto, S., Tripiccione, R., Baudet, C., Massaioli, F., and Succi, S. (1993). Extended self-similarity in turbulent flows. Phys. Rev. E, 48(1):R29. 2.4.2

Benzi R. and Frisch U. (2010). Scholarpedia, the peer-reviewed open-access encyclopedia. [Online; accessed December 16, 2020]. 1.1

Bertoin, J. (2006). Random fragmentation and coagulation processes, volume 102. Cambridge University Press. 5

Bewley, G., Saw, E., and Bodenschatz, E. (2013). Observation of the sling effect. New J. Phys., 15(8):083051. 1.2

Beysens, D., Campi, X., and Pefferkorn, E. (1995). Fragmentation Phenomena-Proceedings Of The Workshop. World Scientific. 5

Biferale, L., Boffetta, G., Celani, A., Devenish, B., Lanotte, A., and Toschi, F. (2004). Multifractal statistics of lagrangian velocity and acceleration in turbulence. Phys. Rev. lett., 93(6):064502. 3.3.1

Boffetta, G., De Lillo, F., and Gamba, A. (2004). Large scale inhomogeneity of inertial particles in turbulent flows. Phys. Fluids, 16(4):L20–L23. 1.3.1

Bortolussi, L. and Gast, N. (2016). Mean-field limits beyond ordinary differential equations. In International School on Formal Methods for the Design of Computer, Communication and Software Systems, pages 61–82. Springer. 5

Bossy, M., Espina, J., Moricel, J., Paris, C., and Rousseau, A. (2016). Modeling the wind circulation around mills with a lagrangian stochastic approach. SMAI-JCM, 2:177–214. 1.1

Bourouiba, L., Dehandschoewercker, E., and Bush, J. W. (2014). Violent expiratory events: on coughing and sneezing. J. Fluid Mech., 745:537–563. 1.1, 1.1, 1.7, F

Boyd, P., Watson, A., Law, C., Abraham, E., Trull, T., Murdoch, R., Bakker, D., Bowie, A., Buesseler, K., and Chang, H. (2000). A mesoscale phytoplankton bloom in the polar southern ocean stimulated by iron fertilization. Nature, 407(6805):695–702. 1.1

Brenner, H. (1964). The stokes resistance of a slightly deformed sphere. Chem. Eng. Sci., 19(8):519–539. 1.3.2, 3.1.2, A

Bretherton, F. (1962). The motion of rigid particles in a shear flow at low reynolds number. J. Fluid Mech., 14(2):284–304. 1.3.2

Brouzet, C., Verhille, G., and Le Gal, P. (2014). Flexible fiber in a turbulent flow: A macroscopic polymer. Phys. Rev. lett., 112(7):074501. 1.16, 1.4.2, F

Butcher, J. and Goodwin, N. (2008). Numerical methods for ordinary differential equations, volume 2. Wiley Online Library. 4.2

Byron, M., Einarsson, J., Gustavsson, K., Voth, G., Mehlig, B., and Variano, E. (2015). Shape-dependence of particle rotation in isotropic turbulence. Phys. Fluids, 27(3):035101. 3.16, 3.3.2, F

Caffarelli, L. (2000). A clay mathematical institute millennium prize problem, existence and smoothness of the navier–stokes equations. [Online; accessed August 10, 2020]. 2.2

Calzavarini, E., Cencini, M., Lohse, D., and Toschi, F. (2008). Quantifying turbulence-induced segregation of inertial particles. Phys. Rev. lett., 101(8):084504. 1.3.1

Castaing, B., Gagne, Y., and Hopfinger, E. (1990). Velocity probability density functions of high reynolds number turbulence. Physica D, 46(2):177–200. 2.3.1

Challabotla, N., Zhao, L., and Andersson, H. (2015). Orientation and rotation of inertial disk particles in wall turbulence. J. Fluid Mech., 766. 1.3.2

Champagne, F. (1978). The fine-scale structure of the turbulent velocity field. J. Fluid Mech., 86(1):67–108. 2.3.1

Chanal, O., Chabaud, B., Castaing, B., and Hébral, B. (2000). Intermittency in a turbulent low temperature gaseous helium jet. Eur. Phys. J. B, 17(2):309–317. 2.4.2

Chevillard, L. (2015). Une peinture aléatoire de la turbulence des fluides. PhD thesis. 2.4.4

Chevillard, L., Roux, S., Lévêque, E., Mordant, N., Pinton, J., and Arnéodo, A. (2003). Lagrangian velocity statistics in turbulent flows: Effects of dissipation. Phys. Rev. lett., 91(21):214502. 2.5

Chong, M., Perry, A., and Cantwell, B. (1990). A general classification of three-dimensional flow fields. Phys. Fluids A, 2(5):765–777. 2.4.4

Cisse, M., Saw, E., Gibert, M., Bodenschatz, E., and Bec, J. (2015). Turbulence attenuation by large neutrally buoyant particles. Phys. Fluids, 27(6):061702. 1.2

Cristiano, S., Leal, A., Phallen, J., Fiksel, J., Adleff, V., Bruhm, D. C., Jensen, S., Medina, J., Hruban, C., and White, J. (2019). Genome-wide cell-free dna fragmentation in patients with cancer. Nature, 570(7761):385–389. 5

Davidson, P., Kaneda, Y., Moffatt, K., and Sreenivasan, K. (2011). A voyage through turbulence. Cambridge University Press. 1.1

Davoudi, J. and Schumacher, J. (2006). Stretching of polymers around the kolmogorov scale in a turbulent shear flow. Phys. Fluids, 18(2):025103. 1.4.2

Dbouk, T. and Drikakis, D. (2020). On coughing and airborne droplet transmission to humans. Phys. Fluids, 32(5):053310. 1.7, F

De Gennes, P. (1979). Scaling concepts in polymer physics. Cornell university press. 1.4

Del Bello, E., Taddeucci, J., Scarlato, P., Giacalone, E., and Cesaroni, C. (2015). Experimental investigation of the aggregation-disaggregation of colliding volcanic ash particles in turbulent, low-humidity suspensions. Geophys. Res. Lett., 42(4):1068–1075. 1.1

Delour, J., Muzy, J., and Arneodo, A. (2001). Intermittency of 1d velocity spatial profiles in turbulence: a magnitude cumulant analysis. Eur. Phys. J. B, 23(2):243–248. 2.4.2

Donzis, D., Yeung, P., and Sreenivasan, K. (2008). Dissipation and enstrophy in isotropic turbulence: resolution effects and scaling in direct numerical simulations. Phys. Fluids, 20(4):045108. 2.5

Dotto, D. and Marchioli, C. (2019). Orientation, distribution, and deformation of inertial flexible fibers in turbulent channel flow. Acta Mech., 230(2):597–621. 1.4.2, 1.17, F

Dotto, D., Soldati, A., and Marchioli, C. (2020). Deformation of flexible fibers in turbulent channel flow. Acta Mech., 55(2):343–356. 1.4.2

Du Roure, O., Lindner, A., Nazockdast, E., and Shelley, M. (2019). Dynamics of flexible fibers in viscous flows and fluids. Annu. Rev. Fluid Mech., 51:539–572. 1.4.1

Dubrulle, B. (2019). Beyond kolmogorov cascades. J. Fluid Mech., 867. 2.3.1

Duchon, J. and Robert, R. (2000). Inertial energy dissipation for weak solutions of incompressible euler and navier-stokes equations. Nonlinearity, 13(1):249. 2.4.3

Durham, W., Climent, E., Barry, M., De Lillo, F., Boffetta, G., Cencini, M., and Stocker, R. (2013). Turbulence drives microscale patches of motile phytoplankton. Nat. Commun., 4(1):1–7. 1.1

EDF (2020). Codesaturne. [Online; accessed December 10, 2020]. 1.1

Estrada, M. and Berdalet, E. (1997). Phytoplankton in a turbulent world. 1.1

Eyring, H. (1935). The activated complex in chemical reactions. J. Chem. Phys., 3(2):107–115. 4.3.3

Fan, F. and Ahmadi, G. (1995). A sublayer model for wall deposition of ellipsoidal particles in turbulent streams. J. Aerosol Sci., 26(5):813–840. A

Ferziger, J., Perić, M., and Street, R. (2002). Computational methods for fluid dynamics, volume 3. Springer. 2.3.2

Frisch, U. (1995). Turbulence: the legacy of AN Kolmogorov. Cambridge university press. 2.2, 1, 2.4.3, 2.4.3

Gardiner, C. (1985). Handbook of stochastic methods, volume 3. springer Berlin. D, F

Gardiner, C. and Chaturvedi, S. (1977). The poisson representation. i. a new technique for chemical master equations. J. Stat. Phys., 17(6):429–468. F

Gay, A., Favier, B., and Verhille, G. (2018). Characterisation of flexible fibre deformations in turbulence. EPL, 123(2):24001. 4.1.2

GESAMP (2015). Sources, fate and effects of microplastics in the marine environment: a global assessment. Journal Series GESAMP Reports and Studies. 1.1

Gewert, B., Plassmann, M., and MacLeod, M. (2015). Pathways for degradation of plastic polymers floating in the marine environment. Environ. Sci.: Process. Impacts, 17(9):1513–1521. 1.4

Gladden, J., Handzy, N., Belmonte, A., and Villermaux, E. (2005). Dynamic buckling and fragmentation in brittle rods. Phys. Rev. lett., 94(3):035503. 1.19, 1.5, F

Glibert, P., Berdalet, E., Burford, M., Pitcher, G., and Zhou, M. (2018). Harmful algal blooms and the importance of understanding their ecology and oceanography. In Global ecology and oceanography of harmful algal blooms, pages 9–25. Springer. 1.1

Goepfert, C., Marié, J., Chareyron, D., and Lance, M. (2010). Characterization of a system generating a homogeneous isotropic turbulence field by free synthetic jets. Exp. Fluids, 48(5):809–822. 1.3.1

Gold, V. M. and Baker, E. (2008). A model for fracture of explosively driven metal shells. Eng. Fract. Mech., 75(2):275–289. 5

Goldstein, H., Poole, C., and Safko, J. (1980). Classical mechanics addison-wesley. Reading, MA, 426. 3.1.1

Good, G., Ireland, P., Bewley, G., Bodenschatz, E., Collins, L., and Warhaft, Z. (2014). Settling regimes of inertial particles in isotropic turbulence. J. Fluid Mech., 759. 1.3.1, 1.8, F

Griffith, L. (1943). A theory of the size distribution of particles in a comminuted system. Can. J. Res., 21(6):57–64. 5

Gross, B., Zheng, Z., Liu, S., Chen, X., Sela, A., Li, J., Li, D., and Havlin, S. (2020). Spatio-temporal propagation of covid-19 pandemics. medRxiv. 1.1

Gustavsson, K., Jucha, J., Naso, A., Lévêque, E., Pumir, A., and Mehlig, B. (2017). Statistical model for the orientation of nonspherical particles settling in turbulence. Phys. Rev. lett., 119(25):254501. 1.3.2

Guzman L., F. C. and Soto, R. (2011). Transverse swimming in a dilute suspension of active swimmer under an oscillating shear flow. APS, 64:R29–005. 1.2

Happel, J. and Brenner, H. (2012). Low Reynolds number hydrodynamics: with special applications to particulate media, volume 1. Springer Science & Business Media. 1.4, 3.1, F

Hayatsu, R., Winans, R., McBeth, R., Scott, R., Moore, L., and Studier, M. (1981). Structural characterization of coal: lignin-like polymers in coals. ACS Publications. 1.4

Henry, C., Krstulovic, G., and Bec, J. (2018). Tumbling dynamics of inertial inextensible chains in extensional flow. Phys. Rev. E, 98(2):023107. 1.4

Hill, R. (2002). Scaling of acceleration in locally isotropic turbulence. J. Fluid Mech., 452:361–370. 3.3.1

Homann, H., Bec, J., Fichtner, H., and Grauer, R. (2009). Clustering of passive impurities in magnetohydro-dynamic turbulence. Phys. Plasma, 16(8):082308. 1.2

Homann, H., Dreher, J., and Grauer, R. (2007). Impact of the floating-point precision and interpolation scheme on the results of dns of turbulence by pseudo-spectral codes. Comput. Phys. Comm., 177(7):560–565. 2.3.2

Homann, H., Guillot, T., Bec, J., Ormel, C., Ida, S., and Tanga, P. (2016). Effect of turbulence on collisions of dust particles with planetesimals in protoplanetary disks. Astron. Astrophys., 589:A129. 1.2

Horn, A. and Merrill, E. (1984). Midpoint scission of macromolecules in dilute solution in turbulent flow. Nature, 312(5990):140–141. 5

Hou, T. and Li, R. (2007). Computing nearly singular solutions using pseudo-spectral methods. J. Comput. Phys., 226(1):379–397. 2.3.2

Huang, K. (2009). Introduction to statistical physics. CRC press. 2.1

Hüfner, J. and Mukhopadhyay, D. (1986). Fragmentation of nuclei, stones and asteroids. Phys. Lett. B, 173(4):373–376. 5

Hughes, B. (1995). Random walks and random environments: random walks, volume 1. Oxford University Press. 5.3.1, 5.3.1

IISD (2017). What are algal blooms and why do they matter? [Online; accessed December 1, 2020]. 1.1

Iyer, K., Sreenivasan, K., and Yeung, P. (2017). Reynolds number scaling of velocity increments in isotropic turbulence. Phys. Rev. E, 95(2):021101. 2.3.1

Jeffery, G. (1922). The motion of ellipsoidal particles immersed in a viscous fluid. Proc. R. Soc. A, 102(715):161–179. 1.3.2, 3.1, 3.1.2, A, A

Johnson, R. (1980). An improved slender-body theory for stokes flow. J. Fluid Mech., 99(2):411–431. 4.1.2

Jones, A., Thomson, D., Hort, M., and Devenish, B. (2007). The uk met office's next-generation atmospheric dispersion model, name iii. In Air pollution modeling and its application XVII, pages 580–589. Springer. 1.1

Kailasnath, P., Sreenivasan, K., and Stolovitzky, G. (1992). Probability density of velocity increments in turbulent flows. Phys. Rev. lett., 68(18):2766. 2.5

Kantsler, V. and Goldstein, R. (2012). Fluctuations, dynamics, and the stretch-coil transition of single actin filaments in extensional flows. Phys. Rev. lett., 108(3):038103. 1.4.1, 1.15, F

Karlin, S. (2014). A first course in stochastic processes. Academic press. 5.3.1

Kaufmyn, W. (2005). Materials science for engineers. [Online; accessed September 1, 2020]. D

Keil, K., Haack, H., and Scott, E. (1994). Catastrophic fragmentation of asteroids: Evidence from meteorites. Planet. Space Sci., 42(12):1109–1122. 5

Kharche, S., Moro, J., Baudet, C., Rousset, B., Fuchs, A., Peinke, J., and Girard, A. (2019). Turbulent velocity measurements in high reynolds cryogenic helium facilities at service des basses températures (sbt). In IOP Conference Series: Materials Science and Engineering, volume 502, page 012201. IOP Publishing. 2.3.1

Khrennikov, D., Titov, A., Ershov, A., Klyuchantsev, A., Pariev, V., and Karpov, S. (2020). Effect of the surface shape of a large space body on its fragmentation in a planetary atmosphere. Mon. Not. R. Astron. Soc., 493(1):1352–1360. 5

Klewicki, J., Foss, J., Wallace, J., Donnelly, R., and Sreenivasan, K. (1998). Flow at ultra-high reynolds and rayleigh numbers. 2.3.1

Koelmans, A., Nor, N., Hermsen, E., Kooi, M., Mintenig, S., and De France, J. (2019). Microplastics in freshwaters and drinking water: critical review and assessment of data quality. Water Res., 155:410–422. 1.1

Kolmogorov, A. (1962). A refinement of previous hypotheses concerning the local structure of turbulence in a viscous incompressible fluid at high reynolds number. J. Fluid Mech., 13(1):82–85. 2.4.3

Krstulovic, G., Cencini, M., and Bec, J. (2013). Effective rates in dilute reaction-advection systems. Submitted to J. F

Kukulka, T., Law, K., and Proskurowski, G. (2016). Evidence for the influence of surface heat fluxes on turbulent mixing of microplastic marine debris. J. Phys. Oceanogr., 46(3):809–815. 1.1

Laidler, K. (1984). The development of the arrhenius equation. J. Chem. Educ., 61(6):494. 4.3.3

Landau, L. and Lifshitz, E. (1959). Course of Theoretical Physics Vol 7: Theory and Elasticity. Pergamon press. 4.1.1, 5.1.1, 5.4

Lanotte, A., Bec, J., Biferale, L., Cencini, M., and Toschi, F. (2010). The rate of collisions of small cloud droplets in turbulent flows. In 13th Conference on Cloud Physics. 1.2

Lauga, E. and Powers, T. (2009). The hydrodynamics of swimming microorganisms. Rep. Prog. Phys., 72(9):096601. 1.2, 2.1

Lee, E., Hembree Jr, D., Rao, G., and Mansur, L. (1993). Raman scattering from ion-implanted diamond, graphite, and polymers. Phys. Rev. B, 48(21):15540. 1.4

Li, C., Sureshkumar, R., and Khomami, B. (2006). Influence of rheological parameters on polymer induced turbulent drag reduction. J. Nonnewton Fluid Mech., 140(1-3):23–40. 1.4

Li, L., Yang, Z., Dang, Z., Meng, C., Huang, J., Meng, H., Wang, D., Chen, G., Zhang, J., and Peng, H. (2020). Propagation analysis and prediction of the covid-19. Infect. Dis. Model., 5:282–292. 1.1

Lindner, A. and Shelley, M. (2015). Elastic fibers in flows. Fluid-Structure Interactions in Low-Reynolds-Number Flows, 168. 1.4.1

Lohse, D. (2020). Die abstandsregel in zeiten von corona. [Online; accessed December 5, 2020]. 1.1

Lundell, F., Söderberg, L., and Alfredsson, P. (2011). Fluid mechanics of papermaking. Annu. Rev. Fluid Mech., 43:195–217. 1.4

Manikantan, H. and Saintillan, D. (2015). Buckling transition of a semiflexible filament in extensional flow. Phys. Rev. E, 92(4):041002. 1.15, F

Marchioli, C. and Soldati, A. (2013). Rotation statistics of fibers in wall shear turbulence. Acta Mech., 224(10):2311–2329. 1.1, 1.3.2

Masrur, A., Yu, M., Luo, W., and Dewan, A. (2020). Space-time patterns, change, and propagation of covid-19 risk relative to the intervention scenarios in bangladesh. Int. J. Environ. Res. Public Health, 17(16):5911. 1.1

Mathai, V., Prakash, V., Brons, J., Sun, C., and Lohse, D. (2015). Wake-driven dynamics of finite-sized buoyant spheres in turbulence. Phys. Rev. lett., 115(12):124501. 1.2

Mavila, S., Worrell, B., Culver, H., Goldman, T., Wang, C., Lim, C., Domaille, D., Pattanayak, S., McBride, M., and Musgrave, C. (2018). Dynamic and responsive dna-like polymers. J. Am. Chem. Soc., 140(42):13594–13598. 1.4

Maxey, M. and Riley, J. (1983). Equation of motion for a small rigid sphere in a nonuniform flow. Phys. Fluids, 26(4):883–889. 3.1.2

McKenna, G. and Simon, S. (2017). 50th anniversary perspective: Challenges in the dynamics and kinetics of glass-forming polymers. Macromolecules, 50(17):6333–6361. 1.4

Mecikalski, J., Feltz, W., Murray, J., Johnson, D., Bedka, K., Bedka, S., Wimmers, A., Pavolonis, M., Berendes, T., and Haggerty, J. (2007). Aviation applications for satellite-based observations of cloud properties, convection initiation, in-flight icing, turbulence, and volcanic ash. Bull. Am. Meteorol. Soc., 88(10):1589–1607. 1.1

Meneveau, C. (2011). Lagrangian dynamics and models of the velocity gradient tensor in turbulent flows. Annu. Rev. Fluid Mech., 43:219–245. 2.4.4

Meneveau, C. and Sreenivasan, K. (1991). The multifractal nature of turbulent energy dissipation. J. Fluid Mech., 224:429–484. 2.5

Mignon, A., Snoeck, D., Dubruel, P., Van Vlierberghe, S., and De Belie, N. (2017). Crack mitigation in concrete: superabsorbent polymers as key to success? Materials, 10(3):237. 1.4

Minier, J. and Peirano, E. (2001). The pdf approach to turbulent polydispersed two-phase flows. Phys. Rep., 352(1-3):1–214. 1.1

Monchaux, R., Bourgoin, M., and Cartellier, A. (2010). Preferential concentration of heavy particles: a voronoï analysis. Phys. Fluids, 22(10):103304. 1.3.1, 1.8, F

Monchaux, R., Bourgoin, M., and Cartellier, A. (2012). Analyzing preferential concentration and clustering of inertial particles in turbulence. Int. J. Multiph. Flow, 40:1–18. 1.1, 1.3.1, 1.3.1

Mordant, N., Crawford, A., and Bodenschatz, E. (2004). Three-dimensional structure of the lagrangian acceleration in turbulent flows. Phys. Rev. lett., 93(21):214501. 2.5

Mordant, N., Delour, J., Léveque, E., Arnéodo, A., and Pinton, J. (2002). Long time correlations in lagrangian dynamics: a key to intermittency in turbulence. Phys. Rev. lett., 89(25):254502. 1.1

Mordant, N., Metz, P., Michel, O., and Pinton, J. (2001). Measurement of lagrangian velocity in fully developed turbulence. Phys. Rev. lett., 87(21):214501. 2.5

Mott, N. (1947). Fragmentation of shell cases. Proc. R. Soc. A, 189(1018):300–308. 5

Mott, N. (2006). A theory of the fragmentation of shells and bombs. In Fragmentation of Rings and Shells, pages 243–294. Springer. 5

Murthy, D., Xie, M., and Jiang, R. (2004). Weibull models, volume 505. John Wiley & Sons. E

Musacchio, S. and Vincenzi, D. (2010). Deformation of a flexible polymer in a random flow with long correlation time. arXiv preprint arXiv:1012.1978. 1.4

Nagata, S. (2000). Apoptotic dna fragmentation. Exp. Cell Res., 256(1):12–18. 5

NASA (2009). Sarychev peak eruption, kuril islands. [Online; accessed December 2, 2020]. 1.2, F

NASA (2010). Phytoplankton bloom in the barents sea. [Online; accessed December 6, 2020]. 1.4, 1.1, F

NASA (2012). Jasmine cyclone. [Online; accessed November 15, 2020]. 2.1, F

NASA (2015). Dwindling diatoms. [Online; accessed December 6, 2020]. 1.3, F

NASA (2018). Summer blooms in the baltic and barents. [Online; accessed December 6, 2020]. 1.4, F

NCAS (2010). Eyjafjallajökull 2010: How icelandic volcano eruption closed european skies. 1.1

Ng, H., Sin, L., Tee, T., Bee, S., Hui, D., Low, C., and Rahmat, A. (2015). Extraction of cellulose nanocrystals from plant sources for application as reinforcing agent in polymers. Compos. B. Eng., 75:176–200. 1.4

Ni, R., Ouellette, N., and Voth, G. (2014). Alignment of vorticity and rods with lagrangian fluid stretching in turbulence. J. Fluid Mech., 743. 4.3.4.1

NOAA (2020). What are microplastics? [Online; accessed December 4, 2020]. 1.1

Obata, A., Ishizaka, J., and Endoh, M. (1996). Global verification of critical depth theory for phytoplankton bloom with climatological in situ temperature and satellite ocean color data. J. Geophys. Res., 101(C9):20657–20667. 1.1

Oberbeck, A. (1876). Ueber stationäre flüssigkeitsbewegungen mit berücksichtigung der inneren reibung. J. für die Reine und Angew. Math., 1876(81):62–80. 3.1.2, A

Obukhov, A. (1962). Some specific features of atmospheric turbulence. J. Geophys. Res., 67(8):3011–3014. 2.4.3

Okubo, A. (1970). Horizontal dispersion of floatable particles in the vicinity of velocity singularities such as convergences. In Deep sea research and oceanographic abstracts, volume 17, pages 445–454. Elsevier. 2.4.4

Orszag, S. (1971). On the elimination of aliasing in finite-difference schemes by filtering high-wavenumber components. J. Atmos. Sci., 28(6):1074–1074. 2.3.2

Orszag, S. (1973). Lectures on the statistical theory of turbulence in fluid dynamics. Proc. of the 1973 Les Houches Summer School of Theoretical Physics, R. Balian & JL Peube, ed. Gordon and Breach, page 235. 2.3.2

Parsa, S., Calzavarini, E., Toschi, F., and Voth, G. (2012). Rotation rate of rods in turbulent fluid flow. Phys. Rev. lett., 109(13):134501. 1.3.2, 1.10, F

Pavliotis, G. (2014). Stochastic processes and applications: diffusion processes, the Fokker-Planck and Langevin equations, volume 60. Springer. D

Pearson, K. (1905). "das fehlergesetz und seine verallgemeiner-ungen durch fechner und pearson". Biometrika, 4(1-2):169–212. 3.3.1

Pereira, A., Mompean, G., Thais, L., Soares, E., and Thompson, R. (2017). Active and hibernating turbulence in drag-reducing plane couette flows. Phys. Rev. Fluid, 2(8):084605. 1.4

Petersen, A., Baker, L., and Coletti, F. (2018). Experimental study of inertial particles clustering and settling in homogeneous turbulence. arXiv preprint arXiv:1812.04055. 1.3.1

Picardo, J., Singh, R., Ray, S., and Vincenzi, D. (2020). Dynamics of a long chain in turbulent flows: impact of vortices. Philos. Trans. R. Soc. A, 378(2175):20190405. 1.4.2

Picardo, J., Vincenzi, D., Pal, N., and Ray, S. (2018). Preferential sampling of elastic chains in turbulent flows. Phys. Rev. lett., 121(24):244501. 1.4.2, 1.18, 2.4.4, 4.4, 4.4, 6, F

Plan, E. (2017). Tumbling, bending, stretching: particles in laminar and chaotic flows. PhD thesis. 1.4.2

Plan, E. and Vincenzi, D. (2016). Tumbling of a brownian particle in an extensional flow. Proc. R. Soc. A, 472(2194):20160226. 1.4

Platt, N., Spiegel, E., and Tresser, C. (1993). On-off intermittency: A mechanism for bursting. Phys. Rev. lett., 70(3):279. 4.3.3

Pope, S. (2001). Turbulent flows. 2.3.2

Powell, T. and Okubo, A. (1994). Turbulence, diffusion and patchiness in the sea. Philos. Trans. R. Soc. B, 343(1303):11–18. 1.4.2

Pozrikidis, C. and Jankowski, D. (1997). Introduction to theoretical and computational fluid dynamics, volume 675. Oxford university press New York. 4.1.2

Prather, K., Wang, C., and Schooley, R. (2020). Reducing transmission of sars-cov-2. Science. 1.1

Pumir, A. and Wilkinson, M. (2011). Orientation statistics of small particles in turbulence. New J. Phys., 13(9):093030. 4.3.4.1

Pyke, R. (1961). Markov renewal processes: definitions and preliminary properties. Ann. Math. Stat., pages 1231–1242. 5.3.1

Quennouz, N., Shelley, M., Du Roure, O., and Lindner, A. (2015). Transport and buckling dynamics of an elastic fibre in a viscous cellular flow. J. Fluid Mech., 769:387–402. 1.15, 1.4.1, F

Qureshi, N., Bourgoin, M., Baudet, C., Cartellier, A., and Gagne, Y. (2007). Turbulent transport of material particles: an experimental study of finite size effects. Phys. Rev. lett., 99(18):184502. 1.3.1

Reuters (2020). Jellyfish keep uk nuclear plant shut. [Online; accessed November 15, 2020]. 1.1

Richardson, L. (1922). Weather prediction by numerical process. Cambridge University Press. 1.1

Rinne, H. (2008). The Weibull distribution: a handbook. CRC press. E

Risken, H. (1996). Fokker-planck equation. In The Fokker-Planck Equation, pages 63–95. Springer. D

Rosti, M., Banaei, A., Brandt, L., and Mazzino, A. (2018). Flexible fiber reveals the two-point statistical properties of turbulence. Phys. Rev. lett., 121(4):044501. 1.4.2, 1.17, 4.1.2, F

Rosti, M., Olivieri, S., Banaei, A., Brandt, L., and Mazzino, A. (2020). Flowing fibers as a proxy of turbulence statistics. Meccanica, 55(2):357–370. 1.4.2

Salazar, J., De Jong, J., Cao, L., Woodward, S., Meng, H., and Collins, L. (2008). Experimental and numerical investigation of inertial particle clustering in isotropic turbulence. J. Fluid Mech., 600:245. 1.1, 1.3.1

Saw, E., Bec, J., Homann, H., Ray, S., Dubrulle, B., and Daviaud, F. (2015). Rapid growth of coalescing droplets and observation of fine structures in turbulent flow. 1.2

Saw, E., Kuzzay, D., Faranda, D., Guittonneau, A., Daviaud, F., Wiertel-Gasquet, C., Padilla, V., and Dubrulle, B. (2016). Experimental characterization of extreme events of inertial dissipation in a turbulent swirling flow. Nat. Commun., 7(1):1–8. 2.3.1

Saw, E., Shaw, R., Ayyalasomayajula, S., Chuang, P., and Gylfason, A. (2008). Inertial clustering of particles in high-reynolds-number turbulence. Phys. Rev. lett., 100(21):214501. 1.2, 3.1.2

Schroeder, C., Babcock, H., Shaqfeh, E., and Chu, S. (2003). Observation of polymer conformation hysteresis in extensional flow. Science, 301(5639):1515–1519. 1.4.1

Sengupta, A., Carrara, F., and Stocker, R. (2017). Phytoplankton can actively diversify their migration strategy in response to turbulent cues. Nature, 543(7646):555–558. 1.1

Shapiro, M. and Goldenberg, M. (1993). Deposition of glass fiber particles from turbulent air flow in a pipe. J. Aerosol Sci., 24(1):65–87. 3.3.1

Shlesinger, M. (1974). Asymptotic solutions of continuous-time random walks. J. Stat. Phys., 10(5):421–434. 5.3.1

Shlesinger, M. and Hughes, B. (1981). Analogs of renormalization group transformations in random processes. Physica A, 109(3):597–608. 5.3.1

Siewert, C., Kunnen, R., Meinke, M., and Schröder, W. (2014a). Orientation statistics and settling velocity of ellipsoids in decaying turbulence. Atmos. Res., 142:45–56. 3.4, 3.4

Siewert, C., Kunnen, R., and Schröder, W. (2014b). Collision rates of small ellipsoids settling in turbulence. J. Fluid Mech., 758:686–701. 1.3.2, 1.12, F

Simon, J., Müller, H., Koch, R., and Müller, V. (1998). Thermoplastic and biodegradable polymers of cellulose. Polym. Degrad. Stab., 59(1-3):107–115. 1.4

Singh, R., Gupta, M., Picardo, J., Vincenzi, D., and Ray, S. (2020). Elastoinertial chains in a two-dimensional turbulent flow. Phys. Rev. E, 101(5):053105. 1.4.2, 6

SmarterEveryDay (2014). Secret of snapping spaghetti in slow motion. [Online; accessed November 2, 2020]. 1.5, 1.19, F

Smetacek, V. (1999). Diatoms and the ocean carbon cycle. Protist, 150(1):25–32. 1.4

Smoluchowski, M. (1917). Versuch einer mathematischen theorie der koagulationskinetik kolloider lösungen. F

Sommerer, J. and Ott, E. (1993). Particles floating on a moving fluid: A dynamically comprehensible physical fractal. Science, 259(5093):335–339. 1.5, F

Squires, K. and Eaton, J. (1991). Preferential concentration of particles by turbulence. Phys. Fluids A, 3(5):1169–1178. 1.3.1

Sreenivasan, K. (1995). On the universality of the kolmogorov constant. Phys. Fluids, 7(11):2778–2784. 2.3.2

Sumbekova, S., Cartellier, A., Aliseda, A., and Bourgoin, M. (2017). Preferential concentration of inertial sub-kolmogorov particles: The roles of mass loading of particles, stokes numbers, and reynolds numbers. Phys. Rev. Fluid, 2(2):024302. 1.3.1, 1.3.1

Svenning, E., Mark, A., Edelvik, F., Glatt, E., Rief, S., Wiegmann, A., Martinsson, L., Lai, R., Fredlund, M., and Nyman, U. (2012). Multiphase simulation of fiber suspension flows using immersed boundary methods. Nord. Pulp Paper Res. J., 27(2):184. 1.4.2

Sykes, C. (1994). No ordinary genius: the illustrated Richard Feynman. Weidenfeld and Nicolson London. 1.5

Szleifer, I. (1997). Protein adsorption on surfaces with grafted polymers: a theoretical approach. Biophys. J., 72(2):595–612. 1.4

Tang, M. and Szoka, F. (1997). The influence of polymer structure on the interactions of cationic polymers with dna and morphology of the resulting complexes. Gene Ther., 4(8):823–832. 1.4

Taylor, G. (1922). Diffusion by continuous movements. Proc. London Math. Soc., 2(1):196–212. 1.1

Thiaville, P. (2020). Thousands of jellyfish in the philippines. [Online; accessed November 16,-2020]. 1.2, F

Thompson, R. (2015). Microplastics in the marine environment: sources, consequences and solutions. In Marine anthropogenic litter, pages 185–200. Springer, Cham. 1.1

Thomson, D. (1990). A stochastic model for the motion of particle pairs in isotropic high-reynolds-number turbulence, and its application to the problem of concentration variance. J. Fluid Mech., 210:113–153. 1.1

Thorin, A. and Forêt, G. (2013). Calcul des structures. 4.1.1

Tornberg, A. and Shelley, M. (2004). Simulating the dynamics and interactions of flexible fibers in stokes flows. J. Comput. Phys., 196(1):8–40. 4.2, C

Toschi, F. and Bodenschatz, E. (2009). Lagrangian properties of particles in turbulence. Annu. Rev. Fluid Mech., 41:375–404. 1.3.1

Van Kampen, N. (2007). Stochastic Processes in Physics and Chemistry. North-Holland personal library. Elsevier, 3rd ed edition. D

Van Sebille, E., Wilcox, C., Lebreton, L., Maximenko, N., Hardesty, B., Van Franeker, J., Eriksen, M., Siegel, D., Galgani, F., and Law, K. (2015). A global inventory of small floating plastic debris. Environ. Res. Lett., 10(12):124006. 1.4.2

Vandenberghe, N. and Villermaux, E. (2013). Geometry and fragmentation of soft brittle impacted bodies. Soft Matter, 9(34):8162–8176. 1.5

Verhille, G. and Bartoli, A. (2016). 3d conformation of a flexible fiber in a turbulent flow. Exp. Fluids, 57(7):117. 1.16, 1.4.2, F

Verma, A., Bhatnagar, A., Mitra, D., and Pandit, R. (2020). First-passage-time problem for tracers in turbulent flows applied to virus spreading. Phys. Rev. Research, 2(3):033239. 1.1, 1.1, F

Vince, J. (2011). Quaternions for computer graphics. Springer Science & Business Media. 3.1.1

Vincenzi, D. (2012). Orientation of non-spherical particles in an axisymmetric random flow. arXiv preprint arXiv:1206.0945. 3.4, 6

Vogel, S. (2020). Life in Moving Fluids: The Physical Biology of Flow-Revised and Expanded Second Edition. Princeton University Press. 2.1

Volk, R., Calzavarini, E., Leveque, E., and Pinton, J. (2010). Dynamics of inertial particles in a turbulent von kármán flow. arXiv preprint arXiv:1001.4943. 1.3.1

Voth, G. and Soldati, A. (2017). Anisotropic particles in turbulence. Annu. Rev. Fluid Mech., 49:249–276. 1.1, 1.2, 1.3.2, 1.11, F

Watanabe, T. and Gotoh, T. (2010). Coil-stretch transition in an ensemble of polymers in isotropic turbulence. Phys. Rev. E, 81(6):066301. 1.4

Weiss, J. (1991). The dynamics of enstrophy transfer in two-dimensional hydrodynamics. Physica D, 48(2-3):273–294. 2.4.4

Weisstein, E. (2002). CRC concise encyclopedia of mathematics. CRC press. 3.1

Wikipedia (2020a). Wikipedia, the free encyclopedia. [Online; accessed December 08, 2020]. 1.3, F

Wikipedia (2020b). Wikipedia, the free encyclopedia. [Online; accessed September 1, 2020]. 2.4.3

Wikipedia (2020c). Wikipedia, the free encyclopedia. [Online; accessed November 20, 2020]. 4

Wilson, J. and Sawford, B. (1996). Review of lagrangian stochastic models for trajectories in the turbulent atmosphere. 1.1

Winker, D., Liu, Z., Omar, A., Tackett, J., and Fairlie, D. (2012). Caliop observations of the transport of ash from the eyjafjallajökull volcano in april 2010. J. Geophys. Res., 117(D20). 1.1

Xu, H. and Bodenschatz, E. (2008). Motion of inertial particles with size larger than kolmogorov scale in turbulent flows. Physica D, 237(14-17):2095–2100. 1.3.1

Xu, H., Pumir, A., and Bodenschatz, E. (2011). The pirouette effect in turbulent flows. Nat. Phys., 7(9):709–712. 4.3.4.1

Yan, B., Wang, H., Peng, Y., Hu, Y., Wang, H., Zhang, X., Chen, Q., Bedford, J., Dewhirst, M., and Li, C. (2006). A unique role of the dna fragmentation factor in maintaining genomic stability. Proc. Natl. Acad. Sci. U.S.A., 103(5):1504–1509. 5

Yeung, P., Pope, S., Lamorgese, A., and Donzis, D. (2006). Acceleration and dissipation statistics of numerically simulated isotropic turbulence. Phys. Fluids, 18(6):065103. 3.3.1

Yoshimoto, H. and Goto, S. (2007). Self-similar clustering of inertial particles in homogeneous turbulence. J. Fluid Mech., 577:275. 1.3.1

Young, Y. and Shelley, M. (2007). Stretch-coil transition and transport of fibers in cellular flows. Phys. Rev. lett., 99(5):058303. 1.4.1

Zephyr (2020). Science photo library. https://www.sciencephoto.com/media/691772/view/normal-brain-blood-flow-mri-and-spect. 2.1, F

Zhang, H., Ahmadi, G., Fan, F., and McLaughlin, J. (2001). Ellipsoidal particles transport and deposition in turbulent channel flows. Int. J. Multiph. Flow, 27(6):971–1009. 3.3.1

Zhao, L., Challabotla, N., Andersson, H., and Variano, E. (2015). Rotation of nonspherical particles in turbulent channel flow. Phys. Rev. lett., 115(24):244501. 1.3.2